LEVEL STRUCTURE OF ^{30}S AND THE ^{29}P$(p,\gamma)^{30}$S REACTION RATE

LEVEL STRUCTURE OF ^{30}S AND THE ^{29}P$(p,\gamma)^{30}$S THERMONUCLEAR REACTION RATE

By

KIANA SETOODEHNIA, B. Sc., M. Sc.

A Thesis

Submitted to the School of Graduate Studies

in Partial Fulfillment of the Requirements

for the Degree

Doctor of Philosophy

McMaster University

McMaster University DOCTOR OF PHILOSOPHY (2011)
Hamilton, Ontario (Physics & Astronomy)

TITLE:	Level Structure of ^{30}S and the ^{29}P$(p,\gamma)^{30}$S Thermonuclear Reaction Rate
AUTHOR:	Kiana Setoodehnia
	B. Sc. (Shiraz University), Shiraz, Iran, 2004,
	M. Sc. (McMaster University), Hamilton, Canada, 2007
SUPERVISOR:	Prof. Alan A. Chen
NUMBER OF PAGES:	xx, 292

Abstract

In order to determine the parent stellar sites for the presolar grains of potential nova origin, it is crucial to know the rates of the thermonuclear reactions which affect the production and destruction of silicon in novae. One such reaction is the $^{29}\mathrm{P}(p,\gamma)^{30}\mathrm{S}$. This reaction also influences type I X-ray bursts. The energy generation and nucleosynthesis in the burst, along with its duration and light-curve structure, are very sensitive to the reaction flow through a few waiting-point nuclei along the rp- and αp-process paths. In particular, network calculations show that the waiting-point nucleus $^{30}\mathrm{S}$ ($t_{1/2}$ = 1175.9(17) ms) is critical.

The structure of proton-unbound $^{30}\mathrm{S}$ states strongly determines the thermonuclear $^{29}\mathrm{P}(p,\gamma)^{30}\mathrm{S}$ reaction rate at temperatures characteristic of explosive hydrogen burning in classical novae and type I X-ray bursts ($0.1 \leq T \leq 1.3$ GK). Specifically, the rate had been previously predicted to be dominated by two low-lying, unobserved, $J^\pi = 3^+$ and 2^+ levels in the E_x = 4.7 to 4.8 MeV region.

The 3^+ resonance was observed a few years ago via a $^{32}\mathrm{S}(p,t)^{30}\mathrm{S}$ measurement. However, the 2^+ resonance remained unobserved. To search for it, we have performed a high energy resolution charged-particle spectroscopy and an in-beam γ-ray spectroscopy to investigate the level structure of $^{30}\mathrm{S}$ above the proton threshold via the $^{32}\mathrm{S}(p,t)^{30}\mathrm{S}$ and $^{28}\mathrm{Si}(^3\mathrm{He}, n\gamma)^{30}\mathrm{S}$ reactions, respectively.

In this work we provide a description of the experimental setup, data analysis and results of both experiments. Moreover, we have calculated the $^{29}\mathrm{P}(p,\gamma)^{30}\mathrm{S}$ reaction rate via state-of-the-art Monte Carlo technique, and have investigated the impact of this updated rate on the abundances of elements synthesized in novae, including those of silicon isotopes.

Acknowledgments

During my graduate studies, I had the honor to interact with many individuals and learn from them. It is not possible to mention everyone here, nevertheless, I would like to take the opportunity and sincerely acknowledge the contributions of several individuals.

First and foremost, I owe my deepest and utmost gratitude to my supervisor, Prof. Alan A. Chen. During the six years I have had the privilege to be his student, he has continually made his support available to me in a number of ways. His very considerate and regular encouragement, supervision and support from the preliminary to the concluding level enabled me to develop a better understanding of the subject. Not only did I learn from him a great deal about nuclear astrophysics, but he also taught me life lessons like generosity and kindness. Therefore, in many ways I have learned much from and because of him. One simply could not wish for a better or friendlier supervisor. I will always appreciate his wonderful suggestions and constant assistance during the course of this work, which would not have been possible without him. He became a mentor for me, and literally changed my life for the better. I will always be very much indebted to him for that.

I would also like to show my gratitude to the members of my Ph.D. committee, Dr. Reza Nejat and Profs. James C. Waddington and William E. Harris, for their guidance and their support throughout my Ph.D. course of study. Prof. Waddington has especially addressed many of my questions and concerns with the research material due to the proximity of his field of research to mine. Prof. Harris and Dr. Nejat have, on the other hand, offered much advice and insight. Being a compatriot, Dr. Nejat has helped me in many ways, for which I am grateful to him. Special thanks are also due to my external committee member, Dr. Daniel Galaviz Redondo from the Universidade de Lisboa, and my internal committee member, Prof. William V. Prestwich from McMaster University.

Furthermore, I would like to sincerely thank Prof. Peter Parker from Yale University, Prof. Shigeru Kubono from the University of Tokyo and Dr. Tetsuro Komatsubara from the University of Tsukuba for their extended direction of the experimental parts of this project. Their profound knowledge has helped me learn to carry out the experiments and analyze the data afterwards. Moreover, in my last stay in Japan, Prof. Kubono took his own time numerously to drive me to visit a doctor and also to a hospital day after day. I cannot thank him enough for that. I would also like to thank Komatsubara-san for inviting me to lunch and dinner many times, and for helping me buy green tea for my father. I would like to additionally thank Dr. Takehito Hayakawa from the Japanese Atomic Energy Agency for lending us his high purity Ge-detectors, so that we could perform the γ-ray spectroscopy measurement.

It is difficult to overstate my gratitude to Prof. William N. Lennard and Mr. Jack Hendriks from the University of Western Ontario for their assistance with making the ^{32}S implanted targets. Prof. Lennard has taught me a great deal about Rutherford backscattering, implantation and related subjects. I cannot thank him enough. He is a very knowledgable and hospitable individual, who knows almost everything about making all sorts of targets. Also I would like to thank Mr. Dominik Seiler from section E12 of the Physik Department of the Technische Universität München for kindly making the Cd target for us.

I would also like to thank Dr. Richard Longland and Prof. Jordi José, both from the Universitat Politècnica de Catalunya (Barcelona). Dr. Longland kindly performed the calculations of the $^{29}\mathrm{P}(p,\gamma)^{30}\mathrm{S}$ reaction rate with state-of-the-art Monte Carlo method, and he patiently and thoroughly answered all my questions. Prof. José, on the other hand, carried out the computational work with the stellar nucleosynthesis models of novae to determine the effect of the $^{29}\mathrm{P}(p,\gamma)^{30}\mathrm{S}$ reaction rate on the resultant stellar yields. I could not have written Chapter 5 of this thesis without their help.

I have been blessed with the acquaintance of Prof. Christian Iliadis from the University of North Carolina at Chapel Hill. He has paramountly aided me via email many times. His kind, thorough and very fast replies to my questions have always amused me. His guidance helped me calculate the input required for the calculation of the reaction rate performed by Dr. Longland.

I would also like to extend my heartfelt gratitude to Prof. Balraj Singh from McMaster University, who represents a live nuclear physics encyclopedia. He inadvertently and without fail provided me assistance with my research especially with the analysis of my γ-ray spectroscopy experiment.

I would also like to send my gratitude to Prof. Denis Burke, an emeritus faculty at

McMaster University, Prof. Peter D. Kunz, an emeritus faculty at University of Colorado, Prof. Gilles Abel from Université du Québec à Montréal and Prof. Peter Sigmund from University of Southern Denmark, who kindly and patiently responded to all my many questions and concerns with the research material, and for giving me detailed discussions on physics theory. Also, Dr. Daniel Bardayan from Oak Ridge National Laboratory (ORNL) Holifield Radioactive Ion Beam Facility has kindly provided me with software with which I could calculate the proton widths for any resonance. Moreover, Dr. Felix Liang from the same facility has assisted me with the code FRESCO. Dr. Antonio M. Moro from Universidad De Sevilla in Spain taught me for the first time how to use FRESCO to perform Distorted Wave Born Approximation calculation with coupled-reaction-channels. Dr. Moro has constantly assisted me with the questions I have had regarding FRESCO. I would like to also thank Dr. Krishichayan from Cyclotron Institute at Texas A&M University for his assistance with understanding the theory of γ-γ angular correlations.

My extra deep thanks go to Dr. Catherine M. Deibel and Dr. Jason A. Clark from Argonne National Laboratory, Dr. Christopher Wrede from University of Washington in Seattle, Dr. H. Suzuki and Dr. Tetsuaki Moriguchi from the University of Tsukuba and many other Canadian, American and Japanese post-doctoral researchers, graduate and undergraduate student-colleagues and collaborators for taking sometimes long overnight shifts during my experiments and also for their constant help with the research. Dr. Suzuki and Dr. Moriguchi specially assisted me with calculations of the angular correlation attenuation coefficients in the middle of the night during my γ-ray spectroscopy experiment.

Among my colleagues, I would like to especially acknowledge Dr. Jun Chen from McMaster University and soon to be Dr. David M. Kahl from the University of Tokyo. I have learned much from them. Jun has always welcomed my questions with a smile even when I have interrupted his own work, and has answered my wide range of questions in the kindest manner. He has impressed me with his knowledge and willingness to help. Daid has fascinated me with his intelligence and his profound knowledge in many distinct subjects at such a young age. His ability to hack computers has always amused me. Being very busy with his own Ph.D. work, collaborations and personal life, Daid was one of the editors of this thesis. I truly appreciate the time he took to write to me all the editorial points. He also helped me a great deal with understanding the signal processing and electronics, answered so many of my questions with illustrations and thorough explanations, and shared his ideas with me on how to write this thesis in a better way. I sincerely will always remember and appreciate his help and friendship. Without doubt

Jun and Daid have assisted me so much with learning physics, programming and even English.

I would like to thank the staff members of the Wright Nuclear Structure Laboratory and the University of Tsukuba Tandem Accelerator Complex. I would also wish to express my thanks to two of the staff members of our department, Mrs. Tina Stewart and Mrs. Rosemary McNeice, for being so tolerant and helpful with my excessive paper work for the numerous extended trips I had.

With a deep sense of appreciation I would like to express my sincere thanks to my parents, Sirous and Parvin Setoodehnia, and to my siblings, Kambiz and Katayoon, for their support and encouragement throughout these years. Their immense faith in my abilities was my main driving force. The sacrifices they made so that I could accomplish what I always wished for is sincerely acknowledged. I dedicate this work to my family for all their love and inspiration.

Last but not least, I thank all of those who supported me in any respect directly or indirectly during the completion of this project, whom I may have forgotten to mention.

This work was funded by the Natural Sciences and Engineering Research Council of Canada (NSERC).

Dedicated to Mom and Dad,
Kambiz and Kathy, with gratitude.

Table of Contents

List of Figures

List of Tables

List of Symbols

M_{Ch}	Chandrasekhar mass
E_x	excitation energy
Γ_γ	gamma width
$M_\odot$	solar mass
$L_\odot$	solar luminosity
Γ_p	proton width
$R_\odot$	sloar radius
E_r	resonance energy
Q	reaction Q-value
$\omega\gamma$	resonance strength
Γ	total resonance width
μ	reduced mass; centroid of the lognormal distribution
λ	de Broglie wavelength
k	Botlzmann's constant
N_A	Avogadro's number
δ_{Xa}	Kronecker delta
σ	cross section; standard deviation
E_0	Gamow energy
Δ	Gamow width
τ	nuclear lifetime
$t_{1/2}$	nuclear half-life
l	orbital angular momentum

J	nuclear spin
π	parity
C^2S	spectroscopic factor
$<\sigma\upsilon>$	stellar reaction rate per particle pair

Acronyms

ADC Analog-to-Digital Converter 56

AGB Asymptotic Giant Branch 10

BGO Bismuth Germanium Oxide 143

CAMAC Computer-Automated Measurement and Control 143

CO Carbon-Oxygen 2

CFD Constant Fraction Discriminator 58

CNO Carbon Nitrogen Oxygen 6

CV Cataclysmic Variable 4

DAQ Data Acquisition 58

DCO Directional Correlation of Oriented nuclei 130

DWBA Distorted-Wave Born Approximation 45

ESTU Extended Stretched Trans-Uranium 43

FWHM Full Width at Half Maximum 78

GDG Gate and Delay Generator 58

GUI Graphical User Interface 60

HPGe High Purity Germanium 129

IMME Isobaric Multiplet Mass Equation 35

LAM Look-At-Me 148

NIM Nuclear Instrument Module 56

NNDC National Nuclear Data Center 83

NS Neutron Star 1

NSERC Natural Sciences and Engineering Research Council of Canada vii

ONe Oxygen-Neon 2

ORNL Oak Ridge National Laboratory vi

PIDC Position-sensitive Ionization Drift Chamber 51

PSD Pulse Shape Discriminator 145

RBS Rutherford Backscattering Spectrometry 46

TAC Time-to-Amplitude Converter 54

TDC Time-to-Digital Converter 143

TPHC Time-to-Pulse-Height Converter 143

SCA Single Channel Analyzer 150

SiC Silicon Carbide 11

TNR Thermonuclear Runaway 6

TTL Transistor-Transistor Logic 143

UTTAC the University of Tsukuba Tandem Accelerator Complex 129

UWO the University of Western Ontario 47

VME Versa Module Eurocard bus 56

WD White Dwarf 1

WNSL Wright Nuclear Structure Laboratory 40

Chapter 1

Compact Stellar Objects

For those stars whose initial mass is equal to or larger than 40% of the solar mass, an extremely dense state of matter is formed at the end of their evolution. Depending on the initial stellar mass, these endpoints, in terms of increasing density, could be White Dwarf (WD) stars, Neutron Stars (NSs) or exotic objects known as black holes. Such objects are collectively referred to as the compact objects.

Here we very briefly describe two astrophysical phenomena, i.e., novae and type I X-ray bursts, that are of interest to this work, which respectively arise from explosive nucleosynthesis on the surfaces of WDs and NSs after accreting matter from their less dense companion stars.

We begin with an introduction to WDs and novae, and proceed to NSs and type I X-ray bursts.

1.1 An Introduction to White Dwarfs

Stars with initial mass of $0.4\ M_{\odot} \lesssim M \lesssim 11\ M_{\odot}$ (see p. xvii for the symbol) eventually become electron degenerate towards the end of their evolution[1]. These stars, depending on their initial mass, may lose most of their mass during the last phases of their evolutionary stage prior to becoming a WD, and give rise to planetary nebulae with

[1]The stars with initial mass of $0.08\ M_{\odot} \lesssim M < 0.4\ M_{\odot}$ are called red dwarfs. These stars also eventually become electron degenerate and turn into a helium WD; however, the time it takes for this process to complete is longer than the age of universe if such stars are single stars and are not in binary systems. Thus, such stars when observed are still in their early evolutionary stage, burning hydrogen in their cores [1] (p. 16 – 17).

central objects. Such objects are the remnants of the initial stars that have turned into small compact objects with a very high density[2] and a nearly isothermal degenerate core that supports itself by electron degeneracy pressure. Such stars are called white dwarfs. This name was used for the first time by Willem J. Luyten [3–6], and originates from the fact that the spectral type of WDs is categorized as class A (white in color). The term white dwarf was then popularized by Sir Arthur Stanley Eddington [7, 8].

1.1.1 The Properties of White Dwarfs

WDs have exhausted all their nuclear fuel, and are thus not able to produce any energy via nuclear reactions anymore, unless they are accreting matter from a nearby companion star. Thus, the single WDs cool down over many billion years or so as heat escapes through their non-degenerate envelope. Many young accreting WDs have been detected as sources of hard X-rays and soft γ-rays [9]. Some of the properties of WDs are discussed below:

- **Core Composition:**

Based on the element(s) that comprise a white dwarf's core, there are three types of white dwarfs:

(a) The least massive white dwarfs called helium WDs, whose masses vary between 0.15 $M_\odot$ to 0.45 – 0.5 $M_\odot$ [10]. Their progenitors were low-mass stars with an initial mass of $0.08 \lesssim M \lesssim 2.2\ M_\odot$ [10] that could not ignite helium in their cores. Helium WDs cannot be produced by the evolution of a single star in isolation [10]. Instead, they result from mass transfer in a close binary system.

(b) The intermediate-mass white dwarfs called Carbon-Oxygen (CO) WDs, whose masses vary between 0.45 – 0.5 $M_\odot$ up to 1.1 $M_\odot$ [10]. Their progenitors were intermediate-mass stars, whose initial masses were $2.2\ M_\odot \leq M \lesssim 9\ M_\odot$. Such stars were able to burn helium in their cores. Thus the cores of CO WDs are made of the ashes of helium burning: carbon and oxygen.

(c) The most massive white dwarfs called Oxygen-Neon (ONe) WDs, whose masses

[2]The mean density of a WD is [2]: $\rho = 2.162 \times 10^6 \times (M/M_\odot)^2$, where M is the initial mass of the progenitor of the WD under consideration. Since WDs can only be made by the stars with initial mass of $0.4\ M_\odot \lesssim M \lesssim 11\ M_\odot$, one can say that the density of a WD varies between $\sim 3 \times 10^5$ – 3×10^8 g/cm^3.

vary between 1.1 $M_\odot$ to 1.38 $M_\odot$ [10]. Their progenitors were more massive intermediate-mass stars with initial masses of $9 \leq M \leq 11\ M_\odot$. In such stars, the cores are hot enough to burn carbon and oxygen into oxygen and neon, respectively. Thus, these stars leave behind WDs whose cores are made of oxygen and neon. Traces of magnesium can be found in those WDs left behind from the most massive intermediate-mass stars that were able to burn a slight amount of Ne into Mg.

- **Mass:**

WDs are supported by electron degeneracy pressure. The maximum mass of a star that can maintain equilibrium between degeneracy pressure and gravity is called the Chandrasekhar mass limit, M_{Ch}, after the Indian astrophysicist Subrahmanyan Chandrasekhar [11]. Its value depends on the composition of the star. For an electron degenerate gas, the limiting value amounts to $\sim 1.44\ M_\odot$. Most[3] single WDs have masses in a narrow range centered at about 0.6 $M_\odot$ [13]. However, observations show that extremely low-mass helium WDs with masses less than 0.3 $M_\odot$ (with the most extreme case of $M = 0.16\ M_\odot$ [14–17]), as well as ultra-massive ONe WDs with masses greater than 1.2 $M_\odot$ (with most extreme case of $M = 1.33\ M_\odot$ [18, 19]) also exist[4]. WDs with masses $\simeq 0.2\ M_\odot$ most likely require compact binary systems [21], and can not be produced by evolution of a single low-mass star because the latter requires a time longer than the age of our universe. While WDs are the most common endpoint of stellar evolution, extremely low mass and ultra-massive WDs are very rare. For example, according to Refs. [19, 21, 24], among the 9316 WDs identified in the Sloan Digital Sky Survey [25], fewer than 0.2% have masses below 0.3 $M_\odot$.

- **Radius:**

Because WDs are electron degenerate, the more massive they are, the smaller they become. WDs have typical radii of $\sim 0.01\ R_\odot$ (see p. xvii for the symbol), which is roughly the radius of the Earth [26] (p. 21).

Having introduced the WD as an example of compact objects, we now turn our attention to the description of novae and their properties.

[3]Single metal-rich Red Giants with strong winds may evolve into single WDs with $M \simeq 0.4\ M_\odot$ [12].
[4]See Refs. [20–22] and Refs. [13, 23] for extremely low mass and ultra-massive WDs, respectively.

1.2 Novae

Roughly 50% of the stars that one observes are found in binary systems [26] (p. 191). Non-destructive periodic explosions on the surface of the WDs in close binary systems cause a sudden increase in the brightness of these otherwise faint stars in the sky. The brightness rises tremendously over a short period of time (1-3 days) through a maximum light output, which declines subsequently. Thus such stars are called novae (new stars). This term was used as early as around 75 AD [27, 28]. Novae release an enormous amount of energy in a short amount of time.

The binary nature of novae was discovered by Walker in 1954 [29]. A few years later, Kraft [30, 31] suggested that all novae are most likely close binary systems with typical orbital periods on the order of hours. Through the characteristics of the novae ejecta during and after the eruption, it is evident that these systems are binaries.

Novae are categorized as a distinct class of celestial objects. Ref. [32] provides an interesting overview of the history of classification of novae and similar objects. Novae have been classified among themselves based on their photometric and spectroscopic properties (see for instance Chapter 1 of Ref. [33]). In particular, the Williams spectral classification [34–37] is widely used for modern observations.

1.2.1 An Overview of Cataclysmic Variables

Nova producing binaries are classified into two groups: Cataclysmic Variables (CVs) and symbiotic stars. The latter systems are not of interest to this work, and are thus not explained here. Ref. [33] covers the evolution of such systems in detail. Here we only introduce the former systems without discussing the evolutionary stages of these binary systems, which can be found in Ref. [33].

CVs are defined as close binary systems with orbital separations approximately equal to $R_\odot$ [10], and short orbital periods of 76.2 – 80 min $\lesssim P_{orb} \lesssim$ 16 h [10, 38, 39], in which a CO or an ONe WD accretes matter from its companion star. In such systems the WD is called the primary star, whose mass can have a wide range up to the M_{Ch} limit, but is usually found to be between 0.5 $M_\odot$ to 1 $M_\odot$ [10, 40]. The companion star, on the other hand, is called the secondary or the donor star, whose mass is typically less than that of the primary. If the ratio of the donor's mass to that of the primary is less than

0.8, the mass transfer from the donor to the primary star via Roche lobe overflow will be stable [33] (p. 47).

Observations show that in more than 95% of all CVs, the secondary star is a low-mass main sequence star; however, in rare cases the secondary is a Red Giant, a small hydrogen rich WD or a He WD, whose mass is very low [10]. In the last case, where the secondary is more evolved than a main sequence star, the orbital period of the system is $P_{orb} \gtrsim 8$ h [33] (p. 25).

As soon as the mass is transferred from the donor to the primary through gravitational radiation [41] or magnetic braking processes [42], a CV is born. For a binary system to be called a cataclysmic variable, the mass transfer must be thermally stable [10]. The mass is transferred to the primary from a disk that surrounds it if: (a) the material in the disk loses angular momentum, which happens due to collisions between gas molecules, viscosity and shock waves; (b) the primary star rotates slowly enough, allowing inflow of material instead of expelling it centrifugally. Mass transfer rate in CVs is roughly between 10^{-11} to 10^{-8} $M_{\odot}$ per year [43, 44].

1.2.2 Classical Novae

There are different types of novae produced in CVs: dwarf novae, nova-like variables and classical novae. Among these, classical novae are the only type in which the explosions occur due to a thermonuclear burning process.

Gerasimovič [45] was possibly the first person who used the term classical nova to describe nova outbursts that recur after periods longer than 300 years. The same term was also used by Payne-Gaposchkin [46], and was generalized later by Warner [47]. However, none of the novae found in the pre-telescopic ancient records that go back to 200 BC (see Ref. [33] § 1.4, and references therein) have been seen to recur, which seems to suggest that classical novae are expected to recur with periods greater than at least a millennium [33] (p. 17). In comparison to the span of a human lifetime, such an event would seem like a one-time deal.

However, by comparing the nova frequency to the stellar death rate in a homogenous stellar population, it is shown [48] that classical novae are recurrent phenomena with a recurrency period of $\approx 10^5$ years[5] [49].

[5]In Ref. [1] (p. 30), the period of recurrency of classical novae is mentioned to be $\approx 10^4 - 10^5$ years.

The term recurrent nova [50], however, refers to a distinct type after the classification of novae into two categories [49]: classical and recurrent novae. The distinction between these two classes arises from differences in the mean binary mass transfer rate [49]. While according to the widely accepted scenario, the secondary stars in binaries that give rise to classical novae are low-mass main sequence stars, in recurrent novae the donors are Red Giants. Hence, classical novae erupt in CVs, whereas recurrent novae originate from symbiotic binaries. Typical accretion rates for classical novae amount to $\approx 10^{-10}$ – 10^{-9} $M_{\odot}$ per year, which explains the long period between explosions.

The observed classical nova frequency in the Milky Way, depending on the selection effects, is 73 ± 24 yr^{-1} [51], 29 ± 17 yr^{-1} [52], 35 ± 11 yr^{-1} [53], 30 ± 10 yr^{-1} [54] or 34^{+15}_{-12} yr^{-1} [55].

It was Kraft's original idea [30, 31], revived by Paczyński [56], that classical novae are powered by a Thermonuclear Runaway (TNR) on the surface of the degenerate WD. The TNR, whose development takes a few hours [33] (p. 168), is a series of nucleosynthetic events which causes the metals observed in the ejecta to be produced. Angular momentum losses driven by dissipative forces cause the hydrogen-rich material in the disk surrounding the WD to be accreted on the WD. This accumulated material is gradually squeezed, and forms an envelope. The material at the bottom of this envelope is heated by the strong surface gravity of the WD, and ultimately the material in the bottom layer of the envelope becomes electron degenerate. The temperature of this layer increases to the point where the hydrogen starts fusing into helium via the pp-chains [57, 58] (also see Ref. [26] (p. 198–199)) and the Carbon Nitrogen Oxygen (CNO) cycles [59, 60]. The nuclear reactions generate energy, and thus the temperature gradually rises. A major fraction of nuclei capable of capturing proton via the CNO cycles are transformed into β^+-unstable nuclei. The energy generation reaches TNR conditions. However, the degenerate matter cannot expand to accommodate the energy released by hydrogen ignition. Therefore, radiation is not the means by which energy is transported. Thus, convection sets in, and transports the β^+-unstable ashes of hydrogen burning via the hot CNO cycles, e.g., ^{13}N, ^{14}O, ^{15}O, ^{17}F and ^{18}F, to the outer cooler regions, where they decay. The sudden release of energy as a result of β^+-decays raises the temperature until it exceeds 10^8 K. This, in turn, increases the entropy of the material, and reduces the pressure. Therefore, the degeneracy is lifted. Once the matter becomes non-degenerate, it will

expand, causing the TNR to be stopped temporarily [61]. Unburned material from the lower-lying shells is transported into the H-burning shell by convection. Thus, H-burning continues. The β^+-decays generate an intense amount of heat that flattens the temperature gradient, and shuts off convection. Due to the production of a huge amount of energy by β^+-decays, the temperature rises extremely rapidly, which forces the nuclear reactions to operate in non-equilibrium burning conditions. As a result, TNR sets in again but this time the matter is non-degenerate and will expand to the point where the ejection of mass, and thus the outburst, takes place.

Classical novae are violent explosions, where the temperature reaches $0.1 - 0.4$ GK [62], and an enormous amount of energy (10^{45} – 10^{46} ergs) is released [63]. Thus, they are the third most energetic eruptions that occur in the universe[6]. They are characterized by a sudden rise in optical brightness from 8 to 18 magnitudes in one to two days, with peak luminosities reaching $10^4 - 10^5\ L_\odot$ [63].

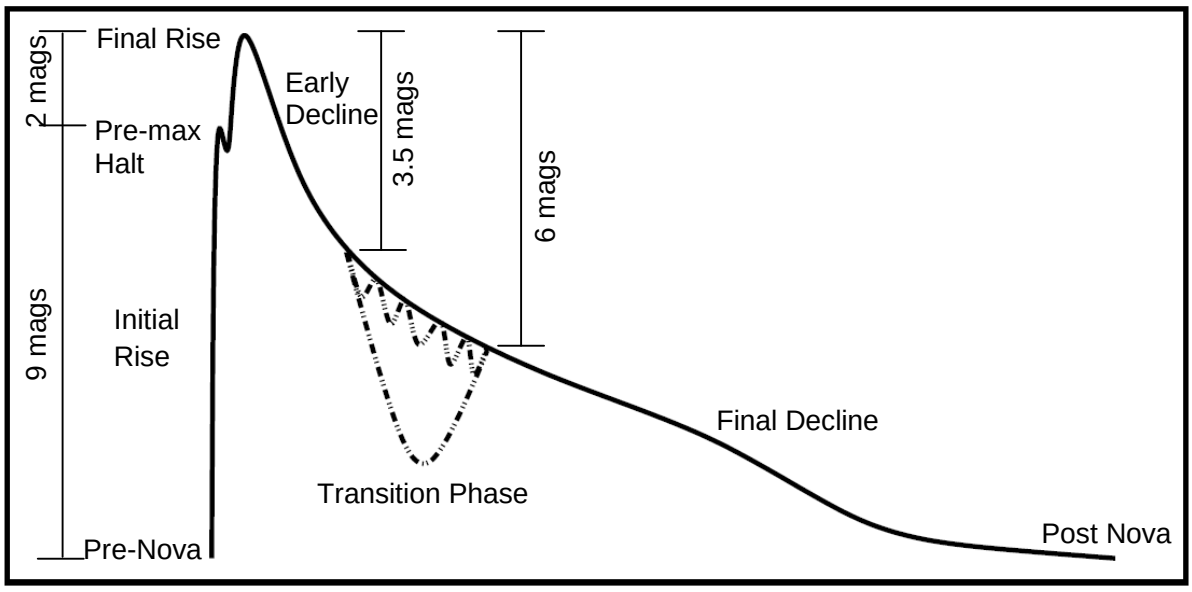

Figure 1.1: Nova light curve taken from Ref. [33] (p. 19). "Mags" indicates magnitude.

A typical classical nova light curve is shown in Fig. 1.1. The luminosity suddenly increases by up to 2 magnitudes below the maximum brightness. This process takes at most 3 days. The brightness usually stays the same at about 2 magnitudes below the maximum luminosity for a few hours to a few days, and finally rises to its maximum. The

[6]The γ-ray bursts and supernovae are respectively the first and the second most energetic explosions that occur in our universe [62].

duration of the latter phase is between 1 or 2 days up to several weeks. The brightness remains maximum for only a few hours to a few days. The luminosity subsequently begins to decline by a smooth initial fall to 3 or 4 magnitudes below the maximum. At this point, three distinct patterns are observed [33] (p. 18):

(a) Some novae fall into a minimum 7 to 10 magnitudes below the maximum, which lasts for months or even years. This minimum is due to the formation of dust in the gas ejected by the eruption [64, 65] (see § 1.2.4 of this chapter). This phase is then followed by an extrapolated decline shown in Fig. 1.1.

(b) Some novae start large amplitude oscillations with periods of $\sim 5 - 15$ days. The change in luminosity during this phase is up to 1.5 magnitudes. Many theoretical ideas have been briefly sketched as explanations for the nova oscillations (see Ref. [66] and references therein); however, since none of these ideas have been tested with independent observations [66], the cause of these oscillations has remained an open question.

(c) A few novae follow their smooth early decline without any noticeable peculiarities.

Ultraviolet observations of old novae indicate that the eruption subsides a few decades after the outburst [67]. Mass transfer from the donor star then resumes and the whole process starts over again.

A classical nova typically ejects $\approx 10^{-5} - 10^{-4}\ M_{\odot}$ [62] of formerly accreted material with mean ejection velocity of $\approx 10^3$ km/s into the interstellar medium [63]. These ejecta show significant nuclear processing relative to solar abundances. Consequently, classical novae give rise to a non-negligible enrichment of the galactic abundance of individual nuclei, e.g., ^{7}Li, ^{22}Na, ^{26}Al, ^{31}P, ^{32}S, ^{33}S, and ^{35}Cl [68] (and references therein), and are major sources of ^{13}C, ^{15}N, ^{17}O in the Galaxy. Hence, they contribute to galactic chemical evolution.

1.2.3 Explosive Nucleosynthesis in Classical Novae

The accreted materials on the WD are heated by compression and by the energy released by nuclear reactions. Hydrogen is burned via the pp-chains in hydrostatic equilibrium during the accretion phase [69]. However, during the final stages of the TNR, hydrogen is burned explosively via the hot CNO sequences [60], which are activated at temperatures higher than 100 MK and under extreme densities. In such conditions, hydrogen burns on sufficiently rapid time scales that β-unstable nuclei will live long enough

to participate in the burning process prior to their decay.

The dominant nuclear reaction flow proceeds close to the valley of stability on the proton-rich side and is dominated by a series of (p,γ) and (p,α) reactions and β^+-decays [63]. Apart from the ^{3}He$(\alpha,\gamma)^7$Be reaction[7], α- and neutron-capture reactions are completely negligible in classical novae [63].

The TNR in novae is triggered by the ^{12}C$(p,\gamma)^{13}$N reaction, and continues via the hot CNO cycle: ^{12}C$(p,\gamma)^{13}$N$(p,\gamma)^{14}$O$(\beta^+)^{14}$N$(p,\gamma)^{15}$O$(\beta^+)^{15}$N$(p,\alpha)^{12}$C. The rate of nuclear energy production via the hot CNO cycles is limited by the half-lives of the slowest and temperature-insensitive β^+-decays, in particular, ^{13}N ($t_{1/2}$ = 598 s), ^{14}O ($t_{1/2}$ = 71 s) and ^{15}O ($t_{1/2}$ = 122 s), as well as the number of seed CNO nuclei present in the envelope.

The observed classical nova ejecta show enrichment in heavy elements [70]. This requires an interaction between the WD core and the surrounding accreted envelope. The agreement between the inferred abundances and the theoretical yields not only validates the thermonuclear runaway model but also imposes limits on the nature of the mechanism responsible for the mixing [71]. However, *mixing* between the WD core material and the H-rich material in the envelope must occur for the seed nuclei to be processed to form heavier elements. This mixing is provided via shear mixing [72], elemental diffusion [73], thermal convection that dredges up the core material to the surface, or self-enrichment by Kelvin-Helmholtz instabilities [62]. Hence, the metallicity of the accreted material increases, and the accreted layers are enriched with heavy elements. This, in turn, increases the opacity of the accreted layers. Therefore, the generated heat is locked in where it is produced, and the temperature increases faster per unit mass accreted. This process will reduce the amount of material being accreted before the onset of the TNR. Thereby, the amount of material ejected by the outburst is also reduced. In general, calculations [74–76] show that the amount of accreted material before the TNR sets in, and thus the strength of the outburst in classical novae, is a function of the WD mass, luminosity and evolutionary history, as well as the composition of the accreted material [77].

The nucleosynthesis pattern in classical novae is very sensitive to details of the explosion, i.e., chemical composition, extent of convective mixing and thermal history of the envelope [71]. The nucleosynthetic endpoint of classical novae is around Ca [63]; however, recent studies [77] show that nova explosions in the most primitive low metallicity bina-

[7]This reaction bypasses the $A = 5$ gap, which cannot be bridged by a (p,γ) reaction.

ries (primordial novae, where the companion star is a metal-poor star) are more energetic than those classical novae where the companion star is a solar metallicity low-mass main sequence star. Also, primordial novae display a larger nuclear activity that extends to Ti and ends around Cu-Zn.

The composition of the nova ejecta depends on the rate of mass transfer between the WD and its companion, the process of mixing between accreted material and the material in the underlying WD core, and the history of the former outbursts of the system. The composition of the underlying white dwarf determines the species and the amount of radioactive material synthesized during nova outbursts. About 30% of novae are outbursts in the systems involving an ONe WD [78]. While short-lived radioactive nuclei ^{13}N and ^{18}F are produced in both types of novae (CO and ONe), the CO novae mainly produce ^{7}Be , whereas the ONe novae are responsible for synthesis of ^{22}Na and ^{26}Al. These isotopes are all γ-emitters, whose γ-lines can be detected, and hence help trace the energetic classical nova explosions. Because of the lower peak temperatures achieved in CO novae, and the limitations on heavy seed nuclei synthesized inside the core of the progenitor star, the main nuclear activity in CO novae does not extend much beyond oxygen. In contrast, the higher mass progenitor stars from which the ONe WDs are produced would have more diversity of heavy elements that participate in the burning process as seed nuclei after being dredged-up from the core during the ONe nova evolution. Also, being more massive, the ONe novae achieve higher temperatures. Therefore, they show a much larger nuclear activity, extending up to silicon or argon [61].

The theoretical predictions of nova nucleosynthesis involve state-of-the-art hydrodynamic models, both spherically symmetric or 1D [68, 79] (see Chapter 5) as well as 2D or 3D [80, 81].

1.2.4 Presolar Grains of Classical Nova Origin

Red Giant Branch stars, Asymptotic Giant Branch (AGB) stars, supernovae and classical novae can produce dust grains that condense in their ejecta, and are eventually ejected into the interstellar medium. Some scholars in the nuclear astrophysics community try to find such dust grains and determine their stellar paternity, which can help others understand the process of formation of such grains, which in turn help constrain our theoretical models of these stellar events.

During the formation of our solar system, the molecular cloud of gas and dust from which our solar system formed $\sim$ 4.6 billion years ago contained such dust grains. A small fraction of these tiny particles were trapped inside what later became asteroids, and therefore were protected from being vaporized as our solar system was being formed. Occasionally, asteroids collide with each other, and thus break into pieces, which may eventually fall to the Earth. These pieces are called primitive meteorites, some of which contain intact tiny dust particles that are literally bits of stars containing anomalous isotopic abundances of various elements. Because such dust particles pre-existed in our solar system's parent molecular cloud they are called presolar grains. In the context of this thesis special attention is paid to a particular type of the presolar grains, those of nova origin. As will become apparent later on, the silicon isotopic ratios in such grains can help us better understand the physics of classical novae.

Different isotopes are synthesized during stellar evolution and explosions and are ejected into the interstellar medium. They get mixed up in space. Therefore, our solar system was formed from an almost entirely homogenized mixture of elements. Hence, the isotopic ratios of the elements are almost identical throughout our solar system. The constituent atoms of presolar grains, on the other hand, are the original atoms formed in their parent source, which did not get mixed up with the atoms formed in the other stars. Therefore, the isotopic ratios in presolar grains are remarkably different from those of our solar system. Presolar grains are thus identified in the laboratory on the basis of their large isotopic anomalies.

Since their discovery [82, 83], 5 different types of presolar grains have been extracted from meteorites [84]: Silicon Carbide (SiC), graphite (C), diamond (C), silicon nitride (Si_3N_4) and oxides. The last are further categorized into three groups: aluminum oxide (Al_2O_3), spinel ($MgAl_2O_4$) and titanium oxide (TiO_2). Among these types, the SiC grains have been the most extensively studied since they are relatively abundant (6 parts per million in the Murchison meteorite [85]) and are present in various classes of meteorites [86].

The meteorites containing presolar grains are broken up and dissolved in strong acids in the laboratories to isolate the presolar grains, which are then studied by means of secondary ion mass- and resonance ionization mass-spectroscopy, ion imaging, and scanning electron- and transmission electron-microscopy [84]. By studying these extra terrestrial

dust particles that are samples of nucleosynthesis frozen in time, one can (a) compare the isotopic ratios measured in presolar grains to those measured in stars by observers, and to those predicted by theoretical models to identify the paternity of the grains; and (b) probe processes that occur inside their parent source that resulted in the formation of such atoms.

While most of the presolar grains found in meteorites have been linked to AGB stars or supernovae [87], infrared observations have confirmed the formation of carbon, SiC, hydrocarbons and O-rich silicate grains in the ejecta of classical novae, thereby suggesting that some fraction of the presolar grains identified in meteorites may come from classical novae [70].

The formation of diatomic and polyatomic molecules and eventually dust grains requires an environment that is well shielded from the increasing hard radiation fields of dramatic stellar explosions like those of novae. At first sight, hence, classical novae might seem to be a hostile environments for dust formation as they are much hotter than the interstellar medium, and possess a harsh, photo-dissociating and photo-ionizing ultraviolet radiation field many orders of magnitude stronger than that of the interstellar medium. However, dust condensation is in principle possible after about 30 – 80 days following the outburst at a critical condensation temperature of about 1000 – 1200 K [33] (p. 170 and 185). At such temperatures, the ejecta are sufficiently cool, neutral and dense that the chemical conditions are conducive to the formation of nucleation sites. Nucleation can occur in regions where there is a significant local density enhancement. This points to the outer edge of the ejecta as the place where dust grains can condense.

The first suggestion that dust forms in nova ejecta was made in 1935 [88], following the eruption of the nova DQ Her in 1934, which displayed a deep minimum in its visual light curve. Many years later, infrared photometry of another nova called FH Ser [64, 65] confirmed that the minimum in the visual light curve is attributed to the formation of dust in the nova ejecta. The formation of a minimum in the luminosity (see Fig. 1.1) is explained by the condensation of the dust cloud that makes the ejecta optically thick, and obscures the central luminous source. The dust grains then re-radiate the absorbed energy. Therefore, the thermal infrared emission rises, and continues until the grain growth ceases due to a decrease in the density of the ejecta as a result of its expansion. At that point, the visible light curve becomes optically thin again, and follows the extrapolated

smooth decline.

Efficient dust formation has been observed in novae. Diatomic molecules have vibrational and rotational transitions that can be detected in the near- and mid-infrared spectra. CN is the first molecule that was observed in the nova ejecta of DQ Her [89]. CO is another molecule that is usually detected in the early stages of a nova evolution and prior to the dust formation epoch [33] (p. 318). The molecule formation prior to the dust formation results from the high density, temperature and metallicity of the nova ejecta that enhance the reaction rates, opening certain reaction paths that are otherwise forbidden. Molecules are thus produced and destroyed on time scales of seconds to hours.

Recent studies have shown that the presence of Al, Ca, Mg and Si in an environment where the abundance of carbon is lower than that of oxygen (such as in ONe novae) can lead to the simultaneous formation of both C-rich dust, e.g., SiC and graphite, and O-rich dust, e.g., oxides and silicates [71]. Moreover, the process of condensation in the nova environment is likely to take place under a non-equilibrium conditions [90]. The processes through which dust grains form in novae are still areas of dispute and open questions still remain to be solved. For instance, despite the fact that the nova ejecta's isotopic abundances predicted from theoretical classical nova models are in general in qualitative agreement with the values measured in presolar grains, they are not quantitatively consistent with the measured values. The achievement of the latter requires some dilution processes, through which the ejecta abundances are mixed with unprocessed material of solar or close to solar abundances [71]. However, the mechanism behind such mixing processes is still unknown.

As dust grains condense, the condensing species, e.g., C in the case of carbonaceous dust and Mg and Si in the case of silicates, are increasingly depleted from the gas in the nova ejecta, and this must be reflected in the ejecta abundances. Evidence for the depletion of C, O, Mg, Si and Fe species from the ejecta where the dust has condensed has been observed [91]. Routine infrared spectroscopy of novae during eruption has revealed a rich variety of mineralogical dust types in nova ejecta, including silicates and hydrocarbons [70].

Shore *et al.* [92] provided evidence that nova grains grow rapidly to large sizes (0.2 – 0.7 μm) as a result of kinetic processes and charged particle interactions with grains that are themselves charged by the radiation field of the nova ejecta. However, Gehrz [93, 94]

showed that due to sputtering and evaporation of the more volatile components of the grains as a result of superheating by the hard radiation of the nova ejecta, the grains become smaller (0.1 – 0.3 μm) than the maximum radius to which they initially grow by the time they reach the interstellar medium.

In general, novae only contribute 3% to the interstellar dust [70], and a very small fraction ($\sim$ 0.1%) to the total Galactic dust [33] (p. 321). As a result, presolar nova grains are exceedingly rare. Historically, presolar grain candidates of nova origin were identified based on their low ^{20}Ne/^{22}Ne ratios [71, 95, 96]. The production of ^{22}Ne was attributed to the in situ decay of ^{22}Na produced in classical nova outbursts that was later locked up in the grains as they condensed from the gas in the ejecta [97]. Less than 1% of the SiC grains that are found exhibit other signatures characteristic of classical nova nucleosynthesis [86, 98, 99]: very low ^{12}C/^{13}C and ^{14}N/^{15}N ratios, very high ^{26}Al/^{27}Al ratios[8], close to or slightly lower than solar ^{29}Si/^{28}Si ratios and excesses in ^{30}Si with respect to ^{28}Si [71].

The SiC grains of potential nova origin are of special interest to this work, and in particular the silicon isotopic ratios of such grains are of special significance (see Chapters 2 and 5).

In the remaining sections of this chapter, we very briefly summarize the properties of neutron stars, and introduce type I X-ray bursts and their significance for this work.

1.3 An Introduction to Neutron Stars

Life of stars with initial mass $M \geq 11\ M_{\odot}$ is terminated by formation of an iron core followed by the core-collapse supernova explosion. What is left from such an explosion, depending on the initial mass, metallicity and mass loss history of the star prior to the outburst, can be a rapidly rotating neutron star (if the initial mass of the progenitor is less than 25 $M_{\odot}$ [100]), which supports itself by neutron degeneracy pressure.

The NSs are the densest compact objects whose surfaces can still be observed. They were called "gigantic nuclei" by Landau, who was the first to predict their existence [101]. However, the term "neutron star" was introduced to the community by the work of Baade and Zwicky [102], who also proposed that these stars are born in supernova explosions.

[8]These ratios have only been determined for two SiC grains [71].

The structure of a NS is far more complicated than a pure neutron gas, as was first suggested in the independent work of Refs. [103, 104]. The outermost layer is considered as the crust, composed of degenerate electrons and iron seed nuclei, which become progressively neutron rich towards the neutron drip line with increasing depth and pressure (towards the core) due to electron captures. Below the crust and above the core, the matter consists of superfluid neutrons in equilibrium with their decay products [105]. However, since there is no vacant low energy state for the emitted electron (from the decay of neutron) to occupy [106], only a few percent of the protons and electrons exist in the main body of a neutron star. Finally, the core material has a density ($\rho \sim 10^{18}$ kg/m^3 [106]) that is several times higher than that of normal nuclear matter. The equation of the state of matter at these densities is largely unknown, and therefore, the composition of the core material is not yet well understood. Ref. [105] discusses a few possibilities for the composition of the neuron star's core.

The NS mass range depends on its equation of the state. However, the measured masses average to $1.35 \pm 0.04\ M_\odot$ [107], and thus they cluster around M_{Ch} ($1.44\ M_\odot$). A couple of NSs have been reported recently whose measured masses are relatively high with respect to the aforementioned average mass. These masses are $1.66 \pm 0.02\ M_\odot$ [108] and $1.97 \pm 0.04\ M_\odot$ [109]. The latter is to date the highest mass measured with confidence [105]. The upper limit placed on the NS mass is recently proposed to be $M_{\rm max} \leq 2.2\ M_\odot$ [110].

No method has yet been proposed to directly measure the radius of a NS [111], and due to the yet unknown NS equation of the state, the relation between its mass and radius is poorly understood. Therefore, the NSs' radii are inferred from [105] thermal emissions from their surfaces in binaries, and from modeling the periodic oscillations observed in the light curve of the X-ray bursts. Such attempts to infer NS radii have favored relatively small values ranging from 9 – 12 km [112–114].

NSs are categorized into different groups, which are enumerated in Ref. [105]. Of principal interest to this thesis are neutron stars in binary systems. In the remaining parts of this chapter, we turn our attention to a particular close binary system involving a NS as a compact object.

1.4 Type I X-ray Bursts

Only about 5% of all neutron stars are members of a binary system [106]. This is because they are mostly formed through a supernova explosions on a single massive star. When such a massive star is initially in a binary system, the supernova explosion generally disrupts the binary system. However, in rare cases the mass ejected due to the explosion may be less than the mass that is left. The latter is the mass of the massive star's remnant (the NS) together with that of the companion star in the binary. Such scenarios can preserve the binary binding between the neutron star and the companion star [115]. Another possibility for saving the binary system from disruption could arise from the kick given to the proto-neutron star during its birth from the asymmetric supernova explosion.

In binary systems containing a NS that accretes matter from its companion, due to the very high gravitational field of the NS, a huge amount of energy is released from the impact of the matter with the NS surface. Therefore, the high surface temperature of the NS gives rise to thermal emissions in the X-ray range. Such binaries thus belong to X-ray binaries.

X-ray binaries exhibit bursting behavior where the luminosity rises by at least an order of magnitude and declines subsequently. Depending on the mass and metallicity of the companion star, and the magnetic field of the NS in the binary, the process of accretion [1] (p. 31 – 32) and the accretion rate can vary.

Type I X-ray bursts ($T = 0.4$ – 1.3 GK) are possibly the most frequent thermonuclear explosions in the universe, and are recurrent energetic thermonuclear flashes in a thin layer on the surface of accreting neutron stars. They exhibit a sharp rise time (1 – 10 seconds) in their luminosity, which is followed by a thermal decline, and softening of the X-ray spectrum [106]. The recurrency period of such bursts varies between hours to days and sometimes even longer. Type I X-ray bursts release 10^{39} – 10^{40} ergs of energy. In contrast, type II X-ray bursts are caused by accretion instabilities as opposed to thermonuclear burning. This latter rare class of objects shows extremely rapid fluctuations in their luminosity that are repeated after only a few minutes.

In what follows, we very briefly explain the processes through which the material is synthesized in type I X-ray bursts.

1.4.1 Explosive Nucleosynthesis in Type I X-ray Bursts

The matter that is accreted from the companion star onto the surface of the NS is rich in hydrogen and helium. Upon impact with the surface of the NS, this matter is heated up to 0.1 GK. The fully ionized matter is compressed in a thin electron degenerate shell as accretion continues. Such temperature and densities are high enough to stably fuse hydrogen into helium via the hot CNO cycles [60].

According to simulations of type I X-ray bursts, the accretion rate ($\dot{M}$) is a significant parameter determining the burning regime [116]. If the accretion rate is low enough ($\dot{M}$ = 2×10^{-10} – 1×10^{-9} $M_{\odot}$/yr [116]), then the hot CNO cycles exhaust hydrogen locally, and a hydrogen free shell made of pure helium is produced, which is called the helium shell. Helium burning is then initiated in such a shell via the triple-α reaction: $\alpha + \alpha \rightleftharpoons {}^{8}\mathrm{Be} + \alpha \rightarrow {}^{12}\mathrm{C}$. Burning continues up to the production of ^{40}Ca by a series of (α, γ) reactions [106]. The helium burning in the pure helium shell, in turn, triggers explosive hydrogen burning on the freshly accreted layer by raising its temperature, and thus lifting its electron degeneracy.

On the other hand, the ignition occurs in the mixed (via convection) hydrogen and helium layer if $\dot{M} \sim 4 \times 10^{-10}$ – 2×10^{-8} $M_{\odot}$/yr. At such high accretion rates, the simultaneous helium burning and the breakout from the hot CNO cycles[9] in the hydrogen shell trigger explosive hydrogen burning. The TNR itself is driven by the so-called rp- and the αp-processes, which convert the initial material rapidly in to iron-peak nuclei and beyond.

The rp-process occurs after the burst ignites, and represents a sequence of rapid proton captures and β^{+}-decays along the proton drip line. The proton drip line nuclei are proton unbound, and therefore, the Q-values for (p, γ) reactions on such nuclei are negative. They are thus photo-disintegrated, and the burning only continues after they β^{+}-decay. Hence, the nucleosynthesis flow has to wait for a time equal to the β^{+}-decays half-lives. Nuclei with long β-decay half-lives, which are in (p, γ)–(γ, p) equilibrium, are called waiting point nuclei. Examples of these nuclei are [117]: ^{22}Mg, ^{30}S, ^{34}Ar, ^{38}Ca, ^{56}Ni, ^{60}Zn, ^{64}Ge, ^{68}Se, ^{72}Kr, ^{76}Sr and ^{80}Zr. The rp-process leads to the synthesis of nuclei up to $A \approx 100$ [118] or slightly beyond [119].

[9]The breakout reactions are the $^{15}\mathrm{O}(\alpha, \gamma)^{19}\mathrm{Ne}$ and $^{18}\mathrm{Ne}(\alpha, p)^{21}\mathrm{Na}$ reactions, which operate at 0.2 GK and 0.9 GK, respectively.

The αp-process, in turn, is characterized by a sequence of (α, p) and (p, γ) reactions that bridge the β^+-decays at waiting point nuclei between $18 \leq A \leq 40$, processing the ashes of the hot CNO cycles up to ^{34}Ar. Beyond this isotope, due to high Coulomb barriers involved, the (α, p) reactions become insignificant contributors to the reaction flow.

In the next chapter, we discuss the significance of ^{30}S, which is the nucleus of interest in this work, in the context of classical novae and type I X-ray bursts.

Chapter 2

Stellar Thermonuclear Reaction Rate Formalism

We now proceed to present a summary of the theoretical formalism that enables us to explicitly and quantitatively calculate stellar thermonuclear reaction rates as a function of temperature.

Astrophysical reaction rates describe the change in abundances of nuclei owing to nuclear processes in an astrophysical environment, such as a hot plasma composed of free electrons and atomic nuclei.

2.1 Stellar Thermonuclear Reaction Rate

The kinetic energy available to various particles in stellar interiors is that of their thermal motion. Hence, stellar fusion reactions, which take place among nuclei of light elements to form heavier ones, are induced by thermal motion, and are thus called thermonuclear reactions [120]. Such reactions are responsible for energy production and nucleosynthesis in stars.

In a simple classical picture, in a thermonuclear reaction of the form $X + a \rightarrow Y + b$, each reactant nucleus can be given a geometrical area, and the areas of both reactants together is referred to as the cross section of reaction, which is denoted by σ.

Even at very high temperatures inside the stellar cores, only very few of the reacting nuclei reach speeds comparable to that of light. It is therefore not necessary to involve

relativistic kinematics.

The quantum effect of tunneling through the Coulomb barrier, discovered by G. Gamow [121], enhances the occurrence of the stellar thermonuclear reactions, and requires the cross section of a reaction to be strongly energy- or equivalently velocity-dependent such that $\sigma = \sigma(\upsilon)$, where υ is the relative velocity between the reactant nuclei.

Despite extreme densities and pressures, the stellar plasma behaves as an ideal gas. When this gas is in thermodynamic equilibrium, each individual nucleus or electron in the hot gaseous stellar plasma has a Maxwell-Boltzmann velocity distribution [122], which is given by [123] (Chapter 3):

$$\Phi_i(\upsilon_i) = \left(\frac{m_i}{2\pi kT}\right)^{3/2} \exp\left(\frac{-m_i\upsilon_i^2}{2kT}\right) \tag{2.1}$$

such that

$$\int_0^\infty \Phi_i(\upsilon_i)\, d^3\upsilon_i = 1 \tag{2.2}$$

where m_i and υ_i are the mass and velocity of the i^{th} particle, and k and T are Boltzmann's constant and the temperature, respectively. Equations (2.1) and (2.2) remain true even for electron and neutron degenerate environments such as white dwarfs and neutron stars, since the nuclei on the surface of such stars still form a normal, albeit dense, gas [124].

In the center-of-mass frame, the total stellar reaction rate per particle pair $<\sigma\upsilon>$ (in units of $\mathrm{cm^3\,mol^{-1}\,s^{-1}}$) is given by (the details are presented in Refs. [123, 125] (Chapter 3 and Chapter 12, respectively)):

$$N_A <\sigma\upsilon> = \left(\frac{8}{\pi\mu}\right)^{1/2} \frac{N_A}{(1 + \delta_{Xa}) \times (kT)^{3/2}} \int_0^\infty E\sigma(E) \exp\left(\frac{-E}{kT}\right) dE \tag{2.3}$$

where N_A is the Avogadro's number; E is the center-of-mass energy and is equal to $\mu\upsilon^2/2$, where μ is the reduced mass; and to avoid counting the identical reactant pairs twice, the total stellar reaction rate must be multiplied by $(1 + \delta_{Xa})^{-1}$, where δ_{Xa} is the Kronecker delta.

The total stellar thermonuclear reaction rate per particle pair is thus found by folding the interaction cross section $\sigma(E)$ with the appropriate energy distribution of the interacting particles in the plasma.

To evaluate the integral in the above equation, it is required to know how the reac-

tion cross section $\sigma(E)$ varies with energy. The specific nuclear properties of the reactant nuclei determine whether the fusion reaction is of non-resonant or resonant form. Depending on each case, the functional form of $\sigma(E)$ is different, and thus the dependence of the total stellar reaction rate on energy will also be different for each case.

2.2 Non-Resonant Reaction Rate

The cross sections of some reactions, e.g., Coulomb excitation, nucleon stripping, nucleon pickup and charge exchange reactions, vary smoothly with incident kinetic energy [125] (p. 31). These so-called direct reactions are single-step transitions between the initial and final states that proceed very quickly ($\sim 10^{-22}$ s [126]). In such reactions there is very little change between initial and final states of the target nucleus. The direct reactions are more likely to occur with heavier projectiles at high incident energies such that the projectiles have de Broglie wavelengths whose scales are similar to the nucleon's size. Therefore, direct reactions only involve interactions between the projectile and very few nucleons on the surface of the target nucleus.

Each state of a nucleus corresponds to a particular state of motion of all the nucleons [127] (p. 2). Direct reactions are expected to populate low-lying excited states in a given nucleus because due to the proximity of the low-lying levels to the ground state, their structures are similar to the latter, having only some minor rearrangement in the state of motion of the nucleons. Some excited states in a given nucleus are stable against particle emission, and are therefore called bound states. They decay via γ-ray or β-emission. Usually, the first few excited states that are still close to the ground state are among the bound states. In contrast, those excited levels which are unstable against particle emission are called resonances, and they have higher excitation energies than the bound states. The higher energy resonances involve major rearrangement of nucleons, and thus are less likely to be populated by direct reactions [127] (p. 5). Hence, the rate of direct reactions is usually dominated by non-resonant contributions.

For those projectiles with incident energies well below the height of the Coulomb and centrifugal barriers of the reactants, the s-wave[1] tunneling probability depends exponen-

[1]The centrifugal barrier vanishes for orbital angular momentum $l = 0$; therefore, clearly the tunneling probability is the highest for $l = 0$, which indicates s-wave transitions.

tially on the Sommerfeld parameter η, which is defined below [123] (p. 156):

$$2\pi\eta = 31.29 Z_X Z_a \sqrt{\frac{\mu}{E}} \tag{2.4}$$

where E is the center-of-mass energy in keV, μ is the reduced mass in amu and Z is atomic number. Due to the exponential behavior of the barrier penetrability, the cross section of the charged-particle-induced nuclear reactions also drops rapidly for incident energies below the Coulomb barrier, and its dependence on energy is of the form [123] (p. 157):

$$\sigma(E) = \frac{1}{E} \exp(-2\pi\eta) S(E) \tag{2.5}$$

where $S(E)$ is called the astrophysical S-factor, and contains all the strictly nuclear effects [123] (p. 157). It does not have a strong energy dependence, and is therefore a smoothly varying function of energy. For this reason, it is often used to extrapolate measured cross sections to low astrophysical energies, where it is difficult to determine the very small cross sections of reactions directly through measurements in laboratories.

By substituting equation (2.5) into equation (2.3), the total stellar reaction rate per non-identical particle pair becomes [123] (p. 158):

$$N_A <\sigma\upsilon> = \left(\frac{8}{\pi\mu}\right)^{1/2} \frac{N_A}{(kT)^{3/2}} \int_0^\infty S(E) \exp\left(\frac{-E}{kT} - \sqrt{\frac{E_G}{E}}\right) dE \tag{2.6}$$

where E_G is called Gamow energy (in MeV) and is defined as [123] (p. 158):

$$E_G = 0.978 \times (Z_X Z_a)^2 \mu \tag{2.7}$$

The strong dependence of the integrand in equation (2.6) on energy comes from the $e^{-E/kT}$ factor, originating from the Maxwell-Boltzmann distribution, and the Gamow factor ($e^{-\sqrt{E_G/E}}$), originating from the barrier penetrability. The former approaches zero for large energies, while the latter vanishes at low energies. The integral in equation (2.6) cannot be solved analytically. Hence, one usually uses the saddle-point method or the method of steepest descent [122, 128]. The product of the two strong energy-dependent factors in equation (2.6) as shown in Fig. 2.1, gives rise to the so-called Gamow peak

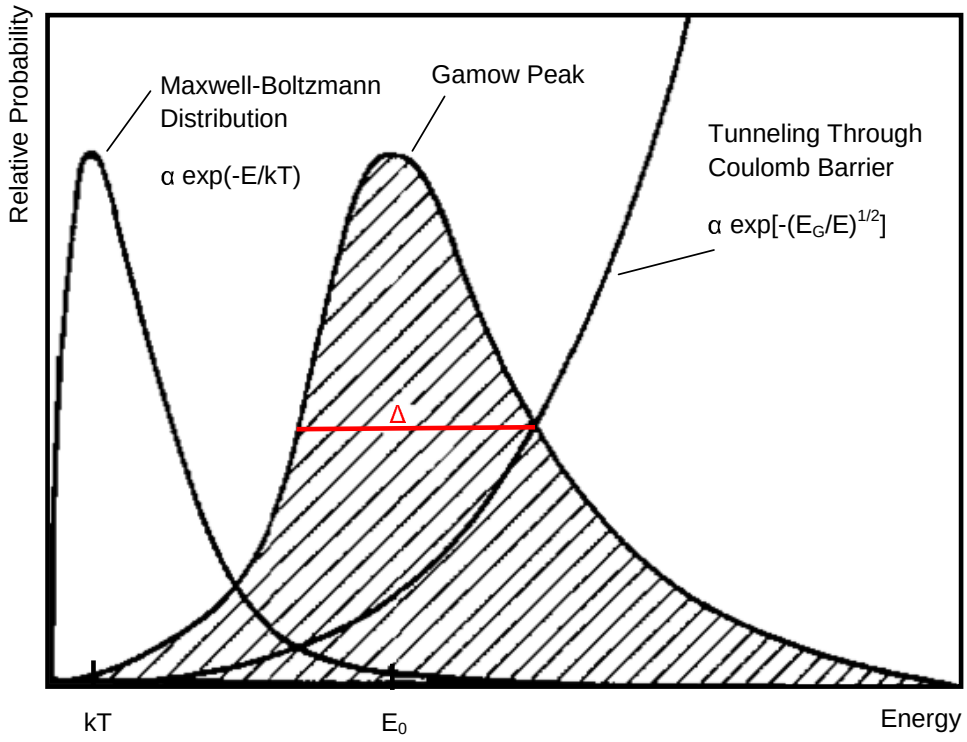

Figure 2.1: The dashed area (not to scale) depicts the Gaussian function derived by convolution of the Maxwell-Boltzmann energy distribution and the penetrability factor. This Gaussian function peaks at the Gamow peak with energy E_0, which is calculated by taking the first derivative of the integrand in equation (2.6). The $1/e$ width of the Gaussian, Δ, is shown by a red band. The area enclosed between the $1/e$ points of a Gaussian function amounts to 84% [129]. The figure is adopted from Ref. [123].

whose centroid is at the energy E_0 defined below [123] (p. 160):

$$E_0 = \left(\frac{kT\sqrt{E_G}}{2}\right)^{2/3} = 1.22\,(Z_X^2 Z_a^2 \mu T_6^2)^{1/3} \tag{2.8}$$

where T_6 is the temperature in units of MK, and E_0 is in units of keV. Out of all the nuclei available to react in stellar fusion reactions, only a small portion, whose energies fall within the Gamow window are capable of fusing together. Therefore, the Gamow peak represents the energy range of effective stellar burning at a given temperature. The Gamow window therefore also defines the energy window within which the reaction cross section has to be known.

In Fig. 2.1, the $1/e$ width of the Gaussian function, whose centroid is located at E_0

is equal to Δ (in keV), which is defined below [123] (p. 161):

$$\Delta = \frac{4}{\sqrt{3}}\sqrt{E_0 kT} = 0.749\,(Z_X^2 Z_a^2 \mu T_6^5)^{1/6} \tag{2.9}$$

For many non-resonant reactions, the astrophysical S-factor is not a constant term, and instead it varies weakly with energy. In most cases, it is adequate to expand the S-factor around $E = 0$ in a Taylor series as follows [1] (p. 181):

$$S(E) \approx S(0) + S'(0)E + \frac{1}{2}S''(0)E^2 \tag{2.10}$$

where the primes indicate derivatives with respect to E, and $S(0)$, $S'(0)$ and $S''(0)$ are in units of MeV·b, b and b/MeV, respectively. Finally, by substituting equation (2.10) into equation (2.6), and after performing some algebra[2], the non-resonant stellar reaction rate per non-identical particle pair can be obtained from the following relations [130] (see also Ref. [1] (Chapter 3)):

$$N_A <\sigma v> = \left(\frac{4}{3}\right)^{3/2} \frac{\hbar N_A}{\pi \mu Z_X Z_a e^2}\, S_{eff}\, \tau^2\, e^{-\tau} \tag{2.11}$$

$$\tau = 4.2487 \left(Z_X^2 Z_a^2 \mu \frac{1}{T_9}\right)^{1/3} \tag{2.12}$$

$$S_{eff} = S(0)\left[1 + \frac{5}{12\tau} + \frac{S'(0)}{S(0)}\left(E_0 + \frac{35}{36}kT\right) + \frac{1}{2}\frac{S''(0)}{S(0)}\left(E_0^2 + \frac{89}{36}E_0 kT\right)\right] \tag{2.13}$$

where S_{eff} in equation (2.13) is given in units of MeV·b, e is the electronic charge and k denotes the Boltzmann's constant.

Another example of non-resonant reactions is the direct capture reaction, which is of the form $X + a \rightarrow Y + \gamma$. Such reactions arise from the capture of the projectile (a) directly into a bound state of the final compound nucleus[3] (Y), together with the emission of a γ-ray with an energy of $E_\gamma = E_i + Q - E_x$, where E_i is the initial projectile's energy, Q is the reaction Q-value, and E_x is the excitation energy of the bound state in the final compound nucleus Y, to which the projectile is captured. Such single-step processes are thus straight transitions from an initial state to the final state.

[2]This algebra is explained in detail in Chapter 4 of Ref. [123] and also in Chapter 3 of Ref. [1].
[3]See the next section for definition of the compound nucleus.

The direct capture reactions are not to be confused with direct reactions. The former are entirely electromagnetic transitions. However, they are considered to be non-resonant reactions because they only involve bound states, and can occur at all projectile energies with a cross section that varies smoothly with incident energy [123] (p. 169).

2.3 Resonant Reaction Rate

Contrary to non-resonant direct reactions, where only one or two nucleons take part in the process [126], there is another type of reaction mechanism, in which the light projectile has low incident energy, and thus its de Broglie wavelength is of the size of the whole target nucleus. Hence, the interaction does not involve an individual nucleon in the target, and instead the projectile is fused with the target, and produces an excited system called the compound nucleus. The latter stays together for a sufficiently long time ($\sim 10^{-18}$ to 10^{-16} s [126]), so that its excitation energy is shared uniformly among its constituent nucleons, which include the incident projectile. This redistribution of energy among many nucleons is initiated by the collision between the projectile and the target, and is finally due to successive collisions between nucleons in the compound nucleus.

When sufficient energy is localized on one or a small group of nucleons through random collisions, they escape from the compound nucleus, and thus the latter system de-excites. This two-step process (formation and subsequent decay of the compound nucleus) is schematically shown by $X + a \rightarrow \mathrm{C}^* \rightarrow Y + b$. If sufficient excitation energy still remains in the final nucleus Y, it will successively decay.

Direct and compound nuclear reactions are not mutually exclusive [131] (p. 68). They both can contribute to a given reaction leading to a particular final state.

A compound nucleus exhibits discrete quasi stationary quantum states, which have a high probability of formation if the center-of-mass energy in the entrance channel $X + a$ matches their excitation energy. In other words, if:

$$Q + E_r = E_x \tag{2.14}$$

where Q is the Q-value of the reaction between nuclei X and a, and thus is the threshold energy; E_r is the so-called resonance energy; and E_x is the excitation energy of a discrete

level in the compound nucleus.

In contrast to bound states, the resonances are those states in the compound nucleus whose excitation energies are above the threshold energy, and therefore the decay channel via re-emission of the particle a for these states begins to be energetically possible. The higher the energy of these states with respect to the threshold, the more unstable they are against particle emission.

Both bound states and resonances in a given nucleus, as well as the ground states of radioactive nuclei, are unstable and will decay. The amount of excitation energy they possess determines the number of channels via which they can decay. For the case of the bound states only two decay channels are energetically possible, and those are the γ-ray and/or β-emission. For resonances, particle emission is also possible. The higher the resonance energy, the heavier the particles that can be re-emitted to de-excite the final nucleus that is formed through a particular resonance.

The effect of such instabilities is to give such a decaying state an imprecise energy due to the Heisenberg uncertainty principle. Therefore, the excitation energies can be considered to have a Gaussian probability distribution with a characteristic total width Γ that is related to the lifetime of the state (τ) via [131] (p. 70):

$$\Gamma = \frac{\hbar}{\tau} = \frac{\hbar \ln 2}{t_{1/2}} \tag{2.15}$$

where $t_{1/2}$ is the half-life of the state. While the excitation energies are typically on the MeV scale, their widths are on the keV scale or much smaller.

Due to formation of resonances in compound nuclear reactions, the rates of such reactions are dominated by resonant contributions. Since the compound nuclear reactions proceed through two steps, their cross section is proportional to the partial widths for the formation and decay of the compound state:

$$\sigma \propto \Gamma_a \Gamma_b \tag{2.16}$$

where Γ_a and Γ_b are the partial widths in the entrance (formation of the compound nucleus) and exit (decay of the compound nucleus) channels, respectively. Γ_b itself can refer to the particle partial width or the γ-ray partial width if more than one decay channels are open, i.e., energetically allowed.

Whether or not a resonant state can be formed via a given reaction channel depends on the selection rules, which originate from angular momentum and parity conservation laws. The former requires that:

$$J_a \oplus J_X \oplus l = J \tag{2.17}$$

where J is the spin of the final resonant state, J_a and J_X are respectively the spins of the projectile and target, and l is the orbital angular momentum. Parity conservation requires that:

$$\pi(J_a)\pi(J_X)(-1)^l = \pi(J) \tag{2.18}$$

where $\pi(J_a)$, $\pi(J_X)$ and $\pi(J)$ are the parities of the projectile, target and final resonant state, respectively.

The presence of a resonance causes a sudden major increase in the cross section of the compound nuclear reactions at energies that are close to the resonance energy. Likewise, at resonance energies the astrophysical S-factor also varies strongly with energy, and one observes peaks in the curve of S-factor *vs.* energy that correspond to resonances.

The cross-section of resonant nuclear reactions can be derived [132, 133] and generalized to all isolated resonances for which the total widths are small compared to the difference in energy between neighboring resonances (in other words, the level density in the compound nucleus is small enough such that the resonances do not overlap significantly in amplitude). The so-called Breit-Wigner formula for the cross-section (in units of barn) of isolated resonances has the following form [1] (p. 192):

$$\sigma_{BW}(E) = \frac{\lambda^2}{4\pi} \frac{2J + 1}{(2J_a + 1)(2J_X + 1)} (1 + \delta_{Xa}) \frac{\Gamma_a \Gamma_b}{(E - E_r)^2 + \left(\frac{\Gamma}{2}\right)^2} \tag{2.19}$$

where λ is the de Broglie wavelength; E is the center-of-mass incident energy; E_r is the center-of-mass resonance energy; Γ_a is the energy-dependent partial width for the formation of the compound nucleus, and corresponds to the entrance channel; Γ_b is the energy-dependent partial width for the decay of the compound nucleus, and corresponds to the exit channel; and Γ is the energy-dependent total width of the resonance or the compound state, and is defined as the sum of the partial widths of all open decay channels

of that resonance:

$$\Gamma = \Gamma_a + \Gamma_b + \cdots \tag{2.20}$$

In the above expression, Γ_a and Γ_b each has to be summed over all possible values of orbital angular momenta and channel spins [1] (p. 192).

There are two kinds of resonances: narrow and broad. The latter are not of interest to this work[4], and thus are not explained here. Refs. [1, 123] give a detailed description of broad resonances and the corresponding reaction rate theory. Depending on the type of the resonances we are dealing with, the resonant stellar reaction rate has a different formalism. Here we only describe that of the narrow resonances.

2.3.1 Narrow Resonance Reaction Rate Formalism

Different definitions are used in the literature to define narrow resonances: a narrow resonance is one whose total width Γ is much smaller than its energy ($\Gamma \ll E_r$) [123] (p. 173); narrow resonances are those whose total widths Γ are much smaller than the width of the Gamow window Δ at a given temperature [1] (p. 203); or a resonance is called narrow if the corresponding partial widths and the Maxwell-Boltzmann factor ($e^{-E/kT}$) are approximately constant in energy over the total resonance width [129].

Considering the last definition of the narrow resonance, the Maxwell-Boltzmann function $e^{-E/kT}$ changes very little over the resonance region, and can be replaced by its value at the resonance energy E_r. In addition, the de Broglie wavelength λ can be replaced by $h/p = 2\pi\hbar/\sqrt{2\mu E}$. Finally, by substituting equation (2.19) into equation (2.3), the stellar reaction rate per non-identical particle pair for a single narrow resonance becomes [1] (p. 192):

$$\begin{aligned} N_A <\sigma\upsilon> &= \left(\frac{8}{\pi\mu}\right)^{1/2} \frac{N_A}{(kT)^{3/2}} \int_0^\infty E\sigma_{BW}(E) \exp\left(\frac{-E}{kT}\right) dE \\ &= N_A \frac{2\hbar^2\sqrt{2\pi}}{(\mu kT)^{3/2}} \exp\left(\frac{-E_r}{kT}\right) \omega \frac{\Gamma_a\Gamma_b}{\Gamma} \int_0^\infty \frac{\Gamma/2}{(E - E_r)^2 + \frac{\Gamma^2}{4}} dE \\ &= N_A \left(\frac{2\pi}{\mu kT}\right)^{3/2} \hbar^2 \exp\left(\frac{-E_r}{kT}\right) \omega\gamma \end{aligned} \tag{2.21}$$

[4] As shall be seen in Chapter 5, the resonances of interest in ^{30}S are all narrow resonances. Therefore, broad resonance reaction rate formalism in inapplicable to this work.

where the quantity $\omega\gamma$ is proportional to the area under the resonance cross section, and is referred to as the resonance strength defined below:

$$\omega \equiv \frac{(2J + 1)(1 + \delta_{Xa})}{(2J_a + 1)(2J_X + 1)} \tag{2.22}$$

$$\gamma = \frac{\Gamma_a \Gamma_b}{\Gamma} \tag{2.23}$$

Therefore, the reaction rate for the narrow resonance case depends on two experimentally measurable parameters, i.e., the resonance energy and strength. When the compound nucleus has more than one isolated narrow resonance inside the Gamow energy window, they all contribute significantly to the resonant cross section, and thus to the reaction rate, as long as the partial width for the decay of each resonance (Γ_b) remains much larger than that of its formation (Γ_a). Therefore, their contributions to the resonant reaction rate per non-identical particle pair add incoherently as follows [1] (p. 193):

$$N_A <\sigma\upsilon> = 1.5399 \times 10^{11} \frac{1}{(\mu T_9)^{3/2}} \sum_i (\omega\gamma)_i \exp\left(\frac{-11.605\, E_{ri}}{T_9}\right) \tag{2.24}$$

where the incoherent sum is over all narrow resonances i. In the above expression, the resonance energies E_{ri} and resonance strengths $(\omega\gamma)_i$ are in units of MeV, and T_9 is the temperature in units of GK. Depending on the resonance energy and strength, it may be the case that the resonant stellar reaction rate is completely dominated by one or a few resonances located inside the Gamow window. In such cases, the lower the resonance energy, the higher its contribution to the reaction rate owing to the Maxwell-Boltzmann exponential factor.

As a rule of thumb, if the energy window covered by $E_0 - 2\Delta$ to $E_0 + 2\Delta$, where E_0 and Δ are respectively the Gamow peak and width, happens to also cover a narrow resonance located at E_r, then the narrow resonance formalism is applicable [129]. The total stellar thermonuclear reaction rate is thus evaluated by adding the non-resonant and resonant reaction rates together at a given temperature.

Very recently, the method of evaluating the expressions of the total stellar thermonuclear reaction rate and its uncertainty as a function of temperature was improved to include statistical probability distributions based on state-of-the-art Monte Carlo tech-

nique. It is beyond the scope of this work to discuss this method. It is explained in full detail in Refs. [129, 134–136], and is used to evaluate the $^{29}\mathrm{P}(p,\gamma)^{30}\mathrm{S}$ reaction rate (see Chapter 5).

The formalism discussed so far was for the "laboratory" reaction rates, assuming that the reactant nuclei are not interacting via Coulomb forces with the free electrons in the stellar plasma or with the other charged-particles, and that the nuclei are in ground states. In reality, however, attraction of free electrons modifies the potential well of the nuclear interaction, decreases the Coulomb barrier, and thus increases the reaction cross section and the thermonuclear reaction rate. On the other hand, at higher temperatures the reactant nuclei in stars can also be thermally excited, and thus the excited states also participate in nuclear reactions. Therefore, in a stellar environment the reaction rates are enhanced.

To include the electron screening effect, the thermonuclear reaction rates presented here must be multiplied by an electron shielding factor f as given in Refs. [137–139], and in Ref. [123] (p. 167 – 168). Stellar enhancement corrections are explained in Ref. [1] (p. 159).

Having described an established procedure of reaction rate estimation, we will now turn our attention to the astrophysical reaction of interest for this work. The ultimate goal of this work is to find the rate of the $^{29}\mathrm{P}(p,\gamma)^{30}\mathrm{S}$ reaction, which has a Q-value of 4394.9(7) keV[5]. The compound nucleus in this reaction is ^{30}S, whose excited states lie both below and above the proton threshold. Therefore, both non-resonant contributions (via proton-capture directly into the bound states of ^{30}S) and resonant contributions to the $^{29}\mathrm{P}(p,\gamma)^{30}\mathrm{S}$ reaction rate have to be considered. Here we first elucidate the importance of ^{30}S.

2.4 Astrophysical Significance of ^{30}S

Sulfur has 24 known isotopes ranging from the most proton-rich isotope, ^{26}S, to the most neutron-rich isotope, ^{49}S, all of which have 16 protons inside their nucleus. Among these isotopes, the stable and naturally occurring ones are ^{32}S, ^{33}S, ^{34}S and ^{36}S with abundances of 95.02%, 0.75%, 4.21% and 0.02%, respectively.

[5]The updated Q-value is calculated from the $^{30}\mathrm{S}_{g.s.}(\beta^+)^{30}\mathrm{P}_{g.s.}$ decay energy measured in Ref. [140].

In this thesis, the main focus is on ^{30}S, which is located on the proton-rich side of the stability line near the beginning of the rp-process reaction path [141], and which β^+-decays to ^{30}P with $t_{1/2} = 1175.9(17)$ ms [140]. ^{30}S was discovered independently by Johnson *et al.* [142] and Robinson *et al.* [143]. A few years later, the positron decay of the ground state of this isotope was restudied by means of a magnetic spectrometer for the first time [144].

Nuclear structure plays an important role in understanding many astrophysical phenomena. Among the structures of all nuclear species that are synthesized via proton capture reactions during explosive hydrogen burning in classical novae and type I X-ray bursts, ^{30}S structure becomes very important in understanding the silicon isotopic abundances in nova ejecta; and the energy generation, nucleosynthesis, light-curve structure and duration of type I X-ray bursts.

In the following the connection between ^{30}S nuclear structure and the aforementioned astrophysical scenarios will be discussed in more detail.

2.4.1 Influence of ^{30}S on the Identification of Presolar Grains of Classical Nova Origin

Presolar grains of potential nova origin were discussed briefly in § 1.2.4. There are a number of critical studies to tighten the links between nova nucleosynthesis and presolar grains: systematic infrared observations are required to understand dust formation in the CO and ONe novae [145]; the mixing between the material in nova ejecta and the solar-like material has to be understood to be able to account for the dilution of the isotopic abundances observed in the grains [33] (p. 131) with respect to those predicted by the simulations; and finally a better knowledge of the rates of the reactions that affect nova nucleosynthesis is required to better comprehend the origin of the isotopic ratios observed in the nova presolar grain candidates. Improving the reaction rates can also constrain nova models and simulations, and affect our understanding of nova energetics and nucleosynthesis [145] (and references therein).

The main nucleosynthesis paths in the thermonuclear runaway that lead to nova outbursts, and the abundances produced therein, can be inferred from the details of the explosions, e.g., the chemical composition of the white dwarf, the extent to which the

convective mixing occurs, and the thermal history of the envelope [71]. Such details can be partially obtained via the laboratory analysis of the silicon isotopic abundance ratios (^{29}Si/^{28}Si and ^{30}Si/^{28}Si) in presolar grains of potential nova origin [71], owing to the fact that the abundances of ^{28}Si and ^{29,30}Si respectively provide us with information on the nature of the underlying white dwarf's core (CO *vs.* ONe), and the peak temperatures achieved during the nova outburst [71], and consequently the overall composition of the nova ejecta.

To explore and improve the silicon isotopic abundances in nova ejecta predicted from nova simulations, the thermonuclear reactions that most strongly affect the synthesis of silicon in novae must be determined and their rates understood. Two such reactions are ^{29}P$(p,\gamma)^{30}$S and ^{30}P$(p,\gamma)^{31}$S. The latter reaction is under investigation by other researchers [146]. Therefore, this work only pursues the former reaction.

Fig. 2.2 on page 33 shows the main nuclear reaction paths in the Si-Ca mass region of an ONe nova [147]. Under the assumption that over the temperature range characteristic of explosive nucleosynthesis in novae (0.1 – 0.4 GK) the ^{30}P$(p,\gamma)^{31}$S reaction rate is slower than the ^{30}P β^+-decay, then if the ^{29}P$(p,\gamma)^{30}$S reaction rate is faster than the β^+-decay of ^{29}P, the net effect is an increase in the production of ^{30}Si via the ^{29}P$(p,\gamma)^{30}$S$(\beta^+)^{30}$P$(\beta^+)^{30}$Si reaction sequence, as well as a simultaneous decrease in the abundance of ^{29}Si, which is the product of the β^+-decay of ^{29}P. Therefore, an excess in ^{30}Si together with the depletion in ^{29}Si observed in some SiC presolar grains could indicate imprints of a nova origin because for instance, no supernova zone is predicted to have enhancements of ^{30}Si and depletion of ^{29}Si at the same time [33] (p. 130). The latter could be because the ^{30}P$(p,\gamma)^{31}$S reaction rate becomes faster than the ^{30}P β^+-decay rate at the higher temperature range characteristic of supernovae. Of course, higher than solar ^{30}Si/^{28}Si and only slightly above solar (or lower than solar) ^{29}Si/^{28}Si ratios must be accompanied by the other isotopic ratios characteristics of nova nucleosynthesis in a particular SiC presolar grain such as very low ^{12}C/^{13}C and ^{14}N/^{15}N ratios, etc.

In a study on the sensitivity of nova nucleosynthesis to uncertainties in thermonuclear reaction rates [148], a change in the ^{29}P$(p,\gamma)^{30}$S rate by 10^4, which was consistent with the rate limits from Ref. [149], resulted in significant changes in ^{29,30}Si abundances by a factor of 3. The ^{29}P$(p,\gamma)^{30}$S reaction rate also affects the subsequent production of ^{31}P, ^{33}S, ^{34}S, ^{35}Cl, ^{36}Ar, ^{37}Ar, ^{37}Cl, ^{38}Ar, ^{39}K and ^{40}Ca nuclei significantly [150]. It therefore

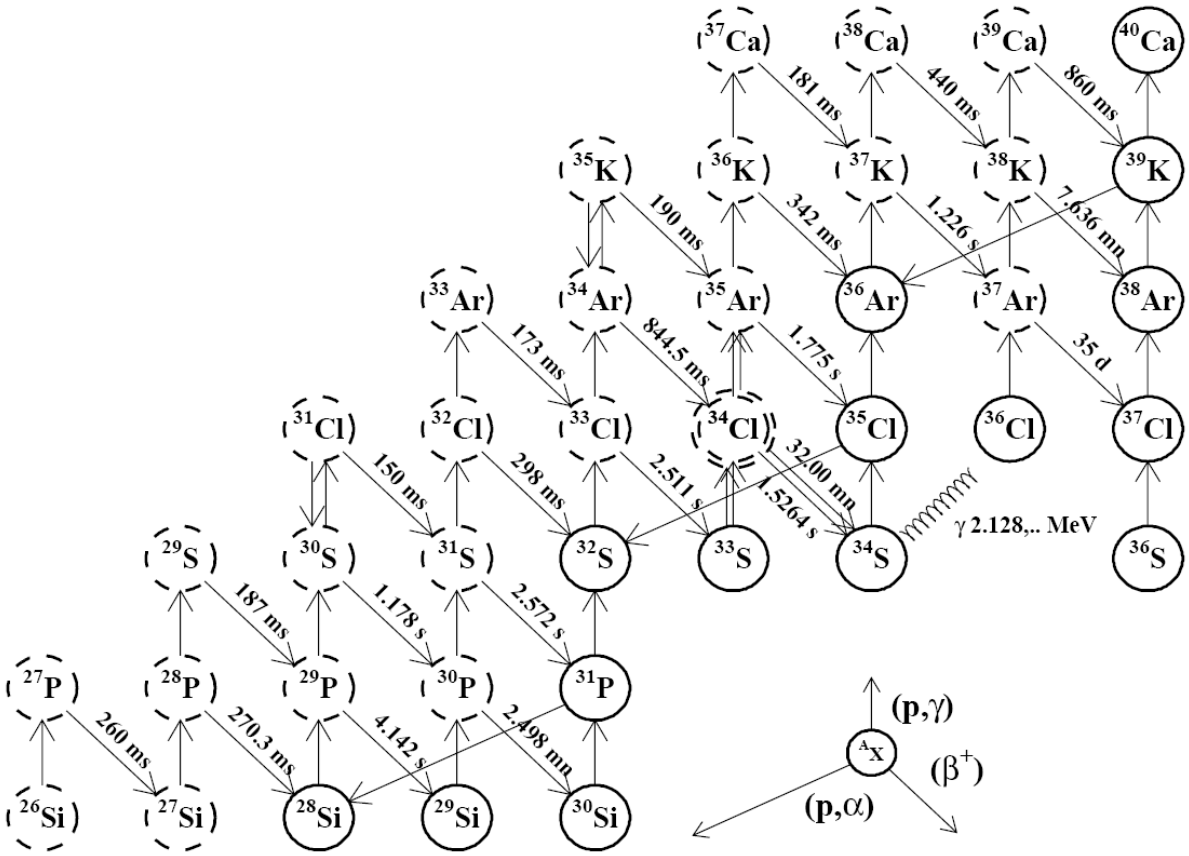

Figure 2.2: The main nuclear reaction paths in the Si-Ca mass region of an ONe nova. The stable and radioactive nuclei are shown by solid and dashed circles, respectively. The numbers on the diagonal arrows indicate the half-lives of the corresponding processes. The half-life of ^{30}S has recently been measured to be 1175.9(17) ms [140]. Thus, the value of 1.178-s shown in the figure is from an older measurement [151]. The figure is adopted from Ref. [147].

has a profound influence not only on the silicon isotopic abundances, but also on the abundances of isotopes heavier than silicon.

The nuclear structure of ^{30}S is important in the determination of the ^{29}P$(p,\gamma)^{30}$S reaction rate as a function of temperature. The occurrence (or non-occurrence) of a certain state at a given excitation energy in ^{30}S can change dramatically the ^{29}P$(p,\gamma)^{30}$S reaction rate, and thus the abundances of the aforementioned elements.

2.4.2 ^{30}S As a Waiting Point in Type I X-ray Bursts

The structure of proton unbound resonant ^{30}S states is also important for determining the ^{29}P$(p,\gamma)^{30}$S reaction rate in the temperature range characteristic of explosive

hydrogen burning in type I X-ray bursts with $0.4 \leq T \leq 1.3$ GK.

The thermonuclear runaway in type I X-ray bursts takes place in the so-called ignition region at the bottom of the accreted envelope, where there is a sudden and rapid increase in nuclear energy generation in the material, whose initial composition is characterized by heavier nuclei with a relatively low helium abundance compared to the accreted matter [117]. As the temperature rises in the ignition region, the proton capture branches become more dominant than the β^+-decays, and the rp-process path leads to the production of ^{30}S via the $^{27}\mathrm{P}(\beta^+,\,\nu)^{27}\mathrm{Si}(p,\gamma)^{28}\mathrm{P}(p,\gamma)^{29}\mathrm{S}(\beta^+,\,\nu)^{29}\mathrm{P}(p,\gamma)^{30}\mathrm{S}$ reaction sequence [117].

The energy released by nuclear reactions in the ignition region raises the temperature in the shallower regions directly above the ignition region, where the density is lower and the helium abundance is higher. When the temperature reaches beyond 10^9 K, the environment is extremely hot and the $(p,\gamma)/(\gamma,p)$ ratio decreases [106] because there are more photons at the tail of the Maxwell-Boltzmann distribution that have enough energy to disintegrate the nuclei whose $Q_{(p,\gamma)}$ is less than 3 MeV [152]. Therefore, the flow through proton capture reactions will be decreased eventually, and the rp-process is altered by a sequence of (α,p) and (p,γ) reactions known as the αp-process. ^{30}S is also produced in the region above the ignition region via the $^{25}\mathrm{Al}(p,\gamma)^{26}\mathrm{Si}(\alpha,p)^{29}\mathrm{P}(p,\gamma)^{30}\mathrm{S}$ reaction sequence [117].

^{30}S can be destroyed via the proton- or α-capture reaction or by β^+-decay. The $^{30}\mathrm{S}(\alpha,p)^{33}\mathrm{Cl}$ reaction has a low cross section [106]. The $^{30}\mathrm{S}(p,\gamma)^{31}\mathrm{Cl}$ reaction, on the other hand, has such a low Q-value (284(7) keV [153]) that a (p,γ)–(γ,p) equilibrium is established between ^{30}S and ^{31}Cl resulting in the photo-disintegration of ^{31}Cl back to ^{30}S. Therefore the latter nucleus prevents a significant reaction flow via proton captures beyond itself, and hence the reaction flow must instead pass through $^{30}\mathrm{S}(\beta^+,\,\nu)^{30}\mathrm{P}$. However, this reaction is the slowest weak interaction in the reaction flow [117] because ^{30}S has a half-life of $t_{1/2} = 1.1759(17)$ s, which is comparable to the typical burst rise time of a few seconds. Thus, ^{30}S causes a significant bottleneck for the reaction flow to ensue. Network calculations confirm that the waiting-point nucleus ^{30}S is a critical one [117, 154] that influences the timescale of the explosion, the energy generation of the burst, and the structure of the resulting light curve [154]. In particular, the $^{29}\mathrm{P}(p,\gamma)^{30}\mathrm{S}$ reaction is the link leading to ^{30}S production in type I X-ray bursts. In burst simulations, this

reaction has been found to be one of the most important reactions in the overall flow as the temperature approaches its peak [155].

The ^{29}P$(p,\gamma)^{30}$S rate was evaluated by Wiescher and Görres [156], and more recently by Iliadis *et al.* [149]. The latter found that their calculated rate was dominated by the 3^+_1 and 2^+_3 proton unbound states in ^{30}S; however, these two states had not been observed in any experiments up to that time. Their energies were thus predicted using the Isobaric Multiplet Mass Equation (IMME) to be 4733(40) keV and 4888(40) keV, respectively. Such large uncertainty in the excitation energies translated, in turn, into large uncertainties in the resonance energies, E_r, and thus a rate uncertainty of orders of magnitude [149], since the rate depends exponentially on E_r.

Without the precise knowledge of the location of the two astrophysically important resonances of ^{30}S that dominate the ^{29}P$(p,\gamma)^{30}$S rate at temperature range of 0.1 – 1.3 GK, the rate of this reaction in the temperature range corresponding to explosive hydrogen burning in novae and type I X-ray bursts remained poorly understood prior to the present study.

2.4.3 ^{30}S Nuclear Structure Studies prior to this Work

After the discovery of ^{30}S [142, 143], the next investigations on this nucleus started with the work of Frick *et al.* [144] via the ^{28}Si(^{3}He, n)^{30}S reaction, where the half-life of ^{30}S was remeasured and the Q-value for the ^{30}S$_{g.s.}(\beta^+)^{30}$P$_{g.s.}$ decay branch was determined. The ^{28}Si(^{3}He, n)^{30}S reaction has been used extensively ever since to investigate the excitation energies of ^{30}S. McMurray *et al.* [157] and Miller *et al.* [158] were among the first to measure the ground state Q-value for the ^{28}Si(^{3}He, n)^{30}S reaction. Later, Frantsvog *et al.* [159] measured the absolute cross section of the ^{28}Si(^{3}He, n)^{30}S reaction as a function of bombarding energy via the charged-particle activation method.

During the time between the experiments of McMurray *et al.* and Frantsvog *et al.*, the excitation energies, spin-parities, differential cross sections, angular distributions and two-nucleon transfer spectroscopic amplitudes (see Chapter 5) of the ground state and a few low-lying bound states of ^{30}S were measured by means of charged-particle spectroscopy experiments via the ^{28}Si(^{3}He, n)^{30}S reaction, and mostly with neutron time-of-flight techniques [157, 158, 160–167]. In all the aforementioned experiments except that of Ref. [164], only a few of the bound states of ^{30}S were populated, and the resulting

excitation energies suffered from rather large uncertainties.

The first published[6] investigation of the energies and spin-parities of the ^{29}P + p resonances in ^{30}S was performed by Paddock [168] via the ^{32}S$(p,t)^{30}$S two-nucleon transfer reaction, using silicon surface barrier detectors. In this experiment, excited states of ^{30}S up to 7.6 MeV were populated. Furthermore, Yokota *et al.* [169] studied the ^{30}S nuclear structure via the ^{28}Si(^{3}He, $n)^{30}$S(p) reaction sequence, and were able to observe the states up to 7.5 MeV. ^{30}S was investigated via a heavy-ion transfer reaction mechanism, with the ^{28}Si(^{12}C,^{10}Be)^{30}S two-proton stripping reaction for the first time [170], and among the states that were populated, some had high energy and spin, e.g., the 6.7 MeV, 8.3 MeV and 9.9 MeV states with $J^{\pi} = 5^{-}$, 6^{+} and (6^{+}), respectively.

Meanwhile, the decay modes, lifetimes and branching ratios of the low-lying levels of ^{30}S were investigated by γ-ray spectroscopy experiments via the ^{28}Si(^{3}He, $n\gamma)^{30}$S reaction, with Ge(Li) detectors [171–173]. Subsequently, Alexander *et al.* [174] also performed a measurement with similar techniques and aims.

In more recent years, elastic scattering and Coulomb excitation measurements on ^{30}S have been performed using a ^{30}S radioactive ion beam [175–178], and useful information has been obtained, e.g., the deformation parameter and the ratio of the multipole transition matrix elements[7] M_n/M_p, etc.

Conjointly, valuable information about the structure of ^{30}S has been obtained via β^{+}-decay studies: Axelsson *et al.* [179] studied the $\beta 2p$ decay of ^{31}Ar. A few years later, Fynbo *et al.* [180, 181] measured the excitation energies of ^{30}S up to 7.9 MeV via the same decay sequence as used by Axelsson *et al.* (^{31}Ar$(\beta^{+})^{31}$Cl(p)^{30}S(p)).
Tables 2.1 to 2.3 summarize the information available chronologically (prior to this work) on the level structure of ^{30}S.

As was discussed earlier, the properties of ^{30}S excited levels become important for determining the ^{29}P$(p,\gamma)^{30}$S reaction rate. At the stellar temperatures characteristic of explosive hydrogen burning in novae and type I X-ray bursts (0.1 – 1.3 GK), the Gamow window of the ^{29}P$(p,\gamma)^{30}$S reaction (Q = 4394.9(7) keV [140]) spans $E_{cm} \approx 700$ – 1770

[6] M. H. Shapiro (University of Rochester) performed an experiment to study the excited states of ^{30}S either prior to the experiment presented in Ref. [168] or at the same time, but his work was left un-published (see Table V and Ref. [25] in Ref. [168]).

[7] This quantity reveals the relative contribution of protons and neutrons to the excitation of a nucleus. M_p is related to the reduced transition probability $B(E2)$ by $B(E2) = M_p^2$ if the transition is from an initial 0^{+} state to a final 2^{+} state.

Table 2.1: Energy levels of ^{30}S prior to this work. The excitation energies are all in keV. Spin and parity assignments are separated from the energies by a dash.

Ref. [157] (^{3}He, n)	Ref. [158] (^{3}He, n)	Ref. [160] (^{3}He, n)	Ref. [163] (^{3}He, n)	Ref. [164] (^{3}He, n)
g.s. – 0^+	g.s. – 0^+	g.s.	g.s. – 0^+	g.s. – 0^+
2210(30) – 2^+	2190(40) – 2^+	2113(15)	2190(30) – (2^+)	2220(25) – (2^+)
3430(30) – 2^+		3291(15)	3390(30) – (2^+)	3410(30) – (0^+)
3710(30) – 0^+			3660(30) – 0^+	3690(30) – (2^+)
				5210(50) – (3^-)
				6110(50) – (5^-)

keV. Therefore, the ^{29}P$(p,\gamma)^{30}$S reaction rate is dominated by contributions from isolated and narrow ^{29}P + p resonances corresponding to ^{30}S states with $4.47 \lesssim E_x \lesssim 6$ MeV.

After the prediction by Iliadis *et al.* [149] indicating that there were two astrophysically important unobserved resonances in ^{30}S, attempts were made to find these two states [150, 182–185]. Bardayan *et al.* [150] remeasured the excitation energies and spin-parities of the states of ^{30}S up to 7.1 MeV by means of the ^{32}S$(p,t)^{30}$S two-nucleon transfer reaction and silicon detectors, and with a better energy resolution than that of Paddock's experiment [168]. In their experiment, a state at 4704(5) keV was discovered and was proposed to be the predicted 3^+_1 state. However, no trace of the other important level was found.

The structure of particle unbound states in ^{30}S remains poorly understood [186, 187]. Hence, further studies are strongly motivated, and in addition to the present work, experiments at several laboratories (e.g., National Super Conducting Laboratory [182, 185], University of Notre Dame [184, 188], and Argonne National Laboratory [183]) are attempting to address these questions.

The main focus of this thesis is on two experiments used to determine the excitation energies and spin-parities of several states of ^{30}S. In both these experiments, the excited states of ^{30}S were populated via two nucleon transfer reactions, namely, ^{32}S$(p,t)^{30}$S and ^{28}Si(^{3}He, $n\gamma)^{30}$S. Such indirect methods to study the properties of the levels of ^{30}S are important, because a direct measurement of the ^{29}P$(p,\gamma)^{30}$S reaction is currently not feasible, since no ^{29}P radioactive ion beam with the required beam intensity ($> 10^8$ pps)

Table 2.2: Continuation of Table 2.1.

Ref. [167][a] (^{3}He, n)	Ref. [168] (p,t)	Ref. [169] (^{3}He, n)^{30}S(p)	Ref. [170] (^{12}C,^{10}Be)	Ref. [172] (^{3}He, $n\gamma$)
g.s. – 0^+	g.s. – 0^+		g.s. – 0^+	
2210 – 2^+	2239(18) – 2^+		2210 – 2^+	2209.9(11)[b]
3400 – 2^+	3438(14) – 2^+			3402.2(14)
3660 – 0^+				3664.2(13)
	3707(25) – (0^+)			
		5145(10)	5140 – (3^-)	
	5207(22)			
	5306(25)	5288(10) – 3^-		
	5426(25)	5425(10) – (1,2)		
	5897(27)	5912(10) – (3,4)		
	(6108(29))	6117(10) – 1^-,(2^+)		
	(6223(30))	6233(10)		
	6415(40)	6393(10) – 0^+		
		6584(10) – (2,3)		
		6810(10)	6700 – 5^-	
	6861(40)	6838(10) – $\geq$4		
		6919(10) – (3,4)		
	7185(35)	7133(10) – (1,2)		
		7294(10) – $\geq$3		
		7338(10) – (1,2)		
		7475(10)		
	7570(45)			
			8300 – 6^+	
			9900 – (6^+)	

[a]The measured excitation energies are uncertain by ± 20 keV to ± 30 keV.
[b]Ref. [171] reports a state at 2210(1) keV, which is the only state observed.

is available.

Table 2.3: Continuation of Table 2.1.

Ref. [173] (^{3}He, $n\gamma$)	Ref. [180] ^{31}Ar(β^+)^{31}Cl(p)^{30}S(p)	Ref. [150] (p,t)	Ref. [188] (^{3}He, n)
		g.s. – 0^+	g.s.
2210.7(5) – 2		2210.7 – 2^+	2200
3402.6(5) – (1,2)		3402.6 – 2^+	
3667.5(10)			
3676(3) – 1		3680(6) – (1^+)	3600
		4704(5) – (3^+)	
5136(2) – (4)			5100
		5168(6) – $4^+ + 0^+$	
	5217.4(7)		
	5389(2)	5383(8) – $(3^-,2^+)$	
	5842(4)	5843(5) – (1^-)	
	(5945(3))		
	6064(3)	6071(11)	6100
	6202(3)		
	6280.1(12)		
	6338.6(14)	6341(5)	
	6541(4)	6532(13)	
	(6643(3))		
	6762(4)	6766(10) – 2^+	
	6855(4)		
	6927(4)		
	7078(7)	7074(9)	
	7123(10)		
	(7237(5))		
	7295(14)		
	7352(8)		
	7485(4)		7400
	7598(4)		
	7693(4)		
	7924(5)		8000
			8700
			9200
			9700

Chapter 3

The ^{32}S$(p,t)^{30}$S Experiment

This chapter presents the experimental setup, data analysis and the results of a charged-particle spectroscopy[1] experiment carried out at the Wright Nuclear Structure Laboratory (WNSL) at Yale University. The reaction under study was ^{32}S$(p,t)^{30}$S, and the experiment was carried out so as to investigate the properties of the ^{30}S excited states above the proton threshold up to $\sim$ 6.8 MeV, with a particular interest in two states, whose energies were previously predicted to be just below 5 MeV [149].

3.1 Experimental Details

The ^{32}S$(p,t)^{30}$S experiment was performed over a total period of 12 days distributed over November-2007, May-2008 and January-2010. There was also a five-days long beamtime scheduled for January-2009; however, due to a technical difficulty, which resulted in the malfunctioning of the detector, that beamtime was all lost, and the data turned out to be useless for the analysis.

The following section is devoted to the experimental apparatus and the setup.

3.1.1 The Ion Source at WNSL: Beam Production

The ions making up a beam are produced in an ion source. A good ion source is capable of providing rather high currents and high charge states of various ion species, whose energy spread is minimum, to allow for measurements with diverse beams. The

[1] The science and study of the spectra is called spectroscopy.

area of the ion-emitting aperture in the ion source must be small enough, so that the beam can be focused on a small spot size [189]. The emittance and brightness of an ion source [189–191] determine the beam diameter, intensity and angular divergence when it emerges from the source [123] (p. 192). The last of these must be kept as small as possible to transmit the beam particles with minimum loss through the acceptance of the next apparatus along the beam line.

Unlike many accelerators, tandem accelerators require negative ions upon entrance. Therefore, the ion sources used in conjunction with the tandem accelerators generate negative ions via charge exchange, high voltage dissociation, sputtering, direct extraction from a plasma or surface ionization, which are well explained in Refs. [192–196]. Among the aforementioned processes, those ion sources utilizing sputtering generate intense currents with low emittance; are reliable and easy to maintain; require small power input; can produce diverse elemental and molecular negative ions, and thus are versatile. Furthermore, the negative ion beam species can be rapidly changed if necessary. As a result, sputtering ion sources are widely used with tandem accelerators. The ion source used for this work at WNSL is also of the sputtering kind.

When a solid surface is bombarded by energetic ions, both neutral and charged particles are ejected by the process known as sputtering. After a milestone paper published by Krohn [197], Middleton *et al.* [198] developed a sputtering ion source utilizing cesium as the bombarding ions. Much work was done to improve this ion source (see Refs. [196, 199–201] and the references therein). Finally, independent studies [202–205] led to development of a cesium sputtering ion source, one of which is used at WNSL.

For this source to operate, neutral cesium atoms are admitted in the form of vapor into a chamber called the ionization chamber. These atoms strike the inner surface of the chamber, which is made of tungsten and is kept at 1000° – 1100° C. Since cesium has a low ionization energy (3.89 eV), when it hits tungsten whose work function is high (4.53 eV), the least bound electrons of the cesium atoms are lost to the tungsten surface. Therefore, the cesium atoms become positive ions via surface ionization process. These ions are then focused to a small spot via an einzel lens and are accelerated towards the exposed tip of the sputter cathode, which is kept at negative potential with respect to the ionization chamber.

The cathode is made of copper, and has a small conical-shaped hole drilled into it,

which is located on the front side exposed to the cesium vapor. The element or compound of interest, which makes up the beam species, should be in the form of a powder compressed and hammered by a tamping tool into the few millimeters-deep hole inside the cathode. The cathode is kept cooled, and therefore, some of the neutral cesium condenses on the front of the cathode exposed to the cesium vapor. Bombarding the beam material in the hole with energetic positively-charged cesium ions results in another sputtering process. Some materials will preferentially sputter negative ions. Other materials will preferentially sputter neutral or positive particles, which pick up electrons as they pass through the condensed cesium layer, producing negative ions. Thus, a large fraction of the sputtered beam ions are negatively charged. The conical shape of the hole inside the cathode serves as an immersion lens to focus the negative ions, which are accelerated to energies up to a few tens of keV towards an extraction electrode, and are focused more properly upon exiting the ion source by the second einzel lens.

To perform the $^{32}\mathrm{S}(p,t)^{30}\mathrm{S}$ experiment, a $^{1}\mathrm{H}^{+}$ (or proton) beam was employed. Since not all elements have positive electron affinities, some inevitably must be in molecular forms, usually a hydride or an oxide. To produce the proton beam, a TiH_2 powder was pressed into the cathode's hole. Titanium hydride powder was chosen specifically because it is an excellent choice for production of H^- beams with rather high intensities [206] (p. 17 – 19).

The cathode was then mounted into the sputtering ion source, where the energetic Cs ions collided with the TiH_2 molecules in the ion-source to produce H^-, TiH^-, TiH_2^- and TiH_3^- ions. If the titanium hydride had any impurity, other molecular or atomic species would also become negatively ionized.

With analogy to normal light optics, beam ions travel similarly like light rays. Light can be focused with mirrors and lenses but in the case of an ion beam, lenses have to be substituted with electric and magnetic fields. Following the extraction from the ion source, all these negatively charged ions were steered via magnetic steerers onto an injector, where they are pre-accelerated to energies up to 200 keV by a 300 kV negative ion injector mounted in 1993 [207]. This injector contains a double focusing, multi-pole corrected 90° bending magnet, and is able to inject beams with all masses from 1 to 250 amu with a mass resolution of 1/200 [207] into the tandem accelerator for the final acceleration stage. From the pre-accelerating platform to the tandem accelerator, the

beam reached intensities of up to 20 μA [207].

The bending magnet downstream of the injector had a magnetic field set such that it would only let H^- beam pass through. Thus, all other molecular or atomic species were stopped at this magnet, whereas, the H^- ions were injected into the tandem accelerator to be accelerated further.

3.1.2 The Yale ESTU Tandem Van de Graaff Accelerator

The WNSL at Yale University [208] (Fig. 3.1) operates the second largest[2] stand-alone electrostatic Extended Stretched Trans-Uranium (ESTU) tandem Van de Graaff accelerator (see Ref. [209] and references therein).

It is 98 feet long and 25 feet in diameter, and consists of a large central terminal, which has five high voltage modules on each side. Each of these modules is 8 feet long [207]. Pure SF_6 gas is used in the accelerator tank as an insulator to prevent corona discharge. The accelerator operates at voltages of up to 20 – 22 MV [210] by transporting and building up charge via Pelletron chains [211]. For the $^{32}S(p,t)^{30}S$ experiment, the terminal voltage was held at $\sim$ 17.24 MV, which was obtained.

Upon entering the tandem accelerator, the negative beam ions (H^-) were further accelerated towards the positively charged terminal located half-way through the accelerator. In the terminal, the H^- ions hit a carbon stripper foil, whose thickness is a few $\mu g/cm^2$.

The so-called equilibrium thickness, over which the probability that a beam particle loses an electron while interacting with the stripper foil becomes equal to that of the beam particle picking up an electron, requires much thicker foils [212–214]. However, the lifetime of the carbon stripper foils depends on the methods by which they are manufactured, their thickness, and the beam characteristics, e.g., energy and mass. The thinner the carbon foil, the less power per unit area is deposited onto the foil by the beam particles as they lose energy while passing through the foil. Therefore, the thinner the foils, the more durable they are [215].

After the H^- beam impinged on the stripper foil inside the terminal, the ions were stripped of their electrons via the carbon stripper foil, therefore becoming positively

[2]The world's largest tandem Van de Graaff accelerator is a vertical accelerator and is operating at ORNL.

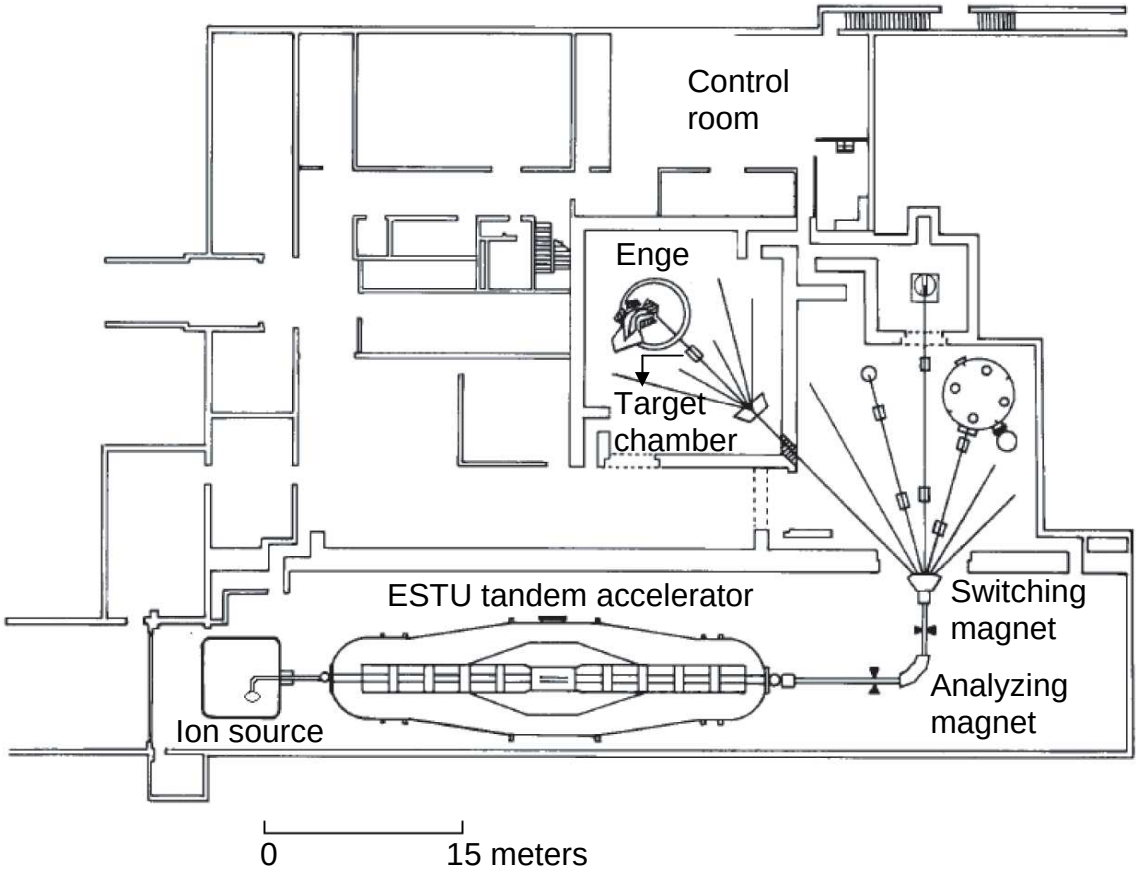

Figure 3.1: Schematic diagram of the Wright Nuclear Structure Laboratory at Yale University. This figure is adopted from Ref. [210].

charged. These positive beam ions were further accelerated back to the ground potential as they were rejected by the positively charged terminal.

Leaving the accelerator, the H^+ beam particles entered an analyzing magnet (see Fig. 3.1 on page 44), which bends a beam of charge q, mass m, velocity v and energy E through a ± 0.5 mm aperture with a central bending radius $\rho = 1.79$ m [216]. The energy of the beam is determined via the following relation:

$$\frac{mv^2}{\rho} = qvB \Rightarrow \frac{P}{\rho} = qB \Rightarrow \frac{\sqrt{2mE}}{q} = \rho B \tag{3.1}$$

where P is the momentum of the beam particles, B is the magnetic field of the analyzing magnet, and the product of ρ and B is called the magnetic rigidity. The purity of the beam is also determined by the analyzing magnet, because only particles with the correct ρ can pass through the analyzing magnet. Any impurity in the beam that had survived

the first magnet prior to the accelerator was thus stopped by the analyzing magnet, whose magnetic field strength was set according to equation (3.1) to 4993.54 G to let only the proton beam through. The analyzing magnet at WNSL has been calibrated by a well-known $^{12}C + p$ elastic scattering resonance at $E_p = 14.231$ MeV [217] at the level of accuracy of $\sim 1/10^4$ [216].

Along the beam line leading to the target, the beam transporting system consists of slits, quadrupole lenses, steerers, beam profile monitors and Faraday cups to tune, diagnose and appropriately set the properties of the beam that is directed on to the target.

The beam was then directed to the target room by means of the switching magnet (Fig. 3.1), whose magnetic field determines which beam line will be used to pass the beam to the target area. For the $^{32}S(p,t)^{30}S$ experiment, the magnetic field strength for the switching magnet was set to 4959.96 G.

The protons obtained their final energy of 34.5 MeV according to the $E = eV(1+q)$ relation [123] (p. 207), where e is the electronic charge, V is the terminal voltage and q is the charge state of the beam. The beam energy was chosen by considering two factors: (i) it must be high enough to overcome the Q-value and the Coulomb barrier of the $^{32}S(p,t)^{30}S_{g.s.}$ reaction, which are -19.614 MeV and 4.415 MeV, respectively. Furthermore, it was required that states in ^{30}S up to an excitation energy of 6.8 MeV be populated. So, the beam had to have enough energy to overcome the Q-value of this latter state, which is -26.4 MeV; (ii) it must be well above the Coulomb barrier also for the reaction to proceed through the direct reaction mechanism, because as described later, the spin-parity assignments for the excited states of ^{30}S were determined by a Distorted-Wave Born Approximation (DWBA) calculation, which is an approach that is only valid for direct nuclear reactions.

The proton beam spot size was determined by directing the beam through a 2 mm diameter collimator placed at the target position into a Faraday cup [216]. This latter element was employed to measure the beam intensity during the experiment for regular check-ups. The beam current during this experiment varied between 5 enA to 95 enA. The limiting factor for the beam intensity during the experiment was the focal plane detector as explained in § 3.1.5. The beam was finally stopped by a Faraday cup located downstream from the target inside the target chamber at 0° with respect to the beam

axis.

Having presented the conditions and physics pertaining to the beam, we can now proceed to a discussion of the targets used for the $^{32}S(p,t)^{30}S$ experiment.

3.1.3 Targets

There were a number of targets that were used during this experiment. Each target consisted of a foil containing the target material mounted on an aluminum frame with a small aperture such that the target size was 5 times bigger than the beam spot size. Five of these frames were mounted on a target ladder made also of aluminium, which was placed in the target chamber kept under vacuum. The target ladder could be rotated and moved up and down manually to place a specific target in front of the beam. The target foils are listed and described below:

• **CdS target:** This target was used as the main target, with which the $^{32}S(p,t)^{30}S$ reaction was investigated during the first and the second phases of the experiment performed on November-2007 and May-2008 (explained later on in this chapter), respectively. It was made by evaporation of 249 ± 25 $\mu g/cm^2$ of CdS onto a 20-$\mu g/cm^2$ natural carbon foil. This target was previously used successfully over the course of many years, and its exact fabrication history has since been misplaced.

The equivalent thickness of the sulfur content of this target was needed for the analysis of the $^{32}S(p,t)^{30}S$ experiment, and was calculated to be 52.3 $\mu g/cm^2$ from the molar masses and the abundances of stable isotopes of Cd and S. However, this theoretical value might not have been sufficiently reliable. The target thickness and its uncertainly are critical input parameters for the error analysis, and thus they must be obtained from a more reliable source, such as Rutherford Backscattering Spectrometry (RBS) or an energy loss measurement.

Therefore, the author requested the data of a scattering experiment performed by a separate group at WNSL, where an 8-MeV $^4He^+$ beam along with the Enge spectrograph (see § 3.1.4) and a silicon surface barrier detector were used to determine the composition and the thicknesses of a number of targets including the CdS target. Through the re-analysis of these data, the experimental equivalent thickness of the sulfur content of the CdS target was determined to be 53 ± 5 $\mu g/cm^2$. This value was then used in the analysis of the $^{32}S(p,t)^{30}S$ experiment.

• **^{32}S implanted target:** This target was employed as the main target with which the ^{32}S$(p,t)^{30}$S reaction was re-investigated during the last phase of the experiment on January-2010. To produce it, 10.4 ± 0.4 μg/cm^2 of ^{32}S was implanted into a 55.9 ± 5.6 μg/cm^2 isotopically pure ^{12}C foil at the the University of Western Ontario (UWO)[3]. The fabrication of this target was a side project during this Ph.D. thesis work, so Appendix A is devoted to the fabrication technique and determination of the thickness of this target.

• **Si target:** This target was used to calibrate the data from the CdS and the implanted targets. It was a free-standing 311 ± 31 μg/cm^2 natural Si foil, supplied by the Lebow Company [218].

• **^{13}C target:** This target was used for subtracting the background produced by the CdS target, and was a 75 ± 8 μg/cm^2 95.6% isotopically enriched ^{13}C foil previously purchased from the ACF-Metals Company [219].

• **^{12}C target:** This target was used for subtracting the background produced by the implanted target, and was a 40 ± 4 μg/cm^2 99.9% isotopically enriched ^{12}C foil purchased from the ACF-Metals Company in 2008.

• **Cd target:** This target was used together with the CdS target for background subtraction purposes. To make this target, 200 ± 20 μg/cm^2 of natural Cd was evaporated onto a 20-μg/cm^2 natural carbon foil. The carbon substrate and the ^{nat}Cd target were both fabricated at the Technische Universität München[4].

The thicknesses of the CdS, Si, ^{13}C, ^{12}C and ^{nat}Cd targets were determined prior to each phase of the experiment from measuring the energy losses of α-particles from an ^{241}Am source through the targets via a silicon surface barrier detector. The uncertainties in these thicknesses were determined to be $\sim$ 10%.

The thickness of the ^{32}S content of the implanted target as well as that of its ^{12}C substrate were measured separately by a RBS measurement performed at the UWO after the implanted target was exposed to the proton beam at Yale University. The resulting uncertainties in the ^{12}C thicknesses were determined to be 4% and 10%, respectively.

[3]Department of Physics & Astronomy, University of Western Ontario, London, ON N6A 3K7, Canada.
[4]Dominik Seiler, Physik Department E12, Technische Universität München, D-85748 Garching, Germany.

3.1.4 The Yale Enge Split-Pole Magnetic Spectrograph

The Yale Enge split-pole magnetic spectrograph was used to disperse tritons produced in the $^{32}S(p,t)^{30}S$ reaction by momentum, and focus them on a detection plane where they were detected.

Since the first generation spectrographs [220–222], the demand for improved precision and resolution in studies of nuclear physics led to further progress in designing these devices [223, 224]. With any given kind of spectrograph, a higher resolving power can be achieved by reducing the target spot size, using a thinner target and decreasing the solid angle of acceptance. However, all these factors reduce the rate of data accumulation, making the required experimental time longer.

A larger solid angle that maintains the resolving power can still be achieved by obtaining two-directional focusing and at the same time keeping the second-order focusing terms, i.e., x/θ^2 and $x/\phi^2 \sim 0$, where θ and ϕ refer to angles in the plane of and normal to the plane of the particle trajectory in the spectrograph, respectively. Third order aberrations, x/θ^3, due to the finite size of the spectrograph's entrance aperture can be corrected by measuring the angle of particles exiting the spectrograph [225]. In 1967, Enge *et al.* [226] designed a new type of spectrograph called the Enge split-pole spectrograph with the purpose of maximizing the ion collection power without sacrificing the energy resolution.

A precise measurement of the momenta of charged particles is determined by this spectrograph [226], which also focuses the particles emerging from the target vertically and horizontally to a position along its focal plane determined by the particle's momentum and charge, and the spectrograph's magnetic field (see equation (3.1)). The spectrograph's design was able to offer second-order double focusing over a broad range of energies, because it utilized two separate iron pole pieces that were split and surrounded by a single copper coil (hence the name "split-pole"; see Fig. 3.2 on page 50). An S-shaped corrective insert after the second pole piece maintains nearly constant dispersion $D \equiv \partial x/\partial(\Delta p/p)$ along the focal plane[5]. Due to the shapes of the edges of its poles and the locations of the pieces within the coil, vertical and the horizontal focusing up to

[5]The ability of the spectrograph to resolve groups of particles with small momentum difference depends on the spectrograph's ion optical magnification and momentum dispersion. The latter measures the displacement in x (horizontal position) at the exit per unit change in δ, where $\delta = \Delta p/p_0$ if a reference momentum p_0 is assumed. The deviation from this momentum is given by δ [227].

second order is achieved for particles from the same reaction channel that have slightly different momenta and are emitted in slightly different directions from the target. The ion optics of this spectrograph is explained in detail in Refs. [227–229].

The Enge spectrograph at WNSL (see Fig. 3.2) is connected to a power supply capable of producing high currents, which are kept constant to a high degree of precision so that the desired magnetic field remains static. The maximum magnetic field generated between the poles of the WNSL Enge Spectrograph is 16.3 kG [230]. This field is perpendicular to the motion of the charged reaction products to spatially separate particles with different magnetic rigidities (see equation (3.1)). Its magnetic field is measured to a fraction of a gauss using nuclear magnetic resonance of hydrogen or deuterium [230]. The Enge spectrograph at WNSL has a dispersion of 1.96, and magnifies the beam spot with magnifications of 0.39 and 2.9 in the horizontal and vertical directions, respectively [216]. It can accept all reaction products whose radii of curvature (ρ) lie on its focal plane between 51.1 cm to 92.0 cm as they are traversing the magnetic field of the spectrograph. Its maximum horizontal and vertical angular acceptances are $\Delta\theta = \pm$ 80 mrad and $\Delta\phi = \pm$ 40 mrad, respectively, where θ and ϕ refer to angles in the plane of and normal to the plane of the particle trajectory in the spectrograph, respectively. The maximum acceptances are $\Delta\theta = \pm$ 10.7 mrad and $\Delta\phi = \pm$ 12.2 mrad, while the maximum total solid angle of the acceptance is 12.8 msr at the spectrograph entrance [216]. However, the maximum solid angle that can be achieved in practice is 10.5 msr instead [231]. Such angular acceptances are provided by a set of horizontal and vertical slits located at the entrance of the magnet. For the ^{32}S$(p,t)^{30}$S experiment, the vertical slit was always set to $\pm$40 mrad, while the horizontal slit was set to $\pm$20 mrad when the spectrograph was at 10° and 20°, and to $\pm$30 mrad at all other spectrograph angles. Thus, the resulting solid angles were 2.8 msr and 4.2 msr, respectively. The spectrograph sits on a rotating table which allows the experimenter to vary the scattering angle θ. The reaction products were measured at lab angles of 10°, 20°, 22°, 27.5°, 45° and 62°. The choices for the lowest and the highest angles were limited by the high rate of elastically scattered particles at low angles, which would overwhelm the detector as explained later; and by requiring reasonable statistics, respectively. Angular intervals were to first order estimated with theoretical calculations to determine the angles where various spin parity assignments would show the most pronounced differences.

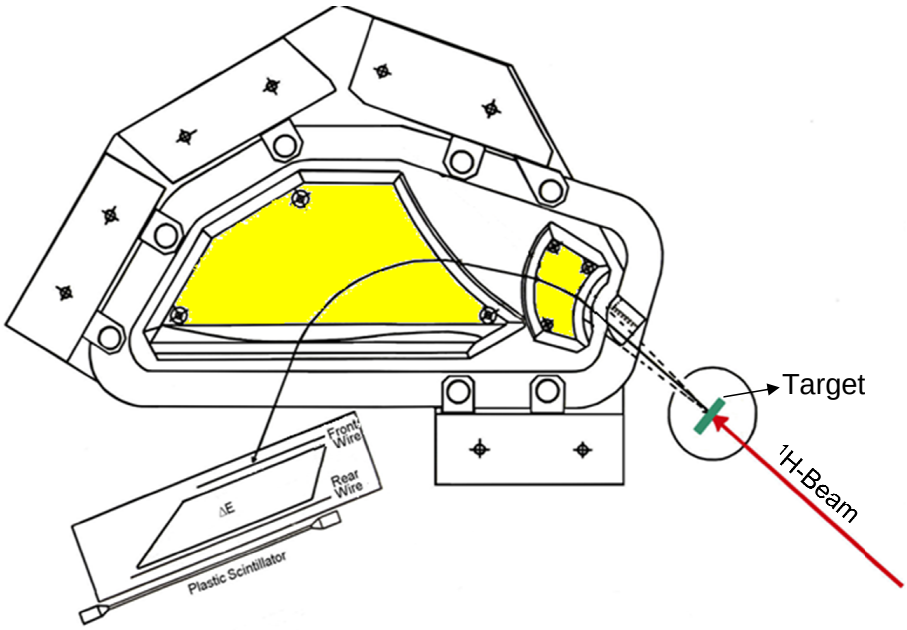

(a) Schematic diagram of the Yale Enge split-pole spectrograph.

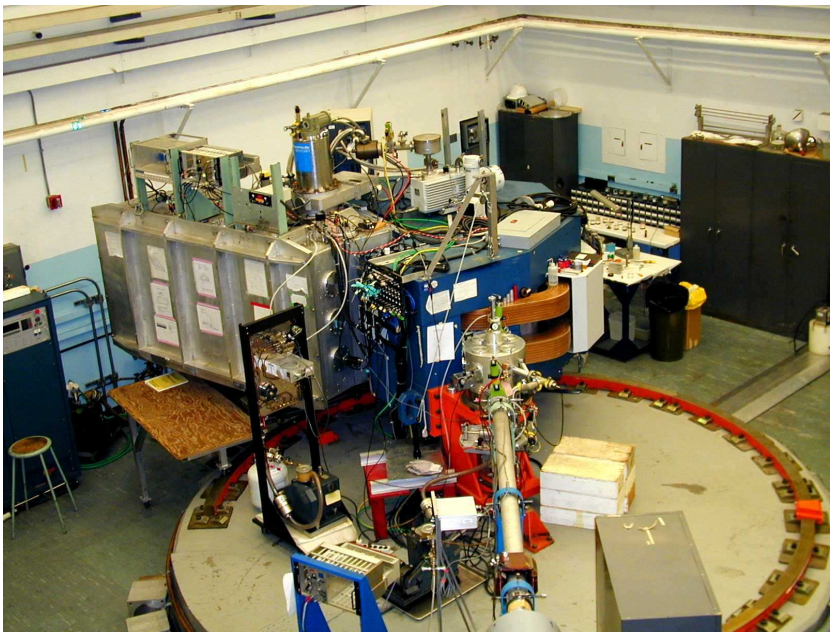

(b) Photograph of the Yale Enge split-pole spectrograph.

Figure 3.2: Fig. 3.2a shows the schematic diagram of the Yale Enge split-pole spectrograph, modified from the original found in Ref. [230]. The particles' energies and angles, through which they enter the spectrograph, determine their trajectories. The yellow regions are the pole pieces. Fig. 3.2b shows an actual photograph of the target room, where the spectrograph, the beam line and the silver cylindrical target chamber located on the beam line and upstream with respect to the spectrograph can be seen. The red track on the ground is a ruler which determines the angle of the spectrograph. The minimum scattering angle of the spectrograph is $\sim 0.1^\circ$ [216].

If the target is positioned parallel to the spectrograph's acceptance aperture, the reaction products travel in the target through a shorter path, and thus lose less energy inside the target. However, the target in this experiment was aligned by eye. Thus, any misalignment of the target introduces a systematic uncertainty in the energy loss of the reaction products as they traverse the target. This systematic uncertainty is discussed in more detail later.

3.1.5 The Focal Plane Detector

When the beam hits the target, a number of reactions including the reaction of interest occur. The trajectory of each reaction product in the magnetic field of the spectrograph is defined according to equation (3.1) by a radius of curvature, ρ. The detection system is located at the focal plane of the Enge spectrograph, covering a momentum range corresponding to about $70 \lesssim \rho \lesssim 86$ cm.

The detection system is assembled from a gas-filled Position-sensitive Ionization Drift Chamber (PIDC) and a plastic scintillator that is optically coupled to a photomultiplier tube on the right and left sides. As the reaction products traverse the ionization chamber, the PIDC measures their energy loss, ΔE, as well as their positions along the focal plane. The particles passing through the ionization chamber are stopped by the scintillator, where their residual energy, E_{res}, is measured. ΔE, along with E_{res} and position are then used to identify particle species and determine their momenta.

A rectangular 26"-long, 8.5"-high and 3"-deep aluminium box with two epoxied windows of 0.25 mil[6] aluminized mylar makes up the PIDC. This box is filled with isobutane gas (also known as methylpropane (C_4H_{10})) at typical pressures of 100 – 200 Torr. The choice of the isobutane gas pressure is made to ensure that the reaction products of interest can penetrate through the PIDC without losing all their energy. In the $^{32}S(p,t)^{30}S$ experiment, the pressure of the gas was set to 150 Torr. The isobutane gas is forced to steadily flow in and out of the chamber to minimize contamination buildup, and to allow the energy loss of the particles to remain constant.

The reaction products are energetic charged-particles. Therefore, upon entering the ionization chamber they interact with the isobutane gas primarily through Coulomb forces between their positive charge and the negatively charged orbital electrons within

[6]One mil, also known as thou, is a unit for measuring length, and is equal to 0.001 inch.

the gas atoms. Such interactions, depending on the proximity of the encounter, result the removal of electrons from the gas atoms, thereby ionizing them. The electrons gain kinetic energy at the expense of charged-particles' energy loss. The resulting electron-ion pairs must be separated in order to keep them from recombining to form neutral atoms. This is done by applying an electric field inside the drift region, where the electron-ion pairs are produced.

The drift region inside the PIDC is bounded between a cathode plate and a field shaping apparatus containing a Frisch grid [232]. These elements together are intended to create a highly uniform vertical electric field that is perpendicular to the cathode plate and the Frisch grid. The field shaping system is comprised of five rectangular interlocking pieces of circuit boards that make up a cage whose sides are parallel to the front, back, top and two sides of the PIDC (see the yellow-brown part in the top panel of Fig. 3.3). Four of these five boards each holds 10 equally spaced one-mil-thick gold-plated tungsten anode wires that are positively biased. A smooth uniform 0.25"-thick plate of aluminium spanning the bottom side of the PIDC is negatively biased, and thus serves as the cathode plate, atop of which sits the field shaping apparatus. For the ^{32}S$(p,t)^{30}$S experiment, the cathode plate was held at -700 V. Above the cathode plate and parallel to it, there is the fifth board located at the top side of the field shaping apparatus. This board is also parallel to the focal plane of the spectrograph, and contains $\sim$ 50 wires/inch [233] soldered to the board on both sides. The wires run parallel to the cathode plate. These wires are grounded, and thus make up the Frisch grid. The wires in the field shaping apparatus are connected to the cathode plate and the Frisch grid via a chain of 10 MΩ resistors.

As the reaction products traverse the drift region, the electron-ion pairs are produced causing the reaction products to lose energy. The drift of the electron-ion pairs inside the drift region gives rise to a signal from the cathode, the height of which is proportional to the energy loss, ΔE, of the reaction products.

On top of the Frisch grid, there are two position sensitive apparatuses. The upstream and the downstream assemblies are called the front and rear assemblies, respectively. Each of these assemblies consists of two printed circuit boards connected at a right angle to each other (see the green pieces in the top panel of Fig. 3.3). The board that is parallel to the spectrograph, and is thus in the plane of the cathode plate, has 220 lead-coated

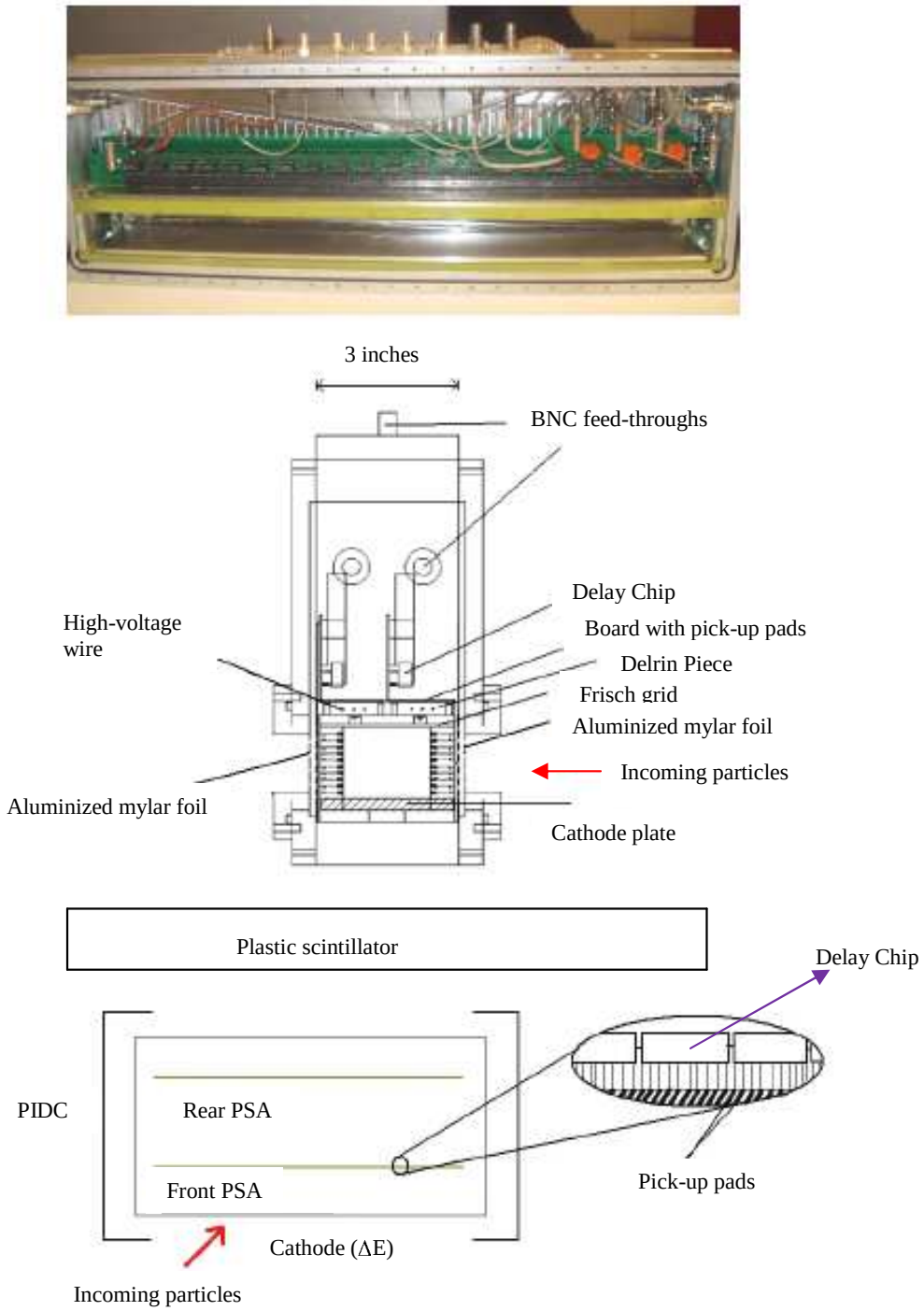

Figure 3.3: (top) A photograph of the interior of the position-sensitive ionization drift chamber (PIDC), looking from the front. The yellow pieces are the boards belonging to the field shaping system. The field shaping wires are too thin to be observed in the image. (middle) Schematic side-view of the PIDC, to scale. For simplicity, the field-shaping wires are not shown. (bottom) Simplified schematic top-view of the focal plane detection system (not to scale). The diagram is adopted from Ref. [216].

copper pick-up pads [216]. Each pad is 0.09"-wide, 1.4"-long and is separated from the next pad by 0.01". These pick-up pads are tilted at 45° relative to the focal plane so that they lie along the average entrance angle of the particles incident on the focal plane. At either end of the board, there is a delrin piece attached to the metal supports that are placed above and below the board along its length. Three high voltage one-mil-thick gold-plated tungsten wires run parallel to the focal plane, and are threaded through these pieces for each position sensitive apparatus. The wires are separated by 0.25" from each other, and only the middle ones from each assembly are used due to technical restrictions [233]. The middle wires of the two position sensitive assemblies are called the front and rear wires, and are 10 cm apart from each other. The other board, which connects at a right angle to the board with the pads, houses the delay chips and the circuitry for biasing the wires and taking the signals. There are 44 delay chips, each of which has 10 taps and 50 ohm impedance. Each tap delays the signals by 5 ns. The true delays of these chips have been measured to be between 63 – 65 ns for the front position sensitive assembly and 60 – 62 ns for the rear position sensitive assembly [216].

Once the electrons pass through the Frisch grid on their way to the front and rear wires, they are accelerated and produce an electron avalanche. This induces a signal, which is picked up by the pick-up pads nearest to the avalanche. This signal then travels to both ends of the position sensitive assembly passing through the delay chips. The time difference between the two end signals determines how many delay chips the signal has passed through, and thus can be used with a Time-to-Amplitude Converter (TAC) to deduce the front and rear positions of the reaction products passing through the detector. The position of the particles can be measured with a resolution of ≈ 1 mm [230]. In the $^{32}\mathrm{S}(p,t)^{30}\mathrm{S}$ experiment, the front and rear wires were biased to +1650 V. This voltage was particularly chosen in conjunction with the isobutane gas pressure of 150 Torr, so that the gas would not break down electrically. If the gas pressure and the voltages on the wires are too high, apart from the danger of breaking the windows, the rate at which ions are produced is much greater than the number of ions collected by the cathode. Therefore, there will be a positive charge buildup, which can cause a continuous discharge in the detector [234] (p. 141). A beam intensity that is too high also results in a high rate of ionization in the gas, which for the same reason causes the detector to spark. Thus, the limiting factor for the beam intensity in the $^{32}\mathrm{S}(p,t)^{30}\mathrm{S}$ experiment was the detector

count rate.

Upon exiting the PIDC, the reaction products enter a flat, 6.35-mm thick, polyvinyltoluene Bicron BC-404 scintillator[7]. When struck by reaction products, the scintillation material absorbs their residual energy, and thus the scintillation atoms are excited. These atoms subsequently scintillate, i.e., de-excite by emitting the absorbed energy in the form of light. Since the scintillator is optically coupled at each end via a fish-tail light guide to a photomultiplier tube, the scintillation light rays hit the photo-cathode of each photomultiplier tube, producing a number of photo-electrons by the photoelectric effect. The resulting photoelectrons are accelerated toward a string of dynodes kept at successively higher potentials, which generate more electrons as secondary particles. These particles are finally collected by the anode. In the ^{32}S$(p,t)^{30}$S experiment, the scintillator was biased at +1800 V.

Each photomultiplier tube has an anode, which produces a signal used for timing purposes. The timing resolution of the scintillator's anode signal is $\approx$ 10 ns, whereas the time resolution of the PIDC is $\approx$ 100 ns [225]. On the other hand, there will be a final dynode signal from each photomultiplier tube, the height of which is roughly proportional to the residual energy of the incident reaction products. These two dynode signals can be combined in software according to the following equation to produce a final energy signal from the scintillator [235]:

$$E = \sqrt{E_1 E_2} \tag{3.2}$$

where E_1 and E_2 are proportional to the heights of the two dynode signals.

The experiments are usually planned so that the reaction products of interest are focused by the spectrograph at the middle wire of the front position sensitive assembly (front wire). This is because due to multiple scattering of the ions in the gas, the resolution of the rear wire, which is further away, is worse. The location along the path of the reaction products where they are focused by the spectrograph on the front wire depends on the reactions and the excitation energies of the nucleus of interest. Thus, the detector's position must be changed depending on the reaction under study. If this is not done, the resulting kinematic broadening degrades the energy resolution (see § 3.2.7). The detection system is controlled remotely, and can be moved forward or backward

[7]Saint-Gobain Corporation, P.O. Box 860, 750 E. Swedesford Road, Valley Forge PA 19482-0101 USA.

on a track. The optimal position of the front wire for the excitation energy of interest produced by the reaction of interest is found from a semi-empirical relation (see Ref. [227] for more information):

$$z = 56.7k + 55.5 \tag{3.3}$$

where z is the detector's position in cm, and k is the kinematic broadening (see § 3.2.7) and is equal to [227]:

$$k = \frac{-1}{p}\frac{dp}{d\theta} \tag{3.4}$$

where p is the momentum of the incident particle and θ is the particle's angle in the laboratory system. The analysis software package at WNSL offers a Java-based program called JRelKin [236] that calculates k. The relation between z and k has been found from the resolution of α-particles from the ^{25}Mg$(p,\alpha)^{22}$Na and ^{13}C$(p,\alpha)^{10}$B reactions as a function of z [216].

3.1.6 Signal Processing via the Electronics

Upon interaction of the incident radiation (which could be photons or particles) with a detector, a charged particle is liberated, which is then collected either directly, e.g., in semiconductor detectors, or indirectly, e.g., in scintillation detectors. Therefore, an electrical pulse is generated, whose maximum voltage is proportional to the collected charge and thus to the energy deposited in the detecting medium. The radiation's incident energy is the most basic information that must be extracted from that voltage pulse.

This pulse is a continuous signal, and thus is called an analog pulse, which can be shaped. The analog signal is converted by an Analog-to-Digital Converter (ADC) module to digital data. This module is sensitive to the maximum amplitudes of the input signals, and converts those amplitudes into discrete values expressed in a binary form. Hence the ADC outputs a digital pulse.

A standard Nuclear Instrument Module (NIM) housed in a 16-channels Versa Module Eurocard bus (VME) crate (CAEN V260N [216]) was used to process all the timing and analog signals from both components of the detection system, i.e., the PIDC and the scintillator. Fig. 3.4 shows the layout of the electronics used for this experiment. The PIDC itself produced a number of signals:

(a) An energy signal from the cathode plate contained the information about the

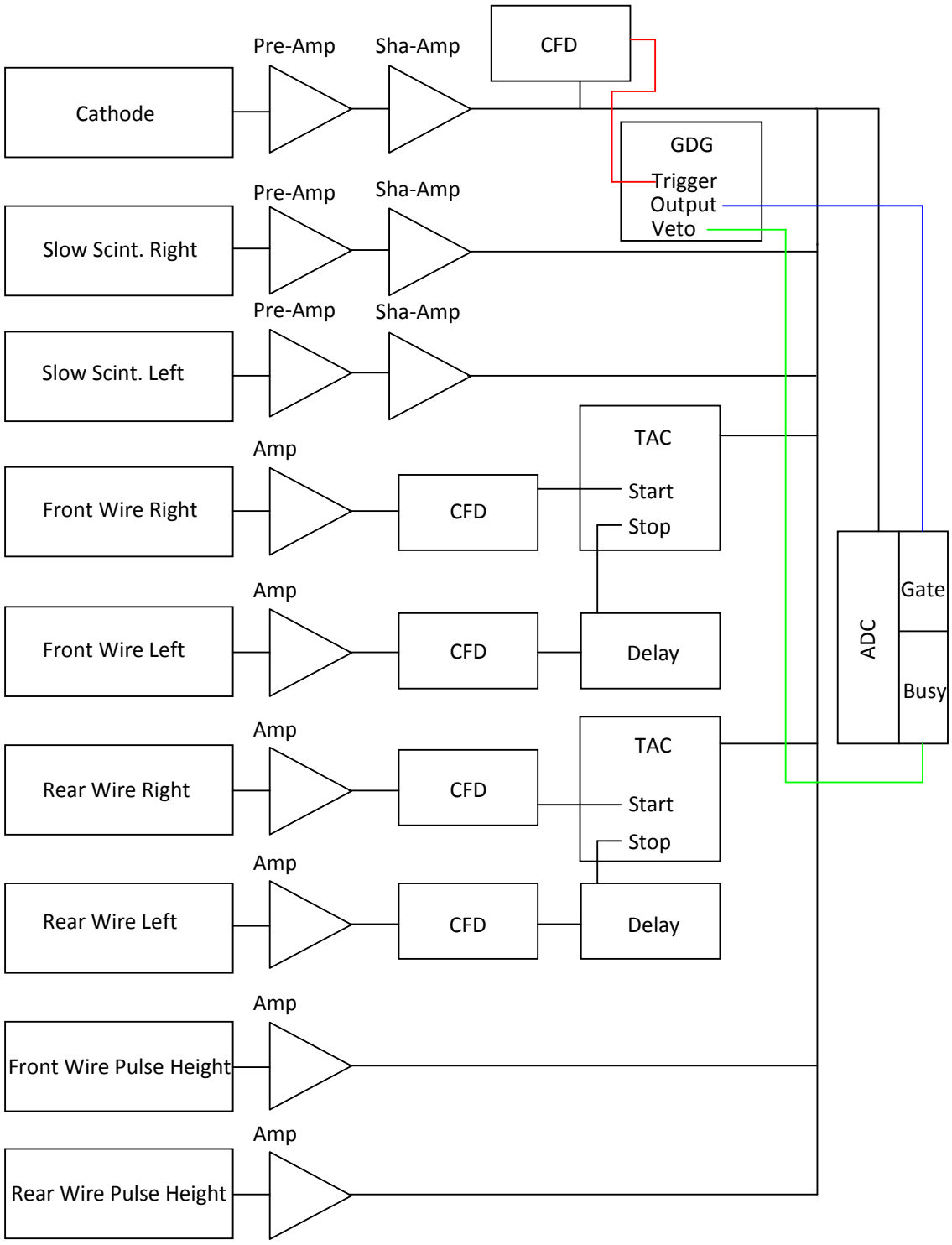

Figure 3.4: The schematic diagram of the electronics used in the $^{32}\mathrm{S}(p,t)^{30}\mathrm{S}$ experiment for signal processing. Abbreviations are as follows: Pre-Amp: Pre-Amplifier; Amp: Amplifier; Sha-Amp: Shaping Amplifier; SCINT: Scintillator; CFD: Constant-Fraction Discriminator; ADC: Analog-to-Digital Converter; TAC: Time-to-Amplitude Convertor; and GDG: Gate-and-Delay Generator. The colorful lines are just for the purpose of clarity.

energy loss, ΔE, of the reaction products. This signal was pre-amplified, and the signal-to-noise ratio was improved via a shaping amplifier. Finally, it was fed into a 32-channel VME-6U CAEN V785 ADC module.

(b) The cathode timing signal was used as the trigger for the Data Acquisition (DAQ) since the cathode was much less sensitive to background than the scintillator. The cathode timing signal was split after amplification and was used to define the event gate[8]. The latter was achieved by first passing the signal through a Constant Fraction Discriminator (CFD), which both accurately gave the true time pick-off of the initial rise of a pulse (which was under the signal noise) independent of the pulse shape, and set a threshold for the pulse height we defined to be a true event. The CFD then outputted a low-background authentic timing signal, which was passed to the trigger of the Gate and Delay Generator (GDG) module, which then counted down for 10 μs, and outputted a STOP signal afterwards. During this gate width of 10 μs, the VME crate acquired the incoming data to a memory buffer as an event and the ADC continued to accept other signals associated with that event while digitizing the maximum amplitudes of these voltage signals that arrived. Clearly, another cathode signal may have occurred during this 10 μs window, which would have prolonged the trigger signal, irreversibly prolonging the previous event and destroying the validity of the previous data written to the memory buffer. As such, when the GDG sent a gate signal to the ADC, the ADC in turn sent a logic veto signal to the GDG until it had finished processing the event, disabling the GDG from changing the gate condition.

(c) The signals from the middle wires of the upstream (front) and downstream (rear) position sensitive assemblies of the PIDC ultimately provided the position information. Each of the front and rear wires had two timing signals coming from the right and the left ends of that wire. These signals were amplified and passed through a CFD. While the timing signal from the right-end of each wire was fed directly into a TAC to act as the start, the timing signals from the left-ends of the wires were first delayed by a fixed time, and were then fed into the associated TAC to stop its operation. The delay was such that the STOP signal arrived at a time later than the START signal. The difference in time between the START and STOP times indicated how many delay chips along the

[8]The gate in this context is a logic pulse that acts like a switch, and allows some input signals to pass if a certain condition is met; otherwise, the input signals are blocked.

wires the signal had passed through, and thus could be used to deduce the front and rear positions of the reaction products passing through the detector. The output signal of each TAC, together with the amplified pulse height signals of both wires were then fed to the ADC module.

The scintillator detector had four signals: two anode signals and two dynode signals from two photomultiplier tubes, each coupled to one side of the scintillator. The anode and dynode signals were called "fast" and "slow" scintillator signals, respectively. The former would have been used if the scintillator were chosen to be used instead of the cathode to trigger the DAQ. This was not the case for the $^{32}\mathrm{S}(p,t)^{30}\mathrm{S}$ experiment. Thus, only the slow scintillator energy-signals were used. The slow scintillator signals from both photomultiplier tubes at the end of the scintillator were amplified and shaped in a shaping amplifier before feeding into the ADC module. These two signals contained information about the residual energies of the reaction products when stopped in the scintillator.

The scalars module, also housed in the VME crate, received logic signals to measure the scintillator rate, the cathode rate, the raw events presented to the acquisition system, the events accepted by the acquisition system, beam current integrator and a clock signal. The scalars were used primarily to determine the deadtime by monitoring the count rate on the detector, which should have not been too high to avoid overwhelming the detector. The clock signal was used to count the time between the start and stop of each run, which in turn was defined by the experimenter when he/she started saving the data onto a computer. The beam current integrator scalar was used to calculate the average beam intensity, as well as to calculate the total charge deposited by the beam.

When the count rate in the detector was too high, for instance due to high beam intensity or if the isobutane gas pressure had dropped significantly, the front and rear wires sparked. This caused the VME crate to be busy, and thus the DAQ was automatically halted temporarily, during which no events would be accepted by the electronics. In this case, the wire voltages were manually reset, and the acquisition was resumed manually.

3.1.7 The Data Acquisition System

After all signals were processed, the multi-parameter event-based raw data were packed and sent by the VME crate to a 8-kbytes memory buffer, which was stored in a

computer running the Vx-Works real time operating system. When this buffer was filled completely, the data were transferred via a LAN to a data analysis machine running GNU/Linux.

A Java-based software package, called Jam [237], ran on the data analysis machine, which was responsible for saving all the raw data to disk. Both the online and offline data analysis during and after the experiment are performed with Jam. Thus the experimenter is afforded the convenience of running offline analysis on almost any computer of choice, since the only requirement is a Java Virtual Machine.

Being powerful and yet simple to learn/use, Jam provides a platform independent data analysis package and a Graphical User Interface (GUI), which is used by the experimenters to load a piece of code written in Java, called the sort routine. This code can be modified easily according to the needs of the experimenters. In this code, one can define as many 2D and 1D histograms as required for displaying the raw data. One can also set a conditional statement on a histogram, so that it can only be filled with data if that condition is satisfied. These conditions are called the software gates. Jam then sorts the raw data into these histograms according to the instructions written in the sort routine. The sorting relies on selecting the particles of interest by the experimenters, and setting software gates around them. With these gates, the conditions for the conditional statements in the sort routine are satisfied, and thus the conditional histograms will be filled with data. 2D histograms can also be turned into 1D histograms with the use of these gates. The gates can be reset as many times as one wants, and each time, Jam sorts the data with the new gates. All histograms and the gates information for a particular run can be saved to a file. The spectra can also be exported as text files.

Jam also provides a fitting routine with which one can fit the peaks observed in a spectrum with a gaussian function to find the properties of the peaks. Moreover, Jam interacts with the VME crate to retrieve the scalar information during the experiment [225]. This information is saved in the raw data, and can be accessed anytime during offline analysis. Moreover, using Jam, one can import spectra as text files, and do all kinds of basic applications with the spectra, i.e., multiplication, division, subtraction, combination, projection, re-normalization, as well as overlaying and shifting spectra. Gain shift corrections can also be applied.

The analysis and the results of the $^{32}\mathrm{S}(p,t)^{30}\mathrm{S}$ experiment will be presented next.

3.2 Analysis and Results

As mentioned before, the experimental data were acquired during three separate runs in November-2007 (2 days), May-2008 (5 days) and January-2010 (5 days). The triton measurements of the ^{32}S$(p,t)^{30}$S reaction were made with experimental parameters shown in Table 3.1. The beam energy spread in all these runs was $\sim \Delta E/E = 6 \times 10^{-4}$.

Table 3.1: Experimental parameters for the ^{32}S$(p,t)^{30}$S experiment.

E^a (MeV)	B^b (kG)	${\theta_R}^c$ (degree)	$\Delta\theta^d$ (mrad)	$\Delta\phi^e$ (mrad)	Ω^f (msr)	z^g	Date	Target^h
33.5	9.5	9	±30	±40	4.2	54.5	5/2008	CdS
34.5	10	10	±20	±40	2.8	54.4	10/2007	CdS
34.5	10	20	±20	±40	2.8	53.4	10/2007	CdS
34.5	10	22	±30	±40	4.2	53.2	5/2008	CdS
34.5	10	22	±30	±40	4.2	53.2	1/2010	Implanted
34.5	9.5	27.5	±30	±40	4.2	52.6	1/2010	Implanted
34.5	9.2	45	±30	±40	4.2	51.1	1/2010	Implanted
34.5	10	62	±30	±40	4.2	50.1	5/2008	CdS

[a] Beam energy.
[b] Magnetic field of the spectrograph.
[c] Reaction angle in the lab system, which is the spectrograph's angle.
[d] Horizontal slit for the spectrograph acceptance.
[e] Vertical slit for the spectrograph acceptance.
[f] Solid angle covered by the spectrograph.
[g] Focal plane detector's position.
[h] The main target used for measuring the ^{32}S$(p,t)^{30}$S reaction (see § 3.1.3).

In May-2008, due to a technical difficulty with the tandem accelerator during the first 28 hours of the beamtime, the beam energy could not be raised to reach 34.5 MeV. Therefore, the data set at 9° was acquired with a slightly lower beam energy of 33.5 MeV. These data were analyzed and used along with the data at other angles for determination of ^{30}S excitation energies. However, since the cross sections of the observed excited states depend upon the incident beam energy, they would inevitably be slightly different from those of the states populated by the 34.5 MeV beam. Therefore, these data were not used for determination of spins and parities of the ^{30}S excited states.

3.2.1 Particle Identification

When the proton beam hits the target, various reactions, e.g., (p, d), (p, t), and (p, α), as well elastic and inelastic scattering occur on the target material provided that the Coulomb barriers and Q-values of the reactants are overcome by the incident beam energy. Thus, the raw data consisted of all these different reaction product groups.

When necessary, by raising the cathode threshold, the minimum pulse height (in volts) of the signals from the cathode plate accepted by the ADC was increased, in order to reduce the high counting rates produced in the detector by energetic protons and deuterons. This kept the deadtime below 3%. By tweaking the cathode gain, the particle groups could be separated (increasing the gain) or squeezed together (decreasing the gain) on the 2D histograms. However, care was taken to not eliminate the tritons by raising the cathode gain too much.

Each particle groups, e.g., p, d, t and α, has distinct kinematics, and thus is momentum separated by the spectrograph. The detector results in distinct signals for energy loss, residual energy and position for these separate particle groups. Thus, by using Jam along with the sort routine, the raw data are displayed in four main 2D histograms: energy loss ΔE *vs.* residual energy E_{res} (Cathode *vs.* Scintillator); ΔE *vs.* the position along the front wire[9] (Cathode *vs.* Front); E_{res} *vs.* the position along the front wire (Scintillator *vs.* Front); and the position along the rear wire *vs.* that along the front wire (Rear *vs.* Front). Each of these four histograms has an associated gate that can be applied on the data displayed.

The location of each particle group on these 2D histograms can be simulated (see Fig. 3.5) using the TAJSimulation software[10]. With these simulations, the particle groups of interest were identified in all four 2D raw (ungated) histograms, and then a software gate was drawn around the particles of interest in each of those histograms, which are shown in Figs. 3.6 and 3.7.

While the signals from each photomultiplier tube at each end of the scintillator were used to derive the total residual energy of the reaction products, only the signal from

[9] As discussed before, the front wire is focused, so the position of particles along this wire is used in the particle identification.

[10] It is a Java-based code written by Dr. Kazim Yildiz for the VAX machines, and modified by the former nuclear astrophysics graduate students at WNSL. This program simulates particle ID on the focal plane detector at WNSL, and can be downloaded from Ref. [238]. Its output must be processed by PAW to produce screen graphics and a postscript file.

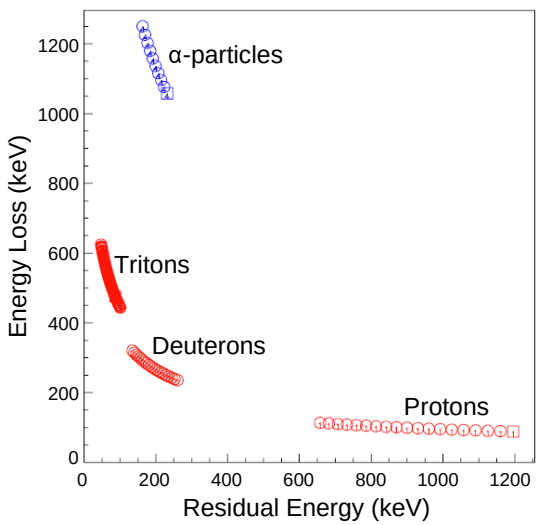

(a) Cathode *vs.* Scintillator.

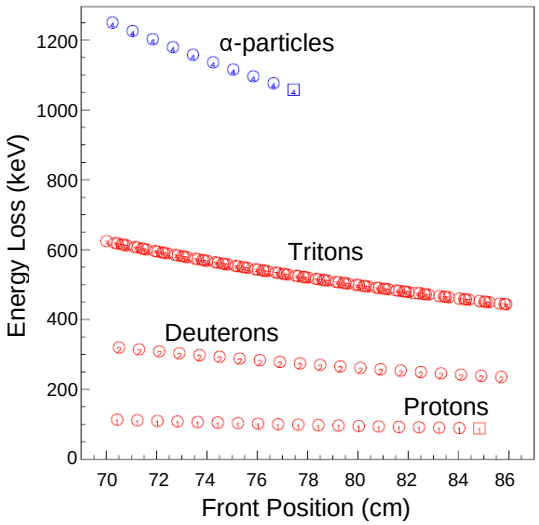

(b) Cathode *vs.* Front Position.

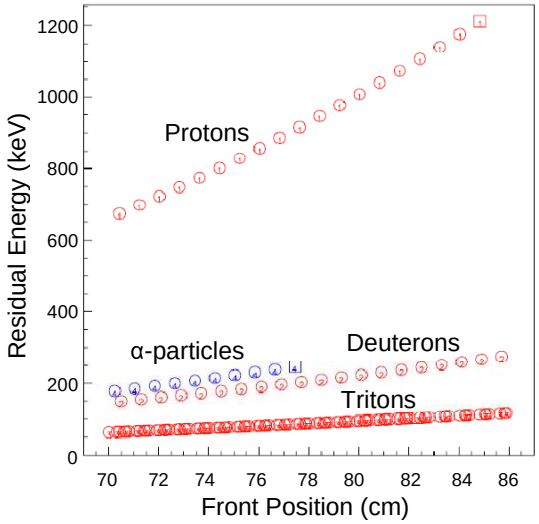

(c) Scintillator *vs.* Front Position.

Figure 3.5: Example of the location of various particle groups on 2D raw histograms, simulated by TAJSimulation program according to the experimental parameters for $\theta_R = 10°$. These simulated histograms show the particles in the (top) ΔE *vs.* E_{res} diagram, (middle) ΔE *vs.* the position along the front wire diagram, and (bottom) E_{res} *vs.* the position along the front wire diagram.

the left (with respect to the beam direction) photomultiplier tube (PMT2) was used for particle identification. This is because the right one always had a much higher gain across the residual energies detected. As a result, the amplitude of the signals for different residual energies did not change as rapidly for the left photomultiplier tube as for the right one. Thus, the different particle groups in the aforementioned histograms are more focused if only the signal from the left photomultiplier tube is used as opposed to using

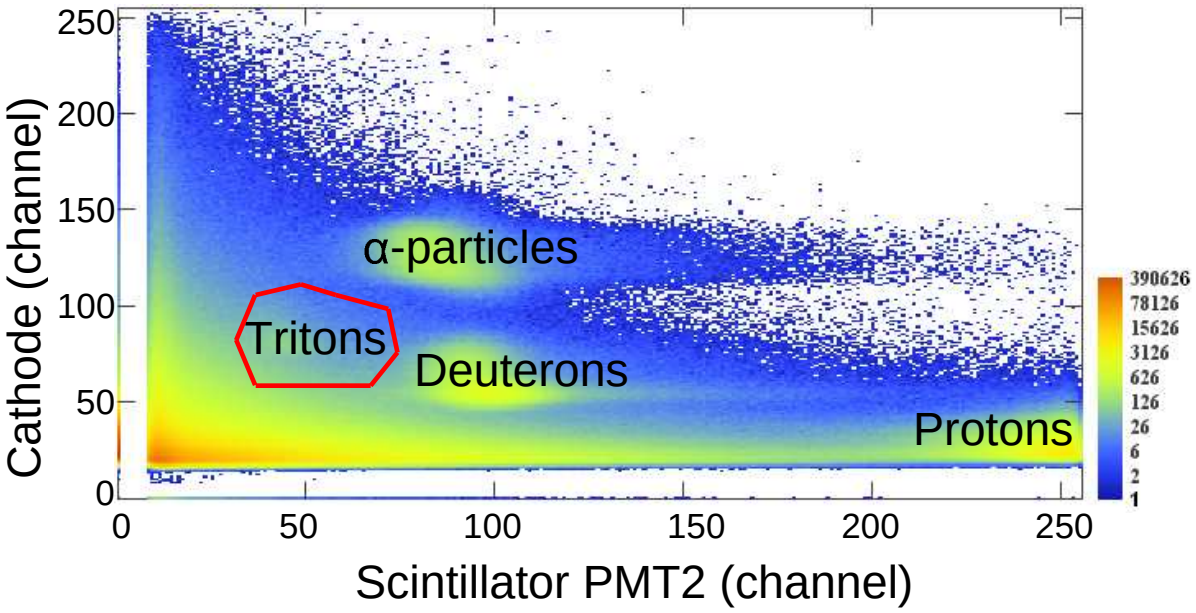

(a) ΔE *vs.* $E_{res.}$

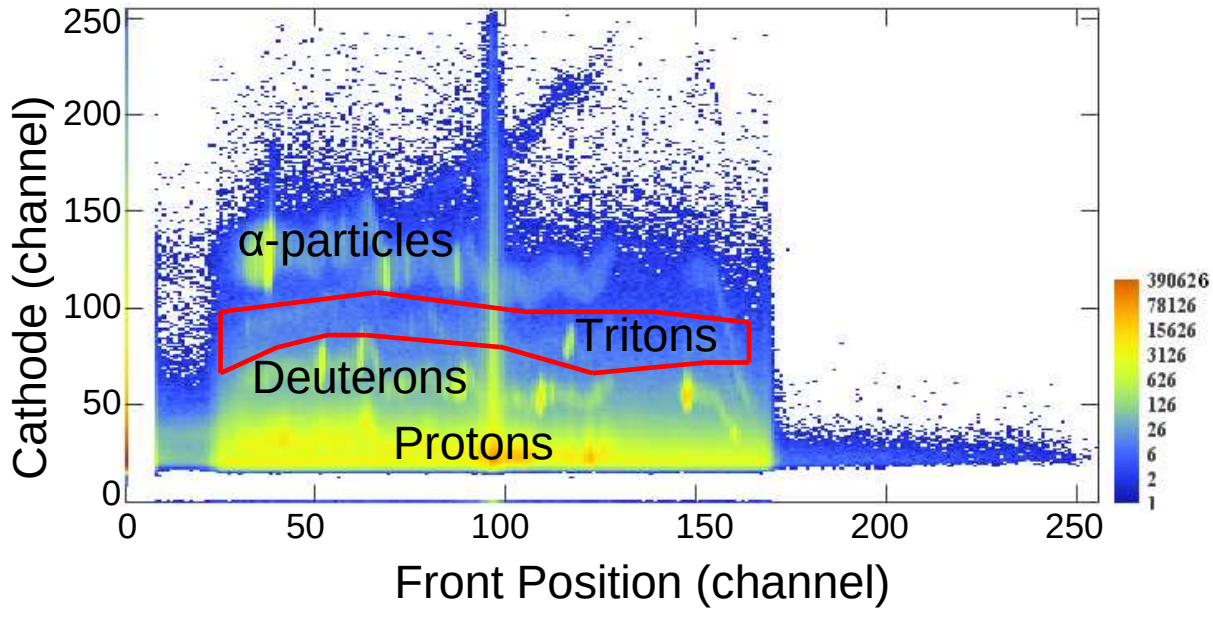

(b) ΔE *vs.* position along the front wire.

Figure 3.6: The main 2D ungated (raw) histograms selected from the 10° data with the corresponding gates shown as red bands around the particles of interest (tritons). The gates shown in the images are modified for clarity. The actual gates used in the analysis are similar but tighter; however, those gates are bands filled with dark red color, which obscure the tritons in the image. That is why they are modified for the viewer to see the particles of interest. Groups corresponding to each particle species are labeled. The color band to the right of each histogram shows the intensity in counts. The x- and y-axes are both in channels with arbitrary units. From a comparison between these histograms and the ones in Fig. 3.7 with the simulated histograms shown in Fig. 3.5, the particles of interest were identified.

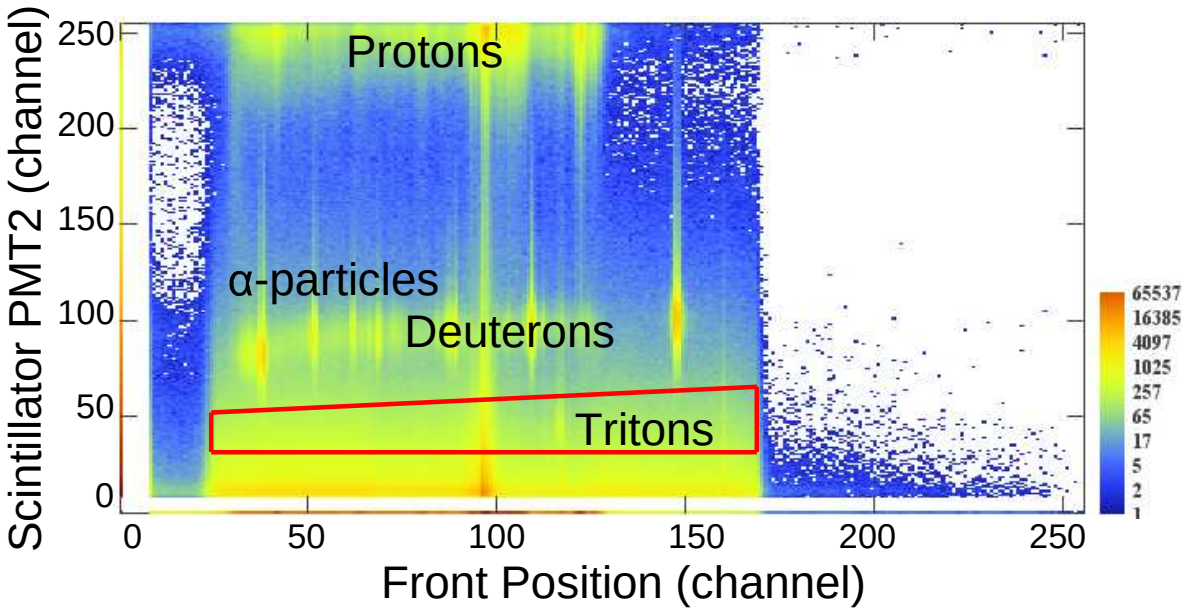

(a) $E_{res.}$ *vs.* position along the front wire.

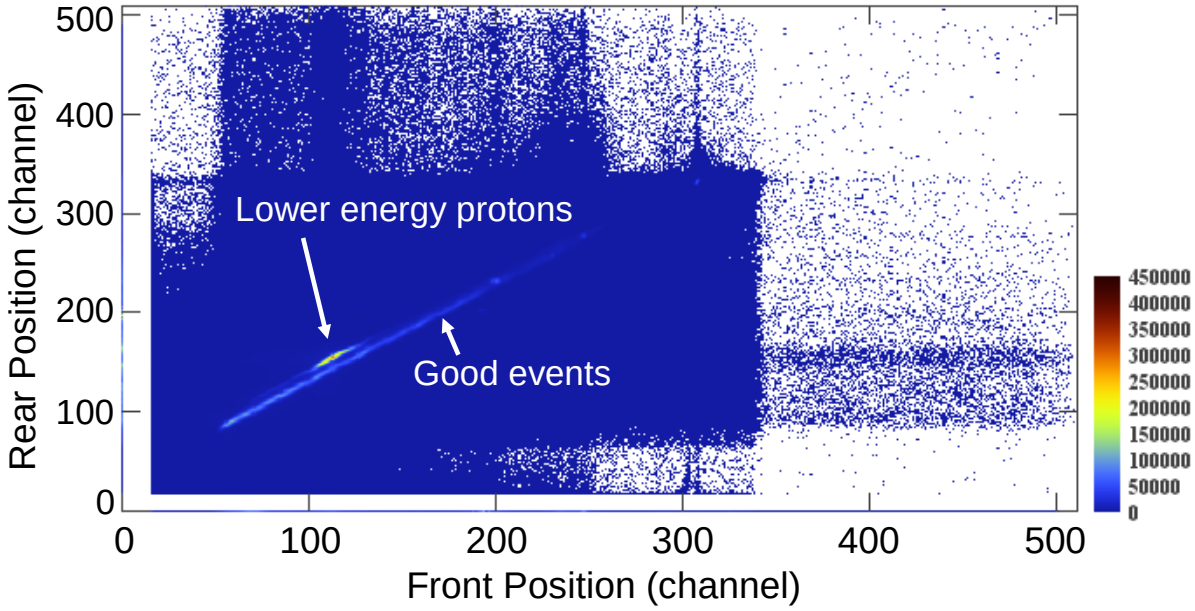

(b) Position along the rear wire *vs.* position along the front wire.

Figure 3.7: The main 2D ungated histograms selected from the 10° data with the corresponding modified gate shown as a red band around the particles of interest (tritons). The vertical and horizontal lines that are visible on the front position axis around channels 10 and 170 (on the top histogram), and on the rear position axis around channels 65 and 350, respectively, are the edges of the detector. The intensity band of Fig. 3.7b is plotted in logarithmic scale for clarity. For the same reason the gate is not shown on this histogram, but it is a tight narrow rectangle around the "good events", which are those with detector entrance angle close to 45°. Thus, the gate on the rear *vs.* front position histogram discards the scattered events that degrade the energy resolution and hamper particle identification.

the signals from both photomultiplier tubes [233].

The gate on the rear position *vs.* front position 2D histogram was used to eliminate the particles that are scattered from the acceptance slits of the spectrograph, or within the spectrograph itself. Such particles appear in this histogram as events that have no correlation between their rear and front positions.

In the original sort routine, apart from the 2D ungated histograms discussed before, three additional gated histograms had been defined: cathode *vs.* scintillator gated only on cathode *vs.* front position, cathode *vs.* front position gated only on scintillator *vs.* front position, and scintillator *vs.* front position gated only on cathode *vs.* scintillator. These histograms could only be filled from sorting the data if those gates were set. One can observe the effects of these gates by filling these histograms and can separate the particles of interest from the overlapping particle groups that were not of interest.

For the ^{32}S$(p,t)^{30}$S experiment at lower angles, the triton group overlapped with the tail of the deuteron group and sometimes even α-particles, such that the three gated histograms were not enough to define a clean gate around the tritons and further gates were required.

As mentioned before, there are 4 main histograms, each with one gate. Thus, there can be 12 histograms defined with only one gate applied on each, 12 histograms defined with two gates applied on each, and 4 histograms defined with 3 gates applied on each. Out of these 28 configurations, 3 were already defined. Thus, the sort routine was modified to include the additional 25 histograms.

In the offline analysis, since the gate on the rear *vs.* front position histogram eliminates the scattered particles, this gate was set first. The data were then sorted through this gate, and were displayed on the other three main histograms mentioned before. The application of the rear *vs.* front gate alone made the three main histograms much cleaner than their ungated counterparts (see the top panel in Fig. 3.8). The other 3 gates were also set after resorting of the data for the second time. Every time a gate was set on a histogram, its effect could be displayed on many histograms by sorting the data, and that was how the quality of a gate was checked. If the gates still contained particles that were not of interest, they would appear in the other histograms when the data were resorted. In that case, a new tighter gate was drawn around the particles of interest. This process was repeated many times until a clean cut around the tritons was obtained, which was

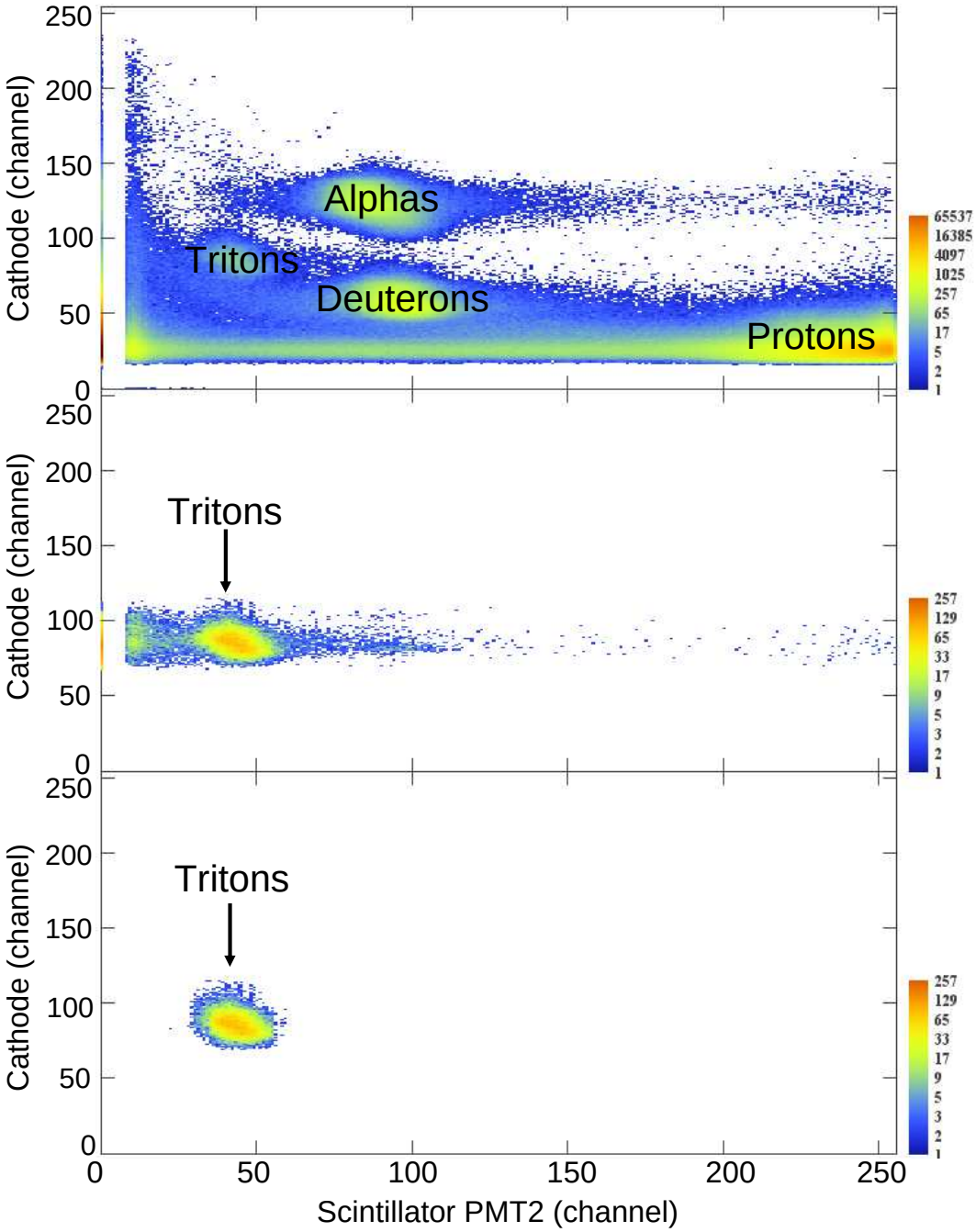

Figure 3.8: (top) ΔE *vs.* E_{res} histogram, where only the rear *vs.* front position gate was applied. In comparison with the ungated counterpart shown in Fig. 3.6a, this histogram is clearly a lot cleaner. (middle) The same data when the cathode *vs.* front position gate was applied in addition to the rear *vs.* front position gate. (bottom) The same data when the scintillator *vs.* front position gate was applied in addition to the rear *vs.* front position and the cathode *vs.* front position gates. The only particle group that is left is that of the tritons. This method can be applied to all other histograms to ensure a clean final cut around the tritons.

not contaminated by the presence of other particle groups.

3.2.2 Triton Spectra

After the clean gates were made around the tritons, all the runs with identical experimental parameters, e.g., magnetic field, reaction angle, cathode threshold, cathode gain, etc., were sorted one by one for the last time through these gates, and the final 1D histograms corresponding to the focal plane spectra of tritons were produced for each individual two-hour-long run. The data in these latter histograms contained all the events that passed through all four gates, and were subsequently overlayed on each other, two at a time, to ensure that the peaks' centroids were not shifted with resect to each other. If there was no shift observed, these 1D histograms were added together via Jam to obtain the final focal plane spectrum of tritons at that specific reaction angle. For those runs where the cathode gain had changed or the magnetic field of the spectrograph had drifted, a shift in the peak centroids was observed. In these latter cases, the change in the centroids (in channel) were calculated, and by using Jam the shifted spectra were shifted back to match the unshifted spectra. Finally, all the spectra corresponding to a specific reaction angle were added via Jam to derive the final spectrum at that angle.

The triton spectra obtained for the ^{32}S$(p,t)^{30}$S reaction for all measured angles are shown in Figs. 3.9 to 3.11 (the spectrum at 22° obtained with the implanted target is shown in Fig. 3.13 on page 75). The abscissas of the figures are in channels (in arbitrary units). The focal plane of the spectrograph spans channels 0 to 4095 (corresponding to 51.1 cm $\lesssim \rho \lesssim$ 92 cm). The detector, however, only covers channels 500 to 2500, corresponding to $70 \leq \rho \leq 86$ cm.

At 10° and 20°, due to the production of the ground states of ^{12}C and ^{13}C via proton elastic scattering off the natural carbon substrate in the CdS target, too much ionization was being produced in the PIDC for the front and rear wires to handle. This is because these scattering processes have high cross sections, and therefore the leakage current on the wires was increased by 20% to the point where the wires sparked frequently. The DAQ was interrupted when the wires sparked.

To overcome this challenge, there were a number of options: (a) reduce the bias voltage on the wires, which was unsatisfactory as it results in a poorer energy resolution; (b) reduce the beam intensity, which was also unsatisfactory unless absolutely necessary,

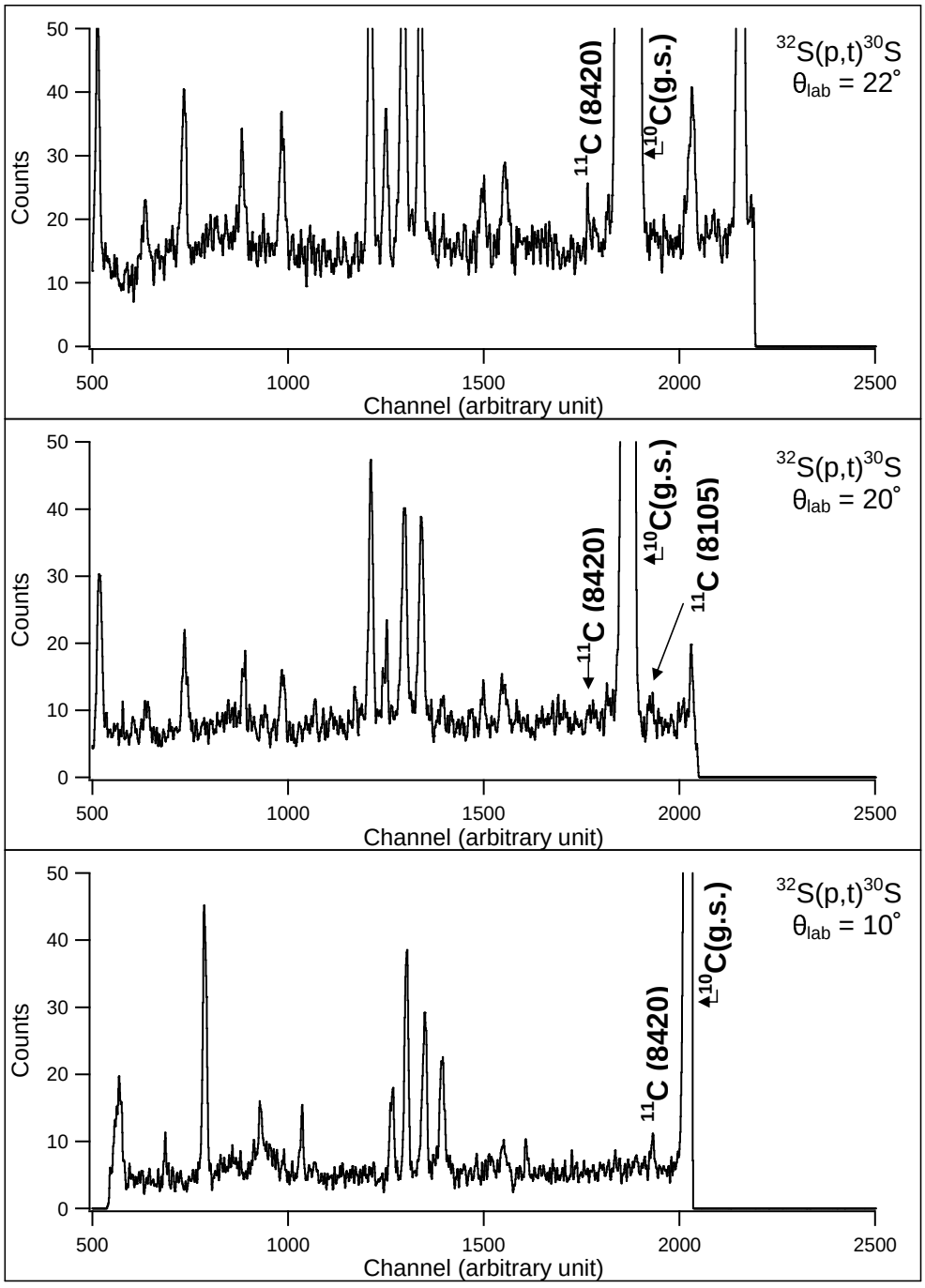

Figure 3.9: Triton spectra from the $^{32}\mathrm{S}(p,t)^{30}\mathrm{S}$ reaction with the CdS target at selected angles. A few peaks from $^{12}\mathrm{C}(p,t)^{10}\mathrm{C}$ and $^{13}\mathrm{C}(p,t)^{11}\mathrm{C}$, produced from reactions on the natural carbon substrate of the CdS target, are identified and labeled with their energy in keV. All other peaks are excited states of ^{30}S. For 10° and 20°, an aluminum plate along the focal plane blocked the channel region greater than ≈ 2050, where elastically scattered particles reached the focal plane. At 10°, the spectrum is shifted slightly to the right due to the difference in reaction angle, and thus the $^{10}\mathrm{C}_{g.s.}$ is cut in half by the aluminium piece. At 22°, the channels greater than ≈ 2200 are cut by the gates.

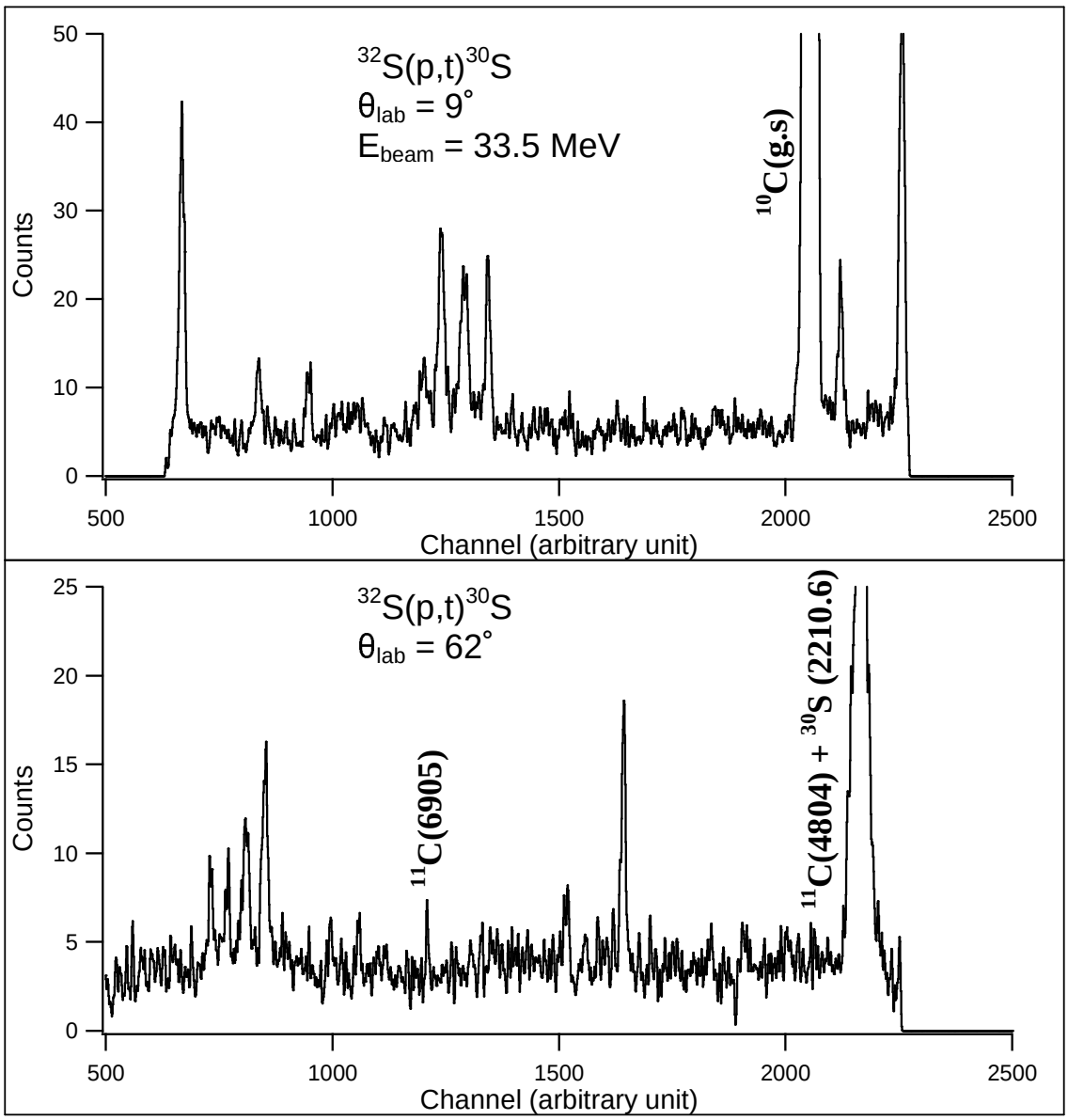

Figure 3.10: Triton spectra from the ^{32}S$(p,t)^{30}$S reaction with the CdS target at selected angles (continued). The spectrum at 9° is collected by a 1-MeV lower beam energy. The spectra are shifted with respect to each other because of the change in magnetic field of the spectrograph from one angle to the next. No aluminium piece was used at these angles to block a part of the focal plane. However, the channel region greater than ≈ 2300 was cut by the gates. All the observed peaks belong to ^{30}S unless otherwise stated, in which case the peaks are labeled with their energy in keV and the nucleus of origin. At 62°, the first excited state of ^{30}S overlaps partially with a state of ^{11}C that is produced by the (p,t) reaction on the ^{13}C content of the CdS target's backing.

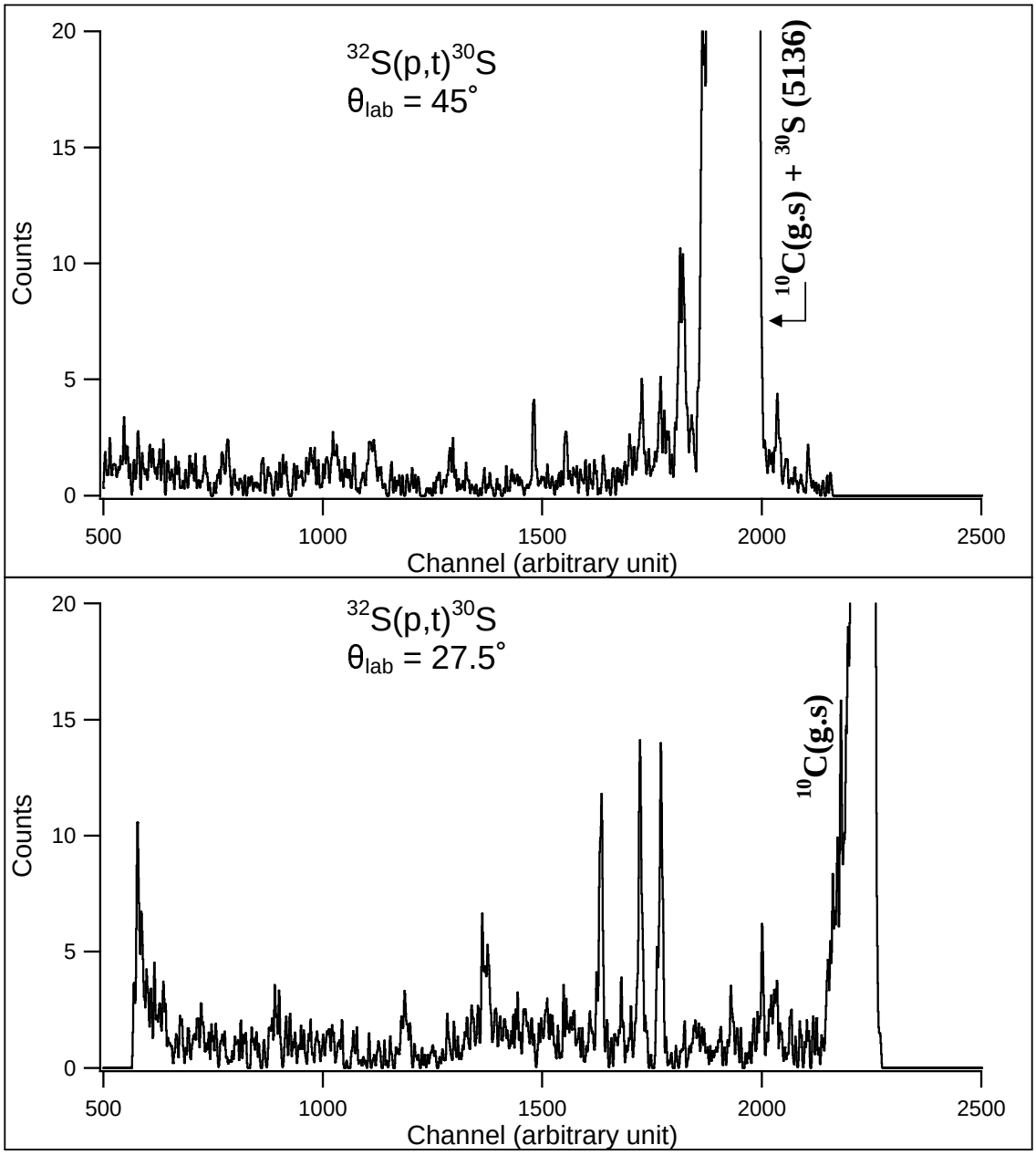

Figure 3.11: Triton spectra from the ^{32}S$(p,t)^{30}$S reaction with the ^{32}S implanted target at selected angles. At 27.5°, the aluminium blocker was used to block the channel region greater than $\approx$ 2300, where the intense elastically scattered protons reached the focal plane. These channels are cut by the gates at 45°. Again, the spectra are shifted with respect to each other because of the difference in magnetic field settings as well as the reaction angle. All the observed peaks belong to ^{30}S, unless otherwise stated, in which case the peaks are labeled with their energy in keV and the nucleus of origin. At 45°, the ground state of ^{12}C has mostly obscured a state in ^{30}S at 5163 keV. With respect to the spectra obtained with the CdS target, the yields are lower for those obtained with the implanted target because the sulfur thickness of this target was lower than that of the CdS target by a factor of 5.

because a lower beam intensity drops the rate of data production, and thus increases the runtime per fixed beamtime. This ultimately results in lower statistics, which in turn makes the analysis painstakingly difficult and less accurate; (c) change the magnetic field of the spectrograph or reduce the gas pressure, both of which would result in shifting the positions of the tritions along the focal plane for the particles of interest. This was also unsatisfactory because the excited states of interest might end up completely removed from the detection plane, or obscured by other contaminant peaks; (d) reduce the solid angle of detection by moving the spectrograph's horizontal slits closer to each other, which is yet another unsatisfactory option, because it too decreases the statistics; (e) block the location along the focal plane where such intense elastically scattered protons were detected. This was the most desirable way of overcoming the challenge, and was achieved with a $\sim$ 3-cm long aluminum plate that was placed in front of the detector at that location.

The position of this piece of aluminium could be set remotely by a motorized track. It was very important to not block the locations where the tritons of interest were being detected. On the cathode *vs.* front position histogram, each vertical band, within the bigger, almost horizontal band corresponding to a particle group (see Fig. 3.6b), corresponds to an excited state in the residual nucleus. The aluminium piece was moved until the vertical bands corresponding to the ground states of ^{12}C and ^{13}C, within the proton band on the cathode *vs.* front position histogram, disappeared. The ionization rate dropped, and the DAQ was resumed.

However, as it is obvious in Fig. 3.7b, the aluminium piece was not thick enough to block all the high energy protons. These protons punched through the metal piece, and appeared on the rear position *vs.* front position histogram as lower energy protons in the form of a separate band on the top of the band corresponding to "good events". This band is shown in Fig. 3.7b. This was confirmed by gating around the "lower energy protons" in the rear position *vs.* front position histogram, and displaying the data that had gone through that gate on the cathode *vs.* scintillator (PMT2) histogram. According to the simulated histogram shown in Fig. 3.5a, those events were scattered protons whose energy loss and residual energy were respectively minimum and maximum compared to those of the other particle groups.

At higher reaction angles, e.g., 22° and 62°, the intense scattered protons were off the

focal range covered by the detector, and thus no aluminium piece was used to block a part of the focal plane position at those angles.

As seen in Figs. 3.9 to 3.11, (p,t) reactions on the natural carbon substrate in the CdS target, as well as on the isotopically pure ^{12}C substrate in the implanted target, produced some contaminant peaks in the triton spectra; however, the spectra obtained with the CdS target also showed a relatively high and almost flat background at all angles, e.g., $\sim$ 14 counts/channel at 22° and $\sim$ 6 counts/channel at 10°. To find the source of this flat background, a ^{nat}Cd target evaporated on natural carbon backing, as well as a pure ^{13}C target (see § 3.1.3) were used.

3.2.3 Background Subtraction

The background from (p,t) reactions on the Cd and carbon in the CdS target was measured with the ^{nat}Cd and the ^{13}C targets, respectively. As seen on the top panel in Fig. 3.12, no unambiguous triton peaks were observed with the ^{nat}Cd target except the ground state of ^{10}C from the natural carbon backing, indicating that reactions on the Cd component of the CdS target only contributed a relatively flat background to the ^{32}S$(p,t)^{30}$S data.

The ^{13}C$(p,t)^{11}$C contaminant reaction was not measured at 10° and 20° runs during November-2007, because these runs were short test runs to see whether or not the two astrophysically important states in ^{30}S (see Chapter 2) could be observed. This reaction was only measured at 9° and 62° during May-2008, and did not contribute significantly in producing background in the spectra of the reaction of interest at these angles. During the run in May-2008, the experimenter on shift had forgotten to change the targets during the experiment at 22°. Therefore, the background with ^{13}C target and the calibration with the Si target were not measured at the latter angle. A typical triton spectrum obtained with the ^{13}C target is shown in the middle panel in Fig. 3.12. This reaction produced low intensity, broad background peaks.

In conclusion, the main contaminant peak in the triton spectra with the CdS target was from the ^{12}C$(p,t)^{10}$C$_{g.s.}$ reaction, with its peak location away from the region of interest.

To reduce the flat background produced by the Cd component of the CdS target, the ^{32}S$(p,t)^{30}$S reaction was remeasured in January-2010 with a ^{32}S implanted target (see

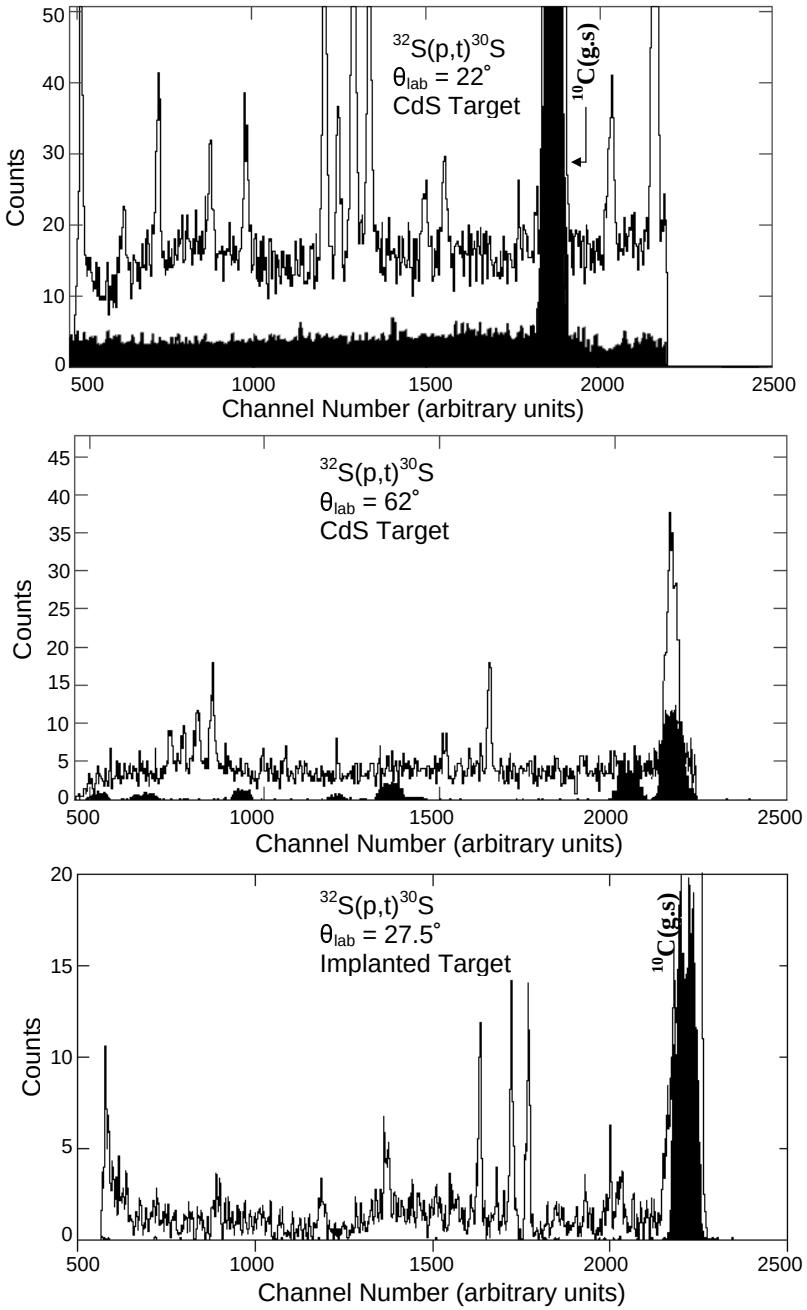

Figure 3.12: Various triton background spectra that contributed to the total yields in the triton spectra of the ^{32}S$(p,t)^{30}$S reaction. On each spectrum, the top spectrum is obtained with the main target labeled, while the filled spectrum is the background spectrum measured with (top) a ^{nat}Cd target on a carbon backing, (middle) a ^{13}C target and (bottom) a ^{12}C target, all normalized to the ^{32}S$(p,t)^{30}$S data. The ^{13}C and Cd components in the CdS target contributed a few contaminant peaks and a negligible flat, and a relatively high and flat background in the ^{32}S$(p,t)^{30}$S spectra, respectively. The implanted target was fairly clean, and thus had a relatively low background. The main contaminant peak in the triton spectra of the reaction of interest with both targets was from the ^{12}C$(p,t)^{10}$C$_{g.s.}$.

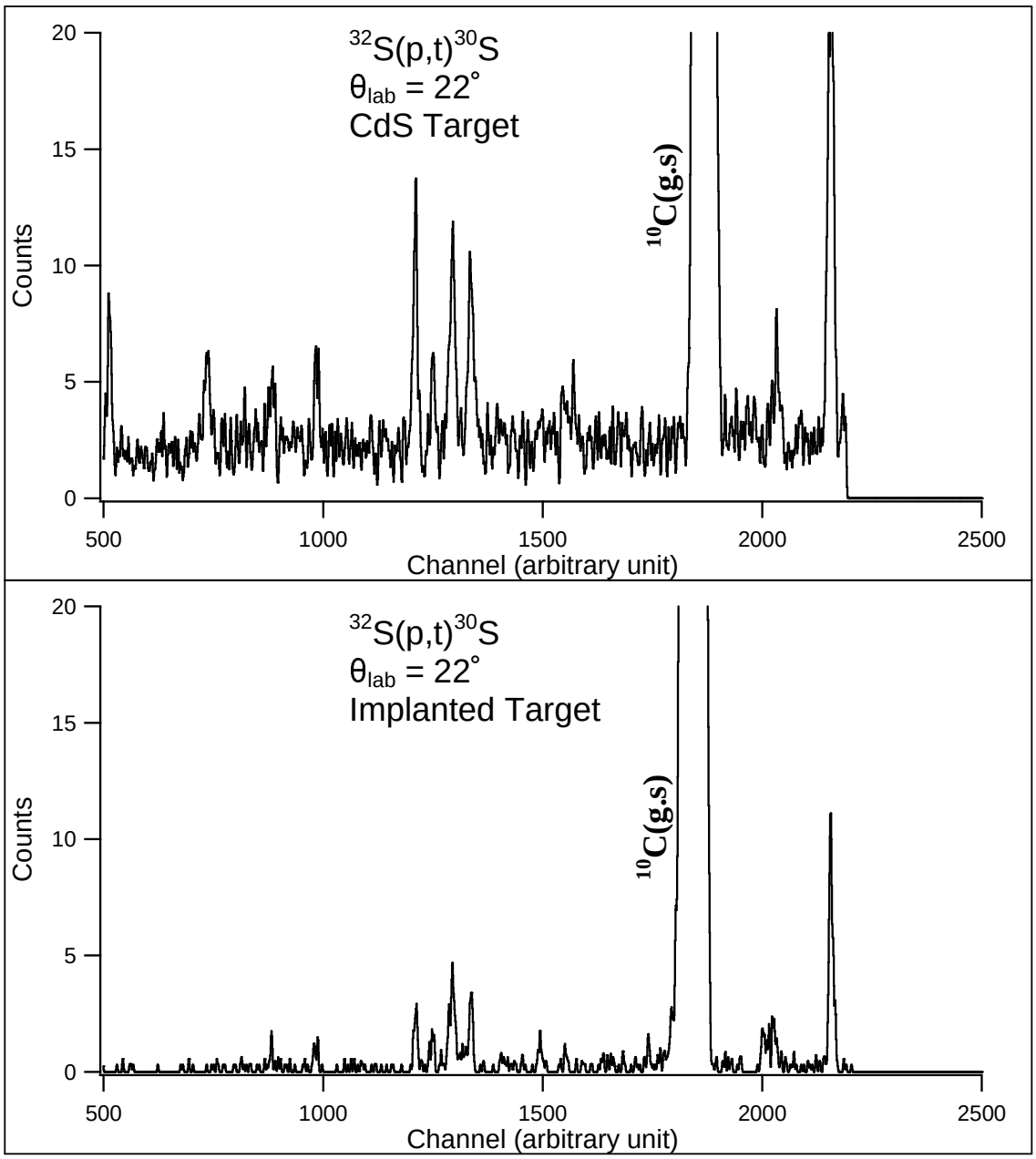

Figure 3.13: The triton spectra from the ^{32}S$(p,t)^{30}$S reaction with (top) the CdS target at 22°, in comparison with that measured with (bottom) the ^{32}S implanted target at the same angle. The yield of the $^{10}C_{g.s.}$ peak in the spectrum obtained with the CdS target is normalized to that in the spectrum obtained with the implanted target, so that the background levels could be compared. The background is clearly reduced by more than a factor of 2 as a result of using the cleaner implanted target.

§ 3.1.3 and Appendix A). The latter target was much cleaner, in terms of the diversity of the isotopes contained, and thus as expected produced much less background (Figs. 3.12

and 3.13). The ^{32}S implanted target had an isotopically pure ^{12}C substrate. To take into account the background produced by the ^{12}C substrate, an isotopically pure ^{12}C foil (see § 3.1.3) was used as a target in January-2010. However, from measuring the ^{12}C$(p,t)^{10}$C reaction, the only contaminant peak that was observed was again the ground state of ^{10}C (see the bottom panel in Fig. 3.12).

The yields of the measured background reactions at each angle were obtained from the corresponding spectra, and were normalized to the time spent on the ^{32}S$(p,t)^{30}$S reaction with the main targets[11] at the same angle. The normalization was performed according to the following equation [123] (p. 289):

$$Y_{nb} = Y_{tm} \times \frac{q_b}{q_t} \times \frac{\Delta x_b}{\Delta x_t} \tag{3.5}$$

where for example in the triton spectrum obtained from the CdS target, Y_{tm} is the total measured yield (in counts) under a contaminant peak that is produced by a background reaction in the main spectrum; Y_{nb} is the yield under the same peak from the spectrum obtained by the background target, e.g., ^{13}C, normalized to the time spent on the main target; q_b and q_t are the total accumulated beam charges with the background target run and the main target run, respectively; and Δx_b and Δx_t are the thickness of the background target and the equivalent thickness of the background material in the main target, respectively. Equation (3.5) is correct under the assumption that the total and background yields are measured under identical detection solid angles. If this is not the case, the equation must be corrected for the differences in solid angles.

For the regions in the spectra that are free of peaks, the Y_i's in equation (3.5) are the counts/channel obtained by taking the area of a portion of the spectrum, and dividing that area by the number of channels covering that area. For any individual spectrum in the absence of a background measurement, this is also how one gets the counts/channel background of the spectrum.

These normalized background yields were then subtracted via Jam from those of the corresponding ^{32}S$(p,t)^{30}$S spectra to obtain the final spectra of interest, which were fitted as described in the next subsection.

[11] CdS or the implanted target.

3.2.4 Peak Identification and Fitting

The analysis software package at WNSL, includes a program, called SpecPlot (also known as Plotter [239]) which is also a Java-based code[12] that simulates and plots the position spectra on the focal plane detector for multiple reaction channels according to the kinematics of the reactions involved, and by taking into account the thicknesses of the gas and the windows inside the detector. The input file for this program resembles that of the TAJSimulation software. These codes are both written specifically for the detector at WNSL, and they both calculate the residual energies of various particles when they stop in the scintillator. SpecPlot further calculates the energies and positions along the focal plane for the recoil nuclei by taking the excitation energies as input, and thus can be used to identify the peaks observed in a spectrum. An example of a simulation with SpecPlot is shown in Fig. 3.14.

Out of the four main 2D histograms previously mentioned, only the rear *vs.* front position is 512 × 512 channels^2 (see Fig. 3.7b). The other three are all 256 × 256 channels^2 each (see Fig. 3.6a). The triton spectra are 1D histograms where the abscissas span 4096 channels[13]; therefore, the channel number corresponding to a peak on the triton spectrum can be tracked down to find the corresponding triton group in the 2D histograms. For example, if a peak is observed in the triton spectrum spanning channel numbers 2006 to 2045, the corresponding triton group would span channels 125 to 128 on both axes of the cathode *vs.* scintillator histogram. This is how the experimenter knows how extended the gates should be on a particular histogram.

The shapes of the peaks in the final background-subtracted focal plane spectra of the $^{32}\mathrm{S}(p,t)^{30}\mathrm{S}$ reaction were to a very good approximation described by Gaussian functions. Thereby, they were fitted using a least-squares multi-Gaussian fit function, offered by an analysis software package called Igor Pro [240], to fit a number n of peaks as follows:

$$y(x) = y_0 + \sum_{i=1}^{n} A_i \exp\left[-\left(\frac{x - x_i}{w_i}\right)^2\right] \tag{3.6}$$

where y_0 is the baseline for the cluster of the peaks under consideration, and A_i, x_i and

[12] Written by Dr. Dale Visser, a former graduate student at WNSL.

[13] However, only channels 500 to 2500 are covered by the actual detection plane. Anything beyond these channels is still on the focal plane of the spectrograph, but is not detected.

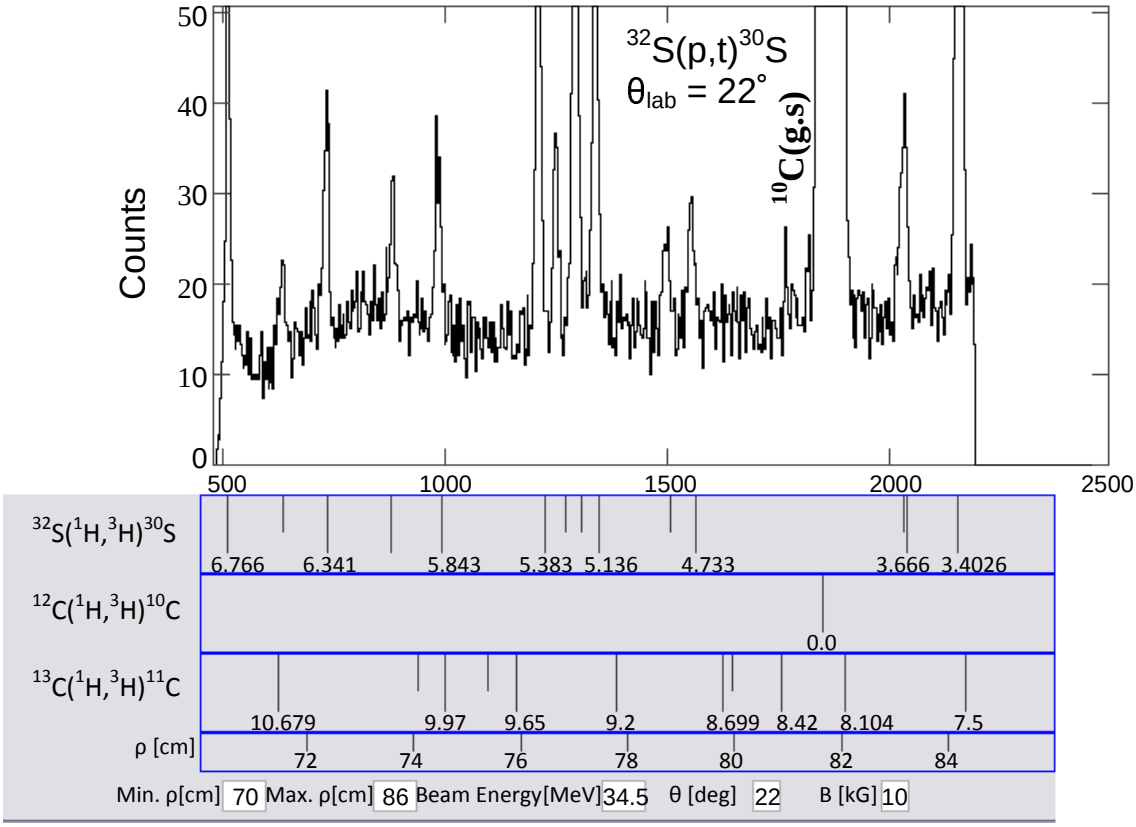

Figure 3.14: (top) The triton spectrum from the ^{32}S$(p,t)^{30}$S reaction with the CdS target at 22°. The abscissa is channel number in arbitrary units. (bottom) The simulation from SpecPlot for the locations of the excited states of ^{30}S, ^{10}C and ^{11}C from the ^{32}S$(p,t)^{30}$S, ^{12}C$(p,t)^{10}$C and ^{13}C$(p,t)^{11}$C reactions, respectively. On the SpecPlot panel, each vertical black line represents an excited state, some of which are labeled by their energies in MeV. At the bottom of the SpecPlot panel, ρ, the radius of the curvature (in cm), the beam energy (in MeV), reaction angle and the magnetic field of the spectrograph (in kG) are shown. The ^{11}C states do not show up as individual peaks in the triton spectrum from the ^{32}S$(p,t)^{30}$S reaction, except for the 8.420 MeV state, because the equivalent thickness of ^{13}C in the backing of the CdS target is very low (~ 0.22 μg/cm^2).

w_i are respectively the amplitude (intensity), centroid and width (standard deviation of the peak centroid) of the i^{th} peak at Full Width at Half Maximum (FWHM).

Although, the background level (baseline) could be taken as a flat line in the triton spectra, the local background level was not constant over all regions; therefore, not all the peaks in the spectra had the same level of baseline background. Thus, each spectrum was divided into as many groups of regions as required, where each region had a number of peaks whose baselines were roughly at the same level.

By estimating the baseline level (in counts/channel) for each region determined from

Jam, the initial noise level was preset, and Igor Pro then automatically could find a number of peaks in that region based on how the local number of counts in that region changed with respect to the initial noise level. If the number of peaks found was not satisfactory, the initial noise level was tweaked until the actual observed peaks in the region were found by the program. The initial properties of these peaks (the free parameters in equation (3.6)) were then pre-estimated by the program. Finally, the actual fits were performed using the multi Gaussian fit function described above without any of the free parameters held fixed, and with the final baseline function of each region chosen to be either a flat line or a polynomial up to the third degree, whichever fitted the data the best.

Some peaks with low statistics were also fitted by a Lorentzian and a Voigt multi fitting function in Igor Pro to ensure that the low statistics had not caused the shapes of such peaks to be skewed. However, from visual comparison between these latter fits with the Gaussian fits, it turned out that all the peaks were indeed described better by Gaussian fits. For comparison, almost all peaks from the triton spectra at 10° and 20° were also fitted using asymmetric exponentially weighted Gaussian functions, also available in Igor Pro; however, these latter fits gave the same results for peaks' centroids as the regular Gaussian fits. The widths and areas of the peaks determined by both methods were also consistent with each other for most cases. However, the regular Gaussian fits described the peaks visually better, and therefore these were used in the analysis. The visual appearance of a fit is not the sole criterion for accepting the fit. Instead, the value of χ^2 determines the goodness of a fit.

It should be noted that the widths of the contaminant peaks were in general much wider than those of ^{30}S, because the detector's position was chosen such that the states of ^{30}S were in focus along the focal plane. The peaks corresponding to ^{30}S states, on the other hand, did not have identical widths but differed by only a few channels at most. Thus, an average width was adopted for all ^{30}S peaks of each triton spectrum.

The ^{30}S peaks in each spectrum were then refitted with their widths held fixed to the value of the average width of the corresponding spectrum, and the resulting centroids were compared with those from the fits, where no parameter was kept fixed. With few exceptions, the centroids in both methods were consistent to within 1σ (standard deviation). Thus, the centroids, widths, and areas of the peaks extracted from those fits (along with their uncertainties) where the parameters were left free to change, were used

for further analysis described in the next subsection.

There were a few cases where according to the SpecPlot simulation two peaks were expected to be observed close to each other but only one peak appeared on the focal plane spectrum with a width that was wider than usual. In such cases, those two expected peaks overlapped, indicating a non-resolved doublet[14]. Such a peak was first fitted to one Gaussian function, and its fit parameters were extracted. Its width was compared to the average width of the peaks in the corresponding spectrum. If the width of the peak in question was at least 50% wider than the average width, then it was fitted to two Gaussian functions with either one or both of the widths fixed to the value of the average width, depending on how much wider with respect to the average width that original peak was. The centroids and areas along with their uncertainties were then extracted from this fit, and were used for further analysis.

If, on the other hand, the width resulting from the fit using one Gaussian function was less than 50% of the average width, the peak was treated as a singlet. In such a case, the fit parameters resulting from the fit using a single Gaussian function were used for further analysis.

3.2.5 Calibration

In order to connect the peaks in a spectrum to excited states of ^{30}S, the channel axis has to be converted to an energy axis. In the triton spectra of the ^{32}S$(p,t)^{30}$S reaction, once the tritons' energies are obtained, one can simply relate each triton peak to the corresponding ^{30}S recoil nucleus using the reaction kinematics, and thus obtain the energies of the excited states of ^{30}S recoils. This is done by calibrating the focal plane position spectrum, which is the main subject of this subsection.

At each reaction angle[15], the triton spectrum from the ^{28}Si$(p,t)^{26}$Si reaction (see the bottom panel in Fig. 3.15) was obtained with a Si target (see § 3.1.3) under identical experimental settings to those of the ^{32}S$(p,t)^{30}$S measurements, and was used as a calibration spectrum to momentum-calibrate the focal plane.

Depending on the reaction angle, at least four narrow and well-isolated peaks corre-

[14]The 0_2^+ and 1_1^+ bound states in ^{30}S form a doublet whose states are $\sim$ 10 keV apart.

[15]The only exception was at 22° during the experiment in May-2008 for the reason discussed earlier.

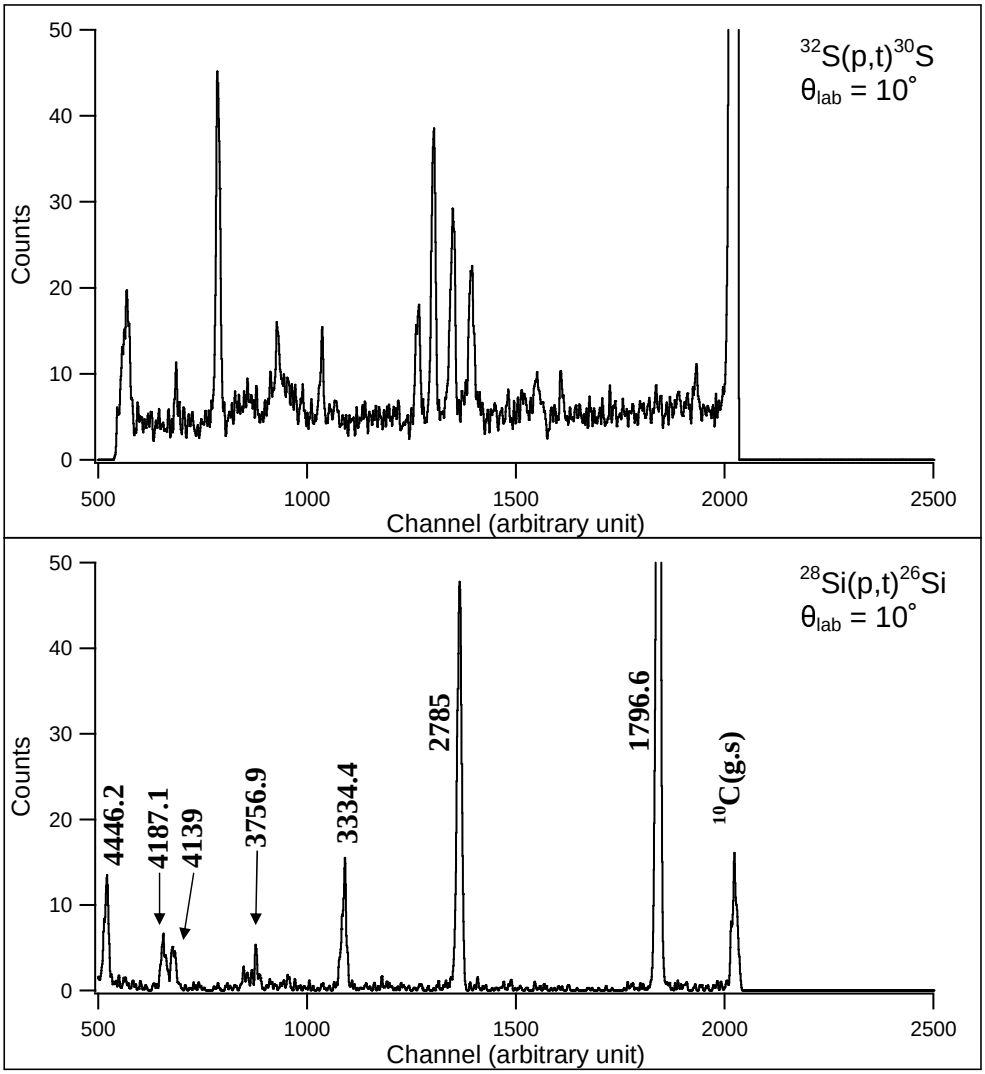

Figure 3.15: The triton spectra from (top) the ^{32}S$(p,t)^{32}$S reaction with the CdS target at 10°, and (bottom) the ^{28}Si$(p,t)^{26}$Si reaction with the Si target at 10°. The latter reaction was used as the calibration reaction to momentum-calibrate the focal plane. The excited states of ^{26}Si are labeled with their energy in keV. The Si target was a clean target, and thus had been used frequently for calibration in various experiments. The exposure of this target to various high energy beams had caused a few μg/cm^2 of natural carbon to buildup on the surface of this target (see text). (p,t) reactions on this thin layer of carbon was responsible for the production of ^{10}C$_{g.s.}$ observed in the bottom spectrum. During the ^{28}Si$(p,t)^{26}$Si measurement, unlike for the ^{32}S$(p,t)^{30}$S measurement, no aluminium blocker was used.

sponding to bound states[16] in ^{26}Si were observed in the triton spectra of the ^{28}Si$(p,t)^{26}$Si reaction. These peaks covered the nearly whole range of the detection plane, and were

[16]The proton threshold for the ^{25}Al$(p,\gamma)^{26}$Si reaction is 5517.43 ± 3.04 keV [241]. Thus, any state in ^{26}Si whose excitation energy is below this value is considered to be a bound state.

Table 3.2: The ^{26}Si excitation energies (in keV) measured in other work. The numbers in parenthesis are the uncertainties in the last digit(s).

Ref. [242] (p,t)	Ref. [243] ^{16}O(^{12}C, $2n\gamma$)	Ref. [244] (^{3}He, n)	Ref. [245] (^{3}He, ^{6}He)	Ref. [246] (p,t)	Ref. [167] (^{3}He, n)	Ref. [168] (p,t)	Ref. [247] (^{3}He, n)	Adopted (Weighted Average)
g.s.	g.s.				g.s.	g.s.	g.s.	g.s.
1796.6(8)	1797.3(1)[a]				1800(30)	1795(11)	1795.9(2)	1796.6(4)
2785.0(17)	2786.4(2)[a]				2780(30)	2790(12)	2783.5(4)	2785(7)
3334.5(25)	3336.4(6)				3330(30)	3339(19)	3332.5(3)[a]	3334.4 (10)
3751(4)	3756.9(2)				3760(30)		3756(2)	3756.9(2)
4138.3(28)	4139.3(7)	4138(4)	4144(8)	4155(2)[b]	4140(30)		4138(1)	4139.0(7)
4188(4)	4187.1(3)	4183(4)	4211(16)			4183(11)		4187.1(3)
4446.1(5)	4446.2(4)				4450(30)	4457(13)	4446(31)	4446.2(4)
4807.4(25)	4810.7(6)				4810(30)	4821(13)	4806(43)	4810.5(6)

[a]The uncertainty in this value was adjusted by a factor of 2 by the AveTools program to obtain the uncertainty in the weighted average.
[b]The uncertainty in this value was adjusted by a factor of 3 by the AveTools program to obtain the uncertainty in the weighted average.

fitted with the same procedure as described in the previous subsection. From the SpecPlot simulations, these peaks were identified with excited states of ^{26}Si. A typical triton spectrum of the ^{28}Si$(p,t)^{26}$Si calibration reaction is shown in Fig. 3.15.

The excitation energies of ^{26}Si shown in Fig. 3.15 were determined by taking weighted averages of the corresponding energies listed in Table 3.2. It should be noted that these excitation energies may not be in sequence, since only those excitation energies are reported whose corresponding peaks have been observed in the triton spectra of the ^{28}Si$(p,t)^{26}$Si reaction in our measurements, and have been used as calibration points to momentum calibrate the triton spectra of the ^{32}S$(p,t)^{30}$S reaction.

The weighted averages were calculated following the standard procedure followed by the nuclear data evaluators of the National Nuclear Data Center (NNDC), where a FORTRAN-90-based tool[17] called AveTools [248] is used. This program combines three different statistical methods to calculate the averages of experimental data with uncertainties. These methods are: the limitation of relative statistical weight method, the normalized residual method and the Rajeval technique. Since a detailed description of these methods can be found in Ref. [249], they are not described here.

In calculating the weighted averages and their associated uncertainties, AveTools calculates a $\chi^2/(N-1)$, where $N-1$ is the number of degrees of freedom, as a measure of the consistency of the whole data set. Therefore, $\chi^2/(N-1)$ provides the information on the deviation of the individual points from the mean. If this term is less than or equal to 2, the weighted average is considered as the recommended value [250]. If, on the other hand, $\chi^2/(N-1) > 2$, the weighting factors, the uncertainties in the data points or both are adjusted by AveTools to reduce all the weights, and to move the weighted mean closer to the unweighted average until a value of less than 2 is obtained for $\chi^2/(N-1)$. In the rare cases where the data points deviate too much from each other and do not overlap, the adjustment may become too large. In such cases, the unweighted means have to be used as the recommended values [250]. Finally, whenever the associated uncertainty in the weighted average is smaller than the minimum experimental uncertainty in the data set, the latter is used as the uncertainty in the weighted mean.

To calibrate the triton spectra of interest, another Java-based program contained in the WNSL analysis software package, called SPANC [251], was used. To run this program,

[17] It is distributed by Prof. T. Kibédi and Prof. T. W. Burrows.

one needs to describe the content, stoichiometry and thickness of the target materials; the reactions and their kinematics used in the experiment; and define the centroids (in channel) and the energies in (MeV) of the peaks which are to be used for calibration of the spectra.

SPANC assumes that the nuclear interaction point in the target is exactly halfway through the specified interaction layer, and calculates the beam energy loss up to this point according to the formulas given in Refs. [252, 253]. The beam energy loss is subtracted from the beam initial energy, and the result is used in the 2-body kinematics calculation for deriving the initial energy of the specified reaction products. SPANC then calculates the energy loss of the latter particles through the remainder of the target via the same energy loss formulas used for the beam. The final energies of the reaction products are calculated taking into account the scattering angle into the spectrograph. With this energy, SPANC automatically calculates (based on equation (3.1)) the position along the focal plane, ρ (in cm), along with an uncertainty for the reaction products, and consequently from the input excitation energies it calculates ρ for the residual nuclei, whose corresponding peaks are used as calibration peaks. Such ρ-values are called the expected radii of the curvature, ρ_{exp}.

SPANC then performs linear regressions to fit the position along the focal plane, ρ (in cm), as a function of the centroid channel for the calibration peaks via a polynomial of up to the 8^{th} degree.

The calibration fit obtained by SPANC is as follows:

$$\rho_{fit} = a_0 + \sum_{i=1}^{8} a_i \left(channel \; - \; channel \; [0]\right)^i \tag{3.7}$$

where *channel* [0] is the unweighted mean of all the centroids of the calibration peaks. It is an exact value, and thus is not really a parameter of the fit. Rather, it is a constant shift of the data made in order to reduce the covariance between the a_0 and a_1 terms. The a_i's are the fit parameters determined by SPANC, and *channel* refers to the given centroid of each of the peaks.

The goodness of the calibration fit is determined via its χ^2/ν and "p-value", where ν is the expectation value for the χ^2/ν distribution, and thus is the number of degrees of freedom; and the p-value is the probability that χ^2/ν would be equal to or greater

than the calculated value if the fit does, in fact, represent the true calibration curve. Good fits have both values of χ^2/ν and p-value near unity. The p-values greater than 0.5 still indicate a good fit. The true check of the goodness of fit is via inspection of $\delta = \rho_{exp} - \rho_{fit}$ divided by its 1σ error for each centroid, where ρ_{fit} for each centroid is obtained from equation (3.7). The 1σ uncertainty in δ comes from the contributions from the uncertainty in the excitation energy assigned to a calibration peak, and the uncertainty in its centroid, which are added quadratically. Finally, SPANC calculates the excitation energy for the residual nucleus of interest given its centroid[18]. The uncertainty in excitation energy is also calculated by considering the uncertainty in ρ.

Since SPANC calculates the excitation energies of the recoil nuclei based on the radius of curvature of the corresponding light reaction product and the energy losses in the target, the actual target layers and their thicknesses are important and have to be known.

The Si target was a self supporting natural silicon foil, and thus had no carbon backing. However, as seen in the bottom spectrum in Fig. 3.15, there was a small peak wider than the others that appeared to be located at a position, where according to SpecPlot simulations the tritons from the ^{12}C$(p,t)^{10}$C reaction populating the $^{10}C_{g.s.}$ were expected to reach the focal plane. Moreover, assuming that this peak corresponded to the $^{10}C_{g.s.}$, it moved with reaction angle as kinematically expected, which confirmed its origin. Therefore, it was assumed that natural carbon had been built up on the surface of the Si target as a result of frequent exposures of this target to various high energy beams.

Thus, the ^{26}Si excited states observed in all the measured triton spectra of the ^{28}Si$(p,t)^{26}$Si reactions were used as calibration points to calibrate via SPANC the energy corresponding to the centroid of the peak that was attributed to $^{10}C_{g.s.}$ in those spectra. The thickness of the carbon layer in the Si-target was then varied until the excitation energy of the carbon peak determined by SPANC was reduced to zero. This thickness was 3.5 ± 0.5 μg/cm^2 for the measurements in November-2007 and May-2008, and 4.8 ± 0.9 μg/cm^2 for the measurement in January-2010.

The latter estimated carbon thickness was confirmed when an isotopically pure ^{12}C target was used during the beamtime in January-2010 in conjunction with the same Si target. During this experiment, the Si target and the ^{12}C target were both used under the

[18]This value is not exact, and has an associated uncertainty obtained from the Gaussian fits.

same experimental conditions at 22°, 27.5° and 45°. The yields under the $^{10}C_{g.s.}$ peaks in the triton spectra of the $^{12}C(p,t)^{10}C$ and $^{28}Si(p,t)^{26}Si$ reactions were determined from the fitting procedure. Thus, by using equation (3.5), the equivalent thickness of carbon layer on the Si target was found to be 5.0 ± 0.5 $\mu g/cm^2$ for the measurement in January-2010.

Similarly, the implanted target showed traces of Si-contamination[19], which originated from keeping the target under vacuum with the presence of silica gel in the vacuum chamber (see Appendix A). Silica gel was primarily used to keep the foils from absorbing moisture prior to pumping down the chamber containing the foils. However, without knowing that it would be problematic, the chamber was pumped down while silica gel was still inside the chamber. Such a significant sudden decrease in the pressure breaks the bonds between silicon and the other materials in the silica gel, and therefore, silicon is gradually evaporated and over time ends up deposited onto the target foils [254]. There was no way to determine the thickness of this contamination layer via the RBS because of the proximity of the ^{28}Si and ^{32}S masses. However, by using the yield under the first and second excited states of ^{26}Si that showed up as contaminant peaks in the triton spectrum of the $^{32}S(p,t)^{30}S$ reaction at 9° during January-2010, we estimated the thickness of the Si-layer in the implanted target to be $\sim 1.0 \pm 0.5$ $\mu g/cm^2$. This layer was added to the implanted target for all the corresponding target related calculations.

Lastly, the target angle with respect to the beam is also important as it changes the actual target thickness seen by the beam particle. At WNSL there is no motorized track to determine the angle between the target and the incident beam precisely, and the target ladder is moved manually each time when the experimenter wants to change a target. The experimenter visually checks to ensure the target ladder and the beam are at a right angle. However, this may introduce an uncertainty in our analysis, because the experimenter may not be able to distinguish a few degrees between the axes. Thus, to ensure that the target angle was not at an angle that would significantly change the target thickness, for each triton spectrum at least three ^{26}Si states were used for calibration, and then the excitation energy of one of the most prominent peaks of the same nucleus (not used as a calibration peak) was determined. Then the Si-target thickness was varied until the excitation energy determined from the calibration matched the mea-

[19]This was confirmed in a $^{32}S(d,t)^{31}S$ experiment for studying ^{31}S states in a separate experiment in Munich.

sured value. That target thickness was then compared to the 311-μg/cm^2 (which is the nominal thickness) to determine the angle at which the target was positioned[20]. The maximum target angle that was determined this way was 9° when the spectrograph was positioned at 20°.

The calibration peaks and the corresponding calibration fits with respect to the spectrograph angle are given below:

• **10° Data:** The 1796.6-, 2785-, 3334.4-, 4139.0-, 4187.1- and 4446.2-keV states of ^{26}Si and the 5136-keV level of ^{30}S were used as calibration points. The latter excited state was used as an internal calibration point, and its energy is the weighted average between the values measured in Refs. [169, 173]. The resulting calibration fit was a polynomial of order 2 with χ^2/ν of 1.13 and a p-value of 0.96. It should be noted that the prominent peaks of ^{26}Si were first used to calibrate the smaller peaks in the corresponding spectrum, and after confirmation of their energy, they were used as calibration points to improve the calibration fit. Similarly, the peak corresponding to the ^{30}S state that was finally used as internal calibration point was first calibrated via the states of ^{26}Si to ensure its identification.

• **20° Data:** The 1796.6-, 2785-, 3756.9-, 4139.0- and 4187.1-keV states of ^{26}Si and the 5136-keV level of ^{30}S were used as calibration points, which resulted in a calibration fit of a polynomial of order 2 with χ^2/ν of 0.99 and a p-value of 0.86.

• **22° Data (from the 2008 measurement):** Unfortunately, no triton spectrum corresponding to the ^{28}Si$(p,t)^{26}$Si reaction was available for this measurement. Thus, we had to solely rely on an internal calibration only. The triton spectrum corresponding to the ^{32}S$(p,t)^{30}$S reaction was initially calibrated by the ^{26}Si states from the corresponding spectra at spectrograph angles of 10° and 20°. This was not ideal of course but it was the first preliminary step. Since in SPANC the reaction angle is an input parameter, the difference between the reactions' kinematics is taken into account. Such a calibration fit resulted in energies for the ^{30}S peaks at 22° that were up to 10 keV different from the expected values. The gates were thus set around the deuterons, and 4 of the states of ^{11}C from the ^{12}C$(p,d)^{11}$C reaction were observed that covered the whole range of the ^{30}S spectrum. These peaks were then used to calibrate the triton spectrum corresponding to

[20]If the target thickness when it is positioned at a right angle to the beam is Δx, the thickness when it is positioned at an angle θ will be $t = \Delta x/\cos\theta$.

the ^{32}S$(p,t)^{30}$S reaction. This calibration was only used as a guide since the difference in reaction kinematics between (p,t) and (p,d) reactions makes the calibration less reliable. This method also reproduced the energies of ^{30}S with differences up to 20 keV. Thus, in the end the SpecPlot simulations were used as a guide to identify the peaks, and thus an internal calibration was obtained using the 3402.6-, 5136-, 5842.6- and 6763-keV states of ^{30}S, which are the weighted averages between the corresponding values (excluding the 5912-keV state in Ref. [169]) measured in Refs. [150, 168, 169, 172, 173, 180]. The resulting calibration fit was a polynomial of degree 2 with χ^2/ν of 0.89 and a p-value of 0.81. To check the goodness of this fit (and all other calibration fits), the $\delta = \rho_{exp} - \rho_{fit}$ divided by its 1σ error for each centroid was plotted. An example of this plot is shown in Fig. 3.16.

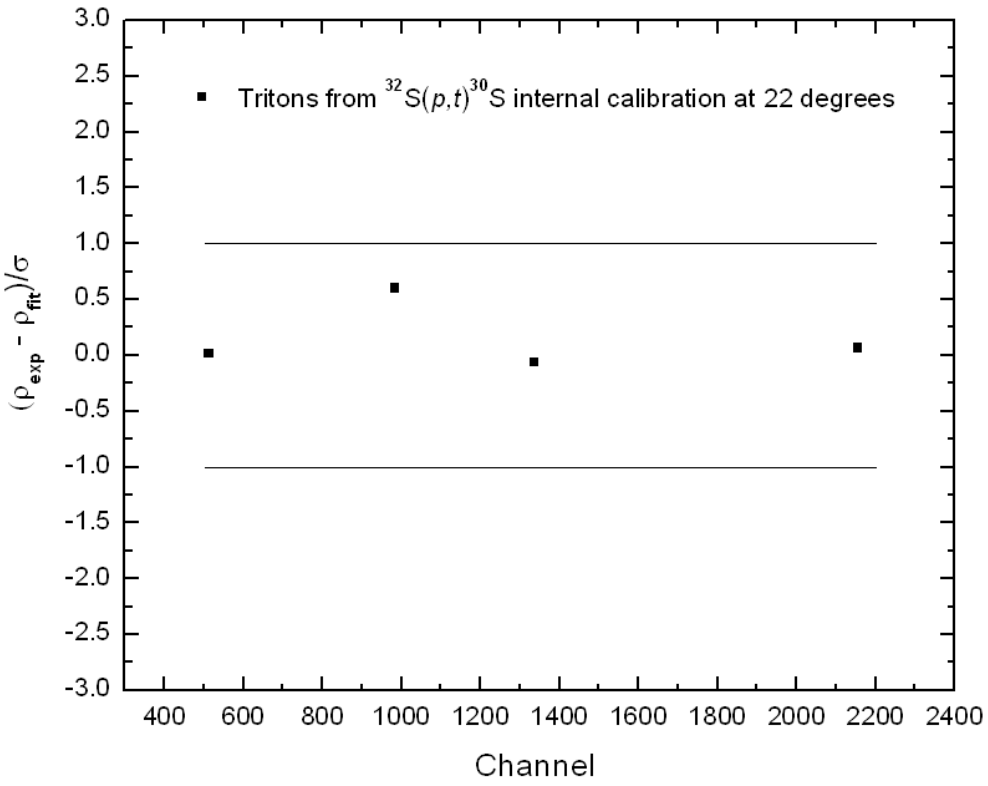

Figure 3.16: The filled squares show the quantity δ, where $\delta = \rho_{exp} - \rho_{fit}$ represents the residuals from second degree polynomial fit to the momentum of tritons from the ^{32}S$(p,t)^{30}$S reaction. The 1σ error in this quantity is introduced by the uncertainties in the calibration energies and the uncertainties in the centroids. The scatter in δ is contained within the allowed 1σ level shown by the solid lines.

• **22° Data (from the 2010 measurement):** The 1796.6- and 2785-keV states of ^{26}Si and the 3402.6- and 5136-keV levels of ^{30}S were used as calibration points. The calibration fit was a polynomial of degree 2 with χ^2/ν of 1.03 and a p-value of 1.

• **27.5° Data:** The 1796.6-, 2785-, 3334.4-, 4446.2- and 4810.5-keV states of ^{26}Si were used as calibration points. The calibration fit was a polynomial of degree 2 with χ^2/ν of 0.82 and a p-value of 0.96.

• **45° Data:** The 1796.6-, 2785-, 3334.4-, 4446.2- and 4810.5-keV states of ^{26}Si were used as calibration points. The calibration fit was a polynomial of degree 2 with χ^2/ν of 0.96 and a p-value of 0.87.

• **62° Data:** The ground state, as well as the 1796.6- and 2785-keV states of ^{26}Si and the 2210.6-, 3402.6- and 5136-keV levels of ^{30}S, were used as calibration points. The calibration fit was a polynomial of degree 3 with χ^2/ν of 1.4 and a p-value of 0.86.

With such calibration fits, the excitation energies of ^{30}S states were determined from SPANC at each angle.

3.2.6 Excitation Energies in ^{30}S

To calculate the final uncertainties in the excitation energies of ^{30}S at each measured angle, three sources of uncertainties were considered: significant contributions from statistical uncertainties in the peaks' centroids, contributions arising from the uncertainties in the targets' thicknesses, and the relative uncertainty in the Q-values of the ^{28}Si$(p,t)^{26}$Si and ^{32}S$(p,t)^{30}$S reactions. This last uncertainty affects the initial tritons' energies, and thus the energy losses through the targets.

The statistical uncertainties turned out to be at most 2 keV for the implanted and the CdS targets. SPANC does not take into account the systematic uncertainties in the target thicknesses. Thus, the target thicknesses were varied to the lowest and highest values, and with each limit the energies of ^{30}S excited states were obtained from the same calibration fits. The average excitation energy differences due to target thicknesses were 1 keV and 2 keV for the implanted and the CdS targets, respectively. Finally, the mass of ^{30}S was uncertain to 3 keV [241], which made the Q-value of the reaction of interest to be 3 keV uncertain. This also introduced another source of systematic uncertainty into our results. However, in a very recent measurement the ground-state to ground-state electron capture Q-value of ^{30}S was measured to be 6141.61(19) keV [140]. From this

Q-value, the mass of ^{30}S was determined in this work to be 29.98490731(393) amu. Thus, the new uncertainty in mass of ^{30}S is 0.4 keV. Under the assumption that these systematic and statistical uncertainties are Gaussian distributed and are mutually independent, they were added in quadrature. Therefore, the ^{30}S excitation energies at those angles measured with the CdS target were up to 3 keV uncertain, and those measured with the implanted target were up to 2 keV uncertain.

Lastly, to obtain the final ^{30}S excitation energies measured in this work, a weighted average was calculated, using AveTools, for each state over all the angles. The uncertainties in the weighted averages were also determined via AveTools. However, in a few cases where the uncertainty in the mean was smaller than the minimum uncertainty in the measured excitation energies, the latter was adopted as the final uncertainty.

The final nuclear energy levels of ^{30}S are presented in Table 3.3 and are shown in Fig. 3.17.

Note that due to the conservation of energy, the more energetic the tritons, the less energetic their corresponding ^{30}S recoils. Also, the more energetic the tritons, the less they can be bent by the magnetic field of the spectrograph. Therefore, such tritons will appear on the higher end of the axis corresponding to the radius of curvature ρ, which is related linearly to the channel axis. Hence, the excitation energy of the ^{30}S recoils increases from right to left.

All the measured energies in this work correspond to the states that were measured before, except for the 4812-keV state, which is observed in this measurement for the first time. If the peak is produced from the reaction of interest, then the extracted excitation energy should not change with angle. If, on the other hand, the peak were actually from a contaminant reaction, then the extracted excitation energy would appear to shift lower as a function of angle. We do not observe any significant shift in the excitation energy of this state over the 5 measured angles[21]. Thus, we have discovered a new level [255], which is also observed in a subsequent γ-ray measurement explained in the next chapter. Moreover, with respect to the previous ^{32}S$(p,t)^{30}$S experiments, all the measured excitation energies from the present work have smaller uncertainties by at least 40% (see Table 3.3).

[21]This peak is obscured by a contaminant peak at 27.5°, which found its way into the triton spectrum of interest at this angle from the tail of high energy deuterons.

Table 3.3: Nuclear energy levels of ^{30}S from the present and the past ^{32}S$(p,t)^{30}$S measurements. Those states that were used as calibration points are marked by an asterisk. The uncertainties are in the last digit(s).

Ref. [168]		Ref. [150]		Present Work	
E_x (keV)	J^π	E_x (keV)	J^π	E_x (keV)	J^π
g.s.	0^+	0000(4)	0^+		
2239(18)	2^+	2210.7*	2^+	2208(3)	
3438(14)	2^+	3402.6*	2^+	3402.6*	
3707(25)	(0^+)	3680(6)	(1^+)	3681(3)	$(1^+, 0^+)$
		4704(5)	(3^+)	4688(2)	3^+
				4812(2)	(2^+)
		5168(6)	$4^+ + 0^+$	5136*	(4^+)
5207(22)				5225(2)	(0^+)
5306(25)				5315(2)	$(3^-, 2^+)$
5426(25)		5383(8)	$(3^-, 2^+)$	5393(2)	(3^+)
		5843(5)	(1^-)	5849(2)	$(1^-, 2^+, 4^+)$
5897(27)				5947(2)	
		6071(11)		6055(3)[a]	(1^-)
		6341(5)		6345(3)[b]	(0^+)
		6532(13)		6536(3)	(2, 3)
		6766(10)	2^+	6768(3)[c]	(2^-)

[a] In Ref. [168], a state was observed whose existence, and thus its excitation energy, were tentatively determined. The latter was reported to be 6108(29) keV. It is unclear if this state is the same as the state observed in the present work at 6055-keV. In Ref. [169], there was a state observed at 6117(10) keV, which may perhaps be the same state as the 6108(29) keV state.

[b] It is ambiguous whether or not the 6415(40) keV state observed in Ref. [168] is the same level. Its energy is much closer to that observed by Yokota *et al.* [169] at 6393(10) keV.

[c] The 6861(40) keV state observed in Ref. [168] is much further away in energy from the present state, and is much closer to that observed by Yokota *et al.* [169] at 6810(10) keV.

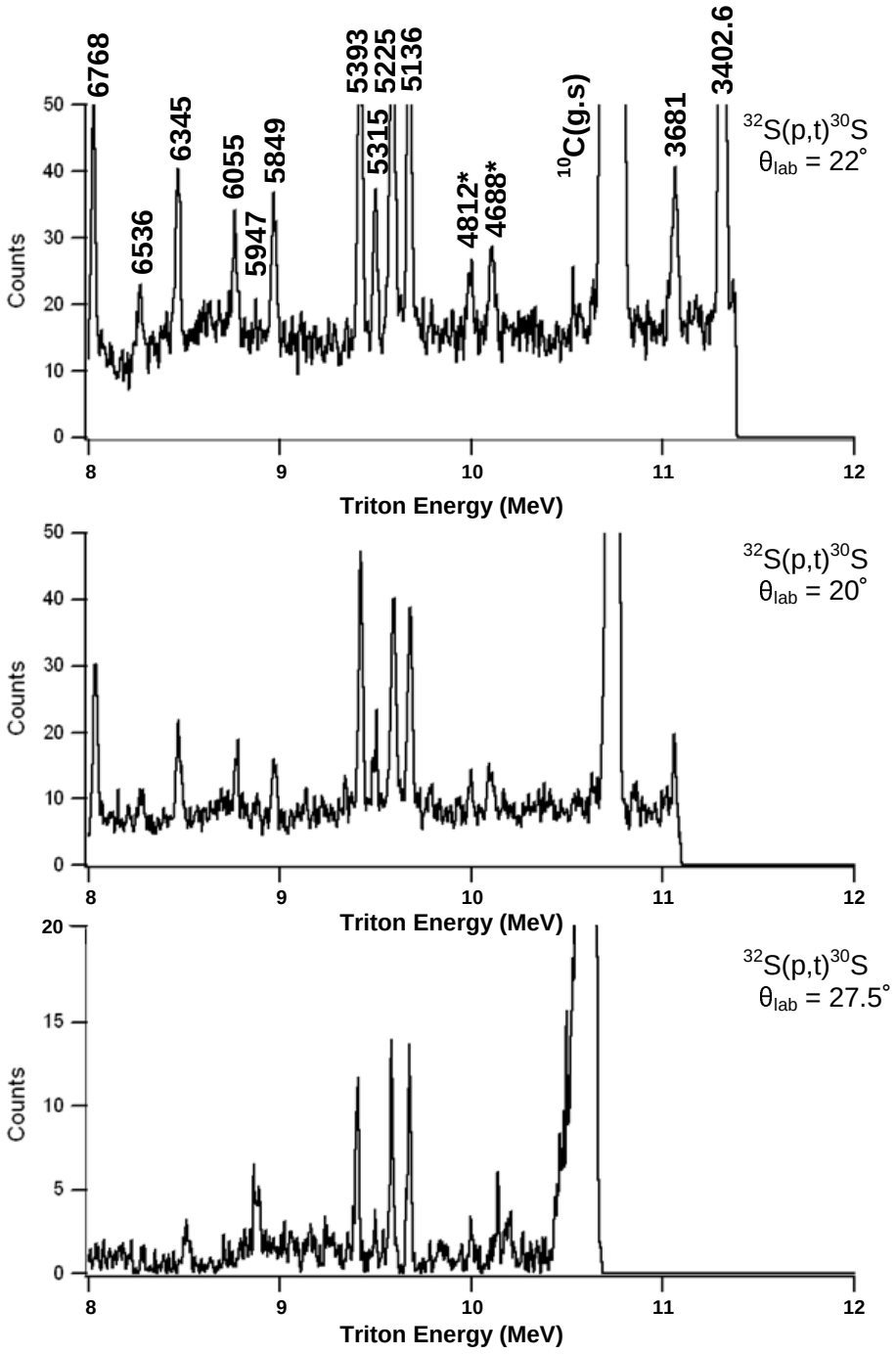

Figure 3.17: Triton spectra from the ^{32}S$(p,t)^{30}$S reaction (top and middle) obtained with the CdS target, and (bottom) obtained with the implanted target. Peaks corresponding to ^{30}S states are labeled with energies in keV. For 20°, an aluminum plate along the focal plane blocked the right side of the spectrum, where elastically scattered particles reached the focal plane, and thus the 3402.6-keV state is largely cut. In the other spectra, the gates have cut the non-relevant regions on the right side. At 27.5°, the spectrum continues on the left side to cover lower energy tritons; however, that part is not shown since the top and middle spectra do not cover that range.

In the next section of this chapter, it will be obvious that the other astrophysically important state predicted in Ref. [149] is most likely the 4688-keV state measured in the present work. However, the excitation energy of this state is not in agreement even within 2σ level with that observed in Ref. [150]. One possible reason is that the energy resolution in the measurement of the latter work was worse (a factor of 3 poorer than ours) such that the two astrophysically important states were not resolved, and thus the excitation energy of 4704(5) keV measured in Ref. [150] falls in between the energies of the two astrophysically important states.

In this case, if the differential cross sections of the state corresponding to our 4688-keV were higher at the measured angles than those of the state corresponding to the 4812-keV state measured in our work, then the centroid of the unresolved doublet (the 4704-keV state) would be shifted toward the state whose cross section is higher. Perhaps, this may explain why the measured energy in Ref. [150] is higher and yet still closer to our measured value of 4688-keV.

Table 3.3 only provides the results of the measurements that were performed using the same reaction, e.g., ^{32}S$(p,t)^{30}$S. For an earlier publication of part of this work [255], which was based on our measurements with the CdS target, the target thickness uncertainties were ignored. However, the Q-value at that time was uncertain by 3-keV. Also, the calibration fit at 20° was improved after the target's angle with respect to the beam direction was considered. Thus, the energies and their uncertainties in the present work are slightly different (5 keV at most) from those in Ref. [255]. Moreover, the addition of two new measurements with the implanted target at different angles made a small change in the overall final excitation energies reported in this thesis.

As seen in Table 3.3, most of the measured energies in the present work are in agreement within $1-2\sigma$ with those measured in the previous ^{32}S$(p,t)^{30}$S measurements. The 5947-keV state observed in the present work is inconsistent with the 5897-keV level observed in Ref. [168]; however, it is in very good agreement with the 5945-keV level observed in Ref. [180]. The existence of the latter state was tentative when it was observed for the first time in Ref. [180]. In our measurement, on the other hand, this state is seen at 10°, 20°, 22° and 27.5°. At the last angle, this state is a moderately prominent peak (see the bottom panel in Fig. 3.17). We therefore confirm the existence of this level in our experiment.

3.2.7 Energy Resolution

The peaks on the triton spectra of the ^{32}S$(p,t)^{30}$S reaction correspond to the excited states of ^{30}S recoils. Each peak has a Gaussian shape as discussed before, and has a certain observed width to it, which comes from a number of factors:

• The intrinsic width of each excited state due to the Heisenberg uncertainty principle, which is calculated via equation (2.15).

• The spread in beam energy, also known as beam energy straggling, which in turn is caused by three processes: (a) the beam particles are not completely mono-energetic when they leave the ion source, and instead have an energy distribution [123] (p. 292); (b) the thermal motions of the target atoms cause a thermal Doppler broadening in the beam energy distribution, which smears the effective beam energy distribution. For the gaseous and the solid targets, this effect is estimated in Refs. [256, 257] and Ref. [258], respectively; (c) the spread in beam energy becomes more pronounced as a result of the statistical fluctuations in the number of collisions between the beam particles and the target that slow the beam down [123] (p. 294).

• The energy straggling of the reaction products [259], which is a spread in the energies of the reaction products as they lose energy traversing the target. This effect is most likely very negligible for light reaction products (e.g., tritons) and is caused by two main factors: (i) differences in the path lengths of the reaction products in the target, since the reaction products lose different amounts of energy depending on the reaction position inside the target; (ii) target non-homogeneities and non-uniformities: the contaminants in the target or non-uniformities in the target thickness change the effective stopping power[22] over the target thickness, which cause further straggling in the energy of beam particles as well as the reaction products. For the ^{32}S$(p,t)^{30}$S reaction, the beam spot size was $\sim$ 2 mm, which was much smaller than the target diameter of $\sim$ 1 cm. Thus, any potential target thickness non-uniformities was expected to contribute negligibly to the total energy resolution. The straggling of the energy loss, $\delta(\Delta E)$ (in keV), for heavy ions in a target of thickness t (in mg/cm^2) is approximated by [260]:

$$\delta(\Delta\, E) = 30\,\varsigma\,\sqrt{\frac{Zt}{A}} \tag{3.8}$$

[22] $S(E) = -dE/dx$, where E is particle energy in eV, and dx is the target thickness in g/cm^2 [123] (p. 233).

where ς is the average charge of the ion in the target, Z is the atomic number, and A is the mass number of the ion.

• The kinematic broadening shown in Fig. 3.18 on page 97. A magnetic spectrograph used to study nuclear reactions is normally required to focus particles leaving the residual nucleus in the same state to the same spot on the detector independent of the direction of emission. However, the energies of these particles vary with the emission angle. The more the path lengths of the particles produced at the same position in the target but emitted into the spectrograph with different angles vary, the better the momentum resolution. This is because as the change in magnetic rigidity, $B\rho$, becomes more significant, the dispersion becomes higher, and thus the resolution gets better. Leaving uncorrected, the kinematic broadening effect thus results in loss of energy resolution. As was discussed briefly in § 3.1.5, the kinematic factor, k, is defined as $k = -\frac{1}{p}\frac{dp}{d\theta_R}$, where p is momentum and θ_R is the reaction angle. This factor can also be determined for non-relativistic cases from the following equation [227]:

$$k = \frac{\sqrt{\frac{M_b M_e E_b}{E_e}}\sin\theta_R}{M_e + M_r - \sqrt{\frac{M_b M_e E_b}{E_e}}\cos\theta_R} \tag{3.9}$$

where M_b, M_e and M_r are the masses of beam, ejectile (light reaction product) and the recoil nucleus (heavy reaction product), respectively; E_b and E_e are the beam energy and the ejectile's energy, respectively; and θ_R is the reaction angle, at which the spectrograph is positioned.

The kinematic broadening comes from two factors that affect the angle of emission of the reaction products:

(a) The angular spread in the beam due to a finite emittance of the ion source, which gets worse as the beam particles interact with the target atoms and are scattered by them. Assuming a constant emittance, ϵ, the contribution of this effect to the total energy resolution is [227]:

$$\left(\frac{\Delta E}{E}\right)_b = \frac{2k\epsilon}{x} \tag{3.10}$$

where $\epsilon = x\Delta\theta_b$, x is the target spot size, $\Delta\theta_b$ is the angular spread in the beam and k is the kinematic factor defined before.

(b) The angular spread in reaction products, which is caused by the finite solid angle of the spectrograph[23], and the target finite spot size (as opposed to a point-like target) that diverges the reaction products by multiple small angle Coulomb scattering. The momentum, and ultimately the energy, depends on the incident angle, by which the particles enter the spectrograph. This angle is affected by the small angle scattering events. The contribution of this effect in the total energy resolution[24] is given by [227]:

$$\left(\frac{\Delta E}{E}\right)_t = \frac{2Mx}{D\rho} \tag{3.11}$$

where M is the magnification of the spectrograph, D is the dispersion, and ρ is the radius of the curvature. Consequently, the total contribution of the kinematic broadening to the total energy resolution is given by [227]:

$$\left(\frac{\Delta E}{E}\right)_k = \sqrt{\left(\frac{\Delta E}{E}\right)_b^2 + \left(\frac{\Delta E}{E}\right)_t^2} \tag{3.12}$$

where the index k indicates kinematic broadening.

• The intrinsic detector resolution, which comes from the fluctuations in the signals arising from those events that deposited the same energy in the detector. The smaller these fluctuations are, the smaller the width of their distribution; and therefore, the better the energy resolution [235] (p. 114).

These fluctuations come from a number of sources [235] (p. 114): (a) random drifts of the operating characteristics of the detector during the course of the measurement; (b) random noise within the detector and in the electronics, which process the signals arising from the detector. The geometric non-uniformities in the detector chamber, e.g., variation in the wire diameters, non-uniformities on the cathode plate, and the variations in gas pressure and gas purity, as well as instabilities in the high voltage applied to the detector components also cause noise; (c) the most significant factor that contributes to these fluctuations is the statistical noise, which is caused by the fact that the charge generated within the detector from interacting incident particles (or radiation) is a discrete quantity.

[23]The closer the acceptance slits are to each other, the less angular divergence is introduced to the ejectiles as they enter the spectrograph. This is due to the fact that $dE/d\theta$ decreases. Better energy resolution is thus obtained.

[24]See Refs. [260, 261]

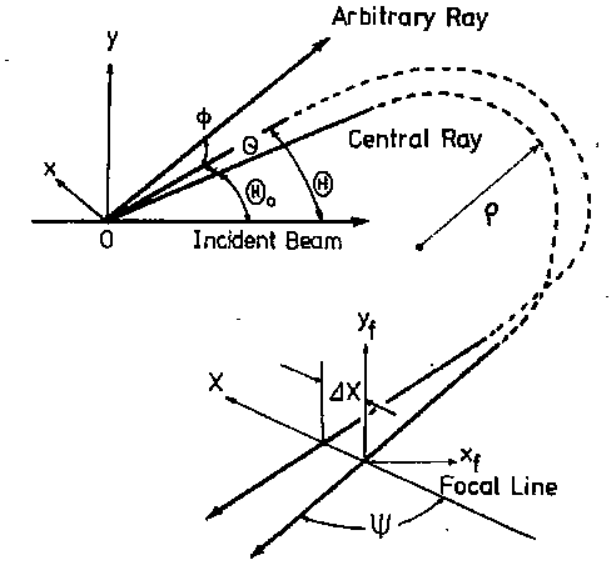

Figure 3.18: Schematic representation of kinematic broadening taken from Ref. [262]. The particles emitted into the spectrograph with slightly different ejection angle, do not end up on the same position along the focal plane, unless the kinematic correction is made. Abbreviations: O: Object point of the spectrograph, Θ: scattering angle in the horizontal direction, Θ_0: scattering angle of the central ray, θ: inclination angle of the ray defined by $\Theta - \Theta_0$, ϕ: inclination angle of the ray in the vertical direction, x: horizontal deviation of particle ray with respect to the particle ray with $\theta = \phi = 0$, y: vertical deviation of particle ray, ρ: radius of the curvature, X: arrival position of a particle along the focal line, ΔX: horizontal deviation of arrival position of an arbitrary particle with respect to the particle with $\theta = \phi = 0$, ψ: tilting angle of the focal line.

Thus, it is subject to random fluctuations from event to event.

A combination of all the aforementioned items contributed to average (over angle) widths[25] of $\sim$ 13 and $\sim$ 10 channels for the ^{30}S states in the triton spectra obtained with the CdS target and the ^{32}S implanted target, respectively. The locations of the centroids of the peaks corresponding to the ^{30}S states were determined in channels and in energy from the peak fitting procedure and calibration, respectively. Therefore, for each spectrum, a plot of energies of the peaks observed in that spectrum *vs.* their centroids (in channel) was made, and was fitted with a first degree polynomial. Thus, the slope (in keV/channel) was determined from the fit. This slope was then multiplied by the average width (in channel) of the peaks in that spectrum[26] to convert the average width to energy

[25]Peaks' widths were determined by the Gaussian fits as explained in § 3.2.4. Average widths for ^{30}S states were then calculated for each spectrum.

[26]Only those peaks corresponding to ^{30}S were used. This is because the contaminant peaks were out of focus, and thus would inevitably have larger observed widths.

(in keV). This width gave the energy resolution of that spectrum. The same procedure was repeated for each spectrum obtained with the same target. Of course, the energy resolution gets worse at higher reaction angles due to higher kinematic broadening. Thus, to obtain a final energy resolution of the measurement with a given target, the energy resolution at each angle was averaged.

The aforementioned average widths of 13 and 10 channels were thus converted to 28 keV and 22 keV average energy resolution in the ^{32}S$(p,t)^{30}$S measurements with the CdS and the ^{32}S implanted targets, respectively. The energy resolution achieved in the present work are improved over those of Ref. [168] (90 keV) and Ref. [150] (80 – 120 keV) by at least a factor of ~ 3.

3.2.8 Isobaric Multiplet Mass Equation

12 proton unbound states of ^{30}S with $E_x < 6.8$ MeV were observed in the present work, and their energies are listed in Table 4.3. The energy of the 4688-keV state is not consistent (even within 2σ) with that of the proposed 3^+_1 state measured in Ref. [150]. However, it is much closer in energy to the latter state than the 4812-keV level, observed here for the first time. Therefore, the 4812-keV state is a potential candidate for the astrophysically important 2^+_3 state.

Moreover, in Ref. [180] a state was measured at 5945 keV, whose existence was considered to be tentative. A state at 5947 keV is observed in our measurements at 10°, 20°, 22° and 27.5°, and it moved kinematically with angle as expected. Thus, the existence of the tentative state measured in Ref. [180] is now confirmed.

All other levels observed in the present work have been previously measured but also have unknown or tentatively assigned spin-parities (see Tables 2.1 to 2.3). However, constraints on the J^π assignments can be obtained from comparisons with the mirror nucleus ^{30}Si, and with guidance from the IMME predictions for the ^{30}S excitation energies.

3.2.8.1 Theoretical Aspects of the IMME

Under the assumptions that the specific nuclear properties of all isospin multiplet members are identical, and that all charge dependent forces are two-body in character, the relation between the masses of a given isospin multiplet can be written to the first-

order as [263]:

$$M(A,T,T_z) = a(A,T) + b(A,T)T_z + c(A,T)T_z^2 \tag{3.13}$$

where A, T and T_z are the mass number, isospin and isospin projection, respectively. The above equation is known as the IMME. The $a(A,T)$, $b(A,T)$ and $c(A,T)$ coefficients are respectively related to the isoscalar, isovector and isotensor Coulomb displacement energies between isobaric analog states, with small contributions from other charge dependent effects (such as the electromagnetic spin-orbit interaction), and are defined as follows [263]:

$$a(A,T) = \frac{1}{2}(m_n + m_H)A + \langle TTz|H_0|TTz\rangle + E_c^{(0)}(A,T) - T(T+1)E_c^{(2)}(A,T) \tag{3.14}$$

$$b(A,T) = (m_n - m_H) - E_c^{(1)}(A,T) \tag{3.15}$$

$$c(A,T) = 3E_c^{(2)}(A,T) \tag{3.16}$$

where m_n and m_H are the masses of the neutron and proton, respectively; $E_c^{(0)}(A,T)$, $E_c^{(1)}(A,T)$ and $E_c^{(2)}(A,T)$ are the isoscalar, isovector and isotensor Coulomb energies, respectively, that are the eigenvalues of the Hamiltonian of the Coulomb interaction; and the quantity H_0 is the charge-independent part of the nuclear Hamiltonian [263] (p. 303). These terms are defined as follows [263]:

$$E_c^{(0)}(A,T) = \left\langle \alpha T \| H_c^{(0)} \| \alpha T \right\rangle \tag{3.17}$$

$$E_c^{(1)}(A,T) = \frac{-1}{\sqrt{T(T+1)}} \left\langle \alpha T \| H_c^{(1)} \| \alpha T \right\rangle \tag{3.18}$$

$$E_c^{(2)}(A,T) = \frac{1}{\sqrt{T(T+1)(2T-1)(2T+3)}} \left\langle \alpha T \| H_c^{(2)} \| \alpha T \right\rangle \tag{3.19}$$

$$H_c = H_c^{(0)} + H_c^{(1)} + H_c^{(2)} \tag{3.20}$$

where the α coefficients are the quantum numbers apart from T and T_z; and $H_c^{(0)}$, $H_c^{(1)}$ and $H_c^{(2)}$ are respectively the isoscalar, isovector and isotensor Hamiltonians. In particular, the term $a(A,T)$ includes the average Coulomb energy for a given multiplet, while $b(A,T)$ contains an average electrostatic energy increase between a newly created proton and the core, and $c(A,T)$ contains the change in electrostatic energy repulsion between the valence protons. The coefficient $b(A,T)$ has a negative value, while $c(A,T)$ has a

positive value [264].

The energies of the $2\,T\,+\,1$ members of an isobaric multiplet are shifted relative to each other mostly because of the electrostatic interaction between the protons in the nucleus.

In an isobaric triplet, $T = 1$, equations (3.17) to (3.19) are transformed into [265]:

$$E_c^{(0)}(A,1) = \frac{1}{3}\left[E_{Coul}(A,1,-1) + E_{Coul}(A,1,0) + E_{Coul}(A,1,+1)\right] \tag{3.21}$$

$$E_c^{(1)}(A,1) = \frac{1}{2}\left[E_{Coul}(A,1,-1) - E_{Coul}(A,1,+1)\right] \tag{3.22}$$

$$E_c^{(2)}(A,1) = \frac{1}{6}\left[E_{Coul}(A,1,-1) - 2E_{Coul}(A,1,0) + E_{Coul}(A,1,+1)\right] \tag{3.23}$$

where $E_{Coul}(A,T,T_z)$ is the Coulomb displacement energy as a function of mass number, isospin and isospin projection. For an isobaric triplet where $T = 1$, T_z could be -1, 0 and 1. Equation (3.23) can be rearranged to have a general form found in the literature as follows:

$$E_c^{(2)}(A,T) = \frac{1}{6}\left[\Delta E_{Coul}(A,T,T\,-\,2|T\,-\,1) - \Delta E_{Coul}(A,T,T\,-\,1|T)\right] \tag{3.24}$$

where $\Delta E_{Coul}(A,T,T\,-\,2|T\,-\,1)$ is the difference between the Coulomb displacement energies of the $(A,T,T\,-\,2)$ and $(A,T,T\,-\,1)$ isobaric multiplets. For the specific case of isobaric triplet, $T = 1$, the above equation becomes [265]:

$$E_c^{(2)}(A,1) = \frac{1}{6}\left[\Delta E_{Coul}(A,1,-1|0) - \Delta E_{Coul}(A,1,0|+1)\right] \tag{3.25}$$

Thus, combining the equation above with equation (3.16) gives [265]:

$$c(A,1) = \frac{1}{2}\left[E_{Coul}(A,1,-1) - 2E_{Coul}(A,1,0) + E_{Coul}(A,1,+1)\right] \tag{3.26}$$

This last equation for an isospin triplet is equivalent to [266]:

$$E_x(T_z = -1) = 2E_x(T_z = 0) - E_x(T_z = 1) + 2\left[c\,-\,c(g.s.)\right] \tag{3.27}$$

where E_x is the excitation energy; T_z = -1, 0 and 1 refer to the isospin projection of

the proton-rich, self-conjugate[27] and neutron-rich members of the triplet, respectively; and c and $c(g.s.)$ are the isotensor Coulomb displacement energies as functions of atomic mass and isospin for the isobaric triplet in an excited state, and the ground state triplet, respectively.

Consequently, the excitation energies of proton-rich nuclei can be estimated from experimentally well known E_x values of the corresponding self-conjugate and neutron-rich nuclei.

3.2.8.2 Determination of ^{30}S Excitation Energies via the IMME

The nucleus of interest for the present work is ^{30}S, whose excitation energies are to be estimated with the IMME. ^{30}S is the proton-rich member of the $A = 30$ isospin triplet with T_z = -1. The other two neighboring members of this family are its neutron-rich mirror nucleus ^{30}Si with $T_z = 1$, and the self-conjugate member ^{30}P with $T_z = 0$. Together, the states of these nuclei are analogs to one another, and their structures are nearly identical.

In order to calculate via equation (3.27) the excitation energies of ^{30}S, the last term in equation (3.27), $c - c(g.s.)$, has to be determined first. From equation (3.25) it is obvious that:

$$E_c^{(2)}(30,1) = \frac{1}{6}[\underbrace{(E_{Coul}(^{30}S) - E_{Coul}(^{30}P))}_{\Delta E_{Coul}(A,1,-1|0)} - \underbrace{(E_{Coul}(^{30}P) - E_{Coul}(^{30}Si))}_{\Delta E_{Coul}(A,1,0|1)}] \tag{3.28}$$

Thus, if $E_c^{(2)}(30,1)$ is found, then equation (3.16) determines the isotensor Coulomb displacement energy, c.

The ΔE_{Coul} terms in equation (3.25) have been measured experimentally and determined theoretically for some states. The latter values are given in Table 3.4. The theoretical values have been calculated using first order perturbation theory with the Hamiltonian defined in equation (3.20).

The adopted values listed in the last column in Table 3.4 were used together with equations (3.25) and (3.16) to determine the isotensor Coulomb displacement energies, c, along with their associated uncertainties for each state labeled by its J^π-value in

[27] Nuclei with the same number of protons and neutrons are called self-conjugate. They do not have mirror nuclei.

Table 3.4: Differences in Coulomb displacement energies, ΔE_{Coul}, for $A = 30$ isobaric triplet members. The numbers in parenthesis are the uncertainties in the last digit(s).

Nuclei Pair[a]	T, J$^{\pi}$ [b]	$(\Delta E_{Coul})_{exp}$ [c] (MeV)	$(\Delta E_{Coul})_{exp}$ [d] (MeV)	$(\Delta E_{Coul})_{theo}$ [e] (MeV)	$(\Delta E_{Coul})_{adop}$ [f] (MeV)
^{30}P – ^{30}Si	$1, 0^+_1$	5.6854(26)	5.702(8)	5.811	5.687(3)
^{30}P – ^{30}Si	$1, 2^+_1$	5.7107(27)	5.727(8)	5.471	5.712(5)
^{30}P – ^{30}Si	$1, 2^+_2$	5.6922(29)	5.707(13)	5.702	5.693(3)
^{30}P – ^{30}Si	$1, 1^+_1$	5.7395(40)		5.635	5.7395(40)
^{30}P – ^{30}Si	$1, 0^+_2$	5.6883(40)			5.6883(40)
^{30}P – ^{30}Si	$1, 3^-_1$			5.624	5.624
^{30}P – ^{30}Si	$1, 1^-_1$			5.399	5.399
^{30}S – ^{30}P	$1, 0^+_1$	6.2494(39)	6.239(13)	6.227	6.249(4)
^{30}S – ^{30}P	$1, 2^+_1$	6.1994(40)	6.170(30)	6.153	6.199(4)
^{30}S – ^{30}P	$1, 2^+_2$	6.1465(41)	6.125(30)	6.108	6.146(4)
^{30}S – ^{30}P	$1, 0^+_2$			6.049	6.049
^{30}S – ^{30}P	$1, 3^-_1$			6.029	6.029
^{30}S – ^{30}P	$1, 1^-_1$			5.818	5.818

[a] In equation (3.25), $\Delta E_{Coul}(A, 1, -1|0) = E_{Coul}(A, 1, -1) - E_{Coul}(A, 1, 0)$, where the numbers in the argument are the mass number, isospin and isospin projection, respectively. The isospin projections of ^{30}S, ^{30}P and ^{30}Si are -1, 0 and 1, respectively.

[b] The isospin, and spin-parity of the analog state under consideration.

[c] The experimental value taken from Ref. [264].

[d] The experimental value taken from Ref. [267].

[e] The theoretical value taken from Ref. [267].

[f] The adopted values. When possible, a weighted average (calculated via AveTools) between the values measured in Ref. [264] and Ref. [267] was adopted.

Table 3.4. These Coulomb displacement energies are shown in Table 3.5.

As seen in the last column in Table 3.5, $c(g.s.) = 281.1(24)$ keV is obtained for the 0^+_1 ground state in ^{30}S, which is in very good agreement with the value of 282.0(29) keV, measured in Ref. [264]. Also $E_c^{(2)}(30, 1) = 93.7(8)$ keV is in very good agreement with the measured value of 94.0(10) keV [264].

Unfortunately, the differences in Coulomb displacement energies, ΔE_{Coul}, between $A = 30$ isobaric triplet members have not been measured for all the states. Moreover, among the states for which these terms are known, there are only two resonances at 3^-_1 and 1^-_1, for which ΔE_{Coul} have been theoretically determined. Thus, in order to use equation (3.27) to determine the excitation energies of ^{30}S, an average value was obtained

Table 3.5: Isotensor Coulomb displacement energies for $A = 30$ isobaric triplet analog states.

T, J^π	$E_c^{(2)}(30,1)^a$ (keV)	$c(30,1)^b$ (keV)	$c - c(g.s.)$ (keV)
$1, 0_1^+$	93.7(8)	281.1(24)^c	0
$1, 2_1^+$	81.2(11)	243.5(33)	-37.6(41)
$1, 2_2^+$	75.5(8)	226.5(24)	-54.6(34)
$1, 0_2^+$	60.1(7)	180.3(21)	-100.8(32)
$1, 3_1^-$	64.5^d	193.5^d	-87.6(24)
$1, 1_1^-$	69.8^d	209.5^d	-71.6(24)

[a] From equation (3.25).
[b] $c(A,T)$ is the isotensor Coulomb displacement energy calculated from equation (3.16).
[c] This value is $c(g.s.)$ used in equation (3.27). The isotensor Coulomb displacement energy for the excited states is simply written as c.
[d] This value is based on the theoretical values, and thus has no uncertainty.

from the values of $c - c(g.s.)$ terms, listed in Table 3.5. This average value is -71(11) keV.

In an earlier attempt to use the IMME to estimate the excitation energies of ^{30}S [255], the $c - c(g.s.)$ terms were calculated separately from the ΔE_{Coul} terms measured in Refs. [264, 267], given in Table 3.4, and then a weighted average of the $c - c(g.s.)$ terms was obtained using AveTools. AveTools is very sensitive to the data points, and thus back then this latter term was calculated to be -67(7) keV, which is still in good agreement with the final new value of -71(11) keV.

Moreover, Iliadis *et al.* [149] had used the IMME earlier to estimate for the first time the excitation energies of the two astrophysically important states in ^{30}S in the range of 4.7 to 4.8 MeV, which were unobserved at the time. In that attempt, the ^{30}S excitation energies were first calculated via IMME without using the $2[c - c(g.s.)]$ term [268]. Then, the average deviation in the calculated and the measured ^{30}S excitation energies was obtained. The calculated values were larger than the measured values by almost 100 keV [268]. Such deviations were attributed to the $2[c - c(g.s.)]$ term that had been ignored in the calculations. Therefore, the value of the latter term was estimated to be equal to -100 keV which resulted the $c - c(g.s.)$ term to be -50 keV [268]. Our value of -71(11) keV for this term is different from that of Ref. [149] by 30%.

Equation (3.27) can only be used for the analog states. Unlike ^{30}S and ^{30}Si that are even-even[28] nuclei, ^{30}P is an odd-odd nucleus, and thus its ground state is not 0^+. The ground state of ^{30}P is a 1^+ state, and the first 0^+ state appears at 677.01(3) keV [187]. Therefore, equation (3.27) simply becomes:

$$E_x(^{30}S) = 2E_x(^{30}P) - 2 \times 677.01 - E_x(^{30}Si) - 142 \tag{3.29}$$

where E_x's are the excitation energies in keV, 677.01-keV is the energy of the first 0^+ state in ^{30}P, and $2[c - c(g.s.)]$ = -142 keV.

Table 3.6: The isospin triplet ($T = 1$) analog states of $A = 30$ nuclei up to 6 MeV. The excitation energies are in keV.

^{30}Si[a]		^{30}P[a]		^{30}S[b]	From IMME[c]
E_x (keV)	J^π	E_x (keV)	T,J^π	E_x (keV)	E_x (keV)
0	0^+	677.01(3)	1,0^+		0
2235.321(18)	2^+	2937.46(2)	1,2^+	2208(3)	2144(11)[d]
3498.49(3)	2^+	4182.81(6)	1,2^+		3371(11)
3769.48(4)	1^+	4502.21(9)	1,1^+	3681(3)	3739(11)
3787.72(4)	0^+	4468.33(7)	1,0^+		3653(11)
4810.31(11)	2^+	5576.3(1)	1,2^+	4812(2)	4846(11)
4830.85(4)	3^+	5508.55(8)	1,(2,3)	4688(2)	4690(11)
5231.38(7)	3^+	6051(5)	1,$(3,4,5)^+$	5393(2)	5375(15)
5279.37(14)	4^+	5934(5)	1,(3^+)[e]		5093(15)
5372.2(6)	0^+	5993(5)	1,$(0,1,2)^-$[e]	5225(2)	5118(15)
5487.50(5)	3^-	6093.5(1)	1,3^-	5315(2)	5203(11)
5614.04(13)	2^+	6520.8(5)	1,$(1^+,2^+)$	5849(2)	5932(11)
5950.73(15)	4^+	6648(5)		5947(2)	5849(15)

[a]The experimental excitation energies are from Ref. [187].
[b]The experimental excitation energies are from this work only. The states that were used as internal calibration points are excluded.
[c]Calculated from equation (3.29) together with the states of ^{30}Si and ^{30}P given in this table.
[d]11 keV is the uncertainty in the $c - c(g.s.)$ term, which dominated over all the other uncertainties associated with the terms in equation (3.29).
[e]See text for discussion.

The IMME was only used to calculate the excitation energies in ^{30}S up to $E_x \sim 6$ MeV (see Table 3.6), because apart from very few states, all the other states in ^{30}S whose

[28]The number of neutrons and protons are both even.

measured excitation energies are higher than 6 MeV have either unknown or tentative J^π assignments. In addition, many of the states in ^{30}P in that range of excitation energy also lack firm spin-parity assignments (see Ref. [187]). Therefore, it is a difficult task to find the analog states of $A = 30$ isobaric triplet with $E_x > 6$ MeV.

Table 3.6 shows the measured[29] isospin triplet ($T = 1$) analog states of $A = 30$ nuclei up to 6 MeV in comparison with the theoretical ^{30}S excitation energies obtained in this work from using the IMME. The uncertainty in the latter values comes from proper propagation of the uncertainties [269] in the terms in equation (3.29).

It was difficult to determine which states were the 4^+_1 and 0^+_2 states in ^{30}P that belong to the isospin triplet. The former was ambiguous because there are only two states in the range of interest in ^{30}P, the 5597- and 6051-keV states, whose J^π values may be 4^+. The 5597-keV state results in a prediction for the energy of the analog state in ^{30}S to be $\sim$ 700 keV lower than the measured value. On the other hand, the 6051-keV state is already considered to belong to the 3^+_2 isospin triplet, and it gives the energy of the analog state in ^{30}S to be $\sim$ 200 keV higher than the measured value if it is considered to be the 4^+_1 state.

Similarly, although the 5372-keV state in ^{30}Si is a 0^+ state, there is no firm or even tentatively assigned 0^+ state in ^{30}P that would result in a theoretical value for the excitation energy of the analog ^{30}S state to be in the range of within 100 keV from the measured value. The known 0^+ states in ^{30}P are much further away from the range of interest, and thus were not considered. There are a few states in the 5940 – 6140 keV range in ^{30}P with which the excitation energy of the 0^+_2 state in ^{30}S predicted from the IMME would be close to the measured value; however, their spin assignments do not include $J = 0$. Thus, it was decided to use the 5993-keV state, whose spin is tentatively known to include $J = 0$ but its parity is firmly known to be negative.

For each ^{30}S state, the difference between the measured (from the present work) excitation energy, and that predicted from using the IMME was calculated. These deviations were then averaged. Finally, an unweighted average of 25 keV was obtained. Thus, instead of using the uncertainties in the predicted values obtained from the error propagation, which are shown in Table 3.6, the aforementioned average value was adopted

[29]The ^{30}S measured excitation energies are from this work only. Those states that have been used as calibration are not considered as independent measured values, and thus are not listed in the table. The ground state of ^{30}S was not observed in this work.

as a universal uncertainty in each ^{30}S excitation energy predicted from the IMME. The scatter around the universal average deviation between the measured and predicted excitation energies of ^{30}S was determined in the work of Iliadis *et al.* [149] in a similar manner. In that work, the result was a 40-keV universal uncertainty in the predicted values, which is 1.6 times larger than our 25-keV value.

The current IMME predictions are roughly consistent with those given in Ref. [255]. The differences between the predicted values listed in the present work and those in Ref. [255] are mainly due to the 8-keV difference in the $c - c(g.s.)$ terms as discussed before. Moreover, the 3_2^+ state in ^{30}P that belongs to the isospin triplet was chosen to be the 5934-keV state in Ref. [255], because with this state, the predicted excitation energy for the ^{30}S analog state would amount to 5148 keV, which was consistent within uncertainties with the measured value of 5136-keV state in ^{30}S. At that time, it was thought that this state is the 3_2^+ state. However, we now know (see Chapter 4) that this state is most likely the 4_1^+ state, for which the ^{30}P analog state is now chosen to be the 6051-keV state. As a result, the new predicted value differs from the old one. Similarly, for the 3_1^- state in Ref. [255], the ^{30}P analog state was chosen to be the 6051-keV state, whose spin is tentatively assigned, and while it includes $J = 3$, the parity is positive. This state was chosen because the resulting predicted value was close to the measured value. After a discussion with Dr. Balraj Singh [250], however, it was decided to choose the 6094-keV state of ^{30}P, regardless of the fact that with this state the predicted value for the excitation energy for the ^{30}S analog state is ~ 100 keV less than the value measured in the present work.

3.2.9 Cross Sections

The calculation of thermonuclear reaction rates requires knowledge of the nuclear reaction cross section. As discussed in Chapter 2, the probability for a reaction to occur is expressed in terms of a reaction cross section, σ, which represents a hypothetical effective area around the target atoms. If the incident particle crosses this area, the reaction will proceed with the probability of unity. The cross section varies with the incident energy.

The cross section is related to the total number of interactions between the target atoms and the incident particles that occur per unit time. Assuming that this number

is equal to the total number of emitted interaction products per unit time, then if the detection system does not cover the full 4π sr solid angle around the target, some of the emitted interaction products will be missed. Therefore, instead of obtaining the total cross section[30], one would obtain the differential cross section, $(d\sigma/d\Omega)_\theta$, where the detection probability depends on the scattering angle, θ, into the element of solid angle covered by the detector.

For thin targets the differential cross section in the lab system (in $\mathrm{cm}^2/\mathrm{sr}$) is calculated from the following equation [1, 123] (p. 289 and 336, respectively):

$$\left(\frac{dY}{d\Omega}\right)_\theta = \left(\frac{d\sigma}{d\Omega}\right)_\theta \frac{\nu\rho N_A \Delta x}{A} \frac{q}{ne} \tag{3.30}$$

where $(dY/d\Omega)_\theta$ (in number of counts per steradian) is the differential yield of the reaction, which is the total number of nuclear reaction products detected in the solid angle $d\Omega$ covered by the detector per total number of incident beam particles. Depending on the scattering angle θ, the number of reaction products that reach the detector is different, and thus the differential yield is a function of θ; ν is the number of atoms per molecule, or in other words, the stoichiometry of the atoms of interest in the target material; ρ is the density (in $\mathrm{g/cm}^3$) of the target material; N_A is the Avogadro's number (6.023×10^{23} atoms/mole); A is the atomic or molecular mass of the target (in grams); Δx is the thickness (in cm) of the target atoms of interest; q is the total charge (in Coulomb) deposited by the beam; n is the number of unit charges carried by the beam particles; and e is the electronic charge (1.6×10^{-19} C).

Usually cross sections of charged-particle reactions, e.g., $^{32}\mathrm{S}(p,t)^{30}\mathrm{S}$, are in the range of a few μb/sr to a few mb/sr, where 1 barn is equivalent to 10^{-24} cm^2. To avoid units conversion, and to directly determine the cross sections in the lab system in units of μb/sr, equation (3.30) can be simplified to the following:

$$\left(\frac{d\sigma}{d\Omega}\right)_\theta = \left(\frac{dY}{d\Omega}\right)_\theta \frac{nA}{(3.75 \times 10^3) q\nu\Delta x} \tag{3.31}$$

where Y is the reaction yield; $d\Omega$ is the solid angle covered by the detector (in msr); n, A and ν are as defined before; q is the total charge deposited by the beam (in mC);

[30] $\sigma_{abs} = \sigma(E)$, where E is the incident energy.

and Δx is the target thickness (in mg/cm^2). Due to the presence of three quantities in the denominator which are each a 1000 times less than their counterparts in SI units, there will be a factor of 10^{-9} in the denominator. From e/N_A fraction in the original equation, there will be a factor of 0.266×10^{-42} (in units of Coulomb/number) in the numerator. Thus, there will be a factor of $(0.266 \times 10^{-42})/10^{-9} = 0.266 \times 10^{-33}$ (in units of Coulomb/number) in the numerator, which can be replaced by $10^{-30}/(3.75 \times 10^3)$ in units of Coulomb/number. All units cancel out from both sides of equation (3.31), except cm^2/sr. However, 10^{-30} cm^2/sr can be written as 1 μb/sr, which is what we aimed for.

This formalism is incorporated into a Microsoft Excel macro, called Catkin. In addition to the above calculations, Catkin also performs relativistic kinematics calculations for two-body collisions, and can be downloaded from Ref. [270].

In an experiment involving a beam, the differential cross sections for each of the observed peaks in the spectra can be found separately at each of the scattering angles if the yield under each peak is determined from fitting the peak by a function that best describes it.

The yields discussed here simply represent the areas under the peaks. In our experiment, the Gaussian fits described before provided the areas and their uncertainties. Therefore, to calculate the differential cross section corresponding to each state (peak) via equation (3.31), the total charge deposited by the beam and the equivalent thickness of ^{32}S content in each target (in cm) had to be known. To obtain the former, a Faraday cup was used at 0° in the target chamber to stop the beam, and thus the integrated current was recorded for each run by the scalar module located on the VME crate. These numbers are saved in the raw data and can be accessed during the online and offline analysis. By knowing the full scale for the beam current integrator, these numbers were simply converted to the total charge (in Coulomb) deposited by the beam during each individual run.

Since the reaction of interest is ^{32}S$(p,t)^{30}$S, for obtaining the cross sections of ^{30}S states the target thicknesses of interest were only the equivalent thicknesses of ^{32}S contents of the CdS and the implanted targets. As discussed before, these thicknesses had been measured (see § 3.1.3). To calculate the actual path length of the beam particles in the targets, the measured thicknesses were divided by the cosine of the approximate angles at which the targets were positioned during each run. The determination of these

angles were discussed in the previous subsections.

For calculation of the path lengths of the beam particle as they traverse the implanted target, one factor was left uncorrected: the implanted target was not a completely flat foil, so the actual target thickness as seen by the beam particles may have been slightly different. However, there was no way to correct the thickness for such non-uniformities in the foil. Unlike the natural carbon foils, which are stretched tightly across the aperture of the target frame, it seems that the isotopically pure ^{12}C foils are not as flat, and have small bumps and wavy structures over the aperture of the target frame. They are much more fragile as well, which is due to their method of fabrication (see Appendix A). The potential non-homogeneities of both CdS and implanted targets were also ignored. Any contaminant material other than what was already known from the spectra could have an effect on the target stoichiometry and density, as well as on the energy loss of the particles, since the contaminants change the stopping power of the target material. Again, there was no available solution to determine the structure of these targets as sensitively as required for an ideal analysis.

Equation (3.31) was then used to calculate the differential cross section in the lab system for each state at each spectrograph's angle.

To check whether or not it was required to normalize the cross sections obtained by the CdS target to those obtained by the implanted target, the ^{32}S$(p,t)^{30}$S reaction was remeasured in January-2010 at 22° with the implanted target, and with all other experimental parameters identical to the former measurement performed in May-2008 at the same angle but with CdS target. For those states observed in the former measurement, the cross sections of the ^{30}S states at 22° are in good agreement (if not identical) within their uncertainties with those obtained at the same angle with the CdS target. This implies that there is neither a need to normalize the cross sections obtained at 22° with one target to those obtained at the same angle but with the other target, nor to scale the cross sections obtained with one target to those measured with the other target at other angles.

In January-2010, almost two days of beamtime were spent on measuring the ^{32}S$(p,t)^{30}$S reaction at 9° with a 34.5-MeV beam impinging on the implanted target. However, two factors contributed to a failure of obtaining a clean spectrum: the thickness of ^{32}S content of the implanted target was 5 times lower than that in the CdS target, which caused the rate of the data accumulation to be a lot lower; and due to the low angle of the spectro-

graph, there were a lot of scattered particles, whose tails contaminated the tritons' gates in a way that no clean gates could be drawn around them. As a result, these data were not used for analysis of cross sections or excitation energies.

Since the magnitude of the angle of the spectrograph with respect to the beam axis depends on the reference system (lab *vs.* center-of-mass), the element of the solid angle covered by the detector is not the same in the lab and center-of-mass systems. Consequently, the differential cross sections in the lab system are not identical to those in the center-of-mass system. By convention, the angular distribution of the cross section of each excited state in a nucleus is plotted *vs.* angle in the center-of-mass. These plots provide information about the spin assignment of the state under consideration (see the next subsection).

The conversion of the cross sections obtained in the lab system to those in the center-of-mass system are based on the definition of cross section, which implies that the same number of reaction products are emitted into the solid angle element $d\Omega$ in the direction θ as are emitted into $d\Omega'$ in the corresponding direction θ', where θ and θ' are the angles in the lab and center-of-mass system, respectively.

Therefore [1] (p. 596):

$$\left(\frac{d\sigma}{d\Omega}\right)_{\theta} d\Omega = \left(\frac{d\sigma}{d\Omega}\right)_{\theta'}^{'} d\Omega' \tag{3.32}$$

where the primed values refer to the center-of-mass system. While the cross sections depend on θ, they are independent of the azimuthal angle ϕ. Hence [1] (p. 597):

$$\frac{(d\sigma/d\Omega)'_{\theta'}}{(d\sigma/d\Omega)_{\theta}} = \frac{d\Omega}{d\Omega'} = \frac{d(\cos\theta)}{d(\cos\theta')} = \frac{\sqrt{1 - \gamma^2 \sin^2\theta}}{\left(\gamma\cos\theta + \sqrt{1 - \gamma^2\sin^2\theta}\right)^2} \tag{3.33}$$

where γ is defined by the ratio of velocities of the center-of-mass and of the ejectile (light reaction product) in the center-of-mass system, and is defined as follows [1] (p. 596):

$$\gamma \approx \sqrt{\frac{m_b m_e}{m_t m_r} \frac{E_b}{(1 + \frac{m_b}{m_t})Q + E_b}} \tag{3.34}$$

where m_b, m_t, m_e and m_r are respectively the masses of beam, target, ejectile and the recoil nuclei; E_b is the beam energy; and Q is the Q-value of the reaction.

Finally, by using these formulas the cross section of each observed state of ^{30}S at each scattering angle was determined in the center-of-mass system. Their associated uncertainties were also calculated from those of the cross sections in the lab system as follows: in the lab system, the uncertainties in yields and target thicknesses were dominant sources of uncertainty in the cross sections. These uncertainties were mutually independent, and thus were added together quadratically based on the following formula:

$$\delta\left(\frac{d\sigma}{d\Omega}\right)_\theta = \left(\frac{d\sigma}{d\Omega}\right)_\theta \sqrt{\left(\frac{\delta(\Delta x)}{\Delta x}\right)^2 + \left(\frac{\delta Y}{Y}\right)^2} \tag{3.35}$$

where δ refers to the uncertainty; Y is the reaction yield; and Δx is the target thickness. The uncertainties associated with the cross sections in the center-of-mass system were then simply calculated by multiplying the relative uncertainties in the cross sections in the lab system[31] by the cross sections in the center-of-mass system. An attempt was made to calculate the uncertainties in the cross sections in the center-of-mass system by proper error propagation using equations (3.32), (3.33) and (3.34), which was challenging. Nonetheless, the resulting uncertainties differed from those calculated from the former method by at most 2%. For most states, both methods resulted in almost identical uncertainties. Thus the former method was used due to its simplicity.

3.2.10 Angular Distributions Analysis and Spin-Parity Assignments

- **Distorted-Wave Born Approximation Calculations:**

It was remarked that the differential cross sections for a reaction $A(a,b)B$ depend upon the angle of emission of the ejectile b with respect to the direction of the incident beam a. The reaction products are not, in general, emitted isotropically, that is to say in all directions with equal probability. Therefore, the differential cross sections have angular distributions.

The shapes of these angular distributions carry important information about the angular momentum transferred between the particles during their interactions, and this, in turn, can tell us about the spin and parity of the residual nuclear state.

[31] The relative uncertainty in a quantity x is $\delta x/x$.

These shapes, and the details of the reaction mechanism and its observables, are calculated by a few computer codes using spin-dependent DWBA in a number of interaction methods: one-step zero-range transfer [125] (p. 153), one-step finite-range transfer [125] (p. 152), two-steps zero-range transfer coupled-channels, and multi-steps finite-range transfers coupled-reaction channels. The difference between one- and two-steps is that the former allows nucleon transfer from the target, but blocks the reverse channel, so the transferred nucleon cannot be coupled back to the entrance channel. However, the two-steps interaction allows forward and reverse coupling. Multi-steps interactions are sophisticated interactions between various open channels in both directions [271]. The distorted waves asymptotically describe a plane wave of momentum $\vec{k}$ plus an outgoing (or incoming) spherical scattered wave[32] [272].

To obtain the spin-parity assignments of the states of ^{30}S in the present work, the theoretical angular distribution of the cross section of each state was separately computed (i) using a one-step zero-range transfer with a code called DWUCK4 [272] for natural-parity levels; and (ii) using two-steps finite-range transfers coupled reaction channels[33] with a code called FRESCO [273] for unnatural-parity levels,[34] where natural-parity and unnatural-parity states are the ones, for which $\pi = (-1)^J$ and $\pi = -(-1)^J$, respectively, where π is the parity and J is the spin of the sate.

The spin-parity assignments of the final state in the residual nucleus are determined once the l-transfers are established. To determine the orbital angular momentum that is transferred in the ^{32}S$(p,t)^{30}$S reaction to populate the ^{30}S excited states, the same shell-model assumptions as were used in Ref. [150] were considered, which are described in the following. The valence neutrons in ^{32}S occupy the $2s_{1/2}$ shell. Hence, for those excited states whose spins are thought to be 0^+, two-neutron pairs with total spin $s = 0$ were considered to be transferred from the $2s_{1/2}$, $1d_{5/2}$, and $1p_{1/2}$ orbitals. The experimental data as shown later on confirmed the $2s_{1/2}$ orbitals to be the choice describing the data the best. For 2^+ and 4^+ final states, the $s = 0$ dineutron was assumed to be

[32] Chapter 3 of Ref. [131] discusses the theory.

[33] Chapter 6 of Ref. [125] discusses the theory of coupled-channel DWBA. This reference also describes the code FRESCO in detail.

[34] FRESCO is a rather difficult code to work with. The input files to be later used by FRESCO can be created and modified easily by another code called XFRESCO [274], developed by Dr. Antonio Moro (University of Sevilla). XFRESCO is a GUI for FRESCO, and is written in C. To provide graphical display, it uses the graphical toolkit GTK+. The input files for the FRESCO calculations performed in the present work were made by XFRESCO.

transferred from the $1d_{5/2}$ orbital. The only exception to this was for the 2_1^+ state in ^{30}S, which is known to have a $2s_{1/2} - 1d_{3/2}$ dominant configuration [170]. For this latter case, where there are more than a single shell-configuration contributing to the wave function, the amplitude of the configuration normalizing factor will weight each piece according to their fraction in the total nuclear wave function. This factor was also obtained [275].

For natural-negative-parity levels, one neutron was considered to be transferred from the $1d_{5/2}$ or $2s_{1/2}$ shell, while the other neutron was assumed to be transferred from either the $1p_{1/2}$ or $1p_{3/2}$ orbital. Except for 0^+ final states, the shapes of the theoretical angular distributions were relatively insensitive to the particular choice of shell-model orbitals. After examining the DWUCK4 output for natural negative-parity states, it followed that this code was unable to reproduce the theoretical curves that are available in the literature for such cases. Therefore, a sample input file for another version of the code DWUCK, DWUCK5, was obtained [276]. While DWUCK4 uses one-step zero-range transfer interaction, DWUCK5 uses one-step finite-range transfer interaction, and perhaps that is why the latter code could reproduce the data that are found in the literature. To be more specific, DWUCK4 assumes a zero-range interaction between the proton and the transferred dineutron center-of-mass. Since only the center-of-mass of the transferred neutrons is affected by this interaction, no change can occur in the relative motion of these two neutrons [277]. Thus, one consequence of this treatment is that the ^{32}S(p,t) reaction only reaches that part of the final nuclear state in ^{30}S, in which the transferred neutrons have precisely the same relative motion that they had when they were in the ^{32}S nucleus [277]. A more realistic interaction is the one, which acts between the proton and each individual transferred neutron such that the relative motion of the two neutrons change as the transfer occurs [277]. Finite-range transfer interaction takes this into account, and thus DWUCK5 is more reliable when two neutrons are transferred from two different shells.

For natural positive-parity states, both codes give identical results, and thus DWUCK4 was used as it is more simple to use. For the 3^- state in ^{30}S at 5315 keV, the proposed configuration [170] (and references therein) of $2s_{1/2} - 1f_{7/2}$ was also used; however, this configuration failed to describe the data.

The theoretical curves for angular distributions of the cross sections of the unnatural-parity levels cannot be obtained via codes like DWUCK4 that consider one-step inter-

actions. Hence, multi-steps processes were considered by using FRESCO. The angular distributions for the sequence $^{32}\mathrm{S}(p,d)^{31}\mathrm{S}_{g.s.}(d,t)^{30}\mathrm{S}$, where $g.s.$ refers to the ground state, were obtained for each of the unnatural-parity final states in ^{30}S. The l-transfers were calculated by considering the spins of the nuclei involved in each step, and based on the conservation laws for the total angular momentum as well as parity.

The distorted-waves were calculated by the aforementioned codes for an optical interaction potential well[35] of the form [168]:

$$\begin{aligned} U_{OM}(r) &= V_c(r_{0c}) - V_0 f(r_0,a) - \\ &\quad i\left(W_0 - 4a'W_D\frac{d}{dr}\right) f(r'_0,a') + \\ &\quad \left(\frac{\hbar}{m_\pi c}\right)^2 V_s \frac{1}{r}\frac{d}{dr} f(r''_0,a'')\vec{l}\cdot\vec{\sigma} \end{aligned} \tag{3.36}$$

where the first term is the Coulomb potential of a uniformly charged sphere of radius $r_{0c}\,A^{1/3}$; the second term is a volume Woods-Saxon potential; the third term is a surface Woods-Saxon potential; and the last term is a spin-orbit potential from a volume Woods-Saxon form [272], where l is the orbital angular momentum, and $\vec{\sigma} = 2\vec{s}$ (s is the spin); m_π is the pion mass; c is the speed of light; r_{0c} is the reduced charge radius ($R_c = r_{0c}\,A^{1/3}$); r_0, r'_0 and r''_0 are the reduced radii of the real, imaginary and the spin-orbit potentials, respectively; a, a' and a'' are the diffuseness parameters of the real, imaginary and the spin-orbit potentials, respectively; and V_0 and W_0, W_D and V_s are the real, imaginary and spin-orbit depths of the potential wells, respectively. The function $f(r,a)$ is defined as [168]:

$$f(r_0,a) = \frac{1}{1 + \exp\left(\dfrac{r - r_0A^{1/3}}{a}\right)} \tag{3.37}$$

where A is the atomic mass number and r is the radius of the nucleus.

The optical model parameters used for the DWBA calculations in the present work were taken from Ref. [150] (and references therein), and are given in Table 3.7. Furthermore, for FRESCO calculations, the deuteron and triton wave functions were derived from a Reid soft core potential [278] that was adopted since it is widely used in the literature. In addition, to calculate the required binding energy and separation energy

[35] Potentials with both real and imaginary parts are called optical potentials [125] (p. 73).

Table 3.7: Optical model parameters used in conjunction with DWUCK4, DWUCK5 and FRESCO for the analysis of the angular distributions.

Reaction Channel (MeV)	V_0 (MeV)	W_0 (MeV)	W_D (MeV)	V_s[a] (fm)	r_0 (fm)	a (fm)	r'_0 (fm)	a' (fm)	r''_0[a] (fm)	a''[a] (fm)	r_{0c} (fm)	VSOR[b]	PNLOC[c]
$p + {}^{32}$S	37.1	0	6.875	7.5	1.18	0.66	1.18	0.66	1.18	0.7	1.25[d]		
$t + {}^{30}$S	144	30	0	0[a]	1.24	0.678	1.45	0.841	0[a]	0[a]	1.25		
$2n + {}^{30}$S		0	0		1.25	0.65						25	
$d + {}^{31}$S	90	0	25		1.30	0.62	1.18	0.58			1.25		
$n + {}^{31}$S[e]		0	0		1.2	0.65					1.3	25	0.85

[a] In Ref. [150], there was no spin-orbit interaction considered. Hence, this parameter is taken from Ref. [168]. The other potential parameters are not taken from the latter reference, because those parameters were theoretically determined. However, the parameters in Ref. [150] were measured.

[b] The spin-orbit factor for the real spin-orbit potential, used as input for DWUCK4 and FRESCO [272].

[c] Non-locality parameter used as input for DWUCK4 [272].

[d] This value is widely used in the literature for r_{0c}.

[e] The input parameters on this line of the table are used by FRESCO, and are taken from Ref. [279].

involving ^{30}S and ^{31}S nuclei, their masses were adopted from the most recent measurements [140, 280].

Finally, the DWBA calculations were performed, and the theoretical differential cross sections *vs.* the center-of-mass angles, and thus an angular distribution plot, were obtained for each final state of ^{30}S. These theoretical differential cross sections were in units of fm^2/sr [272], and thus were converted to μb/sr for comparison with their measured counterparts.

- **Spins and Parities of the Individual Levels:**

The scattering angles of tritons in the center-of-mass system depend upon the velocity of the center-of-mass system, as well as the scattering angle in the lab system (see equation (C.38) in Ref. [1]). The kinematics program JRelKin was used to calculate the triton's scattering angle in the center-of-mass system corresponding to each ^{30}S final state for all the spectrograph's angles, where the measurements were performed.

As discussed previously, for each final state of ^{30}S, the measured and theoretical differential cross sections in the center-of-mass system were determined. The theoretical cross sections were then scaled to the measured counterparts by plotting the measured cross sections *vs.* the theoretical ones and fitting the data with a first degree polynomial, which for some cases only passed through the origin when the intercept was a negative number. For such cases, the negative intercept resulted in the scaled theoretical cross sections becoming negative beyond some angle, which is physically meaningless. Thus, the fit was forced to pass through the origin.

Lastly, a plot of the measured differential cross sections together with the scaled theoretical ones *vs.* the center-of-mass angles for each final state of ^{30}S was made. Such triton angular distribution plots are shown in Figs. 3.19 to 3.25, and help determine or constrain the spin and parity of the ^{30}S states. These plots are discussed in the following:

- ***The ground state:*** The ground state of ^{30}S was not observed in the present work at any angle. But since this nucleus is even-even, its ground state has $J^\pi = 0^+$.

- ***The 2208-keV level:*** This state was only observed at 62°, and with one angle there is no point to plot or interpret the angular distribution of its cross section. Thus, apart from its excitation energy, no further information is available on this state from the present work. However, it is known from previous measurements to be the first 2^+

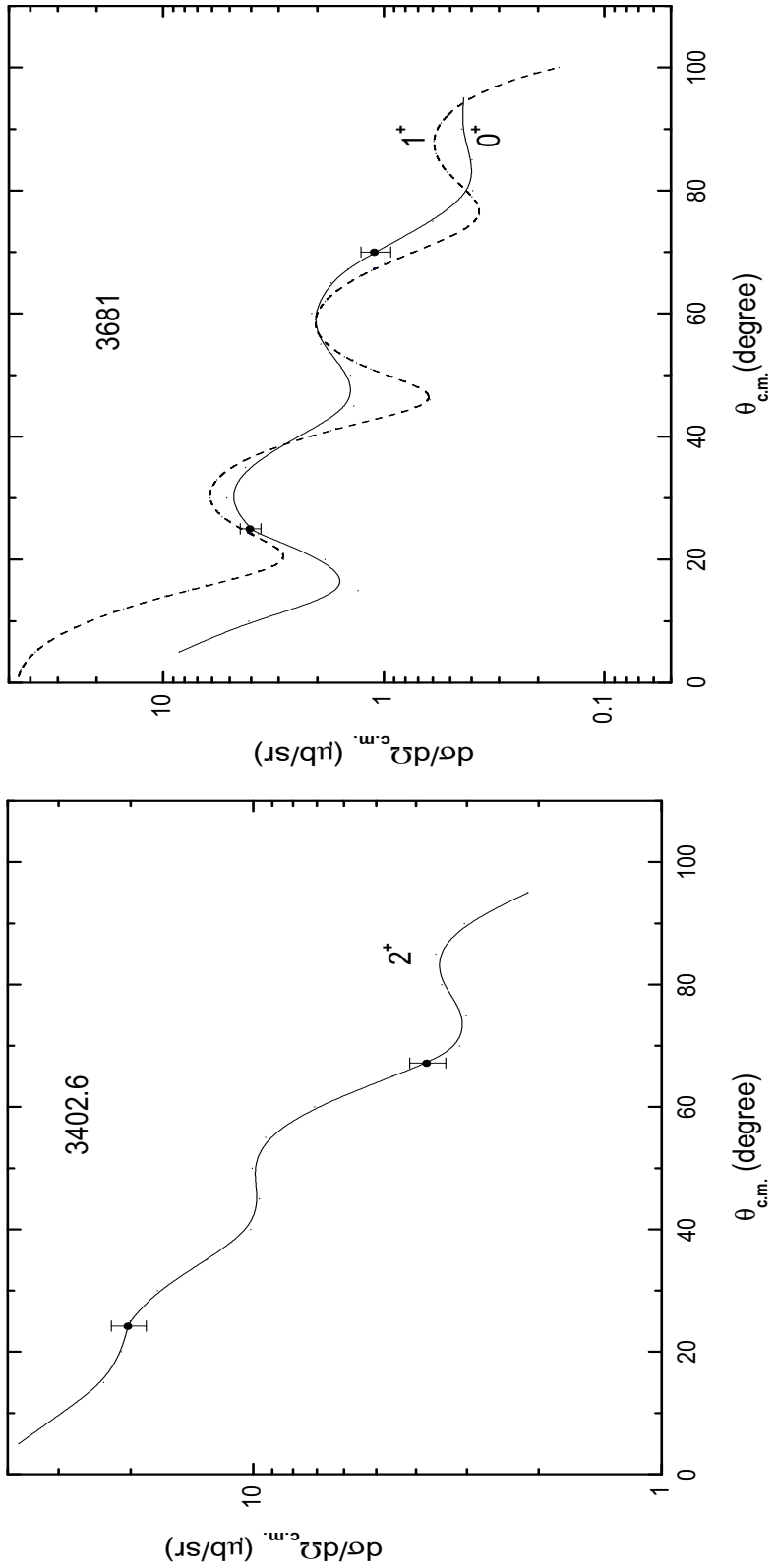

Figure 3.19: Triton angular distributions populating the bound states of ^{30}S compared with the DWBA curves obtained by DWUCK4 for natural-parity levels, and by two-steps FRESCO calculations for unnatural-parity levels. On each plot, the filled circles with error bars are the measured differential cross sections from the ^{32}S$(p,t)^{30}$S reaction, and the solid and dashed curves are the theoretical angular distributions from the aforementioned codes. The excitation energy of the state under consideration is given in keV on the top middle of each plot, and the J^π assignment corresponding to each solid and dashed curve is also given.

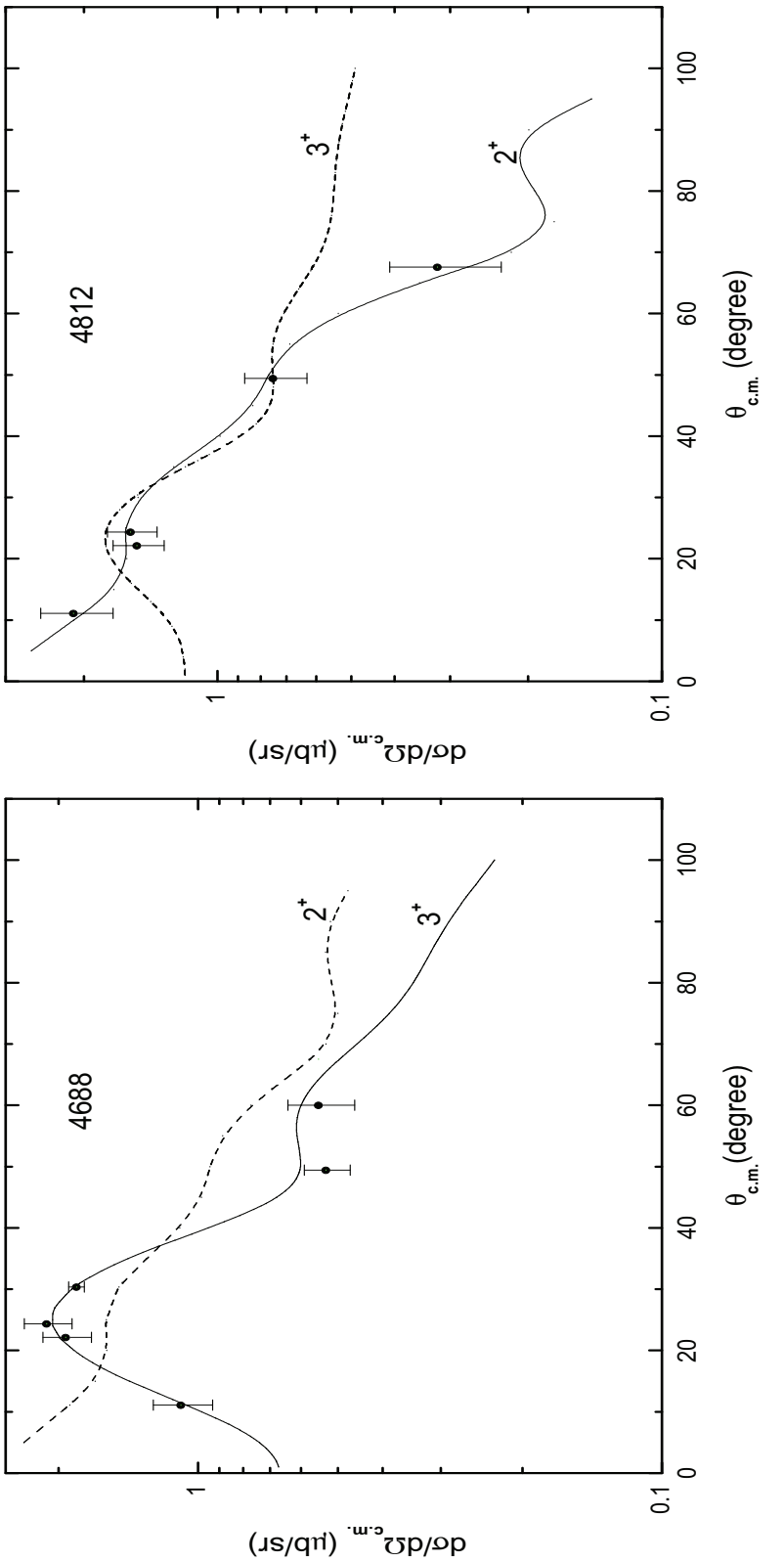

Figure 3.20: Triton angular distributions populating the two astrophysically important resonances of ^{30}S compared with the DWBA curves obtained by DWUCK4 for natural-parity levels, and by two-steps FRESCO calculations for unnatural-parity levels. On each plot, the filled circles with error bars are the measured differential cross sections from the ^{32}S$(p,t)^{30}$S reaction, and the solid or dashed curves are the theoretical angular distributions from the aforementioned codes. The excitation energy of the state under consideration is given in keV on the top middle of each plot, and the J^{π} assignment corresponding to each solid and dashed curve is also given.

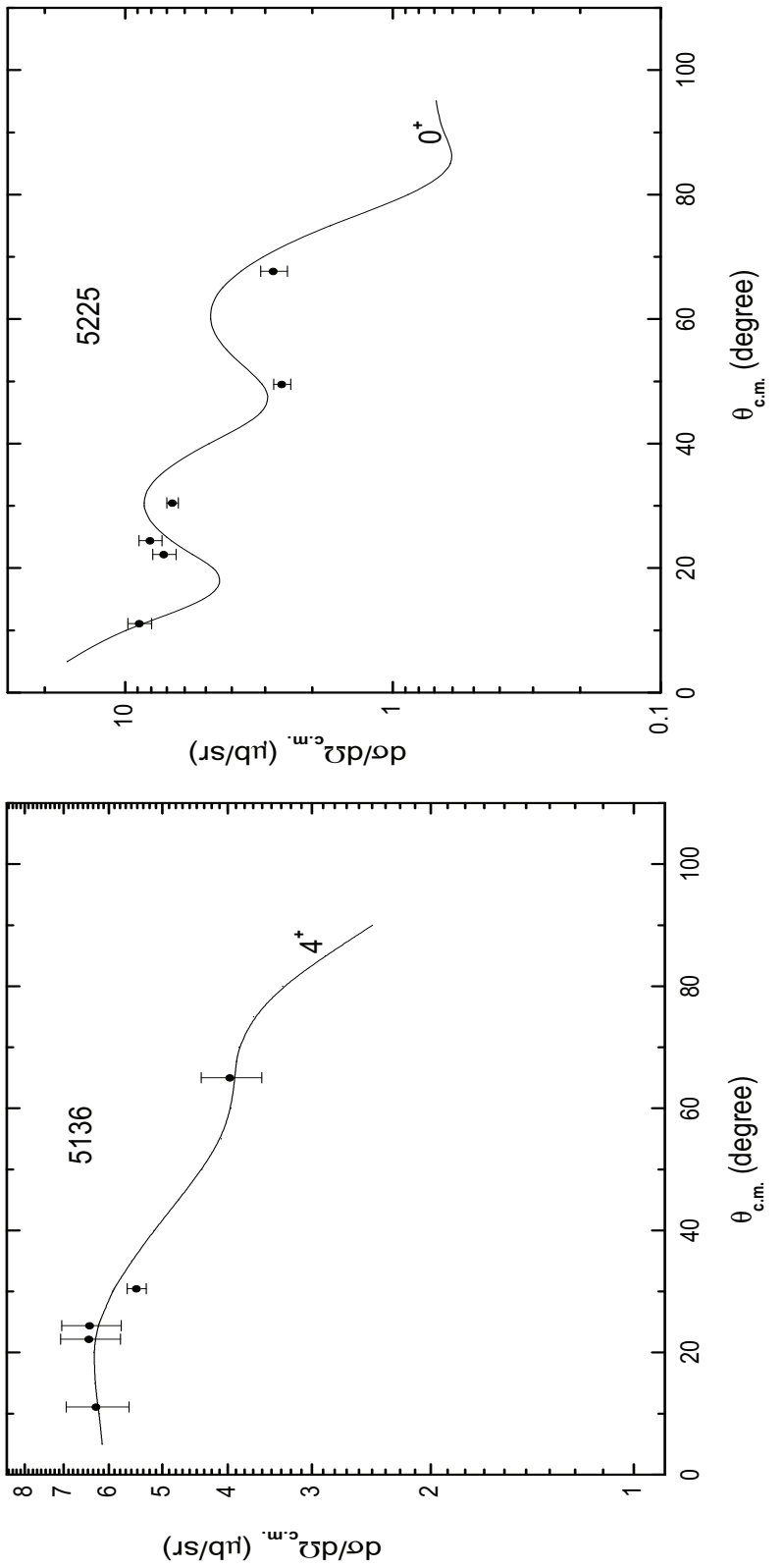

Figure 3.21: Triton angular distributions populating higher-lying resonances of ^{30}S compared with the DWBA curves obtained by DWUCK4. On each plot, the filled circles with error bars are the measured differential cross sections from the ^{32}S$(p,t)^{30}$S reaction, and the solid curves are the theoretical angular distributions from the aforementioned code. The excitation energy of the state under consideration is given in keV on the top middle of each plot, and the J^π assignment corresponding to the solid curve is also given.

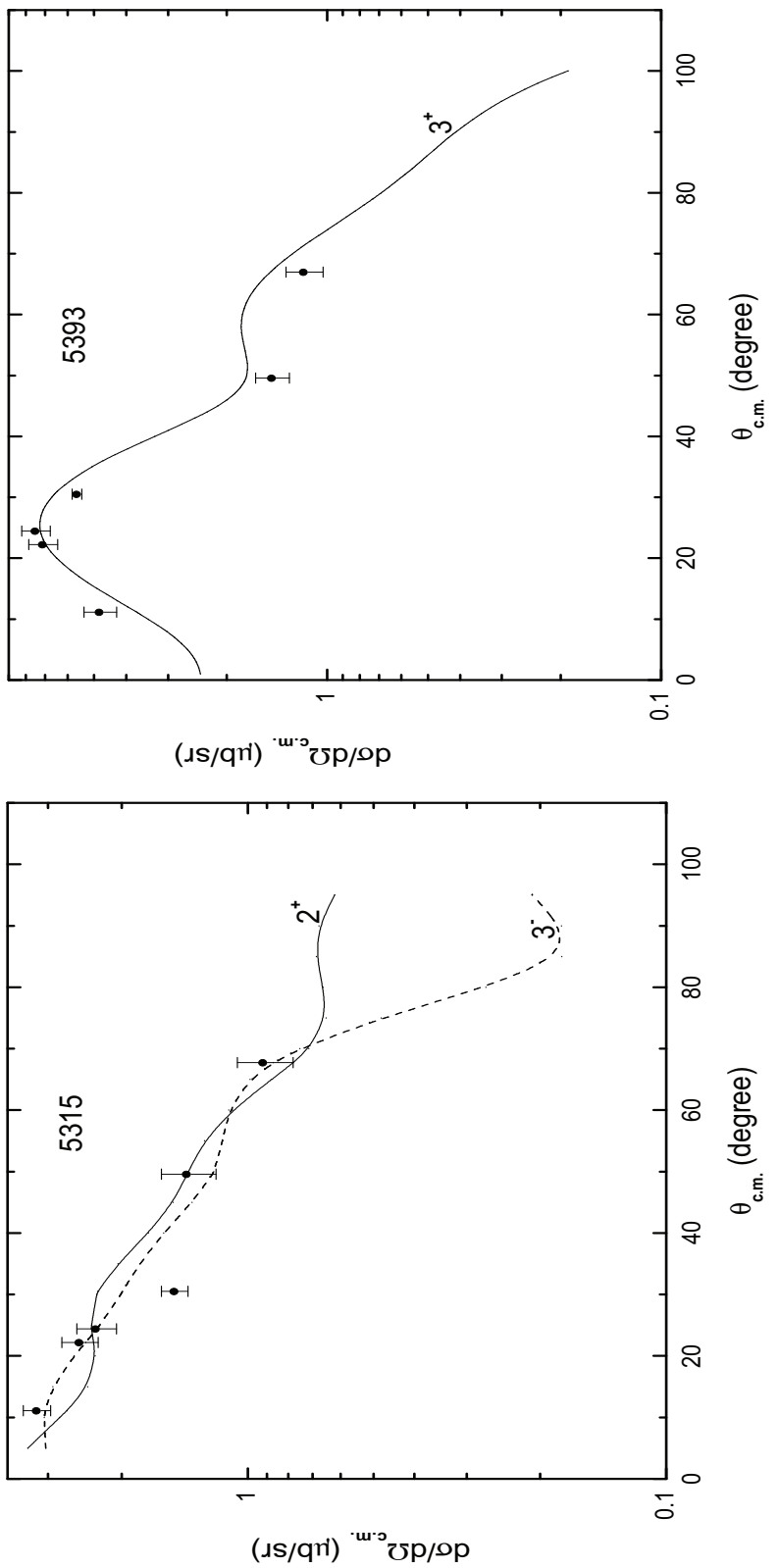

Figure 3.22: Triton angular distributions populating higher-lying resonances of ^{30}S compared with the DWBA curves obtained by DWUCK4 and DWUCK5 for positive and negative natural-parity levels, respectively, and by two-steps FRESCO calculations for unnatural-parity levels. On each plot, the filled circles with error bars are the measured differential cross sections from the ^{32}S$(p,t)^{30}$S reaction, and the solid and dashed curves are the theoretical angular distributions from the aforementioned codes. The excitation energy of the state under consideration is given in keV on the top middle of each plot, and the J^{π} assignment corresponding to each solid and dashed curve is also given.

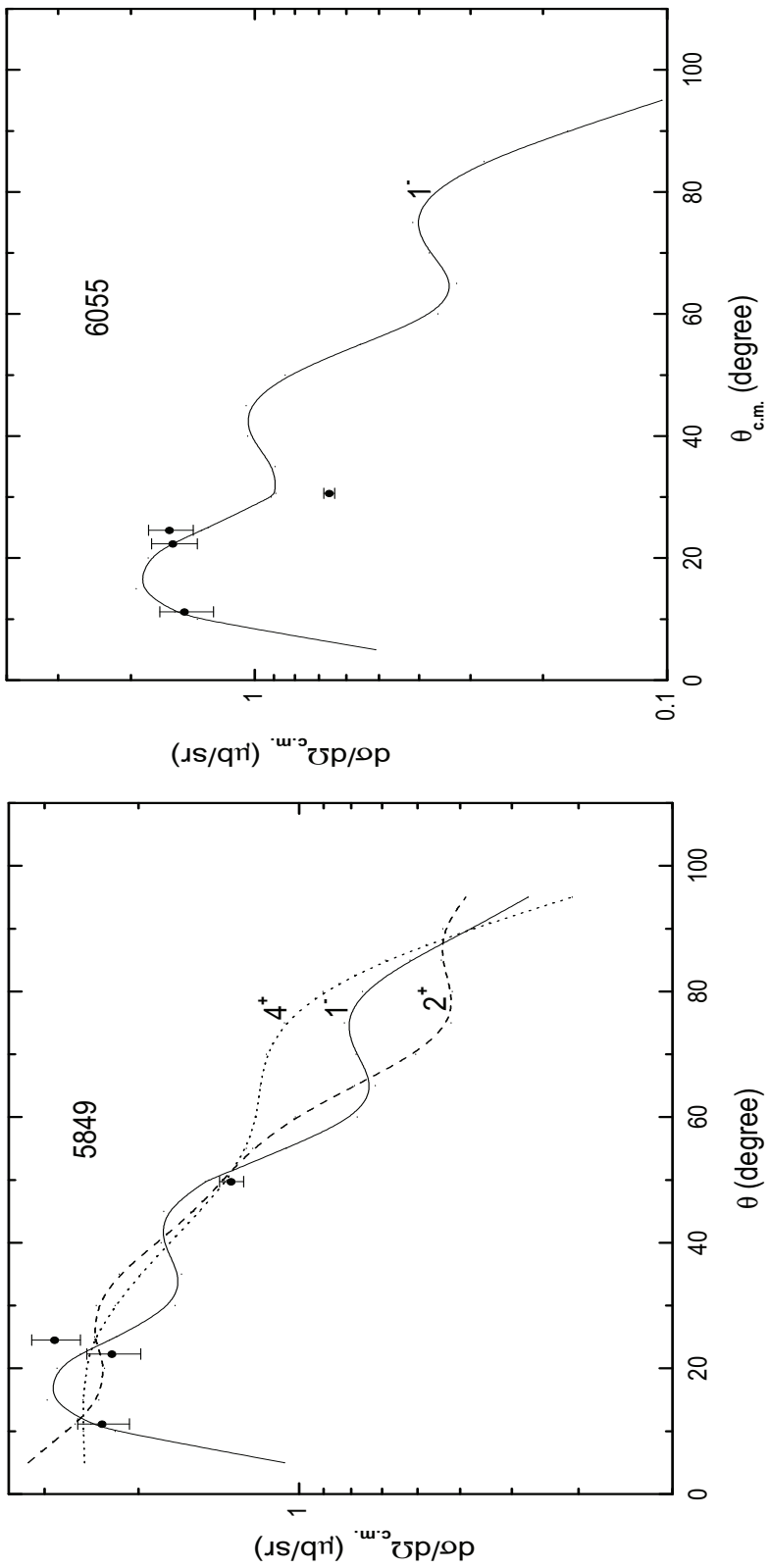

Figure 3.23: Triton angular distributions populating higher-lying resonances of ^{30}S compared with the DWBA curves obtained by DWUCK4 and DWUCK5 for positive and negative natural-parity levels, respectively. On each plot, the filled circles with error bars are the measured differential cross sections from the ^{32}S$(p,t)^{30}$S reaction, and the solid, dashed and dotted curves are the theoretical angular distributions from the aforementioned code. The excitation energy of the state under consideration is given in keV on the top middle of each plot, and the J^{π} assignment corresponding to each solid, dashed and dotted curve is also given.

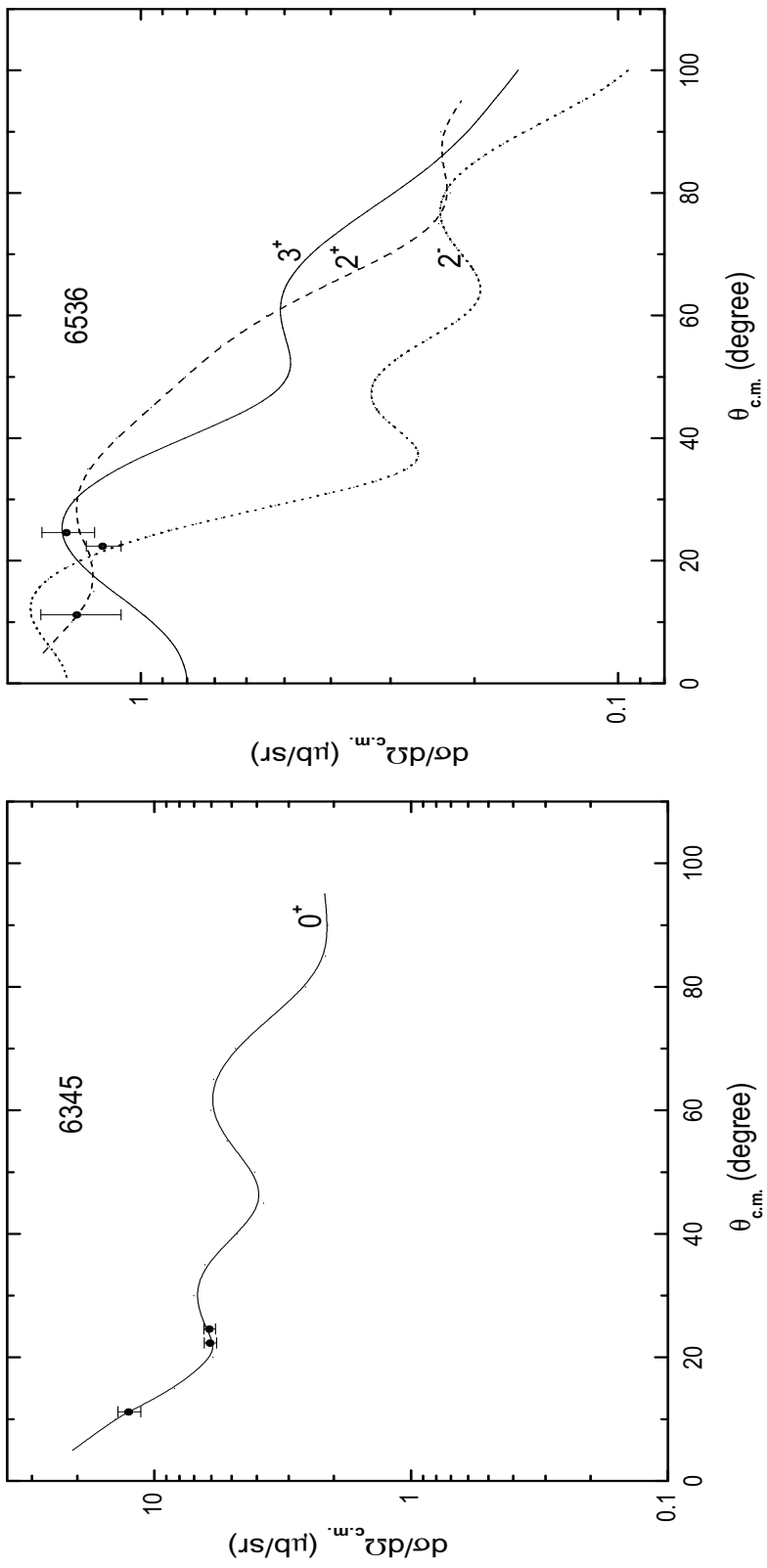

Figure 3.24: Triton angular distributions populating higher-lying resonances of ^{30}S compared with the DWBA curves obtained by DWUCK4 for natural-parity levels, and by two-steps FRESCO calculations for unnatural-parity levels. On each plot, the filled circles with error bars are the measured differential cross sections from the ^{32}S$(p,t)^{30}$S reaction, and the solid, dashed and dotted curves are the theoretical angular distributions from the aforementioned codes. The excitation energy of the state under consideration is given in keV on the top middle of each plot, and the J^{π} assignment corresponding to each solid, dashed and dotted curve is also given.

state.

• ***The 3403-keV level:*** Similar to the previous state, this state was only observed at 22° and 62° (see Fig. 3.19). Two angles are again not enough to be able to say something about the spin-parity assignment of this state. However, this level is known to have a J^π value of 2^+, which is consistent with an $l = 2$ transfer from our data (see Fig. 3.19).

• ***The 3681-keV level:*** This peak is one of the two states that together construct a $J^\pi = 0^+$ and 1^+ doublet in ^{30}S. As previously discussed, the lower-energy state could not be resolved in the present work, and thus no information on its energy or spin-parity is available from this work. The 3681-keV level is the higher energy state in the doublet, and was also observed only at two angles, 22° and 62°. Hence, again the measurements were not enough to extract a conclusive spin-parity for it. In Ref. [168], this state was tentatively assigned to be $J^\pi = (0^+)$. The $n - \gamma$ correlation data in Ref. [173], on the other hand, was best fitted with $J = 1$ assignment. Since in the mirror nucleus in that energy range, there is only one state whose spin is 1, and that is a 1^+ state, the parity of the ^{30}S level observed in Ref. [173] was tentatively assigned to be positive. The triton angular distribution data from the $^{32}\mathrm{S}(p,t)^{30}\mathrm{S}$ reaction measured in Ref. [150] was also best fitted with a 1^+ assignment. However, this assignment was still tentative. From our triton angular distribution data, which unfortunately are only available at two angles, both $J^\pi = 0^+$ and 1^+ are possible, as shown in Fig. 3.19.

It should be noted that there is a considerable difference in the shape of the 1^+ distribution from the present work and the work of Ref. [150]. This is most likely due to the fact that for the FRESCO calculation for this particular state in Ref. [150] the overlap between the s-wave and d-wave components of the deuteron wave function, as well as the non-orthogonality correction, were ignored [271, 281]. The latter accounts for the fact that the states belonging to different partitions[36] are not mutually orthogonal [271].

• ***The 4688-keV level:*** This level has only been observed in the present work and in Ref. [150]. In the latter work, this state was proposed to be the astrophysically important 3^+_1 state. However, its spin-parity assignment was reported as tentative, and its angular distribution as relatively consistent with both $J^\pi = 3^+$ and 2^+ assignments, which is most likely due to the poor statistics observed for this state. Our triton angular

[36]Partitions are defined in a section of the FRESCO input file, where the details regarding masses of the nuclei, Q-values of the corresponding reactions, and reaction channels to be considered are defined.

distribution as shown in Fig. 3.20 is only consistent with a $J^\pi = 3^+$ assignment, which was obtained by FRESCO. Note that unlike the previous unnatural-parity 1^+ state, the shape of the angular distribution for the 4688-keV state in the present work matches very well with that given in Ref. [150]. Apart from $l = 2$ transfer, $l = 0$, 1, 3 ($J^\pi = 3^-$), and 4 transfers were also tried to see if they could describe the data for this state. However, all these possible assignments failed to describe our data. Furthermore, the energy of the 3^+_1 level from our IMME calculation is 4690(25) keV, which is in very good agreement with the measured value. This strongly supports our 3^+ assignment. Therefore, it was concluded that this state is definitely the mirror to the 3^+_1 state in ^{30}Si at 4831 keV [187], which confirms our earlier assumption [255]. Thus, this level is the 3^+_1 astrophysically important state predicted by Iliadis *et al.* [149].

• ***The 4812-keV level:*** This level was observed for the first time in the present work in 5 out of 6 measured angles. At 27.5°, the tail of an intense deuteron group on 3 out of the four main 2D histograms contaminated the location, where the tritons related to this ^{30}S state appeared. Thus, the gates could not remove this overlap, and as a result the area under this peak of interest was not reliable, nor was its centroid. The differential cross section of this state at 27.5° was therefore not extracted. $l = 0$, 2, 3 and 4 transfers were examined but the $J^\pi = 0^+$ and 4^+ did not describe the angular distribution data well. On the other hand, as seen in Fig. 3.20, the triton angular distribution for this level was relatively consistent with both $J^\pi = 2^+$ and 3^+ assignments.

In the mirror nucleus, there are two states in this range of energy: the 4810-keV state and the 4831-keV state [187]. The latter is already assigned to be the mirror level to the 4688-keV state in ^{30}S as explained above. Hence, the former seems to be a possible choice for being the mirror level to the 4812-keV ^{30}S state measured in the present work, in which case the order of the 3^+_1 and 2^+_3 states in ^{30}S are switched in energy with respect to that in its mirror nucleus. Another possibility is that the 4812-keV level may be the mirror state to the 3^+_2 level in ^{30}Si at 5231 keV [187], which is the next level above the 3^+_1 level in that nucleus. This hypothesis, however, seems much less likely due to the 420-keV energy difference, which seems to be too large with respect to the typical energy differences between mirror levels. If this state is the 3^+_2 state, it also naturally raises the question of which state should be assigned as the astrophysically important 2^+_3 state.

In a very recent shell model calculation for the sd-shell in $A = 30$ nuclei using the

USD Hamiltonian with inclusion of a charged-dependent part [282], the energy of the 2_3^+ state in ^{30}S was derived to be near 4800 keV, while that of the 3_1^+ state was calculated to be near 4700 keV [283, 284]. The latter strongly supports our J^π assignment for the 4688-keV state, and the former suggests that the 4812-keV state may very well be the mirror state to the 4810-keV state in ^{30}Si [187]. Also our IMME calculations predict that the next state above the 3_1^+ level in ^{30}S should be the 2_3^+. Our predicted energy, from IMME for the 2_3^+ state is 4846(25) keV. Although our measured energy is in disagreement with the predicted value at the 1σ level, the difference between these energies is much lower than that of the predicted value for the 3_2^+ state and the measured value of 4812(2) keV. Both shell model calculation [283, 284] and our present IMME calculation support the fact that the order of the 3_1^+ and 2_3^+ states in ^{30}S are switched, which is consistent with what we have observed in our measurement.

As another piece of evidence, the γ-ray branching ratio for the γ-decay of this state to the 2_1^+ and 2_2^+ states in ^{30}S were measured[37] at 90°, and were in good agreement within their uncertainties with those of the decay of the 4810-keV state in ^{30}Si to its 2_1^+ and 2_2^+ lower-lying states [285]. It might seem surprising that the two mirror levels occur at the same energy. Although this is a rare case, it is still possible [286]. All this information added together supports a tentative $J^\pi = (2^+)$ assignment for the 4812-keV state, making it the next astrophysically important state predicted by Iliadis *et al.* [149].

• ***The 5136-keV level:*** This state is a prominent peak observed at 5 out of the 6 measured angles in the present work. At 45°, it was partly obscured with the ground state of ^{10}C populated by the (p,t) reaction on the carbon substrate of the implanted target (see the top panel in Fig. 3.11). The background run performed by a carbon target reproduced that contaminant peak; however, its width was at least 10 channels fewer than that of the peak observed in the spectra obtained by the implanted target. The reason for this remains unknown. Therefore, the carbon peak could not be completely subtracted to leave in the peak associated with this state.

This state was used as an internal calibration point, and thus its energy is not independently measured in the present work. The 5136(2) keV comes from the weighted average among the measured values taken from Refs. [169, 173]. Constraints on the J^π assignment of this state come from the study of Kuhlmann *et al.* [173], who concluded

[37] The details of this measurement are discussed in the next chapter of this dissertation.

that the 5136-keV level is most likely a 4^+ state, which is consistent with the tentative assignment made for the same level in Ref. [285] based on its γ-decay. In the shell-model analysis by Wiescher and Görres [156], they concluded that there are most likely at least two levels near this energy: a 4^+ at 5145 keV and a 0^+ near 5.2 MeV. In Ref. [150], a state was observed at 5168(6) keV. The triton angular distribution data in that work could not be fitted with a single angular momentum transfer, which suggested that the latter state was an unresolved doublet consisting of a 4^+ and a 0^+ state. Our triton angular distribution is best fitted with $l = 4$ transfer; however, $l = 0$ and 2 would also be reasonably consistent. However, the latter is much less likely because the 2^+_4 mirror partner occurs at 5614 keV [187], which is 500 keV away from the 5136 keV state.

Our IMME prediction for this state is not very reliable because the 5934-keV state of ^{30}P used in the IMME calculation for this state (see Table 3.6) has a tentative $J^\pi = 3^+$ assignment. Thus, under the assumption that the aforementioned state in ^{30}P is the analog to the 5231-keV state of ^{30}Si (also a 3^+ state), equation (3.29) predicts that the 3^+_2 state in ^{30}S must lie at 5141(30) keV, which is in good agreement with the measured value of 5136(2) keV. This indicates that the 5136-keV state in ^{30}S may be the 3^+_2 mirror partner of the 5231-keV state in ^{30}Si, which is again in disagreement with our triton angular distribution and with the result of our earlier γ-ray measurement [285].

Nonetheless, a tentative $J^\pi = 4^+$ assignment is given to this state (see Fig. 3.21), which is partially based on the γ-ray measurement performed in Ref. [285] (see Chapter 4), making it the mirror to the 5279-keV state in ^{30}Si [187].

• ***The 5225-keV level:*** This state is another prominent peak that was observed at all the measured angles in the present work. There is no conclusive information regarding the J^π assignment of this state in the literature. Our only guides come from an old shell-model calculation [156], which suggested that there should be a 0^+ around 5.2 MeV, and our IMME calculations, which predict a 0^+ state at 5118(30) keV. This is again in disagreement with the measured energy, and seems to be closer to the energy of the previously discussed state. On the other hand, if we assume that this state is the 0^+_2, and work backward using equation (3.29) to calculate the energy of the analog state in ^{30}P, we arrive at 6047 keV, which is in good agreement with the 6051(5) keV state [187]. But the J^π assignment of the latter state is tentatively assumed to be 3^+, 4^+ or 5^+. All this seems to suggest is that due to lack of firm spin-parity assignments for most of ^{30}P states

of interest, our IMME calculations for states with excitation energies above 5 MeV are not very reliable, and should not be used as a guide for determination of the spin-parity of ^{30}S states. Our triton distribution for this state is reasonably consistent with $l = 0$ and 2, and even a J^π value of 3^- seems to describe the data reasonably well. But $J^\pi = 0^+$ fits the best (see Fig. 3.21). Therefore, we suggest that this state may be the mirror to the 0^+_2 state in ^{30}Si at 5372.2 keV [187].

• ***The 5315-keV level:*** This state is also a prominent peak that was observed at all angles measured in the present work. It is known to be a 3^- state [169]. Our angular distribution is best fit by an $l = 3$ angular momentum transfer, but $l = 2$ would also be reasonably consistent (see Fig. 3.22) This state is thus most likely the mirror to the 5487.5-keV state in ^{30}Si.

• ***The 5393-keV level:*** This state was observed at all angles measured in this work. The spin of this level was tentatively assigned to be $J = 1$ or 2 [169]. In Ref. [150], tentative $J^\pi = (3^-)$ and (2^+) assignments were given to this state. Our triton angular distribution is more consistent with $J^\pi = 3^+$ assignment (see Fig. 3.22), and thus we tentatively assign this state to be 3^+, making it the mirror to the 3^+_2 state in ^{30}Si at 5231.38 keV [187].

• ***The 5849-keV level:*** This state was tentatively assigned to be a 1^- state in Ref. [150]. However, the $l = 2$, 3 and 4 could not be excluded. In our data, this level was observed at 10°, 20°, 22° and 45°. Three of these angles are too close to each other to extract a reasonable J^π assignment for this state. Nonetheless, we can rule out $J^\pi = 4^-$ and 2^- assignments. But, 1^-, 2^+ and 4^+ are in reasonable agreement with our data (see Fig. 3.23).

• ***The 5947-keV level:*** This level was too weak to extract a significant angular distribution.

• ***The $E_x > 6$ MeV states:*** With the exception of the 6055-keV and 6768-keV states, which are observed at four angles (see Figs. 3.23 and 3.25), all other states of ^{30}S observed in the present work whose excitation energies are above 6 MeV are only observed at most at three angles, 10°, 20° and 22° (see Fig. 3.24). Due to the proximity of these angles, no reliable spin-parity assignments could be extracted for such states. However, we propose a tentative assignment of 1^- to the 6055-keV state, which is consistent with the results of Ref. [169], but the energy of this state from our data differs from that in

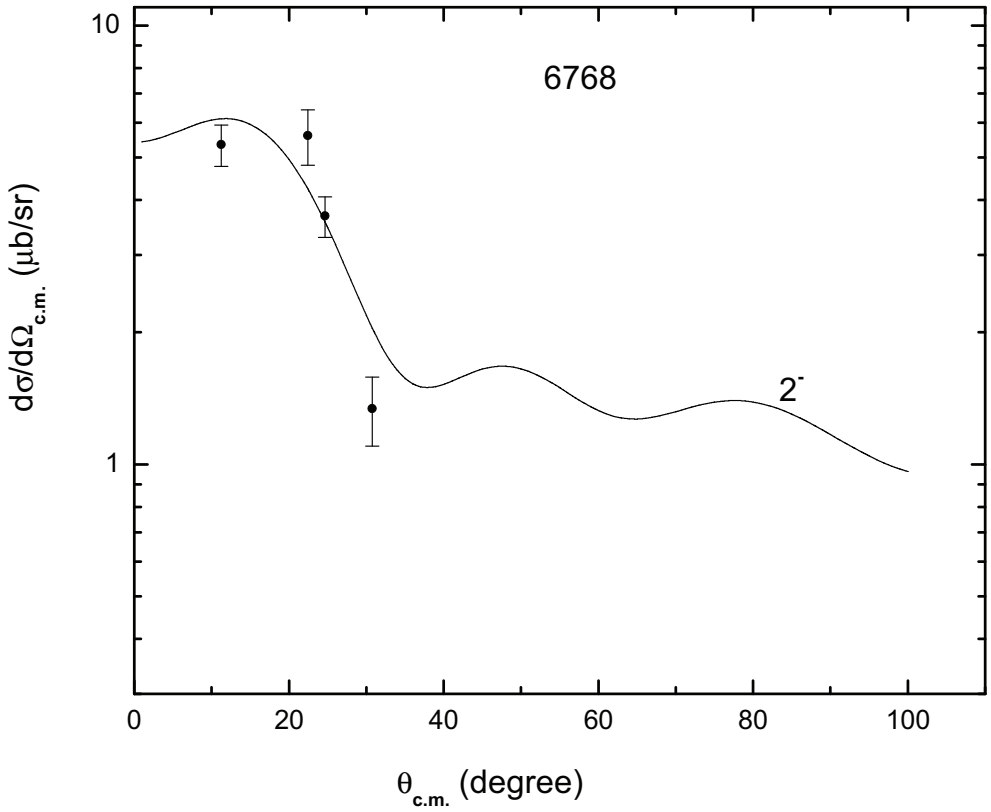

Figure 3.25: Triton angular distribution populating the 6768-keV state of ^{30}S compared with the DWBA curve obtained by FRESCO for $J^\pi = 2^-$ assignment, which seems to fit the data the best. The four measured angles are not sufficient to extract a conclusive result regarding to the spin/parity of this state.

Ref. [169] by 62 keV. We also suggest a tentative assignment of 0^+ to the 6345-keV state, which is consistent with a definite $J^\pi = 0^+$ assignment in an earlier measurement [169]. However, from our data $J^\pi = 2^-$ is another possible choice. Furthermore, we tentatively assign a $J = 2$ or 3 to the 6536-keV state, which is consistent with what was suggested in Ref. [169]. However, an $l = 4$ transfer with negative parity is also reasonably consistent with our data. Lastly, for the 6768-keV state, we confirm $J = 2$ suggested in Ref. [150], and most likely rule out $l = 3$ and 4 transfers. However, it seems that a negative parity would fit our data better than a positive parity. Therefore, we propose a $J^\pi = (2^-)$ assignment to this state.

In the following chapter, we continue investigating the low-lying resonance states of ^{30}S via an in-beam γ-ray spectroscopy using the ^{28}Si(^{3}He, $n\gamma$)^{30}S reaction.

Chapter 4

The ^{28}Si(^{3}He, $n\gamma$)^{30}S Experiment

γ-ray radiation was first identified by a French scientist named Paul Ulrich Villard in 1900 while studying radium [287]. Studying the γ-rays following fusion evaporation reactions provides nuclear structure information about the residual nuclei produced. After the evaporation of the light particles, the residual nucleus is left in an excited state which decays via γ- or particle-emission.

In-beam γ-ray spectroscopy is a modern tool to investigate and assign spins to such excited states. The high energy resolution of High Purity Germanium (HPGe) detectors permits one to separate the many in-beam γ-rays originating from various reactions produced in these experiments.

Having described the astrophysically important states in ^{30}S, here we report on the observation of γ-ray transitions from these two states. We present the experimental setup, data analysis and the results of an in-beam γ-ray spectroscopy experiment carried out at the the University of Tsukuba Tandem Accelerator Complex (UTTAC) to investigate the properties of the low-lying resonances of ^{30}S above the proton threshold.

4.1 Experimental Setup

The low-lying (up to 5.13 MeV) energy levels in ^{30}S were restudied via an in-beam γ-ray spectroscopy experiment using the ^{28}Si(^{3}He, $n\gamma$)^{30}S reaction (Q-value = -0.57 MeV [241]) over a total of 7 days during July-2009 (3 days) and September-2010 (4 days).

In the present work as we shall see, an energy level scheme is deduced from γ-γ coincidence measurements. Furthermore, spin and parity assignments based on angular distribution and the measurements of Directional Correlation of Oriented nuclei (DCO) ratios are made for most of the observed levels of ^{30}S.

In what follows the experimental apparatuses and the setup will be discussed.

4.1.1 The Tandem Accelerator Complex at the University of Tsukuba

Founded in 1973, the University of Tsukuba in Japan houses several research centers including the Tandem Accelerator Complex completed in 1975 [288]. The principal apparatus in this research center is a tandem accelerator, which is constructed vertically to save space on the ground. Like any other tandem accelerator, this one also requires injection of negatively charged beams.

At UTTAC, there are three types of negative ion sources located on the top (9^{th}) floor of the building: a direct extraction duo-plasmatron source [123] (p. 195) for production of ion beams from gaseous materials, a Lamb-shift polarized source [289] for production of polarized ion beams, and a sputtering source very similar to the one described in Chapter 3 for production of ion beams from solid materials.

For the in-beam γ-ray spectroscopy experiment using the ^{28}Si(^{3}He, $n\gamma$)^{30}S reaction, an unpolarized ^{3}He beam was produced in the duo-plasmatron negative ion source.

- **The Duo-Plasmatron Negative Ion Source and ^{3}He Beam Production:**

The duo-plasmatron ion source was first described by Ardenne [290]. The chamber for the duo-plasmatron source at UTTAC is housed within the Lamb-shift polarized source, and is used for unpolarized beams from gaseous materials. It is a reliable source capable of producing large currents (several μA to a few mA) of both negative and positive ions with low energy spread, and high efficiency and brightness.

Unlike the sputtering source at WNSL where the cathode was cooled, in the UTTAC duo-plasmatron ion source the cathode was a hot thin (0.6 mm diameter) tungsten filament. Free electrons were thus produced by thermionic emission[1]. A mixture of ^{3}He

[1]Electrons are emitted from a heated filament because when the metal is heated to such high temperatures that it glows, thermal energy is supplied to the electrons and their energy distribution changes.

and hydrogen gases was separately injected from the gas reservoirs to the chamber between the cathode, the intermediate electrode, and the anode. While the cathode was negatively biased, the anode was kept at +500 V. The intermediate electrode was kept at -160 V, which was less negative than the cathode's voltage.

The filament electrons were accelerated toward the anode and also toward the more positive polarity of the intermediate electrode, and collided with gas atoms, and ionized them producing positive ions[2]. The positive ions were also attracted to the negatively biased intermediate electrode. Therefore, the electrons and positive ions together were focused by the shape of the electric field, and formed a high density plasma that bulged slightly through the anode, which was kept at higher potential difference, forming an arc in a small volume near the funnel-shaped intermediate electrode and the anode.

The concave-shaped arc (the yellow region in Fig. 4.1) helped focus filament electrons, which in turn increased the density of the plasma. The plasma was concentrated in the region between the intermediate electrode and the anode due to a strong axial magnetic field generated by the magnetic coils (see Fig. 4.1). The anode had a small aperture with the diameter of 0.025" [288] (p. 8). The plasma could diffuse into the region just behind the anode through the anode's hole. There, an extraction electrode was kept at -5000 V, and thus it extracted the positive ions from the plasma[3]. The presence of hydrogen gas in the chamber was only for the purpose of stabilizing the plasma for the arc discharge [291].

The extracted positive beam was further constricted by the magnetic field to a narrow focused beam along the axis of the exit aperture. This beam was then introduced to cesium vapor inside the cesium chamber (see Fig. 4.1). When a beam of positive ions is passed through a canal containing a gas or a vapor, the ions may sequentially pickup two electrons and emerge negatively charged [196] (p. 54). This process is called charge exchange. As discussed in the previous chapter, cesium has low ionization energy, and was thus used as electron donor. While passing through the cesium cell, the positive

Some of the electrons may then have sufficient energy to escape from the atoms. The energy that sets them free is equal to $\phi + E_t$, where ϕ is the work function of the metal, and E_t is the thermal energy they obtain.

[2]The colliding electrons could not produce negative ions out of this particular gas mixture, because He is a noble gas and hydrogen has negative electron affinity. For other types of gases in duo-plasmatron ion sources, the electrons can produce both negative and positive ions.

[3]Whenever the gas is such that the filament electrons can produce negative ions out of the gas atoms, this extraction electrode is grounded, and thus it can directly extract the negative ions from the duo-plasmatron ion source. This negatively-charged beam is then injected into the tandem accelerator.

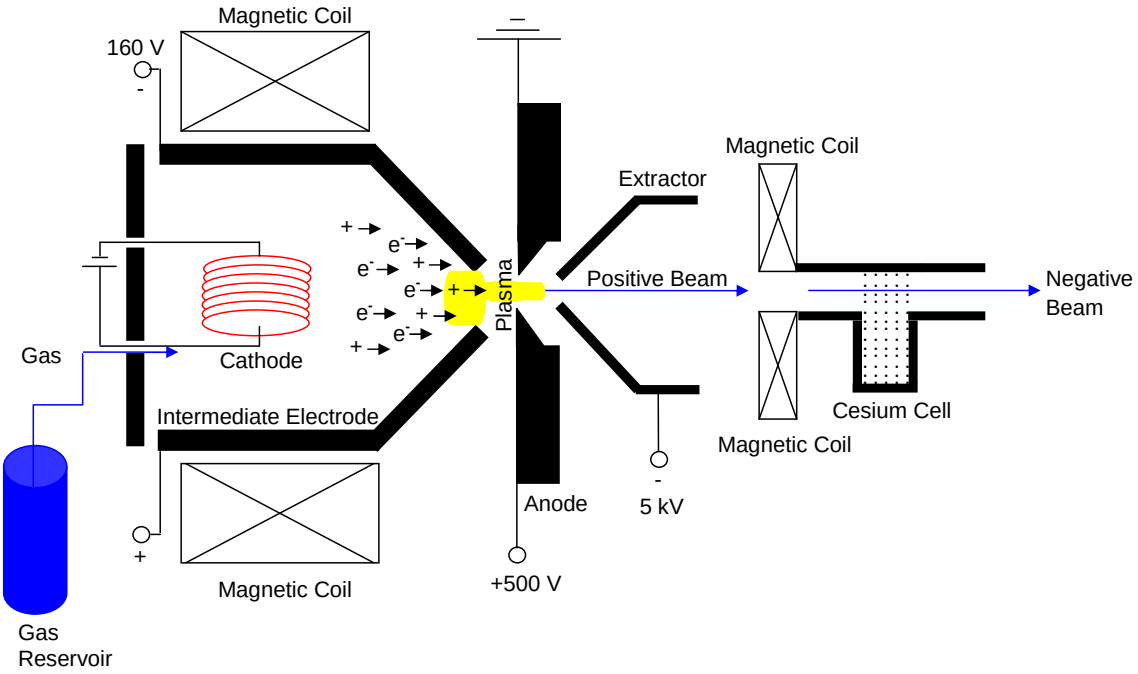

Figure 4.1: Schematic diagram of the duo-plasmatron ion source at UTTAC. The shape of the plasma (yellow region) is not to scale.

cocktail beam ($^3He^+$ and $^1H^+$ ions) was turned into a negatively-charged beam ready to be injected into the accelerator.

This beam gained a few keV in energy emerging from the ion source, and was further accelerated to 135 keV by an injector [288] (p. 8), and inflected by a 90° double focusing inflecting magnet into the accelerator tube. Moreover, the magnetic field of the inflecting magnet was set to stop the H^- beam species. The $^3He^-$ beam then passed through the image slit of the inflecting magnet, and was focused on the object point of the accelerator tube by two Einzel lenses (see Fig. 4.2).

- **The Accelerator:**

The accelerator at UTTAC is a 17.9-m long, 4.8-m in diameter vertical 12 UD tandem accelerator[4] capable of producing high voltages up to 12 MV. This accelerator consists of coupled Van de Graaff accelerators utilizing Pelletron chains as the charging system. Like the ESTU tandem at WNSL, corona discharge is prevented in the tandem at UTTAC via filling the 350-m^3 accelerator tank with pure SF_6 gas.

[4]Refs. [209, 292–294] provide a comprehensive description on different types of tandem accelerators, e.g, MP, UD, STU and ESTU.

The specific details of this accelerator can be found in Refs. [288, 295, 296]. Figs. 4.2 and 4.3 depict the layout of the 12 UD Pelletron tandem accelerator facility.

Although this accelerator is specially equipped with an earthquake ram system, the accelerator column collapsed during Sendai earthquake in March-2011, and as a result of extensive damage to the current accelerator, a new one will be installed.

After exiting from the ion source, the negatively charged $^{3}He^{-}$ beam ions were accelerated toward the positive tandem terminal located in the middle of the accelerator tube, whose potential was kept at 3 MV (with respect to the ground potential). There, the 3-MeV energetic negative particles passed through a 4.5 $\mu g/cm^2$-thick carbon stripper foil[5]. The durability of the stripper foil was important. Therefore, thin carbon stripper foils were chosen.

After passing through the stripper foil, the singly-negative ^{3}He-ions became doubly-positive ions, and were accelerated once again through the second discharge tube of the tandem to the ground potential, gaining an additional 6 MeV in energy[6]. The overall beam energy was hence 9 MeV. The beam energy was chosen to be 9 MeV, because the cross section of the $^{28}Si(^{3}He, n\gamma)^{30}S$ reaction is maximized at this energy (see Fig. 4.4 on page 137). The beam intensity varied between 0.2 to 0.5 enA. It was essential to keep the count rate on the HPGe-detectors less than 14 kHz (in singles mode) to minimize the deadtime and pulse pile-up, which can distort the γ-ray spectrum. Thus, the beam intensity was kept lower than 0.5 enA.

Upon emerging from the accelerator, the beam particles were analyzed by a 90° double focusing analyzing magnet with radius of the curvature $\rho = 1.28$ m, which had been calibrated by the elastic and the inelastic scattering of protons on ^{12}C at $E_p = 14.233$ MeV [296]. Its magnetic field of 2932.5 G was set such that any impurity in the beam species would have been stopped, and only the $^{3}He^{2+}$ beam particles could pass through. The pure $^{3}He^{2+}$ beam was further monitored by a Faraday cup behind the analyzing image slit.

All along the beam line, the beam was steered by magnetic and electrostatic steerers and monitored by a series of Faraday cups and slits. It was also focused by electric and magnetic quadrupole elements (see Fig. 4.2). Furthermore, the pressure inside the beam

[5]For beams heavier than oxygen, nitrogen stripper gas is used at the UTTAC tandem terminal [288].

[6]$E = qV$, where E is the energy, q is the charge of the beam particles and V is the potential difference applied.

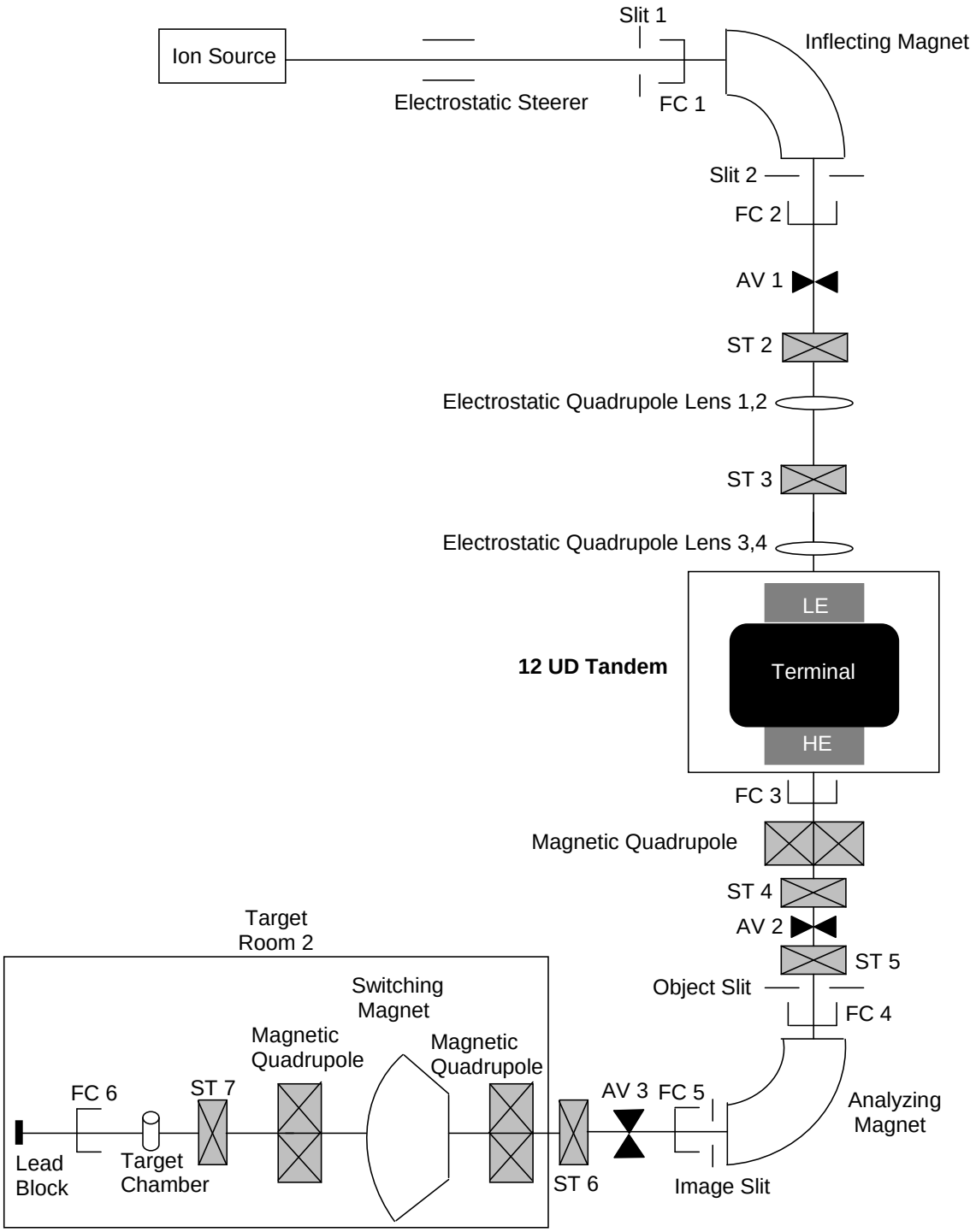

Figure 4.2: Schematic diagram of the beam line at the University of Tsukuba Tandem Accelerator Complex. Abbreviations: FC: Faraday Cup; AV: Pneumatic Valve; ST: Magnetic Steerer; LE: Low Energy; and HE: High Energy.

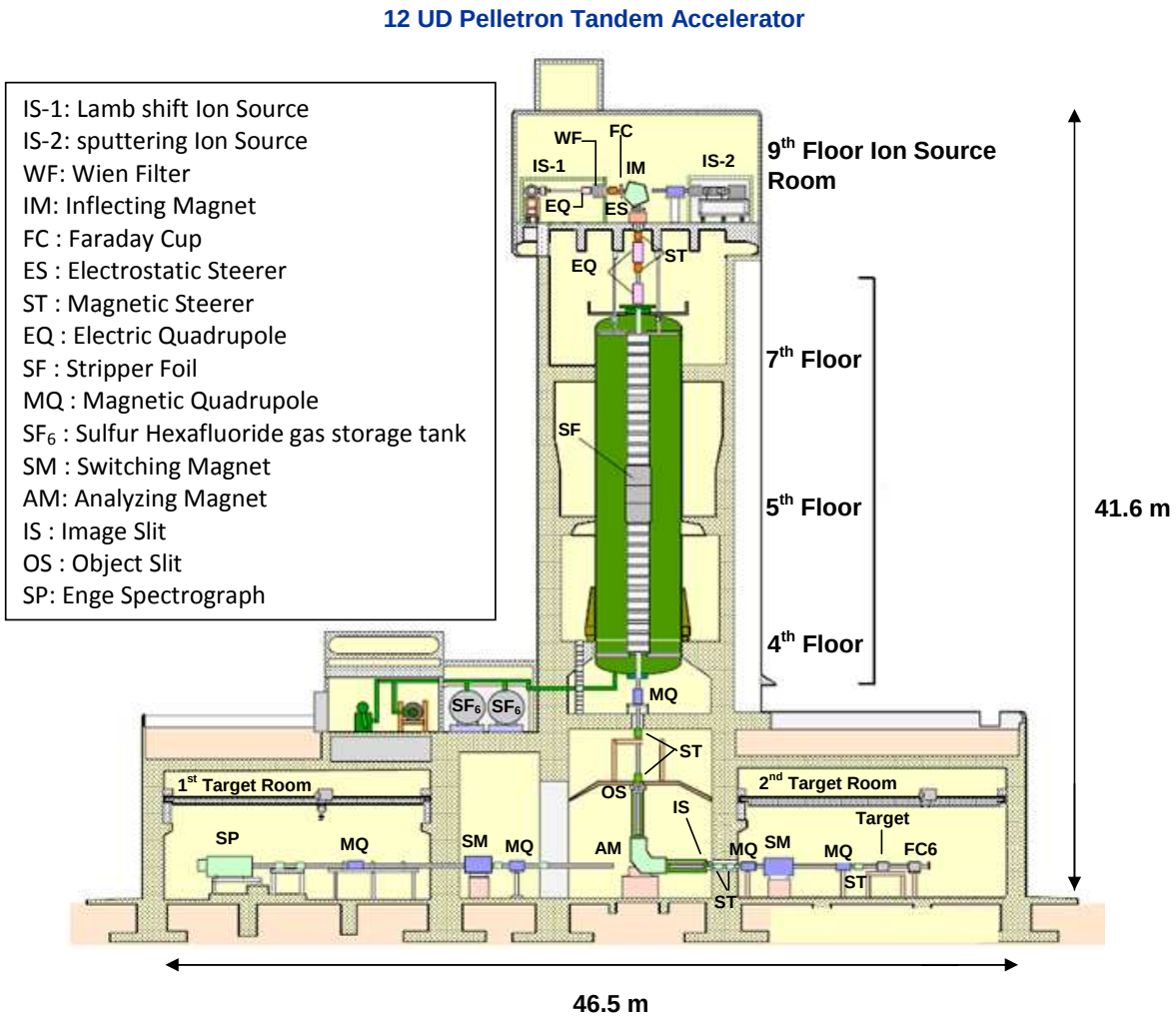

Figure 4.3: Schematic diagram of the University of Tsukuba Tandem Accelerator Complex. The beam line elements are shown also in Fig. 4.2. The inflecting magnet, as well as the analyzing magnet, are mounted on precision rotatable bases, which switch the magnets to different kinds of the ion sources, as well as target rooms, respectively. The Wien filter was not used during our experiment.

line was monitored with various pressure gauges along the beamline.

The analyzing magnet was installed on a rotatable base, which served to direct the beam into one of the two 24 m $\times$ 15 m target rooms.

- **The Target Room:**

The in-beam γ-ray spectroscopy station is located in target room 2, where a switching magnet (B = 4565 G) downstream from the analyzing magnet was used to direct the beam into the beamline of interest.

The beam was further tuned using a ZnS target in the place of the actual experimental target. When the beam hits the ZnS foil, the latter shines, and thus the beam spot was observed through a camera located above the target chamber. The beam was focused onto a ~ 1 mm^2 spot at the center of the target chamber.

The $^3He^{2+}$ beam impinged on a self-standing 25 μm-thick foil of natural silicon, of which the ^{28}Si abundance is 92.23%, epoxied onto an aluminium frame with an aperture whose area was 55 times as large as the beam spot size. This target foil was supplied by the Lebow Company [218]. Two identical Si-targets were mounted on a target ladder made of iron. To minimize the background γ-rays from iron isotopes in case the beam got out of tune and hit the target ladder, the ladder was rotated by 30° with respect to the beam axis. The target chamber was cylindrical in shape with a $\sim$ 3-cm outside diameter. The walls were made of thin stainless steel in order to minimize absorption of γ-rays.

Finally, the beam was stopped in the final Faraday cup (FC 6 in Fig. 4.3) downstream the target, and 37 cm away from the target in target room 2 by a 1 mm-thick lead plate at the bottom of the last Faraday cup (see Fig. 4.2). This last Faraday cup was completely shielded with many lead and iron blocks so that essentially no γ-rays from the beam stopper were detected.

The interaction of the beam with all three stable isotopes of silicon in the target, ^{28}Si, ^{29}Si (abundance: 4.67%) and ^{30}Si (abundance: 3.10%) produced various light reaction products, e.g., p, d, n and α. Therefore, many heavier recoil nuclei were also produced in excited states (see Fig. 4.4) that subsequently de-excited by transitions to lower energy states in the same nuclei to reach their ground states, which might be stable or might decay further (mostly via positron emission).

Those transitions from excited states to the ground states that were of electromagnetic form (γ-rays) were of interest in this in-beam γ-ray spectroscopy experiment, and in particular those γ-rays that were emitted from the ^{30}S recoil nuclei produced via the ^{28}Si(^{3}He, n) reaction were of particular importance because they provide information on nuclear properties of ^{30}S nuclei such as level energies and spin/parities[7]. The γ-rays emitted from ^{30}S nuclei themselves had properties such as energies, emission probabilities and multipolarities that were of interest, and were investigated.

[7]No lifetime measurement was performed here.

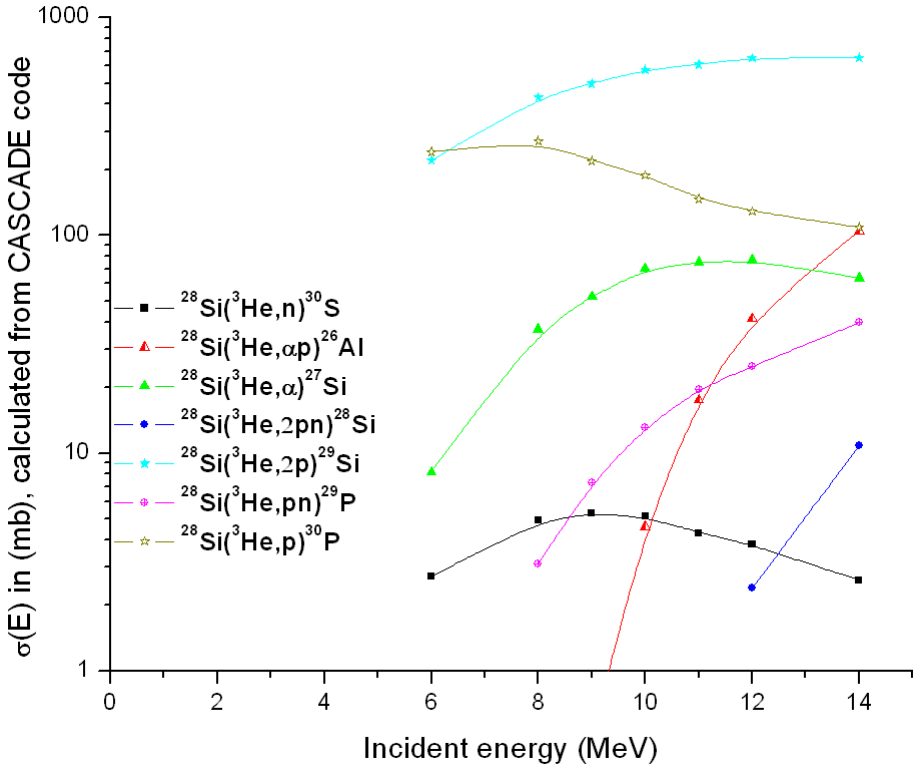

Figure 4.4: Cross section as a function of energy for possible reactions induced by reactions of ^{3}He with ^{28}Si. The cross sections were calculated with the computer code CASCADE [297, 298], made compatible for Unix operating system by Dr. T. Komatsubara [291]. The line that goes through each data point is not a fit, and is there just for clarity. The ^{28}Si(^{3}He, $n\gamma$)^{30}S reaction cross section is lower than almost all other contaminant reactions in the range of incident energy of 6 to 14 MeV. Therefore, the beam energy had to be chosen such that the cross section of the reaction of interest was optimized, and that was at 9 MeV incident energy.

In the following, the detection system used to tag the reactions of interest is discussed.

4.1.2 The Detection System

The most important apparatuses used in the in-beam γ-ray spectroscopy experiment using the ^{28}Si(^{3}He, $n\gamma$)^{30}S reaction, next to the accelerator itself, were the detectors. Two types of detectors were used for this experiment: a liquid scintillator for detecting the light reaction products, i.e., neutrons, thereby measuring the n-γ coincidences; and two solid state HPGe-detectors for detecting the γ-rays from the de-exciting ^{30}S recoils, thereby measuring the γ-ray singles, as well as γ-γ coincidences. These detectors are described below.

- **The Liquid Scintillation Detector:**

Neutrons are neutral. Therefore, in neutron detection systems a technique is used to convert neutrons into prompt energetic charged particles that can therefore be directly detectable. Such techniques depend on the neutrons' incident energy. The energy of the neutrons produced via the ^{28}Si(^{3}He, $n\gamma$)^{30}S reaction in our experiment varied between 2 – 5 MeV. Such neutrons are considered to be fast neutrons [235] (p. 537).

The most popular technique used to detect fast neutrons is via elastic scattering off hydrogen. The reason for this are that the cross section is quite large, and its energy dependence is very well known. Also, when a fast neutron is scattered off a proton, its entire energy can be transferred to the proton; whereas when scattered off a heavier nucleus, only a fraction of the neutron energy can be transferred [235] (equation (15.4) and p. 537).

Among many different types of detectors, organic scintillators are used for fast neutron detection [235] (Chapter 8). In comparison with the inorganic scintillators, the former have smaller temperature dependence, a roughly constant efficiency, small probability for non-radiative transition, e.g., internal conversion or thermal quenching, and a fast decay time (a few ns) for their fluorescent component.

All organic scintillators are based on some sort of hydrocarbon molecules for the elastic scattering off hydrogen to occur. Carbon does not directly affect the response of such detectors because of its low scintillation efficiency and the fact that it is much heavier than the proton, and thus those neutrons less energetic than 8 MeV only transfer a negligible amount of their incident energy to carbon [299].

An organic scintillator dissolved in an appropriate organic solvent is called a liquid scintillator. They are cheap, and are easy to manufacture in different shapes and sizes. Furthermore, liquid scintillators are easily loaded with other additives such as wavelength shifters to make the scintillator more transparent, or to make the emitted light better match the properties of a particular photo multiplier tube.

Perhaps the most important difference between organic and inorganic scintillators is that all organic scintillators are able to discriminate neutrons from γ-rays based on their pulse shape. This is feasible only for some inorganic scintillators. When neutrons interact with the organic scintillation material, they cause protons to recoil, while inci-

dent γ-rays cause the ejection of atomic electrons[8]. This difference in reaction products makes it possible to discriminate between neutrons and γ's. Different ionizing powers of different particles give rise to different excitation mechanisms in the scintillator, and consequently different fluorescent decay time. The most popularly used scintillator for simultaneous neutron and γ spectroscopy is the organic liquid scintillator NE-213 manufactured[9] by Nuclear Enterprises Limited [301]. The basic liquid of this detector is xylene ($C_6H_4(CH_3)_2$) [302, 303]. The other material composition is given in Ref. [304]. Its uniqueness is mainly due to its excellent n-γ pulse shape discrimination properties as a result of differences in time responses to the electrons and protons resulting from incident γ-rays and neutrons, respectively. The light output as a function of energy of the NE-213 detectors for the incident γ-rays is much more linear than that of the incident neutrons [235] (p. 565).

In Phase I (performed over 3 days during July-2009) of our in-beam γ-ray spectroscopy experiment, a NE-213 liquid scintillator encapsulated in a 25-cm in diameter and 10-cm in length cylindrical aluminium container was used for detecting the fast neutrons. The scintillator was optically coupled to a Bialkali R1250 photomultiplier tube 13.3 cm in diameter and 27.6 cm in length, and was biased to -1500 V. This detector was positioned at 40° with respect to the beam axis (see Fig. 4.5a on page 141). The distance between the target and the center of this detector was 21 cm, and therefore the count rate on the liquid scintillator detector was $\sim$ 350 Hz.

This detector had been used over the course of many years. The effect of radiation damage on organic scintillators is mainly in degrading their efficiency, which hardly recovers in time. Due to this reason, as shall be seen in the analysis section, this liquid scintillator did not provide much useful information regarding the neutrons of interest, and therefore it was not used again in Phase II (performed over 4 days during September -2010) of the in-beam γ-ray spectroscopy experiment.

- **The HPGe-Detectors:**

High energy resolution was absolutely necessary for this experiment due to large number of lines in the γ-ray spectra, many of which are separated by only a few keV. The

[8]See Ref. [235] (Chapter 2) for interaction of γ-rays with matter.
[9]This detector was introduced for the first time in Ref. [300].

resolution of other types of γ-ray detectors such as NaI(Tl) would be totally inadequate to separate such lines, whereas the HPGe-detectors have very high energy resolution.

Therefore, in both phases of the in-beam γ-ray spectroscopy experiment, two semiconductor bulletized closed-ended coaxial HPGe-detectors manufactured by ORTEC [305] were utilized. Coaxial detectors are used to detect and quantify γ-rays below 5 keV and up to several MeV. They have much larger active volumes than planar detectors [235] (Chapter 12). One of the unique features of a coaxial detector is its ability to process photons from one end of the cylinder as well as from the entire side area of the cylinder.

In Phase I of the experiment, the detector efficiencies were 70% and 140% relative to that of a 3" $\times$ 3" NaI(Tl) detector[10]. The former detector, hereafter the 70% efficiency detector, was biased to -4800 V (n-type), and had a 73 mm in diameter and 75.2 mm in length Ge-crystal with an active volume of 307 cm^3. This detector was located at 90° with respect to the beam axis, and 3.45 cm away from the target[11] as shown in Fig. 4.5a. The second detector, hereafter the 140% efficiency detector, was biased to +4500 V (p-type), and had a 84.7 mm in diameter and 107.6 mm in length Ge-crystal, whose active volume was 587 cm^3. This detector was located at -90° with respect to the beam axis[12], and 3 cm away from the target as shown in Fig. 4.5a on page 141.

Both detectors were placed as close as possible to the target to maximize the count rates and the solid angles. The $\pm$90° angles were chosen particularly because the aim for Phase I of the experiment was to observe the γ-transitions from the two astrophysically important states of ^{30}S. Therefore, it was essential to detect the γ-rays at 90° to eliminate errors in the γ-ray energy measurements due to Doppler shift caused by the non-zero velocity of the recoiling ^{30}S nuclei during the de-excitation (see equation (4.12)).

The counting rates on these detectors were 8 kHz and 14 kHz (in singles mode) for the 70% and 140% efficiency detectors, respectively. These detectors respectively had 3.2 keV and 3.3 keV resolution (FWHM) at $E_\gamma = 1333$ keV ^{60}Co line.

To reduce the flux of the X-rays, which would contribute to deadtime and pile-up losses, a 10 cm $\times$ 10 cm, 2 mm-thick copper piece was installed in front of each detector

[10] A 7.62 cm in diameter and 7.62 cm in length NaI(Tl) crystal has efficiency of 1.2×10^{-3}, considered as 100% efficiency, for the 1333-keV line of a ^{60}Co source 25 cm from the center of the front face of the endcap of the detector on a line perpendicular to the endcap face [306] (p. 90, 136 and 206).

[11] Such distances given here are between the target and the window of the detector.

[12] The minus sign is not necessary because both -90° and 90° are identical; however, the minus sign here just indicates that this detector was on the opposite side from the other detector at 90°.

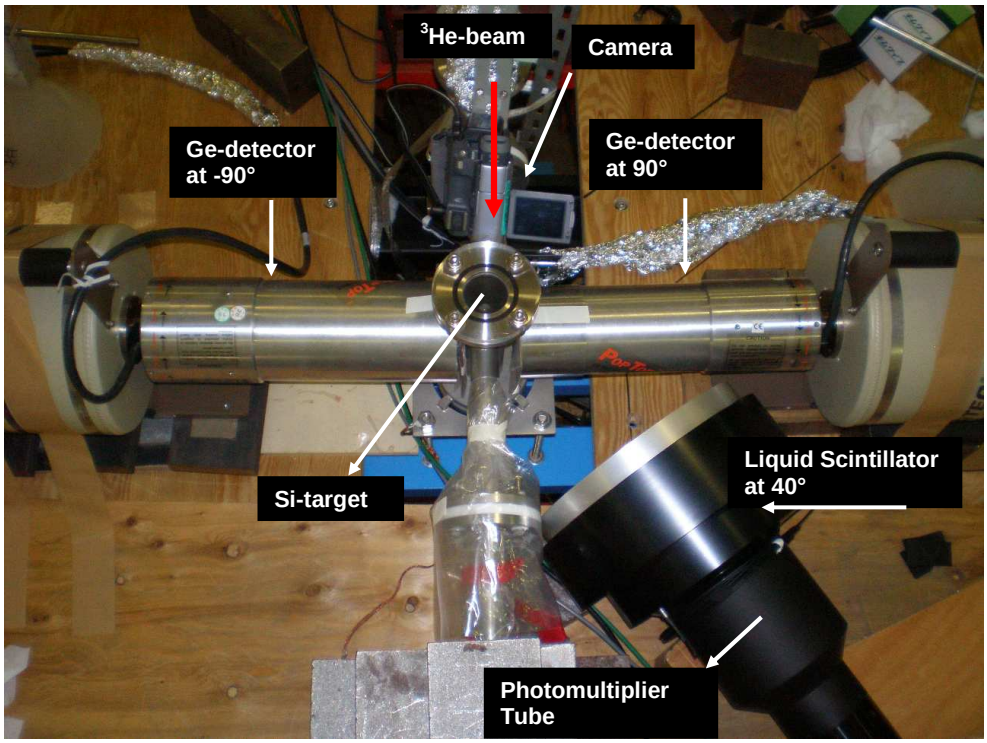

(a) Experimental setup for Phase I.

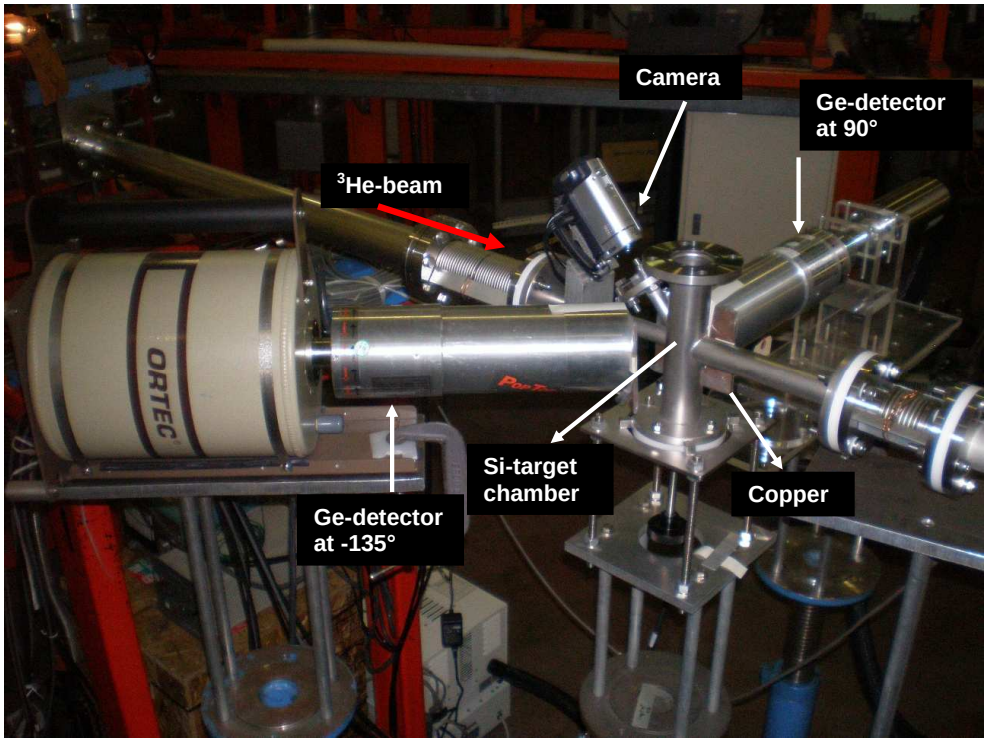

(b) Experimental setup for Phase II.

Figure 4.5: Experimental setup for the in-beam γ-ray spectroscopy experiment using the ^{28}Si(^{3}He, $n\gamma$)^{30}S reaction. The final Faraday cup was shielded with iron and lead blocks.

that covered the whole circular base of the detector. To reduce the noise from the copper pieces that are conductors, they were wrapped in a plastic bag. A computer code called Absorber[13], written by Dr. T. Komatsubara [291] based on Ref. [307], was used to simulate the transition probability through a 2 mm-thick Cu-absorber as a function of energy for photons. According to that simulation, γ-rays with energy below 200 keV were absorbed by 20%, and the γ-rays with $E_\gamma \geq 200$ keV were transmitted through these Cu foils with a probability of at least 90%.

During Phase II of the in-beam γ-ray spectroscopy experiment, an n-type ORTEC bulletized closed-ended coaxial HPGe-detector with 50% efficiency relative to that of a 3" $\times$ 3" NaI(Tl) detector was biased to -3500 V, and positioned at 90°, 3.2 cm away from the target. The Ge-crystal in this detector, henceforth known as the 50% efficiency detector, was 64.8 mm in diameter and 67.7 mm in length, having an active volume of 217 cm^3. Its energy resolution was determined to be 4.4 keV (FWHM) at $E_\gamma = 1333$ keV ^{60}Co line.

In addition to this detector, the 70% efficiency detector was also used again in Phase II, but this time is was positioned at -135° with respect to the beam axis[14]. This particular angle was chosen because in this phase of the experiment, the goal was to measure the γ-γ DCO ratios, which are largest when the two detectors are located at two angles in the same plane with the largest possible difference. To prevent the extensive irreversible radiation damage due to neutrons, the expensive HPGe-detectors are normally not placed at forward angles. Therefore, the safest angle at which they could be positioned started at 90°. Due to the presence of the beamline, the detectors could not be positioned at angles higher than $\pm$135°. Hence, the two angles that would technically provide the largest possible difference were 90° and -135° (see Fig. 4.5b). The rotating detector holders were pivoted about the target position and could be used to set the detectors at any angle with a precision of 1° from zero to $\pm$135°.

In Phase II of the experiment, the closest distance (due to the presence of the beamline) to the target that the 70% efficiency detector could be positioned at -135° was 7.0 cm away from the target. Its resolution remained 3.2 keV (FWHM) at $E_\gamma = 1333$ keV ^{60}Co line.

[13]This code is not publicly available.

[14]Again, the minus sign only indicates that this detector was on the opposite side from the other detector.

To minimize the differences between the experimental setups of Phase I and II of the in-beam γ-ray spectroscopy experiment, the copper pieces identical to the ones used in Phase I were again used in Phase II in front of both HPGe-detectors.

The count rates on the HPGe-detectors during Phase II of the experiment varied between 6 – 15 kHz (in singles mode). The HPGe-detectors were filled with LN_2 every 12 hours. No Compton suppression Bismuth Germanium Oxide (BGO) shield was used during the in-beam γ-ray spectroscopy experiment because the HPGe-detectors had high peak-to-Compton ratios[15] [306] (p. 91), which is due to the fact that pure germanium has a high photoelectric cross section [234] (p. 241).

4.1.3 The Electronics and Data Acquisition System

In addition to the energy of the radiation incident on the detector, the timing information of the initial voltage pulse is also of paramount importance, because it may tag another incident radiation produced from the same reaction. The analog time signals can be digitized by a Time-to-Digital Converter (TDC) module or by a combination of a TAC or a Time-to-Pulse-Height Converter (TPHC) module with an ADC module.

The electronics used for the in-beam γ-ray spectroscopy experiment included NIM analog and logic signal processing modules, a Transistor-Transistor Logic (TTL) module (only used in Phase II), a latch logic module, and the Computer-Automated Measurement and Control (CAMAC) analog-signal digitizing modules. The digital pulse outputted from the ADC was analyzed by the BASS [308] DAQ system at UTTAC. In what follows the aforementioned modules and the DAQ system are separately described for Phase I and II of the experiment.

- **Phase I of the experiment:**

The liberated charges produced in each HPGe-detector were integrated in the corresponding charge sensitive preamplifier, and thus a weak voltage signal was produced, whose height was proportional to the incident energy. The two branches after each preamplifier (see Fig. 4.6) served two purposes: the acquisition of the voltage signal carrying the energy information in its maximum amplitude, and the extraction of a start time

[15]The measured peak-to-Compton ratios at the time of purchase of the 50%, 70% and 140% relative efficiency detectors were 67:1, 73:1 and 85:1, respectively. These values are reported for the 1333-keV line of a ^{60}Co source.

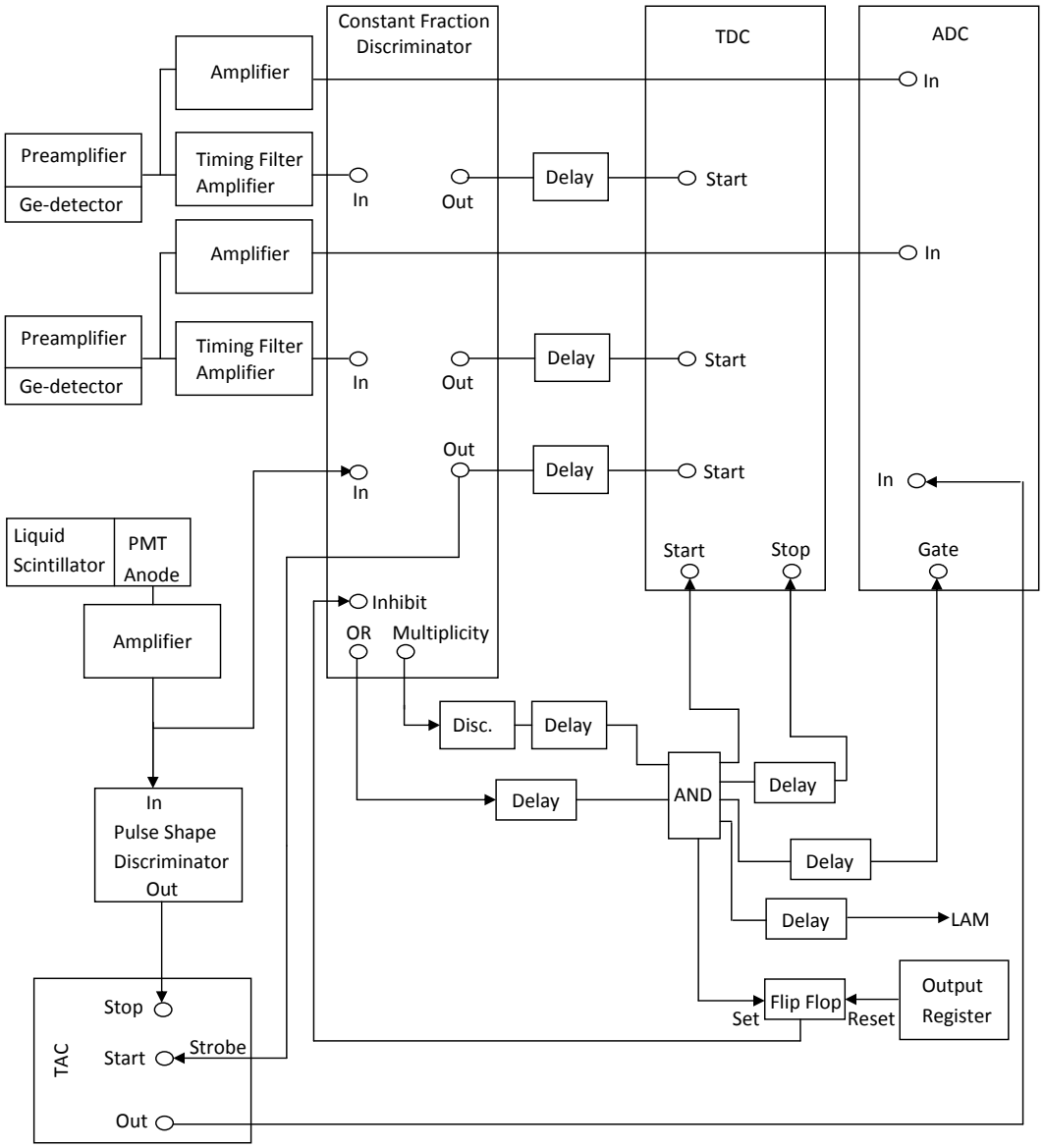

Figure 4.6: The schematic diagram of the electronics used for signal processing in the ^{28}Si(^{3}He, $n\gamma$)^{30}S in-beam γ-ray spectroscopy experiment (Phase I).

signal. The output voltage signal of each preamplifier was filtered[16] at the corresponding triangular shaping amplifier, which in turn amplified the weak input signal and shaped the signal. Its output pulse then reached the multi-channel CAMAC standard ADC (C011 4ch model, manufactured by Hoshin Company [309]) that digitized the voltage pulse.

The preamplifiers' output signals were not optimum for achieving good timing resolu-

[16]Filtering in this context means selecting the signals with correct pulse height [234] (p. 304).

tion. The timing filter amplifiers employed prior to the ORTEC CF8000 CFD offered such signals some amplitude gain and pulse shape optimization in order to improve the time resolution, and to reduce the noise. The output pulses from the timing filter amplifiers had faster rise and fall times and sharper initial edges. Therefore, such baseline-restored output signals could be used for timing purposes.

Since both time and pulse height of the signals had to be extracted, we used a so-called fast-slow system [235] (p. 676) such that the time signals were only accepted for the signals of a specific amplitude. Therefore, signals were divided into two branches: a slow branch and a fast branch. The amplitude branch was considered to be the slow branch, and was used to gate on the fast branch to accept or reject the corresponding time signals. Hence, the fast time branch was first delayed through a fixed delay time via a delay box, which was located after the CFD.

Fast anode analog signals with rise times of ~ 2 ns in the photomultiplier tube, coupled to the liquid scintillator were used to derive their corresponding timing information from this detector.

The latter signals were first integrated and differentiated in a preamplifier (not shown in Fig. 4.6 for simplicity) so that the baselines of the preamplifier output pulses for neutrons and γ-rays were determined by the decay time of the preamplifier input pulses. The shaped signals were then amplified in a linear amplifier, which greatly enhanced the separation of the baselines corresponding to γ-rays and neutrons.

Discriminating between different pulse shapes requires measuring the decay time of each pulse independent of their amplitude. The amplified signals were therefore split and fed into: (i) a current integrator Pulse Shape Discriminator (PSD) to produce an output pulse whose rise time depended on the decay time of the initial pulse, and therefore the pulses generated by neutrons and γ-rays incident on the scintillator could be distinguished; and (ii) the fast time pick-off CFD to establish an exact time reference for a particular pulse. In addition, the CFD minimized the energy dependence of time measurements, called walk. The CFD rejected all pulses except those whose energies were inside a window corresponding to its upper and lower discrimination levels. This threshold was set slightly above the noise level.

The output signal of the CFD was also split into two branches. Part of the CFD output signal was fed into the TDC module after passing through a delay box. The other

part of the output signal of the CFD was used to trigger a timing strobe signal, which is a pulse whose duration is shorter than the time period of its recurrence [291].

The input pulse to the PSD module was integrated for two different times, one short (25 ns) and one long (400 ns) [310]. Both neutrons and γ-rays underwent multiple scattering since the liquid scintillator was a relatively large detector compared with their mean free paths. While the γ-rays travel with the speed of light, the neutrons travel more slowly. So, the signals that arose from neutrons had greater time duration for charge collection, and hence different rise time than those from the γ-rays. Therefore, when the result of the integrations in PSD were weighted for time and were compared, the output pulse showed two bands representing different incident particles (neutrons *vs.* γ-rays) with different pulse shapes.

The CFD strobe signal triggered a START signal for a TAC module, and the STOP signal arrived from the output of the PSD. The TAC produced a voltage pulse from discharging a capacitor between its START and STOP times. The maximum amplitude of that voltage pulse was linearly proportional to the time period measured by the TAC unit. Hence, the TAC output pulse contained the information on the time relation of the γ-rays and neutrons pulses (or the type of the incident radiation). Strobe signals act like a time gate to reject those signals, whose rise time are outside the gate window [291]. Therefore, the TAC automatically suppressed random γ-rays from the background.

The TAC output pulse was then fed into the ADC so that the ADC could convert this pulse into digital data, which could later be examined and reanalyzed if necessary via the DAQ computer. In this way, the exact rise time of the pulses corresponding to neutrons and γ-rays detected by the NE-213 detector could be determined. This time information could be used to accept or reject the type of radiation incident on the scintillator.

During this phase of the experiment, a NIM standard four-fold coincidence unit was used that had up to four inputs and a switch for each input to allow them to be individually enabled or disabled. For example, if the signals from two detectors were required to be in coincidence, then two switches must have been enabled for a 2-fold logic decision, etc. Disabling a logic input, on the other hand, was equivalent to reducing the number of simultaneous inputs required for generation of an output signal, which was in turn a logic signal.

The CFD module had built-in logic functions to minimize external logic requirements.

Whenever a signal exceeded the threshold of the CFD[17], this module generated a fast NIM logic output signal with a width on the order of 144 ns corresponding to the coincidence width. We called this signal "B output" to be consistent with the CF8000 manual provided by ORTEC Company. However, B might be a random name not recognized by the community. The multiplicity output (M in Fig. 4.6) provided a voltage signal[18] with an amplitude proportional to the number of logic B output signals active at any instant. Therefore, the multiplicity simply indicated the number of signals incident on the CFD which had met the CFD threshold requirement. The multiplicity output of the CFD was fed into a discriminator (Disc. in Fig. 4.6) so as to determine the fold number of the time coincidence. A fold number of 2 indicated "coincidence mode" and a fold number of 1 implied "singles mode".

This is because when the electronics were in coincidence mode with the purpose of measuring the n-γ and γ-γ coincidences, two switches were turned on in the coincidence unit, and thus a 2-fold logic decision was in operation on the coincidence unit because it was required that the signals from both Ge-detectors or one Ge-detector and the liquid scintillator to be coincident in time. In singles mode, on the other hand, only one switch was turned on in the coincidence unit.

The delay box after Disc. (discriminator) and OR in Fig. 4.6 ensured that the multiplicity or OR signals and the output of the delay box prior to the TDC arrived at the same time. The multiplicity output was sent to the gate input of a CAMAC coincidence register to open an AND gate [234] (p. 318 – 319), and send the START signal to the TDC so that this module could start recording the time. The data-recording cycle was set in the following manner: the OR output on the CFD module provided a logical inclusive OR function [234] (p. 318) for every active B output. If the OR signal occurred during the period when the AND gate was opened by the multiplicity pulse, the OR output could be used as the master trigger for a coincidence event, in which case the OR signal also opened the gate of the ADC and started the TDC, which received its STOP signal subsequently after a fixed time set by a delay box to ensure the STOP signal arrived after the START signal. At the same time, the OR output set a Flip-Flop so as to block the CFD for subsequent events by sending an input INHIBIT signal to the CFD.

[17]The particular device we used has a constant-fraction ratio of 0.4 set by ORTEC Company.

[18]Note that there is no connection between this voltage and the voltage of the actual signal from the detector.

The total signal processing time from when two γ-quanta hit the detectors until a pulse was available on the output of the coincidence unit was a few hundred nanoseconds. The processing of the energy signal, however, was not finished until after several microseconds. In order to put energy and gate signals in phase, the gate signal must have been delayed. This is why there was a delay box prior to the gate signal that goes into the ADC.

When approximately 7.2×10^8 coincidence events were collected [291], the memory buffer in the latch module [234] (p. 297) was filled. Then, a Look-At-Me (LAM) signal was produced by the CAMAC system, which triggered the data readout system over the CAMAC dataway to the CAMAC crate controller [234] (Chapter 18). The intelligent controller successively commanded the VME front-end processor that included the CAMAC branch driver and a CPU. The CPU was driven by LynxOS, which is a real-time Unix operating system. This system sent the data pack to a host computer running the FreeBSD operating system, hereafter the DAQ computer. Once the data were sent to the DAQ computer, and thus the outputs of the TDC and ADC were registered, the digital data readout was finished. Hence, the VME processor sent an acknowledge signal via the CAMAC branch driver to reset the memory buffer in the latch module with a CLEAR signal from the readout module. The ADC was gated off, and a reset signal was returned from the CAMAC to the Flip-Flop. Then the next event could be recorded. Therefore, the TDC and ADC would be ready to process the data again.

- **Phase II of the experiment:**

The required electronics for HPGe-detectors used in this phase of the experiment are shown in Fig. 4.7a and Fig. 4.7b when they were in singles and in coincidence mode, respectively.

The first few steps of the signal processing of HPGe-detectors in this phase was identical to that described above. The only difference was that we did not use any TDC in Phase II. Therefore, the output of each of the timing filter amplifiers was fed into a CFD. The CFD essentially produced a logic output signal (previously called B output) whenever the amplitude of the input analog signal was above a voltage threshold. This was how the true events were distinguished from low-amplitude signals caused by electronic noise and background radiation. The CFD also provided fast timing reference.

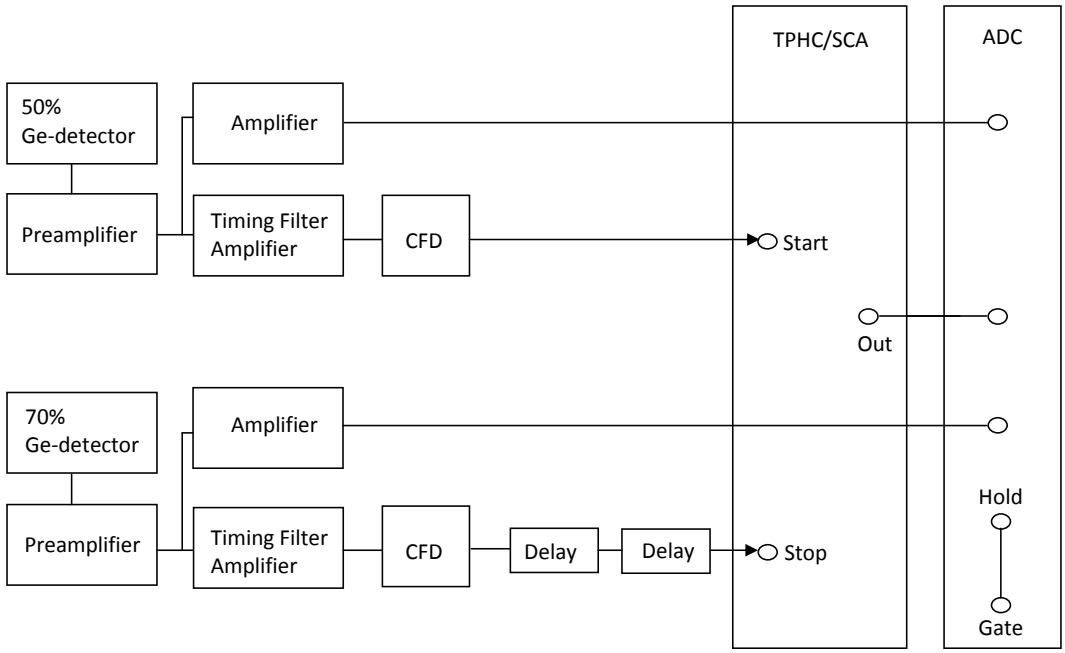

(a) For detectors in singles mode.

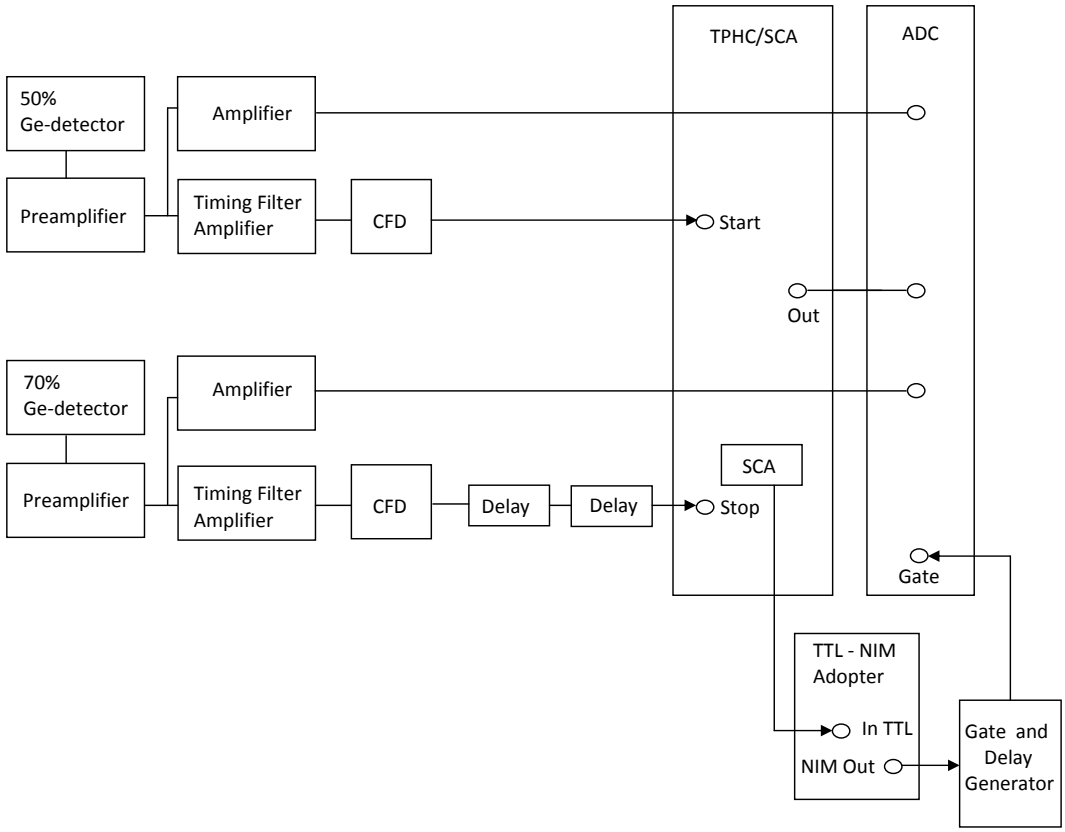

(b) For detectors in coincidence mode.

Figure 4.7: The schematic diagram of the electronics used for signal processing in the ^{28}Si(^{3}He, $n\gamma$)^{30}S in-beam γ-ray spectroscopy experiment (Phase II).

The output signal of this module was used directly to start measuring the time. So, while the output of the CFD signal from one HPGe-detector was used to start a TPHC module, the output of the other CFD from the other HPGe-detector was delayed by 126 ns (each delay box is 63 ns) to stop the time in the TPHC module.

The TPHC module is used for measurements of short intervals in time, and is capable of 0.02% or better resolution in ranges as small as 50 ns [311]. During the interval between the START and STOP pulses, a capacitor was charged. The amplitude of the voltage generated in the capacitor was linearly related to the time interval between these pulses [311]. The output signal of this module was then fed into a multi-channel ADC to convert the timing information into digital data. This was the circuit for the singles mode of electronics. No gate signal was produced here, and thus all pulses into the ADC were recorded.

For the coincidence mode, in addition to the aforementioned circuit, a Single Channel Analyzer (SCA) in the TPHC module was used to produce a logic output pulse only when the linear input pulse from the TPHC module lay between the SCA lower- and upper-level discriminations, which were set to 0 V and 0.49 V, respectively. The difference between lower- and upper-level discriminations was chosen to be small to reduce the chance of recording accidental coincidences. Therefore, the SCA served to select only a limited range of signals' amplitudes from all those signals generated by the HPGe-detectors to permit only certain signals to be passed through, which were in coincidence with each other. The logic output signal of the SCA module had a positive amplitude, and was thus fed into the TTL input of a TTL-NIM adopter module. This latter module produced a standard NIM logic pulse with negative pulse height, and was therefore fed into a GDG, which in turn produced a logic gate signal fed into the ADC only if two events from both HPGe-detectors overlapped, and hence were in coincidence in time.

In the coincidence mode, the ADC was only activated when it received a gate signal from the GDG module. When this device sent a gate signal, it counted down for a set amount of time called the gate width, during which the VME and the CAMAC crates acquired the incoming data to a memory buffer as an event and the ADC continued to take data associated with that event, while digitizing the maximum amplitudes of the voltage signals that arrived. The ADC also sent a logic veto (busy) signal to the GDG until it had finished processing the event, disabling the GDG from changing the gate

condition. When the events were not in coincidence, this gate signal was not generated. Therefore, the ADC only accepted the data corresponding to those γ-rays which were in coincidence from a γ-ray cascade. After the memory buffer was filled, the LAM signal was generated. The next DAQ steps were previously described, and were identical to those of Phase I of the experiment.

4.1.4 The Data Analysis Software Package

On the DAQ computer, the experimenter collects the spectra and saves the data to disk in a typical time window of an hour via a mixed FORTRAN and C software package called Multi Spectra Analyzer, which is written by Dr. T. Komatsubara [291] and is not available to public.

Online data acquisition, data display in 1D histograms, data sorting, as well as offline data analysis are all performed by using this software package. It is powerful and yet easy to learn and use, and can be run on Unix and GNU/Linux operating systems. All basic applications to spectra, e.g., addition, subtraction, compression, etc.; peak fitting by single or multi-Gaussian functions; spectra calibration fits; background subtraction fits; and many more applications can be performed by this single software package. Therefore, it provides the experimenter with everything that is required for the data analysis and display of the γ-ray measurements.

4.1.5 Pre-Experiment Analysis

The resolution of each Ge-detector was determined prior to the experiment via a 23.0 $\pm$ 0.6 kBq ^{60}Co source. In order to pre-calibrate the γ-ray spectra of each detector, the fine gain of the amplifier was set such that each channel of the ADC corresponded to 1.5 keV, giving the ADC response a one-to-one channel-to-energy linear correspondence. This is because that particular ADC has 4096 channels, and therefore if the energy/channel = 1.5 keV/channel, in principle this would allow us to be able to detect γ-rays with energies up to 6 MeV. However, this was just a crude pre-calibration, and as will be seen in § 4.2.3, this response in reality is not in one-to-one accordance.

4.2 Post-Experiment Analysis Methods

Having described the experimental motivation, setup and apparatuses, we will now proceed to the analysis discussion prior to the presentation of the results.

In the following discussion, γ-ray singles and γ-ray coincidence measurements refer to the situations where the electronics were setup in the singles and coincidence modes, respectively, as explained previously.

Two other nomenclatures that are used frequently in the following are the singles γ-ray and coincidence γ-ray spectra. The former refers to the ungated spectrum from an individual detector. This spectrum can be generated both when the electronics are in the singles mode or in coincidence mode with the difference that in the former case the registered count rates are much higher due to the absence of the coincidence veto signal.

In contrast, the coincidence γ-ray spectrum is a gated spectrum that can only be generated when the electronics are set up in coincidence mode. Therefore, this spectrum presents the γ-rays detected by one detector, which are all in coincidence with a particular γ-ray called the gate γ-ray that is in turn detected by the other detector.

In the following few sections, we first introduce the analysis methods and then proceed to the results.

4.2.1 Detection Geometry

To maximize the solid angle subtended by the detectors, they have to be placed as close as possible to the target. The solid angle covered by a HPGe-detector under the assumption that the target is point-like is calculated from the following equation:

$$\Omega = 2\pi \left(1 - \frac{d}{\sqrt{d^2 + r^2}}\right) \tag{4.1}$$

where d is the true distance of the source to the active Ge-crustal; and r is the radius of the Ge-crystal. Although the diameter of the Si-target was 8.4 mm, this target could still be considered as a point-like source because the minimum true source-to-detector distances in our setup were almost 5 times larger than the diameter of the target.

Each HPGe-detector used in our experiment contains the pure-germanium crystal whose first 0.3 μm-thick layer is inactive germanium. The crystal has a 0.3 μm-thick

outside contact layer of germanium implanted with boron ions (for the 50% efficiency detector, this layer is pure boron) to increase the sensitivity of the coaxial detectors to below 10 keV [234] (p. 241). This crystal is then shielded in an aluminium cup while a 0.05 mm-thick aluminized mylar insulator is placed between them. The aluminium cup is then put into an aluminium close-fitting cover with a 0.76 mm-thick end cap window made of beryllium (for the 50% efficiency detector, this thickness is 0.5 mm). There is a 4-mm gap between the end cap to the base of the aluminium cup. Fig. 4.8b presents the schematic diagram of a typical HPGe-detector.

While the knowledge of the source-to-detector distance is absolutely necessary for calculation of the solid angle covered by the detector, this distance alone is not enough, and the distance from the detector's window to the active layer of pure Ge-crystal has to also be taken into account. In addition, the thickness of the copper piece placed in front of the detector window matters as well. Therefore, based on a simple geometrical diagram shown in Fig. 4.8 the true source-to-detector distance d as seen by a γ-ray is calculated from (with all distances in mm):

$$d = K + L + D + 0.3 \times 10^{-3} + B + E + F + M \tag{4.2}$$

where K is the distance from target to the leading edge of the copper piece, L is the thickness of the copper piece, D is the thickness of the beryllium window, 0.3×10^{-3} is the thickness (in mm) of the inactive germanium layer, B is the gap between the end cap to the base of the aluminium cup, E is the thickness of the aluminized mylar insulator, F is the thickness of the outside contact layer, and M is illustrated in Fig. 4.8b and is equal to $J(1 - \cos(45°))$.

Another factor that is important in determination of the solid angle is the radius of the Ge-crystal, r (see Fig. 4.8). The detector specifications sheet normally contains the required information to calculate this length. From the diagram in Fig. 4.8b, this distance was calculated as follows:

$$r = N + 2O \tag{4.3}$$

where N and O are the distances depicted in Fig. 4.8b. N is always given in the detector specifications sheet, and $O = J \sin(45°)$.

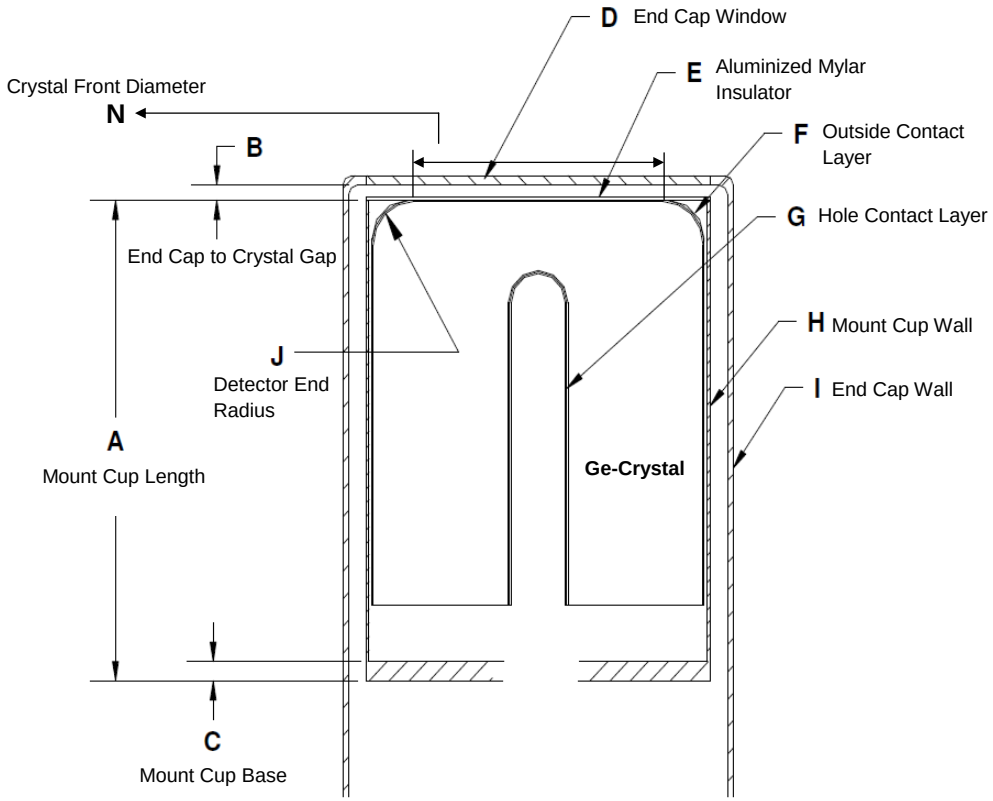

(a) The schematic diagram of a typical Ge-crystal.

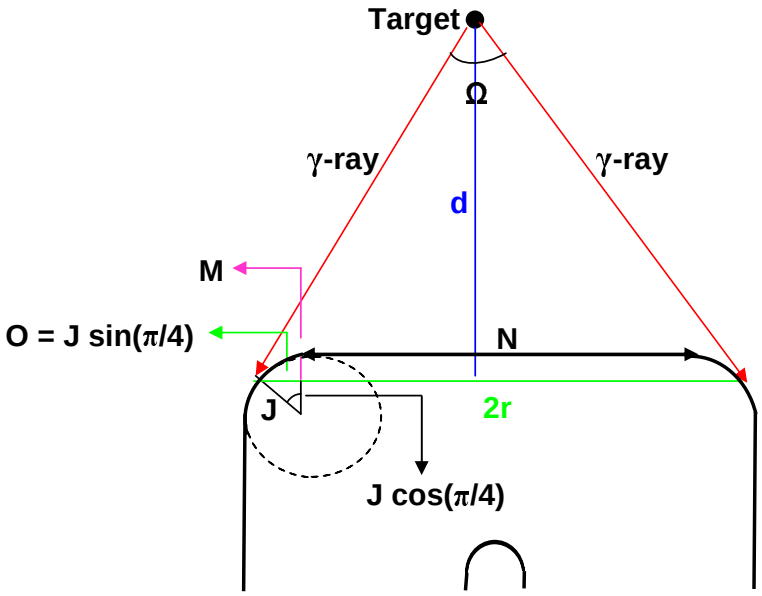

(b) Typical geometry of the Ge-crystal.

Figure 4.8: (top) Schematic diagram of a typical germanium crystal. Labeled thicknesses are either provided in the detector specifications sheet, measured during the experiment, or calculated (see text). (bottom) Geometrical picture used to calculate the distances d and r for equation (4.1). Only a portion of the Ge-crystal is shown.

Thus, the solid angles covered by the HPGe-detectors were 0.6π and 0.7π for the 70%- and 140%-efficiency detectors in Phase I, and 0.5π and 0.23π for the 50%- and 70%-efficiency detectors in Phase II of the experiment, respectively.

4.2.2 Gain Shift Correction

Prior to the start of the experiment, 83.2 ± 3.2 kBq ^{152}Eu, 23.0 ± 0.6 kBq ^{60}Co, ^{241}Am and 370 ± 15 MBq ^{241}Am-Be standard sources[19] were used to test the electronics signals from both HPGe-detectors and the liquid scintillator to ensure they were not faulty or too noisy, and to check for electronics-induced gain shift.

The latter is produced by a number of factors [312] (and references therein)[20]. For our experiment, the main factor was count-rate induced gain shifts that were mainly caused by fluctuations in the preamplifiers output voltage signals. The gain shift causes the peaks corresponding to the γ-rays from the source to move on the channel axis of the spectrum by a few channels over time, which distorts the shape of the peak and degrades the energy resolution.

In our experiment, each ADC channel was set to correspond to 1.5 keV. Hence, fluctuations of a peak over a few channels would correspond to nonphysical gain or loss of a few keV. Since the peaks corresponding to the beam induced γ-rays from different reactions on the target were only a few keV apart in many cases, the untreated gain shift could disturb the calibration of the spectrum, and that would have strong negative effect on the peak identification capabilities.

Therefore, care was given to identify the source of gain shift and isolate or minimize the extent of the gain shift by tweaking the coarse and fine gains of the amplifiers. This was to ensure that the average gain shift during the experiment was kept down to reasonable levels.

After the beamtime was over, all the one-hour-long runs from both HPGe-detectors were individually displayed on counts *vs.* channel 1D histograms via the Multi Spectra Analyzer software package. These spectra are the actual ADC pulse height spectra cor-

[19] These activities are for Phase I of the experiment. During Phase II, the activities of the ^{152}Eu and ^{60}Co sources were reduced to 78.5 kBq and 19.5 kBq, respectively. Being an α-source, ^{241}Am is combined with Be to produce neutrons with well known energy via (α, n) reaction. The ^{241}Am-Be source was not used for the second phase of the experiment because the liquid scintillator was not utilized again. The ^{241}Am-Be source activity was not recorded during Phase I of the experiment.

[20] Also see Ref. [306] (p. 200 – 202).

responding to the HPGe-detectors. They contain many peaks, which are to a very good approximation described by Gaussian functions. These peaks correspond to γ-rays, most of which are beam induced γ-rays that are emitted from de-exciting nuclei produced by various nuclear reactions on the natural Si-target. However, some of the γ-rays are unwanted background γ-rays, which are discussed in § 4.2.6.

A strong doublet corresponding to the 1264.6-keV and 1273.4-keV lines[21] of ^{30}P and ^{29}Si (see Fig. 4.10 on page 162), which were produced by the ^{28}Si(^{3}He, p)^{30}P (Q-value = 6.369 MeV [241]) and ^{28}Si(^{3}He, $2p$)^{29}Si (Q-value = 0.774 MeV [241]) reactions, respectively, was chosen for fit tests among all the peaks in each of the spectra associated to one-our-long experimental runs. The reason why this doublet was chosen is that both peaks were relatively strong transitions, and thus the statistical uncertainties in the fits did not significantly affect the position of the centroids. The two peaks were fitted using the Multi Spectra Analyzer software package with least-squares multi-Gaussian functions of the form given in equation (3.6) in order to obtain the channel numbers corresponding to the centroids of the peaks in that doublet. These two peaks in the doublet were well-resolved peaks.

For this fitting procedure, the widths of peaks were first left as free parameters. If the resulting fits did not describe the peaks well, meaning that the χ^2 was too large or the visual inspection of the fits fail to describe the peaks, the width of one or both peaks were kept fixed, and the peaks were fitted again until a desired fit was achieved with the minimum χ^2.

As the next step, the centroids corresponding to both peaks in the doublet were separately plotted against the run number for all of the one-hour-long runs that had identical experimental parameters, for each HPGe-detector. Since these runs had identical experimental parameters, the shifts in the centroids of the peaks due to the Doppler shift were eliminated for the runs corresponding to the detector positioned at -135°. This analysis was done to check the extent of the gain shift from the preamplifier connected to each HPGe-detector during the experiment. Since the selected doublet was identical in each run, ideally (without the presence of gain shift) the centroids would appear at the same channel number in each run whose experimental parameters were the same as the next run, and the plots would thus show a horizontal line. However, a small gain shift was

[21] The conversion of centroid to energy is explained in the next section.

unavoidable, and thus the line was not perfectly horizontal. The shift in the centroids was for most runs less than 0.8 channel, and thus was negligible. A few runs showed a high gain shift, on the order of 1.7 channels, and thus were shifted back using the Multi Spectra Analyzer software package, such that the doublet's centroids fall on the average centroid location for the other identical runs.

After gain shift correction, the spectra for each one-hour-long run with identical experimental parameters were added together to obtain the final singles γ-ray spectra of both detectors.

4.2.3 Energy Calibration

Two important quantities can be extracted from the ADC pulse height spectrum: γ-ray energies and relative intensities. The former is necessary to identify the peaks corresponding to γ-rays in order to tag their parent nuclei. The γ-ray energy is obtained from the channel number corresponding to the centroid of the associated peak. The relative intensities of the γ-rays are obtained from the areas underneath the associated peaks.

In order to extract the centroid and area of each peak, the peaks were first fitted using the Multi Spectra Analyzer software package with a least-squares single-Gaussian function of the form given in equation (3.6) with $i = 1$ whenever the peaks were reasonably isolated from each other, and with a multi-Gaussian function for the resolved or unresolved doublets. To determine the baseline level of the peak (y_0 in equation (3.6)), the fitting region was defined by the experimenter to be a small region surrounding the peak of interest, so that the fitting routine could determine the background level on both sides of the peak. Background subtraction was then performed by fitting a least-squares polynomial of the first degree to the background on both sides of the peak. The area under the peak was then automatically determined by the fitting routine to be the number of counts above the baseline within the peak region described by a Gaussian function.

To convert the centroids' channel numbers to energies, and the areas to relative intensities, the detector response must be calibrated for both energy and relative efficiency. The latter is explained in the next section. Here we describe the former.

Calibration of the HPGe-detectors was performed before and after the beamtime with

standard γ-ray emitting sources of ^{152}Eu and ^{60}Co, whose β^+-delayed γ-rays[22] have very well-known energies and absolute intensities. Such sources were placed inside the target chamber on a position identical to that of the actual experiment target (Si-target) so that the attenuations and energy losses of the γ-rays from the standard sources and the source-to-detector distance, and thus the detection solid angle, were identical to those of the γ-rays induced by the beam. Although our detectors were placed in close geometry, these sources were small enough (a few mm in diameter) that to a good approximation they could be considered as point-like sources.

Ideally, the standard calibration sources are selected such that the emitted γ-rays have energies in the region of interest for the best calibration of this region. The main nucleus of interest for this experiment is ^{30}S. The states of interest in this nucleus emit γ-rays in the range of a few hundreds of keV to 2 – 3 MeV. The reasonably intense γ-rays that can be detected in a short amount of time from a ^{152}Eu source (see Fig. 4.9a) have energies that range from 122 keV to as high as 1457.6 keV [313]. ^{60}Co and ^{56}Co standard sources, on the other hand, emit intense γ-rays with energies as high as 1332.5 keV [314] and 3451 keV, respectively.

We did not have a ^{56}Co source at hand, and therefore only in Phase I of the experiment did we use a previously irradiated target ladder made of iron, which emitted the same 2598.5-keV [315] γ-ray that emanates from a ^{56}Co source[23]. For Phase II, the ^{56}Fe isotopes of that target ladder had decayed, and thus we had to rely on extrapolating the calibration fit to identify the γ-rays with $E_\gamma > 1.5$ MeV. In both phases of the experiment, the strongest transitions were first identified with the energy calibration from the standard sources, after which the entire detectors' spectra were internally calibrated with these lines and strong ^{30}P transitions. The latter transitions were produce by (^{3}He, p) reaction on the ^{28}Si component of the target.

According to Fig. 4.4 on page 137, the beam could induce various reactions whose cross sections were much more than that of the reaction of interest. Therefore, as seen in Fig. 4.10 on page 162, many radioisotopes, e.g., ^{27}Si, ^{29}Si, ^{30}P, etc., were made, whose de-excitation γ-rays were intense enough to be used as calibration points. The commonly accepted criteria for using a γ-ray's energy as an internal calibration point are: the transi-

[22]The transitions are: $^{152}\mathrm{Eu}(\beta^+)^{152}\mathrm{Sm}^* \overset{\gamma}{\rightsquigarrow} {}^{152}\mathrm{Sm}_{g.s.}$ and $^{60}\mathrm{Co}(\beta^+)^{60}\mathrm{Ni}^* \overset{\gamma}{\rightsquigarrow} {}^{60}\mathrm{Ni}_{g.s.}$.

[23]The transition is $^{56}\mathrm{Co}(\beta^+)^{56}\mathrm{Fe}^* \overset{\gamma}{\rightsquigarrow} {}^{56}\mathrm{Fe}_{g.s.}$.

tion has to preferably have emission probability of, or near, 100% ($M1$ or $E2$ transitions) because such transitions are strong enough such that the statistical uncertainties in their centroids are low, and the probability that their centroids are shifted due to gain shift is small; the transition has to preferably be of energy close to the energy of region of interest in ^{30}S for the final calibration of these γ-rays to be as accurate as possible; and for those γ-rays chosen from the singles γ-ray spectrum of the detector at -135°, the transitions have to be emitted from known excited states with half-lives of higher than 2 ps [250] to minimize the probability of a significant Doppler shift in their centroids.

Some of the γ-rays of ^{30}P satisfy these criteria. While the ^{28}Si(^{3}He, p)^{30}P reaction has a higher cross section than the ^{28}Si(^{3}He, $n\gamma$)^{30}S reaction at this beam energy [165, 316], the background from the former was not a concern because γ-rays from the prompt decay of ^{30}P states were clearly identified in the singles γ-ray spectra. The lines of ^{30}P-related origin did not obscure the γ-rays of interest from the decay of ^{30}S states. Table 4.1 shows the γ-ray energies and the associated parent nuclei used for calibration.

The calibration fit (see Fig. 4.9b) was performed via the Multi Spectra Analyzer software package. The fit was a least-squares linear fit of the form:

$$E_\gamma = a + b \times channel \tag{4.4}$$

where *channel* represents the channel number corresponding to the centroid of a peak, and constants a and b are determined by fitting equation (4.4) to the measured centroids and the known energies of γ-rays from standard sources or the internal calibration points. The fitting program then recalculates the energies of the calibration points from the calibration fit, and outputs the discrepancy (in keV) between the input energies and the energies resulting from the calibration fit. Attention was paid to these discrepancies to ensure that all the calibration points were identified correctly. If this was not the case, the resulting discrepancies were more than 2 keV. For most cases, the discrepancies were below 0.5 keV.

The Multi Spectra Analyzer software package takes the calibration into account when fitting a peak. Therefore, whenever a peak is fitted, the program outputs the peak's centroid, baseline subtracted area, width, and the calibrated energy with the associated uncertainties. This software package treats the calibration points as exact energies, and

Table 4.1: The γ-ray energies used for calibration of the singles γ-ray spectra of the HPGe-detectors. ^{152}Sm, ^{60}Ni and ^{56}Fe result from the β^+ decays of the standard ^{152}Eu, ^{60}Co and ^{56}Co sources, respectively. Their γ-ray energies are taken from Ref. [317], Ref. [314] and Ref. [315], respectively. The energies of ^{30}P are taken from Ref. [187]. The uncertainties are in the last digit(s).

E_γ (keV)	Parent Nucleus	E_γ (keV)	Parent Nucleus
121.7817(3)	^{152}Sm	244.6975(8)	^{152}Sm
344.2785(13)	^{152}Sm	411.1165(13)	^{152}Sm
511.0	Annihilation photons	677.01(3)	^{30}P[a]
708.70(3)	^{30}P	778.9045(24)	^{152}Sm
867.378(4)	^{152}Sm	1085.836(9)	^{152}Sm
1112.074(5)	^{152}Sm	1173.237(4)	^{60}Ni
1212.948(11)	^{152}Sm	1264.57(5)	^{30}P
1332.518(5)	^{60}Ni	1408.011(4)	^{152}Sm
1454.23(2)	^{30}P	1457.643(11)	^{152}Sm
2258.70(10)	^{30}P	2538.95(5)	^{30}P[b]
2598.459(13)	^{56}Fe[c]	3171.69(8)	^{30}P[a]

[a]This level was not used for calibrating the spectrum of the detector at -135°. The corresponding state in ^{30}P has a half-life of less than 2 ps, and thus the centroid was expected to be Doppler shifted.

[b]This state was not a strong transition, but due to its proximity to the energy range of interest, it was used in calibration. The calibration was performed with and without this energy point. The differences were minimal.

[c]This energy was only used for Phase I of the experiment (see text).

thus it does not take into account the uncertainty in the energies of the calibration points. Therefore, the output uncertainty in the calibrated energy is purely due to the statistical uncertainty in the corresponding centroid. The fact that statistical uncertainties in the calibration points were left out did not pose a problem, because as seen in Table 4.1, all the calibration points have very small uncertainties, which if added quadratically with the statistical uncertainties, result in the final uncertainties being identical to the statistical ones.

An example of an energy calibration with standard sources is shown in Fig. 4.9. Although ideally the ADC response is linear with offset $a = 0$ and with the constant b set to 1.5 keV/channel as was discussed in § 4.1.5, detailed energy calibration reveals that the offset is nonzero. It is essential to include the offset to be able to accurately measure the γ-ray energies. This offset becomes particularly important for higher energy γ-rays

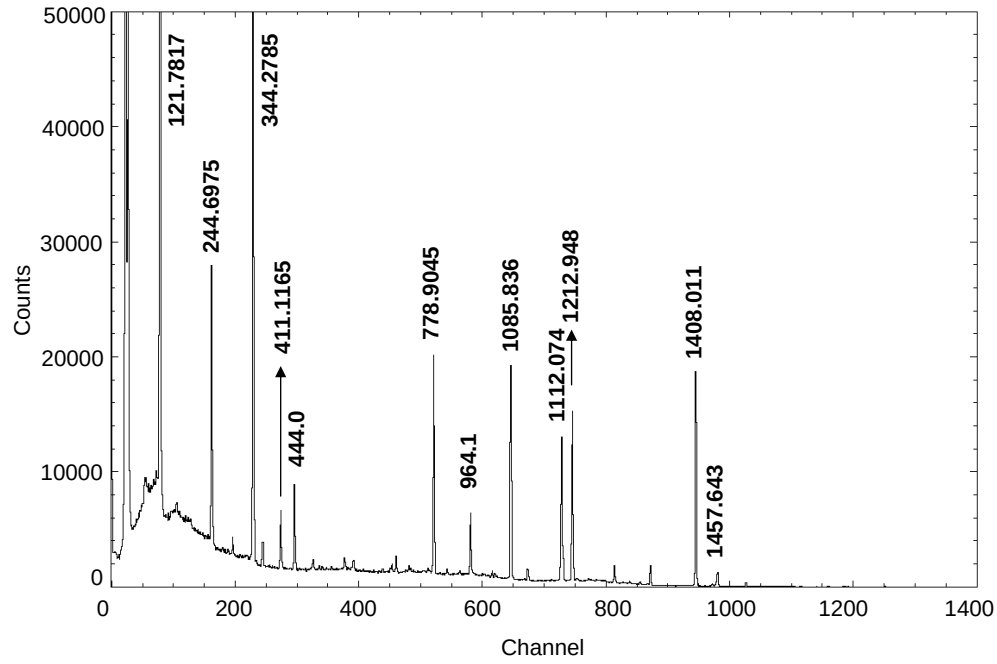

(a)

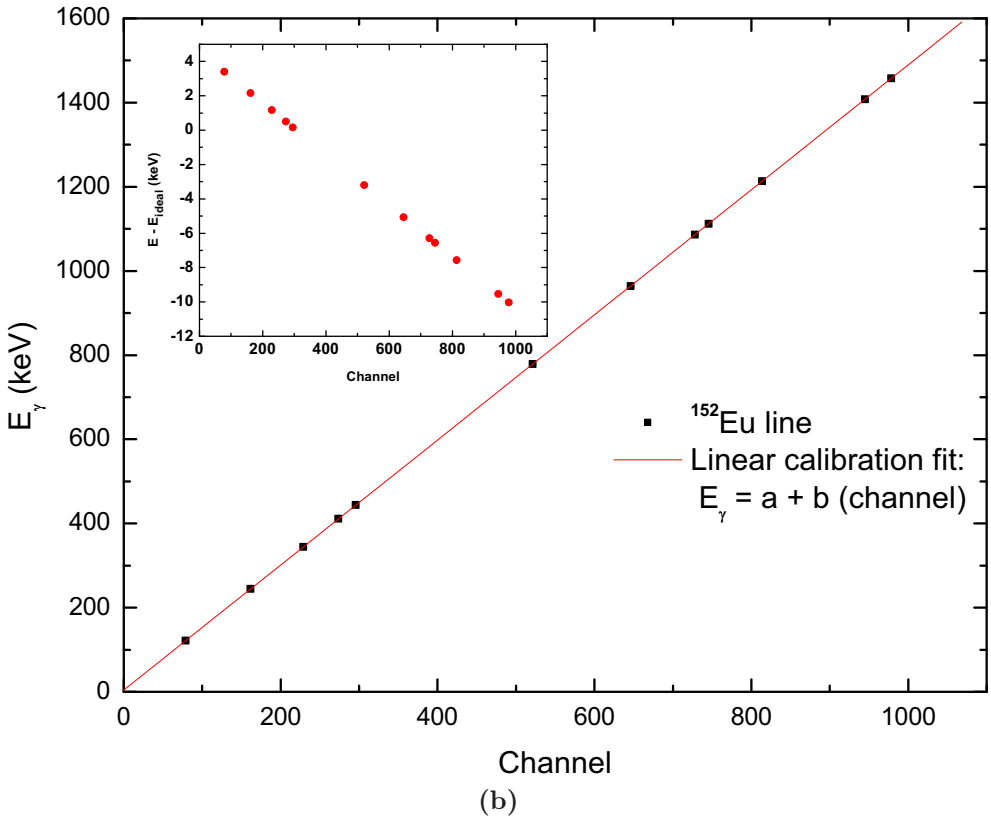

(b)

Figure 4.9: (top) γ-ray spectrum obtained with a ^{152}Eu standard calibration source. The γ-rays are labeled with their energy in keV, and are detected by the HPGe-detector at 90°. (bottom) An example of the calibration fit for the ^{152}Eu standard calibration source. The inset shows the difference between the actual energy calibration, and an ideal ADC response with a = 0 and b = 1.5 keV/channel calibration fit.

(see the inset in Fig. 4.9b).

Finally, with the calibration points presented in Table 4.1 and the fit shown in Fig. 4.9b, the singles γ-ray spectrum of each HPGe-detector was calibrated. A typical spectrum of this kind is presented in Fig. 4.10.

During Phase I of the experiment, both HPGe-detectors were positioned at 90° with respect to the beam axis. Therefore, their singles γ-ray spectra could be added together (see Fig. 4.10) after each detector was separately calibrated.

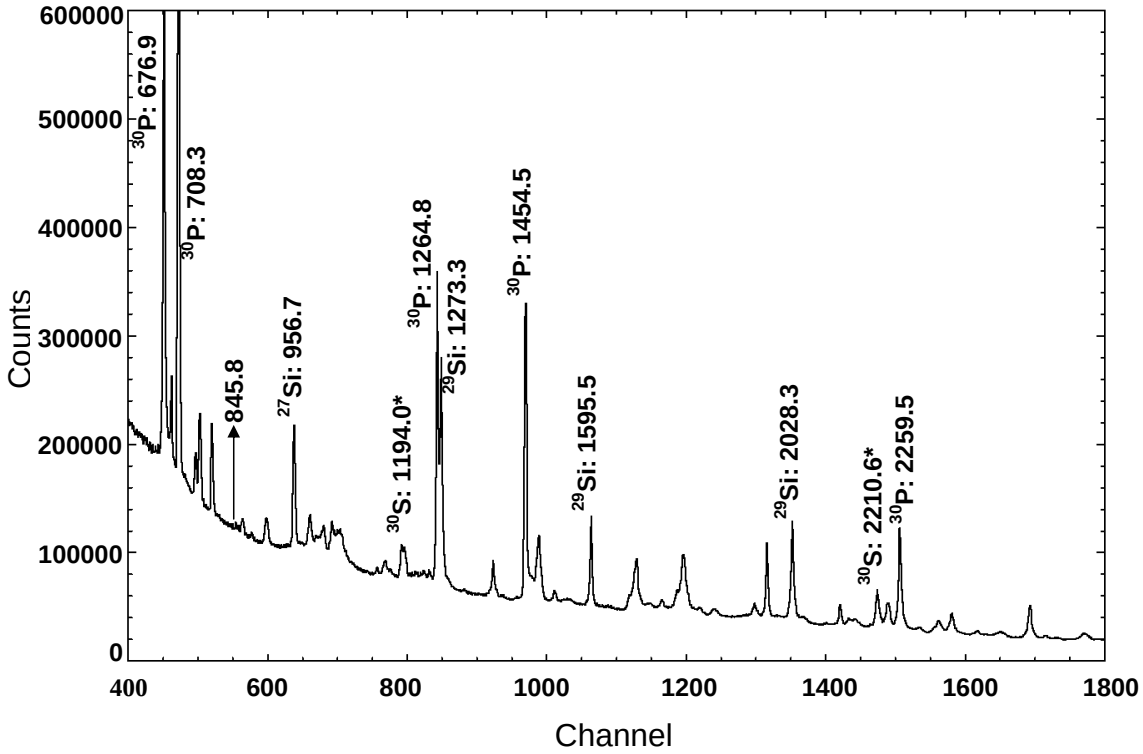

Figure 4.10: The sum of the singles γ-ray spectra from both detectors at 90° resulting from interaction of a ^{3}He beam (E_{beam} = 9 MeV) with the natural Si-target. No lines pertinent to ^{30}S appear below channel 400, and so this region is not shown. Selected strong impurity transitions as a result of competing reactions are identified, and are labeled by their parent nuclei and with γ-ray energies in keV. The 1194-keV and 2210.6-keV peaks originate from levels in ^{30}S (see text), and are labeled with asterisks. The weak transition with energy of 845.8 keV might also belong to ^{30}S (see § 4.3.1).

In the singles γ-ray spectra of both Ge-detectors during each phase of the experiment, two γ-rays were clearly observed at 2210.6 keV and 1194 keV (weighted average energies over angle) that belong to ^{30}S (see Fig. 4.10). From the branching ratios of the low-lying γ-rays of ^{30}S determined in previous γ-ray measurements of Refs. [172, 173], we expected

to see a few γ-rays in the range of 3 MeV. However, these γ-rays did not appear in the singles γ-ray spectra of the present work because most likely they were obscured by the Compton scattered γ-rays from the ^{30}P transitions which appear in the high energy tail of each spectrum or by the intense high energy γ-rays from other nuclei. In hindsight, it would have helped to use an enriched ^{28}Si target, or to use BGO Compton suppression shields around the Ge-detectors.

4.2.4 Determination of Detection Efficiency

In the previous section, it was briefly mentioned that the areas under the peaks are also of paramount importance as they tell us about the number of photons that are emitted with a particular energy, and thus the intensity of the associated γ-rays.

To calculate the intensity of a γ-ray, we first need to know the detection efficiency at that particular energy because the detection efficiency is one of the limiting factors in detecting γ-rays. All the discussion that follows is relevant to the HPGe-detectors as no efficiency measurement was performed to determine the detection efficiency of the liquid scintillator used in Phase I of the experiment.

The detection efficiency is generally defined as the ratio of the response of a detector to the value of the physical quantity that is measured [306] (p. 206). Therefore, for our discussion, where the quantity of interest is the emission rate of γ-rays with a specific energy, the detector response would be how many of such γ-rays are detected. The efficiency is usually calculated and quoted for the full-energy-peak, which refers to the peak in a spectrum corresponding to a γ-ray that has deposited all its energy in the detector, and thus has not escaped or scattered out of the detector.

The intrinsic efficiency of the full-energy-peak is defined as [306] (p. 206):

$$\epsilon(E) = \frac{n(E)}{R(E)} \tag{4.5}$$

where $n(E)$ is the number of counts in a peak corresponding to a detected photon of energy E divided by the measuring time, and $R(E)$ is the rate at which photons of energy E impinge on the detector surface. From this definition, it is clear that the intrinsic efficiency depends on the angular distribution of the incident photons. Therefore, when the detector does not cover full 4π sr solid angle around the source, it is necessary to

measure the solid angle subtended by the detector. This is already explained in the details given earlier.

From equation (4.5), it is also evident that the intrinsic efficiency of a detector depends on the size of the detector, and its distance to the source and the energy of the detected photon. Hence, the efficiencies quoted earlier in this chapter relative to a specific size NaI(Tl) detector are essentially useless for our purposes. Instead, one has to determine the efficiency of each detector as a function of photon energy for the specific geometry at which that detector was located during the experiment. This requires calibration of the detection efficiency.

For the purpose of calibrating the efficiency curve of each detector, the standard secondary[24] calibration source of ^{152}Eu was used before and after the experiment. This source was positioned inside the target chamber in identical geometry to that of the actual experiment with the beam. As mentioned earlier, ^{56}Co was unavailable, and the ^{152}Eu source does not provide β^+-delayed γ-rays with energy higher than 1.5 MeV. Therefore, we had to rely on extrapolation of the efficiency curves to the higher energies to obtain the efficiency of each HPGe-detector for the γ-rays of ^{30}S with energy higher than 1.5 MeV.

An important factor for calibrating the efficiency of a detector as a function of photon energy is that the count rates for calibration runs must be at a reasonable level. Low count rates cause undesirable statistical uncertainties in finding the areas under the peaks corresponding to calibration γ-rays, while high count rates give rise to pulse pile-up and increase the deadtime so that the number of counts in the peaks are reduced. Therefore, the calibration sources' activity must not be too high.

For a standard calibration source with an activity A at the time of measurement, equation (4.5) can be rewritten as [1] (p. 262 and 276):

$$\epsilon(E) = \frac{N_{\text{peak}}}{At\,\dfrac{I_\gamma}{100}\,\dfrac{\Omega}{4\pi}} \tag{4.6}$$

where $\epsilon(E)$ is the efficiency of a detector that subtends the solid angle Ω, N_{peak} is the number of counts under the full-energy peak corresponding to a photon of energy E, t is

[24] See Ref. [306] (p. 211 – 212) for the definition of a secondary calibration source.

the time duration of the calibration run, and I_γ is the absolute intensity of the photon under investigation, divided by 100 to account for percentage. The absolute intensity is expressed as the number of γ or electron capture $E0$ transitions per 100 β-decay of the parent nucleus. In our case this nucleus would be ^{152}Eu. Such intensities are tabulated for γ-rays of the ^{152}Eu standard source in Ref. [317]. The uncertainty in the detection efficiency of each photon can be simply calculated from error propagation methods using equation (4.6). Such uncertainties are mainly due to the statistical uncertainties in determination of areas under each peak, as well as the uncertainties in the measured absolute intensities. The resulting uncertainties in the detection efficiencies for ^{152}Eu γ-rays were very small, and amounted to much less than 1%.

Detector efficiency calibration measurements yield a set of efficiency values at specific γ-ray energies. The next step is to use this set and obtain a calibration efficiency curve which can be fitted with an analytical function, from which the efficiency of that particular detector can be estimated for any γ-ray from another source with an intermediate energy.

Various fitting functions are used in the literature for this purpose (see Table 4.2 on p. 223 of Ref. [306]). However, the most popularly used analytical function which is used to fit the calibration efficiency curve is [235] (p. 449):

$$\ln \epsilon(E) = \sum_{i}^{N} a_i \left(\ln \frac{E}{E_0} \right)^{i-1} \tag{4.7}$$

where $\epsilon(E)$ is the intrinsic efficiency, E_0 is introduced to make the argument of the logarithm dimensionless and can be set equal to 1 keV [306] (p. 220), a_i are constants given by the fitting routine, and N can only be as high as 3 because increasing N to larger values causes unrealistic oscillations. Equation (4.7) is reasonably valid for photon energies between 60 keV to 3 MeV[25], which covers the energy range of interest in this work.

The parameters a_i and their uncertainties are obtained after the fit is performed. However, Ref. [306] (§ 4.2.1.3) discusses in detail why the fitting function and its resulting parameters alone cannot be used to calculate the uncertainty in the detection efficiency of a photon, for which the efficiency has to be calculated from the calibration fit. The uncertainty for such an efficiency value is instead estimated in the aforemen-

[25]For the fits to efficiency curves outside this range, see Ref. [306] (Chapter 4).

tioned reference to be 0.5% in photon energy range from 120 keV to 1.5 MeV, and at least 1% for γ-ray energies between 1.5 – 3 MeV. These values are therefore adopted for the photon energies of interest in this work.

To perform the efficiency calibration fit, a data analysis and graphing software application called Origin [318] was used. It has a built-in fitting function of the form $y = \exp(a + bx + cx^2)$, which is exactly identical to equation (4.7) with $y = \epsilon(E)$; $N = 3$; $x = \ln(E/E_0)$, where $E_0 = 1$ keV; and constants a, b and c that are equivalent to the a_i coefficients with $i = 1$, 2 and 3.

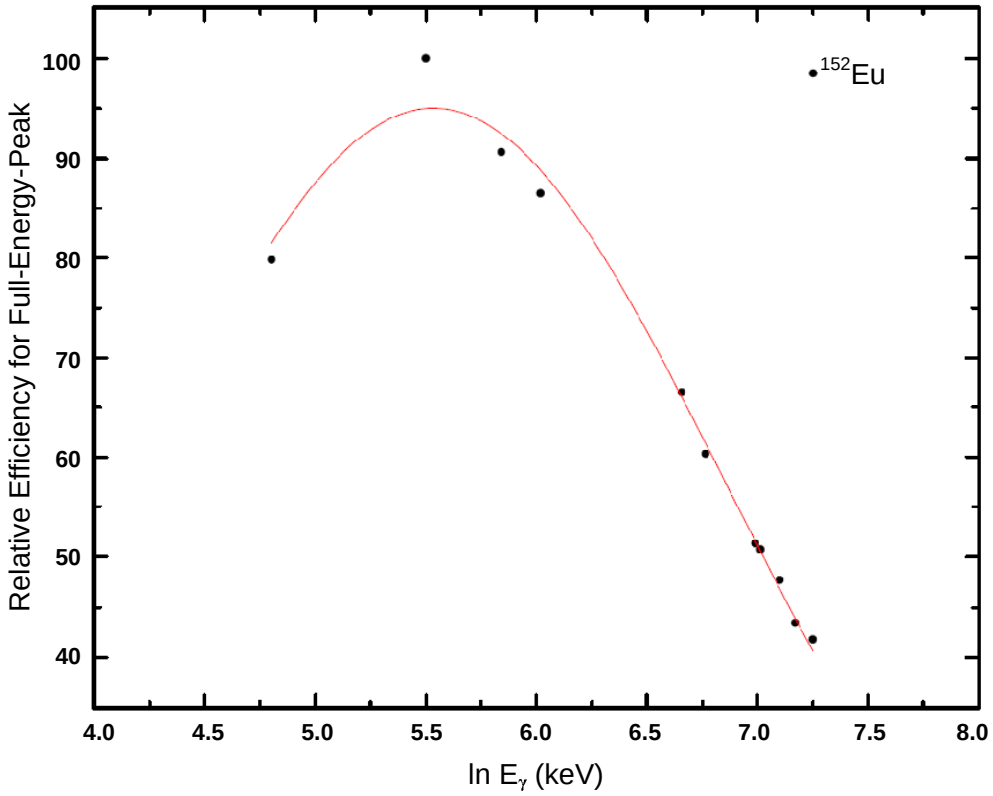

Figure 4.11: Detection efficiency calibration curve for the HPGe-detector at -90° during Phase I of the in-beam γ-ray experiment is shown. The red curve is the calibration fit. The ^{152}Eu source was placed inside the target chamber. Among the β^+-delayed γ-rays emitted from the standard ^{152}Eu source, the highest efficiency of 0.039 was achieved for the 244.7-keV γ-ray. Therefore, the diagram shows the efficiency of all other β^+-delayed γ-rays normalized to a relative efficiency of 100% at $E_\gamma = 244.7$ keV.

This analysis was performed separately for each of the HPGe-detectors that were used in our experiment during the first and the second phases of the experiment. Fig. 4.11

presents a typical efficiency calibration curve and the calibration fit. From such fits, the detection efficiency of ^{30}S γ-rays were determined for each HPGe-detector.

Once the detection efficiency for a particular γ-ray is found, the intensity of that γ-ray can be calculated. This is the next subject of discussion.

4.2.5 Gamma Ray Intensities and Branching Ratios

The total yield of a peak corresponding to a γ-ray transition in a spectrum is the number of counts underneath that peak or simply the area obtained from fitting the peak.

The relation between the areas under the peaks and γ-ray intensities is:

$$I_\gamma = \frac{Y}{\epsilon_{\text{int}}(E)} \tag{4.8}$$

where I_γ is the intensity representing the number of radiation quanta emitted by the source with specific characteristics, e.g., energy and multipolarity; Y is the yield or number of events under the full-energy peak in the spectrum; and $\epsilon_{\text{int}}(E)$ is the intrinsic detection efficiency for the corresponding γ-ray. The solid angle correction must only be taken into account if the absolute intensity per nuclear decay is desired, in which case the angular distribution of the radiation has to be known. This is not the case for our experiment. Hence, it is not necessary to correct for the solid angle subtended by the detector because the detector geometry stayed the same for the runs of interest and the efficiency calibration runs. Therefore, the intensities calculated from the above formula are at a specific detection angle.

To obtain the angle-integrated intensities, one must either place the detector at 55° (see § 4.3.2) or the angular distribution of the γ-rays of interest must be determined.

The uncertainties in the intensities were calculated from:

$$\delta(I_\gamma) = I_\gamma \sqrt{\left(\frac{\delta Y}{Y}\right)^2 + \left(\frac{\delta\epsilon_{\text{int}}(E)}{\epsilon_{\text{int}}(E)}\right)^2} \tag{4.9}$$

where δ is the uncertainty in each parameter. Therefore, the preliminary intensities calculated from the above formula are dimensionless numbers. In γ-ray spectroscopy, it is customary to report the intensities as percentages. Hence, the preliminary intensities of

γ-rays originating from the same nucleus are usually normalized to that of the strongest γ-ray in the whole decay scheme[26], which is considered to be 100%. Such a relative intensity is thus a measure of the strength of each γ-ray compared to that of the strongest γ-ray in the whole decay scheme, which is usually the γ-ray emanated from the decay of the first excited state to the ground state.

Many excited states in a nucleus however decay to more than one low-lying state via γ-ray emission. Therefore, it may be required to know the strength of a particular branch among all possible decay branches from the same excited state. As a consequence, another quantity called branching ratio is defined, which is strongly correlated with the γ-ray relative intensity.

The total probability of decay via γ-emission, Γ_γ, of an excited state can be expressed as the sum of individual partial γ-ray widths for that state. The latter quantity represents the probability of transition to a specific final state j. Thus [1] (p. 54):

$$\Gamma_{\gamma,\mathrm{tot}} = \sum_j \Gamma_{\gamma,j} \tag{4.10}$$

where $\Gamma_{\gamma,j}$ are the partial γ-ray widths. The branching ratio $B_{\gamma,j}$ is then defined as [1] (p. 54):

$$B_{\gamma,j} = \frac{\Gamma_{\gamma,j}}{\Gamma_{\gamma,\mathrm{tot}}} \times 100\% \tag{4.11}$$

In many experiments, however, the quantities $\Gamma_{\gamma,\mathrm{tot}}$ and partial widths $\Gamma_{\gamma,j}$ (in eV) are not determined directly. In such cases the branching ratios are obtained from the relative intensities of each branch.

Under the assumption that all the decay branches via γ-ray emission of a particular excited state are observed, one can re-normalize the relative intensities of those branches to that of the strongest branch. As a result, instead of considering the intensity of the strongest γ-ray in the whole decay scheme of the nucleus to be 100%, the decay branches of each excited state are treated separately. Therefore, among all possible decay branches of a specific excited state, the γ-ray with the highest relative intensity is considered to have a branching ratio of 100%. Then the relative intensities of all other branches of the same excited state are re-normalized to 100% to obtain the branching ratio of each

[26]The γ-ray decay scheme shows a series of γ-ray cascades that together illustrate how the excited states of a nucleus decay via γ-ray emission.

branch.

Quite often, a particular branch is weak enough such that it is not observed in an experiment. Therefore, due to a missing branch, it is not possible to add all the relative intensities of different branches to perform the re-normalization. In such cases, one would have to assume that the branching ratio of the missing branch is equal to that of the mirror branch in the mirror nucleus [285].

4.2.6 Background γ-ray Spectrum

In any γ-ray measurement, the singles γ-ray spectra always contain at least a few γ-rays that are called background. They are produced either by interactions of the cosmic rays with detector material; activation of the materials irradiated by the beam or the light reaction products, specially neutrons during the beamtime; or by the natural background radioisotopes that exist in the laboratory, such as the 2614.5-keV β^--delayed γ-ray line of ^{208}Tl or the 1460.8-keV β^+-delayed γ-ray line of ^{40}K from the $^{208}\mathrm{Tl}(\beta^-)^{208}\mathrm{Pb}^* \overset{\gamma}{\rightsquigarrow} {}^{208}\mathrm{Pb}_{g.s.}$ and $^{40}\mathrm{K}(\beta^+)^{40}\mathrm{Ar}^* \overset{\gamma}{\rightsquigarrow} {}^{40}\mathrm{Ar}_{g.s.}$ transitions, respectively.

It is advisable to identify these γ-rays to decide whether or not to suppress them. In our experiment, to estimate the level of natural radioactivity in the lab, and to identify the strong background transitions that could be present in the spectra of interest, two relatively short background runs without any standard source, target, or beam were taken when the electronics were in singles mode, and two such runs were obtained when the electronics were in coincidence mode. These runs were obtained after the experiment; however, such runs usually need to be taken both prior to, and after the experiment.

A typical background spectrum is shown in Fig. 4.12. This spectrum was obtained at the end of the beamtime, and thus the prompt and β-delayed γ-rays from copper and zinc isotopes are due to activation of stable isotopes in the copper pieces in front of each detector (see § 4.1.2) by neutrons produced by the beam interaction with the target. The other lines are from natural radioactivity originating from the radium and thorium decay chains or from ^{40}K and ^{208}Tl β-delayed γ-rays. No attempt was made to subtract the background spectra from the spectra of interest, because none of the background γ-rays interfered with the γ-rays of interest.

In order to suppress the unwanted γ-rays, γ-γ coincidence measurements were performed.

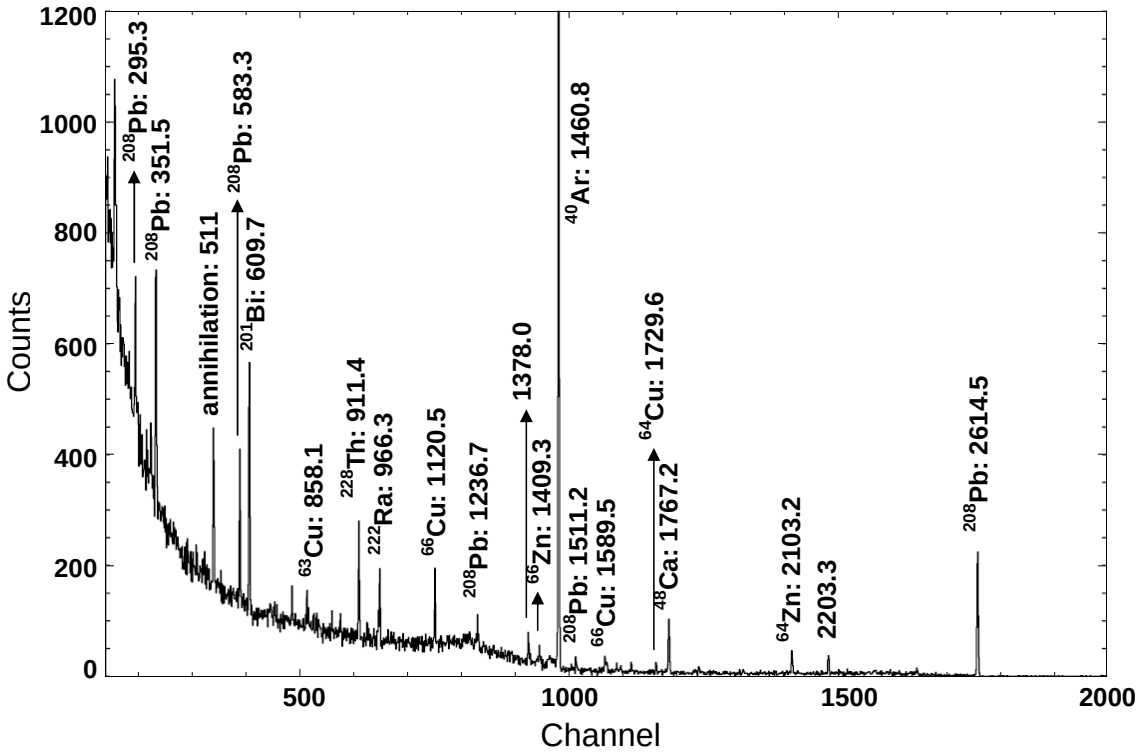

Figure 4.12: A portion of a typical background γ-ray spectrum. The γ-rays are identified after calibration with a ^{152}Eu standard source. They are labeled by their energy in keV and by their parent nucleus. Some have been left unidentified, in which case only an energy (in keV) is shown.

4.2.7 Coincidence Spectroscopy

Not much can be said of nuclear structure using individual γ-rays in a singles spectrum. Therefore, of the various techniques available in γ-ray spectroscopy, coincidence experiments are the most useful. The most common experiments of this type are γ-γ coincidence measurements.

There can be several decay paths to or from the same level; however, two γ-rays feeding or de-exciting the same level will not be in coincidence with each other. Hence, in γ-γ coincidence measurements pairs of γ-rays from the same cascade, connecting two states via one or more intermediate states, are detected simultaneously in two different detectors. Such cascades correspond to one of many decay pathways between levels of the nucleus, and thus the pair of γ-rays that are in coincidence can determine the decay pathways, which lead to the determination of the level structure of the associated nucleus.

Also, the coincidence data can be used to identify previously unknown γ-rays. If two γ-rays are detected in coincidence, they are most likely emitted from the same decaying nucleus (assuming that the accidental coincidences are mostly suppressed). Hence, detecting an unknown γ-ray in coincidence with a previously known γ-ray is enough to firmly establish the origin of that unknown γ-ray. Even if there is no previously known γ-ray, coincidence measurements can still be used to determine all γ-rays which belong to the same nucleus.

Another big advantage of a coincidence experiment is the elimination of certain unwanted or unnecessary data, which can obscure the data of interest. Such elimination is caused because in coincidence measurements only the simultaneous events are recorded, where the actual simultaneity is defined by the response time of the detectors and the electronics used. In our experiment, two events were considered to be in coincidence (simultaneous) if they were detected within 144 ns from each other. This time window must not be too long to avoid the random accidental coincidences that cause background in the coincidence spectra. It should also not be too short such that the true events are not recorded.

As an example of this advantage, one can think of the cases where the γ-rays from a nucleus have energies that are unresolved from stronger lines of a different nucleus. γ-γ coincidences can help clean up the spectrum from the unwanted γ-rays. In Phase I of our experiment, the neutrons emitted from the (^{3}He, n) reactions on the target were used to eliminate from the data those γ-rays produced in the reactions which evaporated only charged particles and no neutrons. This was done by requiring a neutron to be in coincidence with any γ-ray detected. Any γ-ray not associated with a neutron emission would then not be present in the n-γ coincidence spectra.

This is advantageous in two important ways. First, the absence of a large number of γ-rays will reduce the cluster of peaks in the spectra, making it easier to analyze the peaks of interest. This can also be an effective way of resolving two γ-rays which would otherwise appear as one. Second, the peak-to-background ratio of the γ-rays under study will be considerably enhanced due to the elimination from the background of Compton events from the γ-rays associated with the charged particle reactions.

However, as shall be seen later the n-γ coincidence measurement did not teach us anything more than what was already known. Therefore, in Phase II of the experiment,

only γ-γ coincidence techniques were used to assemble the decay scheme of ^{30}S.

Perhaps the only disadvantage of the coincidence measurements is their reduced count rates, thus necessitating longer experiments in order to collect sufficient data.

4.2.7.1 Coincidence Matrices

Coincident γ-rays were detected by two HPGe-detectors placed at $\pm 90^\circ$ (with respect to the beam axis) for Phase I and at 90° and -135° for Phase II of the experiment. Neutrons were detected during Phase I via the liquid scintillator placed at 40° with respect to the beam axis. All detectors and the target were in one plane. The coincidence analyses were performed via construction of γ-γ and n-γ coincidence matrices.

- **γ-γ Coincidence Matrix:**

To understand the basics of the coincidence matrix, Fig. 4.13 demonstrates an example in which a model decay scheme (on the left) consists of three paths through which the highest energy excited state decays to the lowest energy state: a cascade containing γ-rays with energies $E_{\gamma,3}$, $E_{\gamma,2}$ and $E_{\gamma,1}$; another cascade containing γ-rays with energies $E_{\gamma,4}$, $E_{\gamma,5}$ and $E_{\gamma,1}$; and a decay path containing only one γ-ray with energy $E_{\gamma,6}$.

Therefore, a E_γ-E_γ coincidence matrix can be constructed (the right side of Fig. 4.13) with energies of γ-rays detected by one detector placed on the abscissa and those of γ-rays detected by the other detector placed on the ordinate. Each matrix element (black circles on the right side of Fig. 4.13) then indicate a coincidence event between two γ-rays, and thus presence or absence of a particular matrix element implies which γ-rays are in coincidence with each other.

It is immediately obvious that $E_{\gamma,6}$ is not in coincidence with any γ-ray, which means that this γ-ray will only be observed in the singles γ-ray spectrum of each detector assuming that both detectors have reasonable detection efficiency at that energy and that its intensity is not too weak. Therefore, this γ-ray will not appear in the γ-γ coincidence spectrum.

Another fact that may not be so obvious is that this matrix is symmetric with respect to the diagonal blue dashed line in Fig. 4.13 only if both detectors are at the same angle with respect to the beam axis or if all energies from both detectors are corrected with

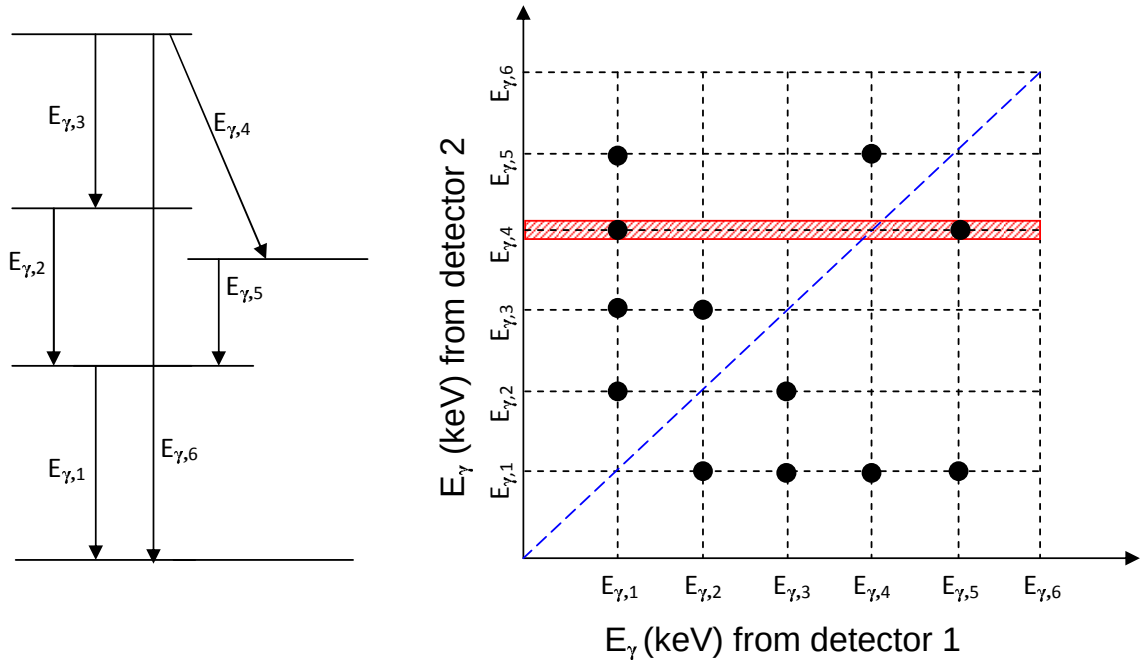

Figure 4.13: An imaginary decay scheme is shown on the left. The corresponding coincidence matrix is shown on the right with the coincidence peaks indicated by black filled circles. The red diagonally-shaded region corresponds to the coincidence gate around the γ-ray with energy $E_{\gamma,4}$, detected by detector 2. It is assumed that the energies are not Doppler shifted, and thus the matrix is symmetric.

respect to the Doppler shift[27]. To understand why this is the case, assume that $E_{\gamma,1} = 1$ keV and detector 1 is at 90°, where no Doppler shift in energy occurs, while $E_{\gamma,2} = 2$ keV and detector 2 is at -135°, where the energies might be Doppler shifted. As a result, while the 1-keV γ-ray from detector 1 is in coincidence with the 2-keV γ-ray from detector 2, the γ-ray, whose energy is 2 keV from detector 1 is not necessarily in coincidence with a γ-ray detected by detector 2, whose energy is 1 keV, because this latter energy may also be Doppler shifted, when detected at -135°. So as long as the energies are not corrected for Doppler shift prior to the construction of the matrix, it may not always be symmetric.

For our experiment, each gain-shift-corrected one-hour-long run containing the raw data, obtained while the electronics were in coincidence mode, was sorted offline via a sort routine written in C. This code then stored the γ-γ coincidence events from each run into a matrix of 4096 channels $\times$ 4096 channels[28] by placing the γ-rays detected by one HPGe-detector on the x-coordinate and those detected by the other HPGe-detector on

[27]This phenomenon is explained in the next section.
[28]The ADC had 4096 channels.

the y-coordinate. In the meantime, the calibration fit of each individual HPGe-detector was read into the sort routine, and thus every channel form each detector was at the same time converted to an energy based on the corresponding calibration fit. Thus, these individual E_γ-E_γ coincidence matrices corresponding to each run were then added together to construct a final matrix containing all the raw data.

This matrix was then projected to both x- and y-coordinates using another software included in the Multi Spectra Analyzer software package. Each of these projections is a 1D counts *vs.* channel (or equivalently energy) histogram that shows the singles γ-ray spectrum of the detector placed at that axis.

The coincidence relationship in the matrix is examined by setting a gate on an individual transition energy upon viewing a preferred matrix projection. This gate is a slice in energy that defines the region of interest for coincidence determination. It is the two-dimensionality of the matrix (y *vs.* x or E_γ *vs.* E_γ) that allows the experimenter to take a slice from the matrix in one dimension, and project that region to the other dimension to see what energies are in coincident with the events inside the gate region. This is illustrated in Fig. 4.13 by the red diagonally-shaded region corresponding to the coincidence gate. This gate is around the γ-ray with energy $E_{\gamma,4}$, detected by detector 2. Once this gate is projected onto the abscissa, a one dimensional counts *vs.* energy (or channel) histogram will be obtained that contains all the γ-rays that are in coincidence with the γ-ray on which the gate was set. It is obvious that this histogram will contain two peaks at energies $E_{\gamma,1}$ and $E_{\gamma,5}$.

However, apart from the true coincident events, the resulting spectrum also contains events that are possibly in coincidence with the smooth background of Compton scattered γ-rays on which the gated γ-ray sits. Therefore, it is essential to find and subtract the background.

The latter process is performed as follows: for each peak of interest in the singles spectrum of a detector (a matrix projection), one energy region defines the peak gate, and two energy slices from the smooth tail of the peak on its both sides shall be defined as the background gates. The sum of the widths of both background gates ideally should be equal to the width of the peak gate; however, it is not necessary that both background gates have identical widths although that would also be ideal.

When a peak is isolated, this process is very easy. However, when the peak is in a

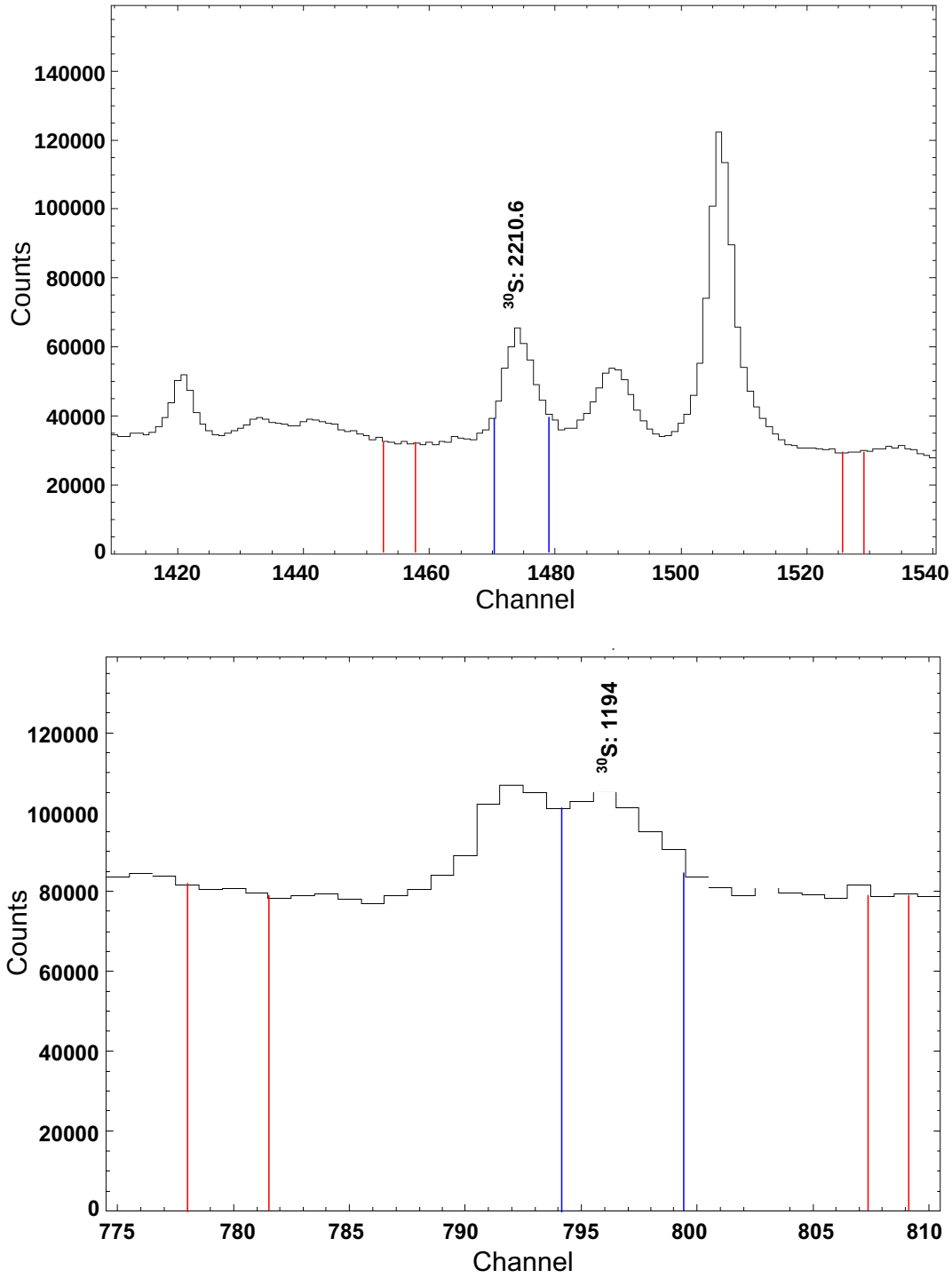

Figure 4.14: Shown above are the peak gates (in blue) and background gates (in red) on the peaks of interest in ^{30}S corresponding to the γ-rays at (top) 2210.6 keV and (bottom) 1194 keV from the singles γ-ray spectrum of the detector at 90°. Both these γ-rays are observed in the singles γ-ray spectra of both Ge-detectors. The 1194-keV γ-ray is partly obscured by another peak, the origin of which is explained in the text (see § 4.3.1).

cluster of peaks close to each other, defining the background gates can be tricky because if the background gate contains some portion of another contaminant peak in the vicinity of the peak of interest, then a lot of unwanted γ-rays are introduced to the gated coincidence spectrum that would make the analysis difficult. It is advisable that in such situations, the background gates are drawn on smooth regions as close as possible to the peak of interest. Fig. 4.14 shows an example of the gates drawn on a γ-ray of ^{30}S that was observed in the singles γ-ray spectra of both detectors.

The generated E_γ-E_γ matrix is a binary file, in which sequential information (the raw data) is stored in a multidimensional array. Binary data are often stored by row, i.e., the column varies most often. Therefore, in old generation computers it would take less computational time to read the matrix across the rows than down the columns. Nowadays, this does not matter anymore. However, in UTTAC the matrices are still read only across the rows. Hence, we also followed the same procedure, and always set the gate on the spectrum that is from the detector placed on the ordinate of the matrix such that the gate is a horizontal slice on a selected row in the binary file as shown in Fig. 4.13. In order to gate on a γ-ray that is observed in the spectrum from the detector placed on the abscissa of the matrix, the matrix is first reversed, such that its newly defined y-coordinate is its old x-coordinate.

In Phase I of our experiment, a gate was made separately along the y-dimensions of the matrix and its reversed matrix on every γ-ray of ^{30}S that was observed in singles γ-ray spectra (the 1194-keV and 2210.6-keV peaks in Fig. 4.10), and the resulting gated coincidence spectra were thus obtained from both detectors. These spectra were added together for the first phase of the experiment because both Ge-detectors were positioned at identical angles. So it did not really matter which detector was selected to be on the y-axis. For Phase II, however, the γ-rays in the singles spectrum of the detector at -135° were Doppler shifted, and as a result the gated coincidence spectra could not be added together. Therefore, it was decided that the γ-rays detected by the HPGe-detectors with 70% and 50% relative efficiencies were placed on the x- and y-axes, respectively, and the gate was made only on the peaks of interest from the detector on the y-coordinate. Being much closer to the target, this detector offered much better statistics, and thus the gate was defined more precisely. The resulting coincidence spectrum then included the γ-rays detected at -135°, which were Doppler shifted. The Doppler shift correction is described

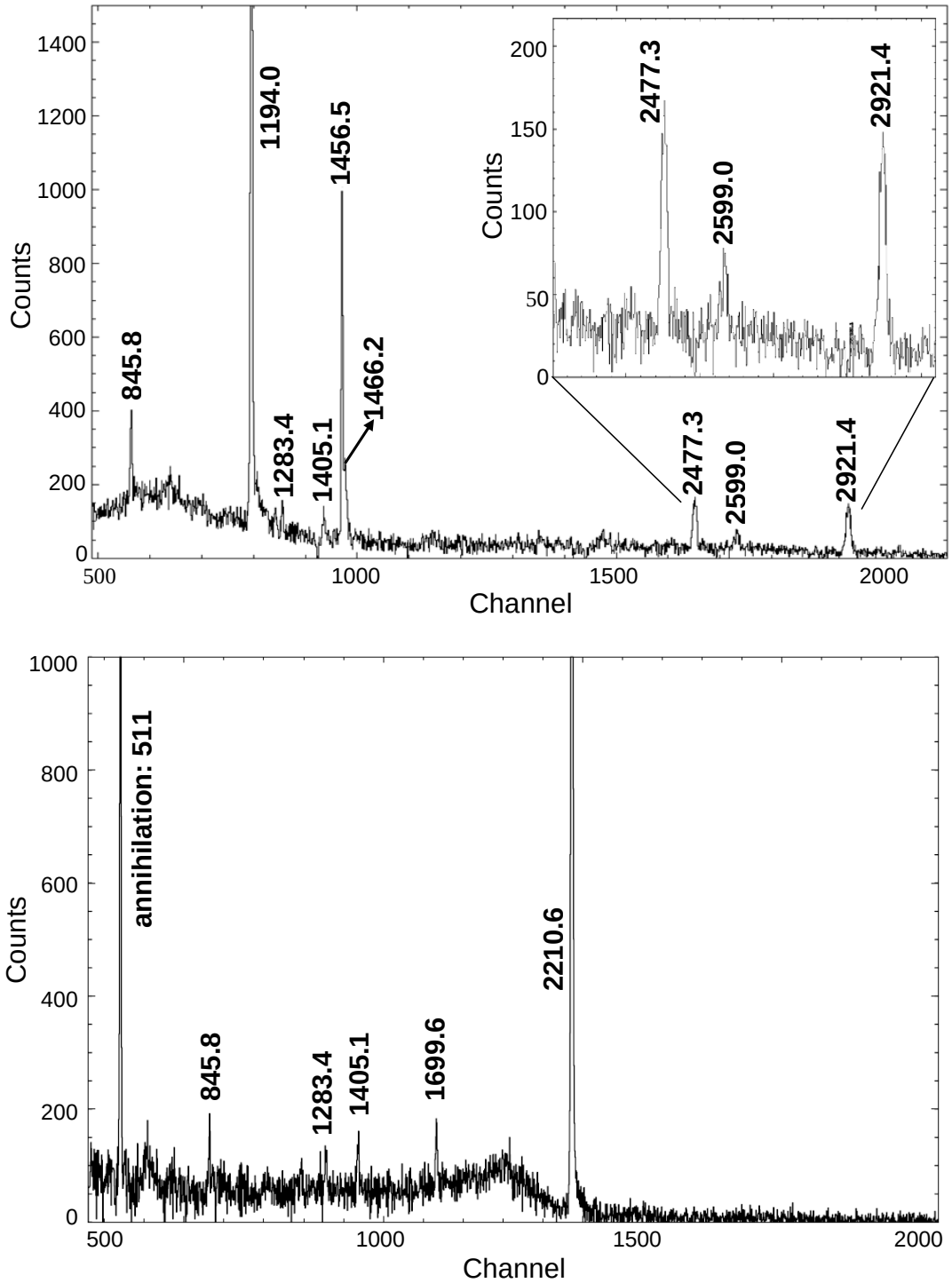

Figure 4.15: γ-γ coincidence spectra measured at 90° obtained from gating on the (top) 2210.6-keV and (bottom) on the 1194-keV transitions of ^{30}S measured in turn at -90°. Peaks corresponding to the transitions from known ^{30}S states are labeled with weighted average energies from the present work (in keV). For more information on the energies, see § 4.3.1.

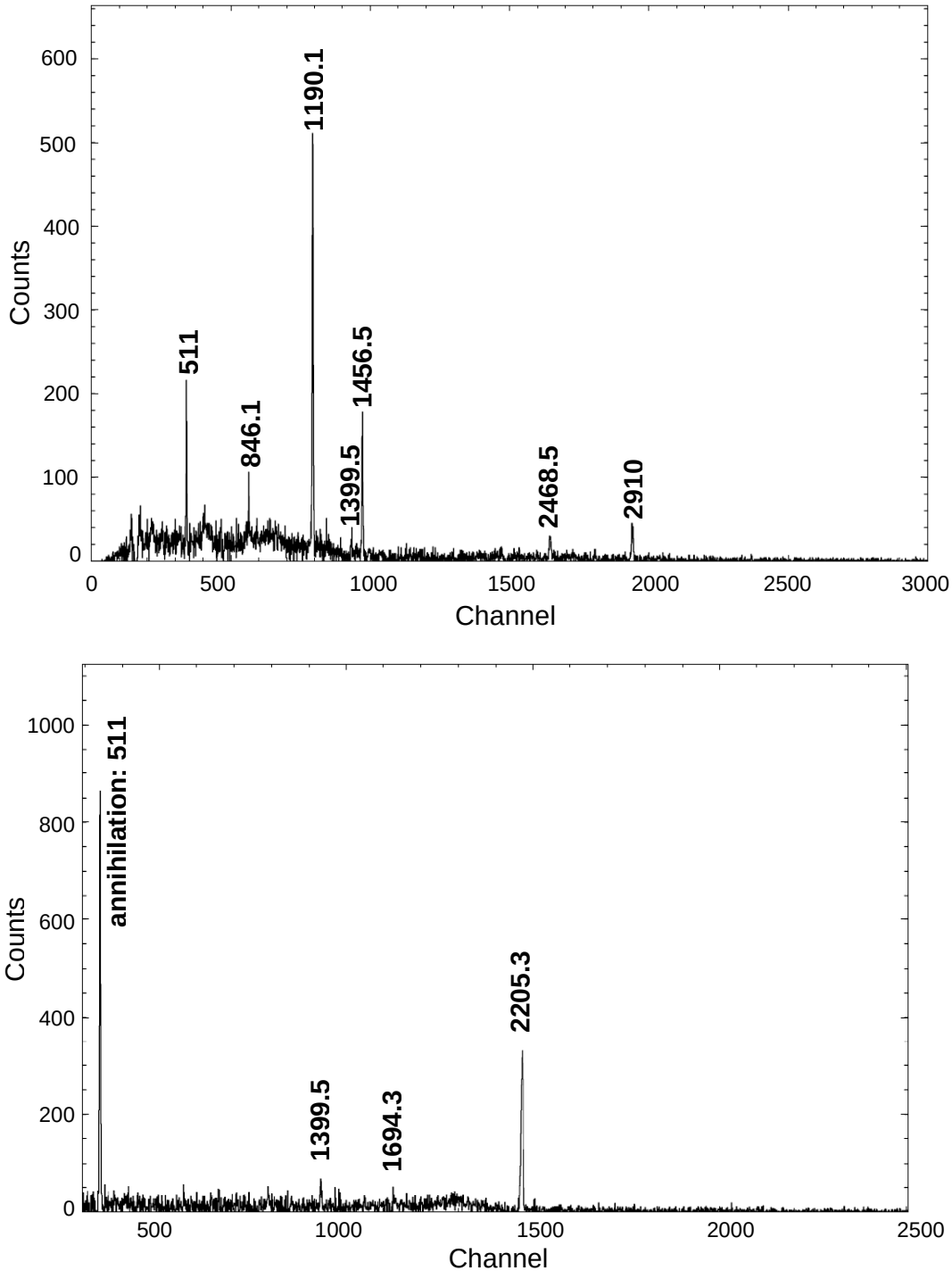

Figure 4.16: γ-γ coincidence spectra measured at -135° obtained from gating on the (top) 2210.6-keV and (bottom) on the 1194-keV transitions of ^{30}S measured in turn at 90°. Peaks corresponding to the transitions from known ^{30}S states are labeled with their Doppler shifted energies from the present work (in keV) (see § 4.3.1). The energies shown on these figures are not yet corrected for Doppler shift.

in the following section.

Finally, Figs. 4.15 and 4.16 respectively show the γ-γ coincidence spectra measured at 90° and -135° obtained from gating on the 2210.6-keV and 1194-keV peaks of ^{30}S. These spectra reveal several additional transitions from ^{30}S states that are in coincidence with the gated γ-rays. Such coincident γ-rays are not observed in the singles spectra perhaps because they are masked by the strong transitions from other nuclei.

The γ-rays that are observed in the coincidence spectra are discussed in detail in § 4.3.1.

- ***n*-γ Coincidence Matrix:**

The reaction channel can be confirmed by requirement of the n-γ coincidence. Prior to construction of the n-γ matrix, the neutron peak was checked from the liquid scintillator's individual one-hour-long runs to correct for any shift in the peak. These runs were then added together. The n-γ coincidence matrix is constructed in the same way as the γ-γ coincidence matrix, except that the ordinate is a time axis corresponding to the time acquired from the TAC for the neutron detector, and the abscissa contains the sum of all those events that were in coincidence with neutrons, and were detected by each Ge-detector. The coincident gate was set around neutrons, and the events in this gate were then projected onto the x-coordinate to obtain the γ-rays' energy spectrum. This spectrum is shown in Fig. 4.17.

The above spectrum contains those γ-rays detected by both the 70% and 140% relative efficiencies Ge-detectors during Phase I of the experiment. As seen in Fig. 4.17, the statistics under each peak is low, and moreover, only those γ-rays corresponding to the de-excitation of the bound states in ^{30}S are observed. Therefore, as all the γ-rays emanating from the bound states of ^{30}S have been previously measured [172, 173], and because no γ-ray from the resonances in ^{30}S are observed in the n-γ coincidence spectrum, this detector was not used again.

Due to very low statistics under the neutron peak, no further n-γ-γ coincidence could be achieved. The low statistics of neutrons were attributed to the degradation in the liquid scintillator efficiency due to radiation damage over time, prior to our experiment.

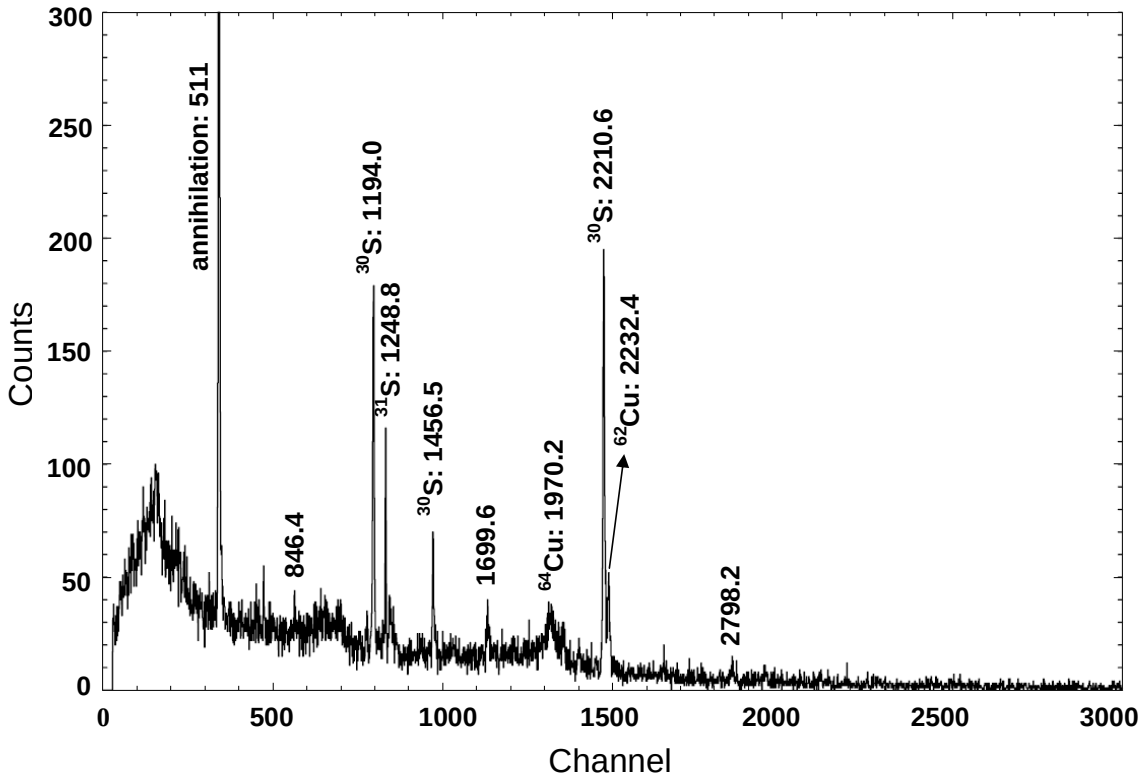

Figure 4.17: n-γ coincidence spectrum obtained by gating on the neutron peak in the spectrum of the liquid scintillator during Phase I of the experiment. The γ-rays are labeled with their parent nucleus and their energy in keV. The origin of the 2798.2-keV γ-ray is unknown, while the γ-ray with energy of 1699.6 keV is from the single escape of the 2210.6-keV γ-ray of ^{30}S, which is the transition connecting the first excited state to the ground state in ^{30}S. The 1248.8-keV γ-ray is originated from the ^{29}Si(^{3}He, $n\gamma$)^{31}S* reaction.

4.2.8 Doppler Shift Correction

According to momentum conservation laws, the reaction products have kinetic energy, and thus the heavier reaction products in fusion evaporation reactions typically recoil at velocity υ. This is why such nuclei are simply called recoil nuclei. If the recoil nuclei de-excite by γ-ray emission while they are still in motion, then the measured γ-ray energies appear to be Doppler shifted. Usually, in experiments like ours, where the beam energy and the incident angular momentum are not too high, and the reaction is taking place in normal kinematics, the recoil energies are on the order of a few MeV. Therefore, such nuclei lose their energy due to interactions with the target material, and stop in the target. If these nuclei de-excite after they have been stopped in the target, then the measured γ-ray energies are not Doppler shifted.

Whenever the measured γ-ray energies are Doppler shifted, Doppler shift corrections have to be performed. The following formula relates the measured shifted energy E'_γ to the corrected unshifted energy E_γ:

$$E'_\gamma = \frac{E_\gamma \sqrt{1 - \beta^2}}{1 - \beta \cos\theta} \tag{4.12}$$

where $\beta = \upsilon/c$ (υ is recoil velocity and c is the speed of light), and θ is the γ-ray emission angle. The above equation is obtained from the Lorentz transformation of time, and by using $E_\gamma = \hbar\, c/\lambda$, and $\lambda = cT$, where T is period and λ is the wavelength.

For our experiment, the recoil velocities of ^{30}S nuclei in the excitation energies of interest were calculated using the kinematics program Catkin under the assumption that these nuclei are emitted parallel to the beam axis. The assumption of the recoil emission angle at 0° comes from the fact that the recoil velocity increases by increasing the angle of emission of the recoil nucleus because the energy of the corresponding light reaction product decreases by increasing angle of emission. Therefore, we used the known unshifted energies of ^{30}S γ-rays measured at 90° to calculate the expected Doppler shifts in energies as a function of emission angles of the corresponding recoil nuclei. Only at 0° could the parameter β give the Doppler shifted γ-ray energies consistent with the uncorrected (for Doppler shift) γ-ray energies measured at -135°.

The resulting recoil energies vary between 1.3 to 1.6 MeV. Therefore, $\upsilon \ll c$, and thus at 90° there is no Doppler shift in γ-ray energies. However, the γ-ray energies at -135° are Doppler shifted as seen in Fig. 4.18.

Once β was found for each ^{30}S excited state, equation (4.12) was used to correct the Doppler shifted energies for the γ-rays measured at -135°. The resulting energies are shown in § 4.3.1, and are in good agreement with those measured at 90°. It should be noted that in our case where the event-by-event kinematic reconstruction was not performed, an average recoil velocity was obtained for ^{30}S nuclei at different excitation energies, and θ was considered to be simply the average angle of detection with respect to the beam axis, rather than the angle to each Ge-detector taken relative to the actual recoil direction.

Having the relevant data only at one angle (-135°), no half-life calculation was perfo-

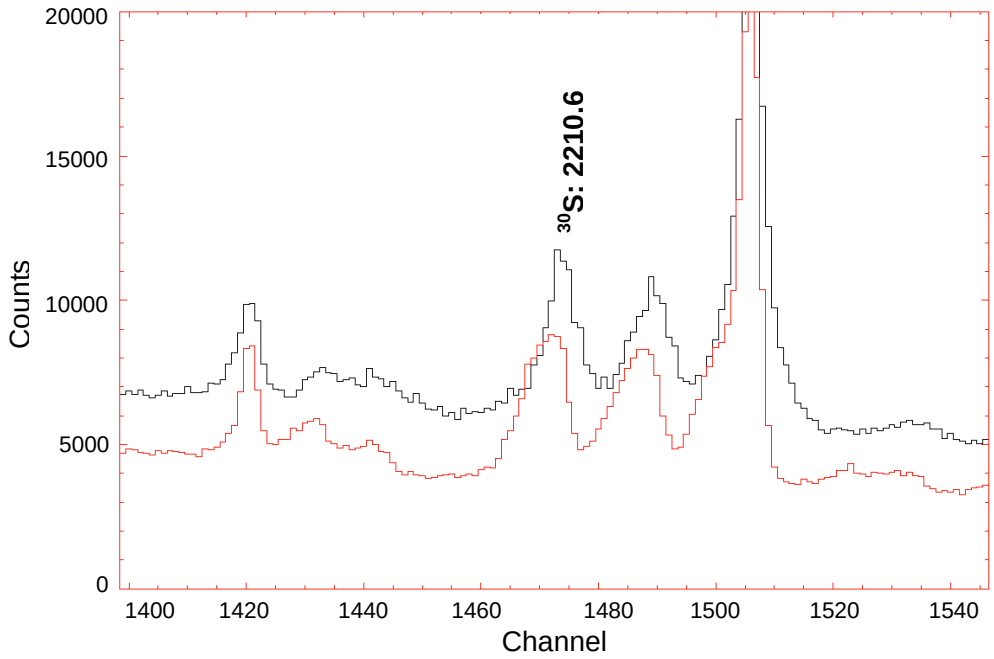

(a)

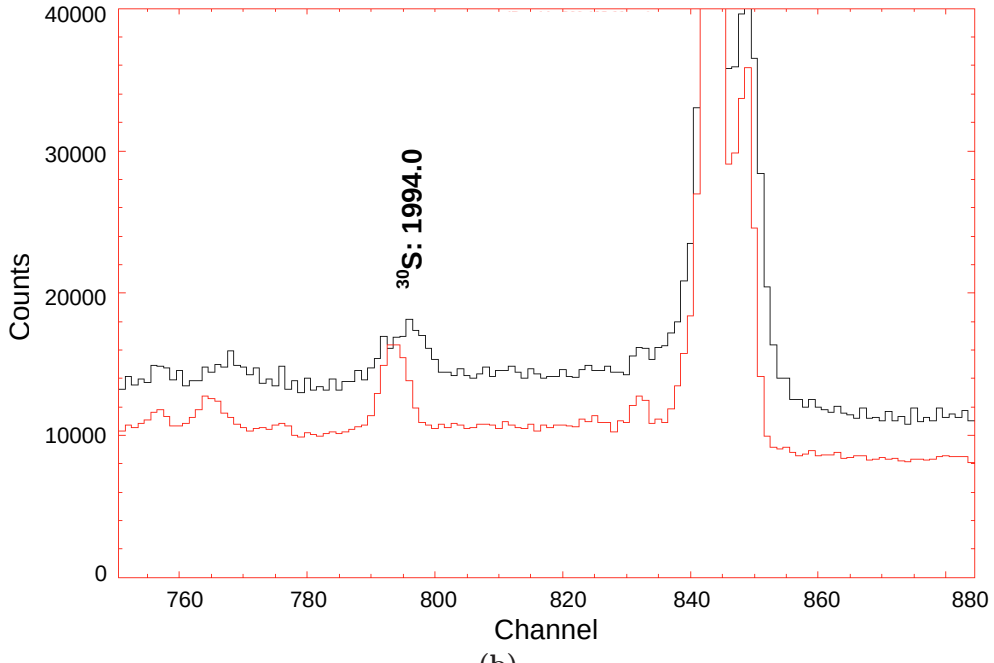

(b)

Figure 4.18: The black spectrum is a portion of the unshifted singles γ-ray spectrum measured by the detector at 90°, while the red spectrum is a portion of the same spectrum measured at -135°, and thus the γ-rays are Doppler shifted. ^{30}S γ-rays are labeled with their energy in keV. The other peaks are from de-excitation of ^{30}P states. The peaks on the red spectra are broader due to Doppler broadening.

rmed for this work[29]. However, attempts were made to estimate the time it takes for ^{30}S recoil nuclei to stop in the silicon target. From comparison of the stop time for each excited state with the half-life of that state (if known), one can determine if a Doppler shift in energy should be expected.

For such estimations, the previously calculated recoil energies of ^{30}S nuclei were used in conjunction with the commonly used energy loss code SRIM [320] to estimate the thickness of silicon required to stop each ^{30}S nucleus. These thicknesses were then used together with proper kinematics formulas to estimate the time it takes for each of these nuclei to stop. The resulting crude estimations confirmed that almost all of the γ-rays de-exciting the ^{30}S nuclei populated in the states with known half-lives and observed at -135° must have been Doppler shifted. The only exception is the 1456.5-keV γ-ray (see Figs. 4.15a and 4.16a), for which the corresponding half-life of the associated state is larger than 2 ps [187], which in turn is larger than the estimated stopping time. The results of this experiment will be presented next.

4.3 Results

4.3.1 ^{30}S Decay Scheme

In the singles spectra, two peaks are observed at 1194.0(1) keV and 2210.6(3) keV, which correspond to the $2_2^+ \rightarrow 2_1^+$ and $2_1^+ \rightarrow 0_1^+$ transitions in ^{30}S, respectively. After placing software gates on these two peaks, γ-decay cascades from higher-lying states are observed. In particular, we observe transitions with energies of 2477.3(3) keV, 2599.0(4) keV and 2921.4(4) keV from ^{30}S proton-unbound states at 4688.1(4) keV, 4809.8(5) keV and 5132.3(5) keV, respectively. Thus, the decay scheme of ^{30}S is obtained.

The ^{30}S radiating nuclei recoil in the direction opposite to that of the emission of the γ-rays as a consequence of the conservation of energy and momentum in the γ-emission process. This recoil energy must also be taken into account when constructing the final excitation energies of the ^{30}S nuclei from its γ-ray decay scheme. The recoil energy E_r is

[29] If the amount of Doppler shift in energy is known for at least two angles, one can set an upper limit on the half-life of the corresponding nuclear level (see equation (4) in Ref. [319]). The 90° data do not count because there is no Doppler shift in γ-ray energies at that angle.

related to the γ-ray energy E_γ by [126] (p. 327):

$$\Delta E = E_i - E_f = E_\gamma + E_r = E_\gamma + \frac{E_\gamma^2}{2Mc^2} \tag{4.13}$$

where E_i and E_f are the energies of the initial and final states involved in the transition, respectively; and Mc^2 is the rest mass energy of ^{30}S in keV. We have used the mass of ^{30}S derived from the results of Ref. [140] to calculate the recoil energies corresponding to each transition. The results of such calculations are also given in Table 4.2.

From the recoil energies and the γ-ray energies, the excitation energies of the first few excited states observed in this experiment are reconstructed to obtain the level scheme of ^{30}S (see Table 4.2 and Fig. 4.19). The measured energies of most of the levels are in agreement with the results from the ^{32}S(p, t)^{30}S measurement discussed in the previous chapter, as well as the results of previous ^{30}S γ-ray measurements presented in Refs. [172, 173]. In particular, the measured energies of the two astrophysically important excited

Table 4.2: The final results for energies and the relative intensities for ^{30}S transitions observed in the present work. The relative intensities are with respect to the strongest γ-ray measured at the same angle. The uncertainties in the recoil energies were negligible, and thus are not presented. The energies of the initial state E_i and the final state E_f are corrected for the corresponding recoil energies. The uncertainties are in the last digit(s).

Gate[a]	E_γ (keV)	E_r (keV)	E_i (keV)	E_f (keV)	$I_\gamma^{90^\circ}$ (%)	$I_\gamma^{-135^\circ}$ (%)
2210.6(3)	846.0(4)	0.01	unplaced	unplaced	3.9(6)	2.8(5)
	1194.0(1)	0.03	3404.7(3)	2210.7(3)	33.5(5)	43.3(10)
1194.0(1)	1283.4(3)[b]	0.03	4688.1(4)	3404.7(3)	1.2(2)	
1194.0(1)	1405.1(4)	0.04	4809.8(5)	3404.7(3)	3.1(4)	1.9(4)
2210.6(3)	1456.5(3)	0.04	3667.2(4)	2210.7(3)	11(3)	13.9(9)
2210.6(3)	1466.2(3)	0.04	3676.9(4)	2210.7(3)	3.1(1)	3.6(6)
	2210.6(3)	0.1	2210.7(3)	g.s.	100.0(10)	100.0(10)
2210.6(3)	2477.3(3)	0.1	4688.1(4)	2210.7(3)	6.0(4)	9.3(9)
2210.6(3)	2599.0(4)[c]	0.1	4809.8(5)	2210.7(3)	1.6(3)	
2210.6(3)	2921.4(4)	0.2	5132.3(5)	2210.7(3)	9.7(4)	18.3(10)

[a]This is the transition on which the coincidence gate is placed.
[b]This transition is not observed at -135°.
[c]This transition at -135° is too weak to obtain a reasonable yield.

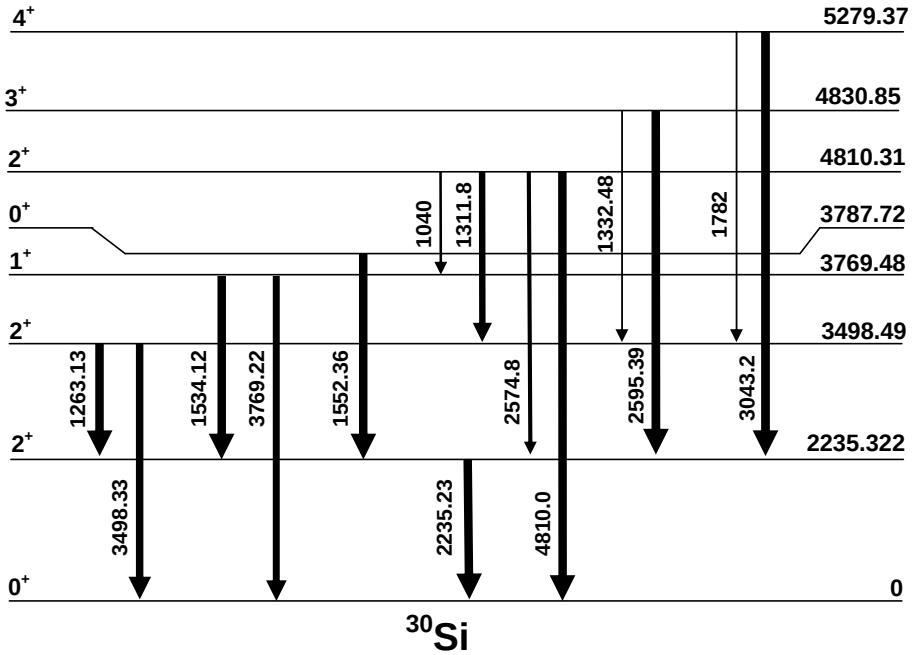

(a) A portion of ^{30}Si decay scheme based on Ref. [187].

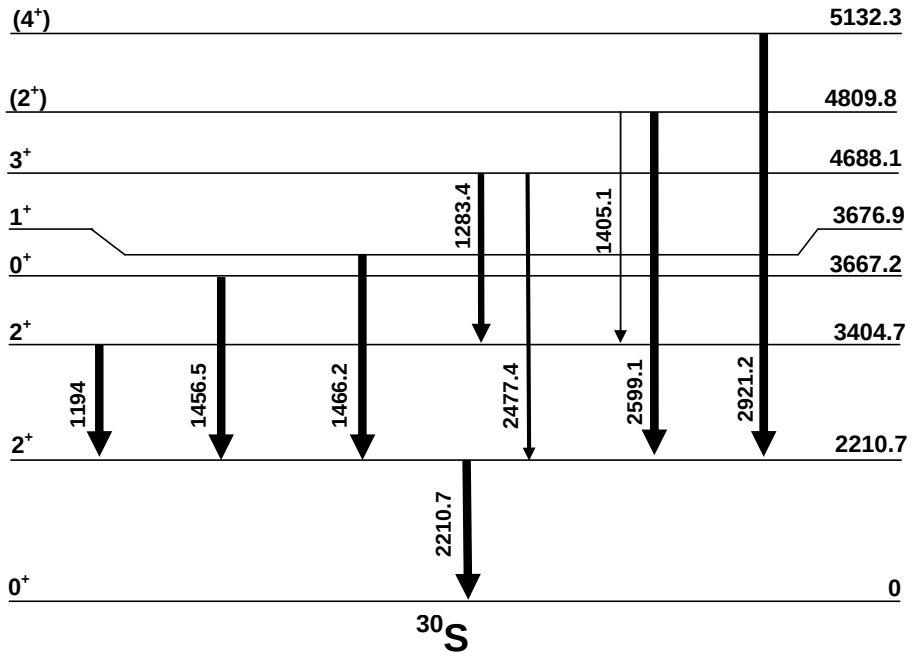

(b) ^{30}S decay scheme based on the results of the present work.

Figure 4.19: (top) A portion of ^{30}Si decay scheme for comparison with that of its mirror nucleus, ^{30}S. The energies are in keV. (bottom) The ^{30}S decay scheme based on the results of the present work. The tentative $J^\pi = 2^+$ value for the 4809.8-keV state is based on the conclusions from Ref. [285], because no J^π value could be obtained for this state from the present work. The γ-ray branches are not to scale; however, the thicker the arrow, the stronger the branch. All the observed γ-rays are shown with their energies (in keV) corrected for the recoil energies of the corresponding ^{30}S excited states, which are also shown (in keV).

states at 4688.1(4) keV and 4809.8(5) keV from the present measurement are in excellent agreement with the 4688(2) keV and 4812(2) keV energies measured from our ^{32}S(p, t)^{30}S experiment.

The energy resolution obtained in the measurement of Ref. [173] was 6 keV which is $\approx$ a factor of 2 worse than ours. The efficiencies of our HPGe-detectors are much better than those of the Ge(Li) detectors used in the experiments presented in Refs. [172, 173]. This is because both of these measurements were performed in early 1970's, and since then the technology of the Ge-detectors has progressed very much. Therefore, the advantage of our present γ-ray spectroscopy experiment with respect to the previous γ-ray measurements of Refs. [172, 173] is the observation of the 1283.4-keV and 2477.3-keV γ-rays corresponding to the decay of the 4688.1-keV state, and the 1405.1-keV and 2599-keV γ-rays corresponding to the decay of the astrophysically important state at 4809.8 keV in ^{30}S. All these γ-rays are absent in the spectra measured in Refs. [172, 173] because in the aforementioned previous measurements a Ge(Li) detector together with a NaI detector were used for the coincidence measurements, which have much worse energy resolution than the HPGe-detectors used in the present work. Hence, both astrophysically important states of ^{30}S remained unobserved in the previous coincidence γ-ray measurements of Refs. [172, 173]. The present work; however, is not the first measurement where the de-excitations of the two astrophysically important states of ^{30}S are observed via γ-ray emissions. We are aware that Galaviz *et al.* [185] have observed the de-excitation via γ-ray emission of the two astrophysically important states of ^{30}S for the first time, but their results are not published yet [321].

In comparing our results with the results of Ref. [173], however, there are discrepancies in the measured energies for two levels: our energy for the 2^+_2 state is $\sim$ 2 keV higher than that of Ref. [173]. Also the energy of the 5132.3(5) keV state from our measurement is lower than the 5136(2) keV energy measured by Kuhlmann *et al.* [173]. The reason for the latter is unclear; however, the inconsistency between the measured energies of the 2^+_2 state originates from the presence of a peak at 1188.6 keV (see Fig. 4.20 on page 187) right beside the peak at 1194 keV on the singles spectra in our measurement.

While the latter peak corresponds to the decay of the 2^+_2 state to the 2^+_1 state in ^{30}S, the former is the double escape peak corresponding to the $2^+_1 \rightarrow 0^+_1$ transition in ^{30}S. This is confirmed first of all by the calibrated energy associated to the left peak at 1188.6

keV on the black spectrum shown in Fig. 4.20. There is a γ-ray with energy close to this energy from ^{30}Si produced from the ^{29}Si(^{3}He, $2p$)^{30}Si reaction, which could potentially be the observed 1188.6-keV γ-ray shown in Fig. 4.20. However, when a software coincidence gate was placed on the 1188.6-keV γ-ray, no other γ-ray of ^{30}Si appeared in the coincidence spectrum. Instead, the coincidence spectrum showed the transitions of ^{30}S which are due to the presence of the tail of the 1194-keV transition inside the gate. As we moved the gate channels away from the 1194-keV peak, the yields of all γ-rays present in the coincidence spectra also decreased accordingly.

Moreover, as is evident from the spectra in Fig. 4.20, the yield under this peak decreases dramatically on the red spectrum measured by the larger detector, where the probability of double escape peaks decreases. In addition to the 1188.6-keV γ-ray, we

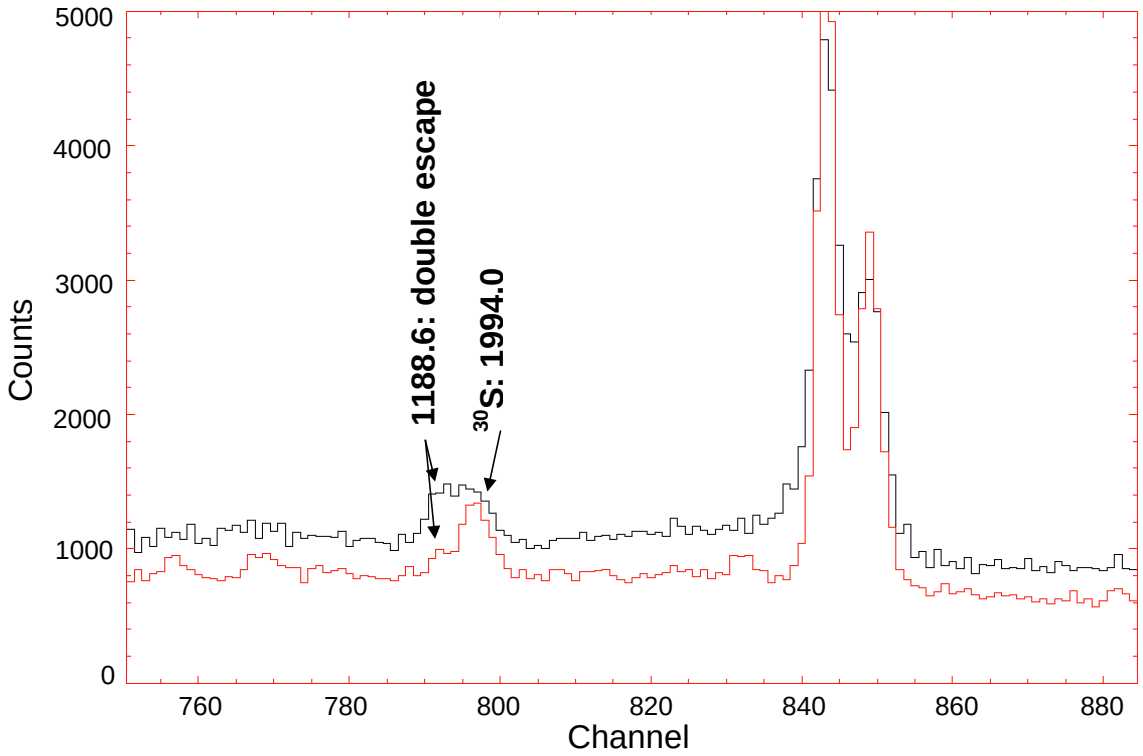

Figure 4.20: The 1194-keV and the double escape peak of the 2210.6-keV transitions of ^{30}S. The red spectrum is measured by the 70% relative efficiency detector placed at -90° for a short time during Phase II of the experiment, while the black spectrum is measured by the 50% relative efficiency detector placed at 90°. The 1188.6-keV transition is the double escape peak of the 2210.6-keV γ-ray of ^{30}S, and its yield has decreased significantly when measured by the larger detector at -90°.

were able to identify a few more single and double escape peaks corresponding to the high energy ^{30}P transitions.

The spectra shown in Fig. 4.20 were taken when both detectors were placed at 90° and so the peaks are not Doppler shifted either. As seen on the red spectrum in Fig. 4.20, the peak corresponding to the 1194-keV γ-ray is the only one that stands out.

The energy of this peak gives rise to the energy of the 2_2^+ state of ^{30}S, measured from the present work, to be $\sim$ 2 keV higher than that measured in Ref. [173]. The latter measurement was performed in the early 1970's when the Ge-detectors were smaller. Thus, it may be quite possible that this double escape peak was also present at that time in their spectra but because of the low efficiency of those detectors, the yields under each of these peaks were such that the two peaks were assumed to be one. In our spectra if we also treat these two peaks as one, we get a level energy for the 2_2^+ state of ^{30}S that is consistent with that measured by Kuhlmann *et al.* [173].

We expected to observe the γ-rays emitted from de-excitations of the 3407.7- and 3676.9-keV states directly down to the ground state in the singles spectra. In addition, if the 4809.8-keV state is the 2_3^+ state in ^{30}S, according to the decay scheme of its mirror level we expect that the $2_3^+ \rightarrow 0_1^+$ transition in ^{30}S is a strong branch (with respect to the strength of the other decay branches of the same level). Therefore, we also expected to observe the 4809.8-keV γ-rays of ^{30}S in the singles spectra. However, the detection efficiency for detecting such high energy γ-rays decreases significantly, and the high energy regions of the spectra obtained in the present work are obscured mostly by wide peaks originating from transitions in ^{30}P. Therefore, we are not able to resolve the 3407.7-, 3676.9-, and 4809.8-keV transitions. Hence, the fact that the $2_3^+ \rightarrow 0_1^+$ transition in ^{30}S is not observed in the present work does not imply that this transition is weak. Based on Ref. [322] where the intensities of the γ-rays of ^{30}Si were measured at 90°, we estimate[30] that the branching ratio of the $2_3^+ \rightarrow 0_1^+$ transition in ^{30}Si is 36 $\pm$ 3 % which should be equivalent to that of the 4809.8-keV $\rightarrow$ g.s. transition in ^{30}S.

We have observed a weak line in the singles γ-ray spectra measured at $\pm$90° (see Fig. 4.10), which also appears in the coincidence spectra at those angles as a more noticeable peak (see Fig. 4.15). The energy corresponding to the centroid of this peak

[30]The $2_3^+ \rightarrow 1_1^+$ transition in ^{30}Si was not observed in the measurement of Ref. [322]. Thus, a branching ratio of $B_\gamma \sim 3.5\%$ was adopted for the aforementioned transition from the previous compilation of Ref. [323].

measured at -90° via γ-γ coincidence measurement is 845.8(4) keV. This line also appears in the coincidence spectrum measured at -135° when gating on the 2210.6-keV γ-ray of ^{30}S. The measured energy at the latter angle is 846.1(4) keV (see Fig. 4.16a), which is consistent with the measured energy at -90°. This seems to suggest that this γ-ray may be emanated from a state whose half-life is more than 2 ps, and thus the energy of the aforementioned γ-ray is not Doppler shifted at -135°. As seen in Fig. 4.15, this γ-ray is in coincidence with both 1194-keV and 2210.6-keV transitions in ^{30}S. In addition, the same γ-ray appears in the n-γ coincidence spectrum shown in Fig. 4.17 and measured at ±90°; however, in the latter spectrum this line is weaker, and thus due to its lower statistics its corresponding energy is determined to be 846.4(11) keV. A weighted average between independent measured energies at -90° and -135° results in E_γ = 846.0(4) keV (see Table 4.2). The origin of this γ-ray is still under investigation. The energy of this transition does not add up to any of the known levels of ^{30}S; however, the fact that it is fairly prominent peak and is in coincidence with two transitions of ^{30}S seems to suggest that this γ-ray may also belong to the decay scheme of this nucleus. Observing this γ-ray in the n-γ coincidence spectrum makes this assumption stronger. The higher lying resonances of ^{30}S may emit a γ-ray in this energy range, but those resonances lie much higher in energy than the proton threshold such that it is improbable that they decay via γ-emission rather than particle emission. Moreover, the latter resonances are most likely not even populated in this experiment. Therefore, this γ-ray has so far remained unplaced in the level scheme obtained from this work.

Finally, the relative intensities from full-energy-peaks of all the observed transitions were calculated based on equations (4.8) and (4.9) at 90° and -135°. For the coincidence spectra, first the yield of the 1194-keV transition was normalized to that of the 2210.7-keV γ-ray from the singles spectra. After the relative intensity of the 1194-keV γ-ray was obtained, it was used to convert the yields of the other γ-rays in the coincidence spectra into relative intensities. These results are tabulated in Table 4.2.

4.3.2 Singles Measurements: γ-Ray Angular Distributions

γ-ray singles measurements are useful spectroscopic tools. The most common measurements of this type include angular distributions, excitation functions and beam induced activity of the target. In our in-beam γ-ray spectroscopy, the only singles γ-ray

measurement performed was the angular distribution measurement.

The reactions induced by the 9-MeV ^{3}He beam proceed through the compound nuclear reaction mechanism. The compound nuclei then decay via evaporation of light particles, e.g., neutrons or protons, etc. The momentum conservation laws and the angular momentum brought into the compound system by the beam causes the recoil nuclei to be either completely or partially aligned or oriented with respect to the direction of the beam[31]. The degree of alignment depends on the formation process.

If we have a collection of oriented nuclei in excited states, the intensities of γ-rays originating from these de-exciting states show angular distributions that no longer have spherical symmetry. Therefore, the direction of emission of γ-rays is correlated with the orientation of nuclei that emit those radiation quanta. The angular distribution measurement is the process of obtaining the relative probability, $W(\theta)d\Omega$, that a particular γ-ray is emitted into the solid angle $d\Omega$ subtended by the detector placed at an angle θ with respect to the direction of the beam. Such intensity measurements, in other words, are related to the probability of transition from the initial to the final nuclear level via γ-emission.

The measurement of angular distribution is perhaps the best method for determinations of the multipolarities and mixing ratios of the γ-transitions involved, and therefore the angular momenta of the participating states in nuclear transitions. Hence, the assignments of the nuclear spins can be made via this technique for those states that de-excite via γ-ray emission. The parities of these states cannot be determined from angular distribution measurements alone [324] (p. 594). Additional measurements of γ-rays' polarization should therefore be performed to determine the parities of the states involved in the electromagnetic transitions. Such measurements; however, were not performed in this work.

The results of angular distribution measurements are more conclusive and precise than those of the measurements of the directional correlations for successive γ-rays emitted from oriented states [250]. The latter is described in the next section. Moreover, measurements of the former, unlike measurements of the latter, require the singles mode of electronics, and thus due to higher count rates in this mode, the angular distribution measurements can be performed in much less time.

[31] In our experiment, the beam and target were unpolarized, and thus were randomly oriented.

The detailed theoretical discussion on angular distribution is outside the scope of this work, and can be found in Ref. [325]. Therefore, in the present chapter only a summary of the angular distribution theory is presented to help comprehend the main focus, which is the measurement and the results.

- **A Brief Treatment of the Theory:**

Theoretically, an individual aligned state with spin j can be represented as a statistical distribution of an ensemble of $2j+1$ magnetic substates m_j (or simply m, where $m = -j$, $\ldots$, j) along an axial symmetry axis, also called the quantization axis, and a reflection symmetry axis. The quantization axis could be chosen to be the beam direction, and therefore the reflection symmetry axis would be the plane at right angles to the beam axis. Each of these components thereby has an associated probability $P(m)$ referred to as the population parameter [325] (p. 50) with the condition that $P(m) = P(-m)$ for an unpolarized aligned state. It immediately follows that if $j = 0$ or $1/2$, the angular distribution is isotropic[32].

This probability distribution is usually treated as a Gaussian function, whose FWHM is σ, and is described in [325] (p. 56):

$$P(m) = \frac{\exp\left(\frac{-m^2}{2\sigma^2}\right)}{\sum_{m'=-j}^{j} \exp\left(\frac{-m'^2}{2\sigma^2}\right)} \tag{4.14}$$

The purpose of the denominator is to normalize the resulting probability to 1. In experiments, the FWHM of this Gaussian distribution can be determined. The Gaussian distribution is chosen in particular among all possible distributions due to randomness of particle and photon emission in the compound nucleus decay [326]. This assumption, however, may not be always true [327]. For nuclear states populated by compound nucleus reactions, it has been well established [328] that the orientation has an oblate shape with respect to the beam axis so that $P(m_i) > P(m_j)$ if $|m_i| < |m_j|$. Hence, the angular momentum is transversely transferred to the compound nucleus [325] (p. 54).

[32]The angular distribution is always symmetric with respect to $\theta = \pi/2$. Ref. [325] discusses the reason for this on page 53.

Thus, it follows that [325] (p. 54):

$$P(m) = \begin{cases} 1 \text{ for } m = 0, \pm 1/2 \\ 0 \text{ otherwise} \end{cases} \tag{4.15}$$

This is confirmed by $\lim_{\sigma \to 0} P(m) = 1$ when $m = 0$ or $\pm 1/2$. Therefore, for oblate alignment when $m = 0$ or $\pm 1/2$, the alignment is called complete, or in other words, $P(m)$ is maximum at $m = 0$ or $\pm 1/2$. In contrast, an incomplete alignment results in an attenuation of the population parameter. The attenuation factors, also known as alignment factors, are defined as [325] (P. 55):

$$\alpha_k = \sum_{m=-j}^{j} \alpha_k^{(m)} P(m) \tag{4.16}$$

where k is even and $k \geq 6$ are ignored due to a rapid decrease of transition probabilities of higher order multipoles. Thus, the higher terms of α_k vanish. By convention α_0 is considered to be unity, while α_2 and α_4 are determined experimentally. These parameters are given in the literature [329] (and references therein) as a function of σ/j (for σ/j in the range of 0.1 – 2), where σ is the FWHM of the population parameter and j is the spin of the initial state emanating a γ-ray.

Rasmussen *et al.* [326] derived a set of simple formulas to calculate α_2 and α_4. These formulas are given in Ref. [326] as a set of two equations labeled by equation (8). In the present work, we attempted to use these two formulas to calculate α_2 and α_4 parameters, which could then be compared with the tabulated values that are calculated via different methods [330] (and references therein). However, the equation provided in Ref. [326] for α_4 (the second equation in the set of equations labeled by equation (8)) failed to reproduce the tabulated values for α_4 parameter. Thus the equation that yields the α_4 parameter most likely carries some printing mistake, and therefore shall not be used. However, using the first equation in the same set of equations in Ref. [326] resulted in α_2 parameters that are identical to the tabulated values, and hence the latter formula is correct, and is given below [326]:

$$\alpha_2^{(m)} = 1 - \frac{3m^2}{j(j+1)} \tag{4.17}$$

where j is the spin of the initial state that de-excites by γ-ray emission, and $m = -j$, $\ldots$, j.

Finally, the theoretical angular distribution function for a transition from a state with spin j_i to another state with spin j_f is defined as [331]:

$$W(\theta) = \sum_{k=\text{even}} A_k P_k(\cos\theta) \tag{4.18}$$

where the coefficients $P_k(\cos\theta)$ are the Legendre Polynomials, and the coefficients A_k are defined as [325] (p. 55):

$$A_k(j_i\lambda\lambda' j_f) = \frac{\alpha_k B_k}{1+\delta^2}\left[F_k(j_f\lambda\lambda j_i) + 2\delta\, F_k(j_f\lambda\lambda' j_i) + \delta^2 F_k(j_f\lambda'\lambda' j_i)\right] \tag{4.19}$$

where j_i and j_f are initial and final spins of the states involved in the transition, respectively; λ and λ' are the multipolarities, e.g., for a $j_i = 2 \rightarrow j_f = 2$ transition, the possible values of (λ, λ') could be (1, 1), (1, 2) which is equivalent to (2, 1), and (2, 2); α_k are the alignment factors; the coefficients B_k and F_k are tabulated for different combinations of j_i and j_f, and can be found in the literature, e.g., Ref. [330]; and δ is the mixing ratio of the transition defined as [1] (p. 54):

$$\delta_j^2 = \frac{\Gamma_j(\overline{\omega}L+1)}{\Gamma_j(\overline{\omega'}L)} \tag{4.20}$$

where $\overline{\omega'}L$ and $\overline{\omega}L+1$ are the magnetic and electric transitions of multipolarity L, and $L+1$, respectively; and Γ_j is the partial γ-ray width corresponding to a state with spin j.

By convention, A_k is unity for $k = 0$, and so is $P_k(\cos\theta)$ for $k = 0$. The coefficients $k \geq 6$ vanish for the reason mentioned previously. The reason why only even k's are allowed is as follows: unlike the plane wave, which does not have a definite parity as a result of being a superposition of the eigenstates of angular momentum, the wave function of the compound nucleus formed in a reaction has a unique parity equal to the product of the parities of the beam and target, and (-1)^l where l is the orbital angular momentum carried by the beam. Therefore the wave function of the entrance channel (beam + target system) and the exit channel (compound nucleus) have the same parity.

For cases like our experiment where the compound nucleus decays by particle emission,

based on the discussion presented in Chapter 2, the compound nucleus is considered to be a resonance with a definite parity. When only one level in the compound nucleus participates in the transition, the wave function describing the outgoing channel of the reaction (the decay of the compound nucleus to the reaction products) has a parity identical to that of the compound nucleus [324] (p. 533 – 535). Therefore, all the nuclear levels participating in transitions at each stage, i.e., from the initial state to the compound nucleus and from the latter to the final state, have a unique spin and a well defined parity. Conservation of parity then restricts the differential cross section, or in other words, the γ-ray intensity to be symmetric about $\theta = \pi/2$ [324] (p. 533 – 535) because the intensities are independent of the azimuthal angle ϕ, and the parity operator is defined as a reflection of (θ, ϕ) to ($\pi - \theta$, $\pi + \phi$). The intensity can be written as a polynomial with respect to $\cos\theta$, and it follows that only even terms are permitted (see also Ref. [1] (p. 603)).

- **Experiment:**

To perform the angular distribution measurement, during September-2010, the 50% relative efficiency detector was located at +90°, while the location of the 70% relative efficiency detector was varied between -90° to -120° with the increment of 10°, and it was also placed at -135°. The duration of each of these five runs were identical, and amounted to one hour each. It was essential that the 70% relative efficiency detector dominated the DAQ due to its higher relative efficiency for detection of γ-rays, and that this detector was the one that measured intensities at different angles. Therefore, the 50% relative efficiency detector was moved farther away from the target such that the distance to the target was 10.3 cm. The 70% relative efficiency detector was, however, 7 cm away from the target.

The singles γ-ray spectra were then obtained for both detectors at five different angles. Numerous γ-rays were identified from different reactions and background sources. The main γ-rays of interest to this work were two low-lying γ-rays of ^{30}S at 2210.6 keV and 1194 keV, which were found through calibration of the spectra via a ^{152}Eu standard source[33].

To determine the angular distribution of a γ-ray transition experimentally, the number of counts per unit beam charge must be recorded for that γ-ray as a function of the angle

[33]The calibration runs were taken prior to the experiment, and at the angles and other conditions identical to each of the production runs. The source was positioned at the target position.

subtended by the axis of the associated detector and the direction of the beam. Due to the finite solid angle of the detector, this measured yield is in fact the differential yield ($dY/d\Omega$), and is thereby not the true distribution $W(\theta)$. Hence, the experimental number of counts must be corrected and normalized to $W_{exp}(\theta)$.

In our experiment, we could not determine the total charge deposited by the beam due to a faulty beam current integrator. Therefore, to take into account the fluctuation of the beam intensity during each run and possible target degradations or the changes in the target profile, etc. that could affect the areas under the peaks of interest, the 50% efficiency detector was used as a monitor detector fixed at $\theta_1 = 90°$ with respect to the beam, while the 70% relative efficiency detector was at a different angle[34]. For every (θ_1, θ_2) angular pair, from the singles γ-ray spectra of the 50% efficiency detector calibrated by a standard ^{152}Eu source, an intense peak corresponding to the 708.7-keV γ-ray of ^{30}P was chosen and fitted by a Gaussian least-squares fit to extract its area and the associated uncertainty. At the same time the peaks corresponding to the 2210.6-keV and 1194-keV γ-rays of ^{30}S were also fitted[35] from the singles γ-ray spectrum of the 70% relative efficiency detector, also calibrated by a ^{152}Eu source. Each of the latter areas was then divided by the area under the intense peak of ^{30}P measured via the 50% relative efficiency detector at +90° to normalize the intensities (yields).

Two things to note are that the counts do not need to be corrected for efficiency and solid angle because such corrections are already made when the yields are normalized, and the angular distribution measurement can only be performed for the γ-rays that are observable in the singles γ-ray spectra. Therefore, the angular distributions of all the other transitions in ^{30}S that did not appear in such spectra could not be determined.

After normalization of the yields, the uncertainties in those yields were then calculated by separately adding in quadrature the relative uncertainty in the yield of each ^{30}S peak to that of the aforementioned ^{30}P peak.

Finally, the normalized relative yields for each peak of interest were plotted against $\cos^2(\theta)$ where θ is the detection angle, and these data were fitted (see Fig. 4.21) using a

[34] θ_2 = -90°, -100°, -110°, -120° and -135°.

[35] The peak corresponding to the 2210.6-keV γ-ray transition of ^{30}S in the spectra at -110°, -120° and -135° did not have a Gaussian shape. Instead there was an exponential tail that sat on top of the Gaussian (see Fig. 4.18). Therefore, the area of this peak was obtained by a least-squares fit of a convoluted Gaussian-plus-exponential function to account for the exponential tail.

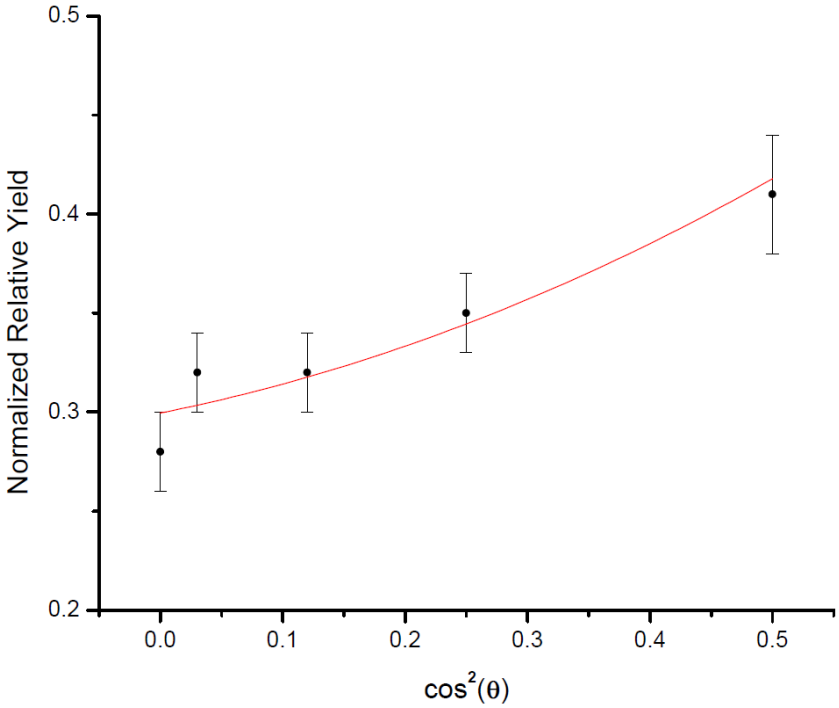

(a) The 2210.6-keV γ-ray from the $2_1^+ \rightarrow 0_1^+$ transition in ^{30}S.

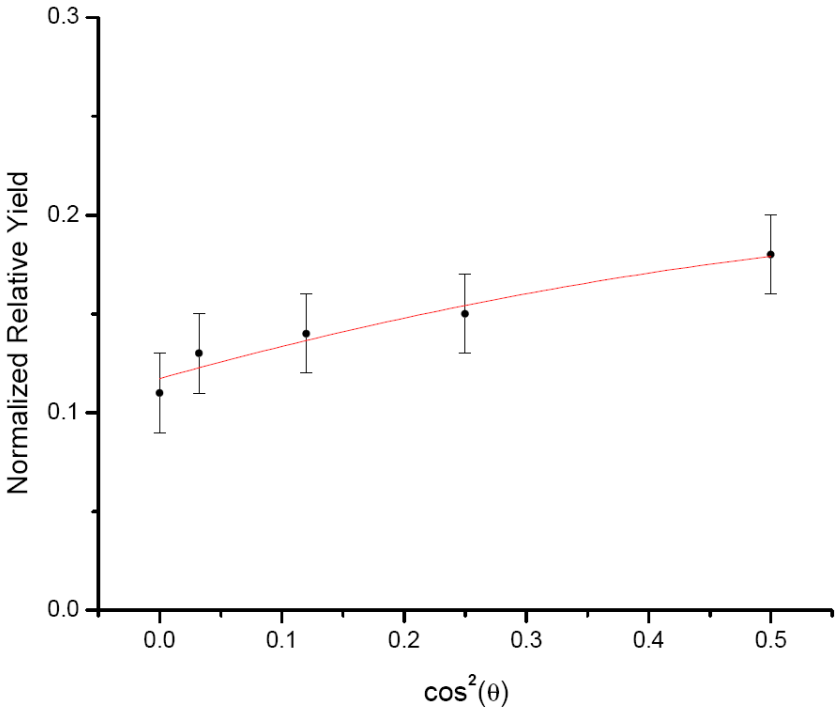

(b) The 1194-keV γ-ray from the $2_2^+ \rightarrow 2_1^+$ transition in ^{30}S.

Figure 4.21: Experimental angular distributions of γ-rays of ^{30}S. The solid lines are the best fit to the Legendre polynomials. The error bars are large due to low statistics.

least-squares fit function of the following form via Origin [318]:

$$W(\theta)_{exp} = A_0 + A_2 P_2(\cos\theta) + A_4 P_4(\cos\theta) \tag{4.21}$$

where the coefficients A_i are extracted from the fit, and $P_2(\cos\theta)$ and $P_4(\cos\theta)$ are the Legendre polynomials, and are given below:

$$P_2(\cos\theta) = \frac{1}{2}(3\cos^2\theta - 1) \tag{4.22}$$

$$P_4(\cos\theta) = \frac{1}{8}(35\cos^4\theta - 30\cos^2\theta + 3) \tag{4.23}$$

- **The 2210.6-keV Transition of ^{30}S:**

The 2210.6-keV γ-ray corresponds to the $2_1^+ \rightarrow 0_1^+$ transition in ^{30}S. Due to the momentum and parity conservation laws, this transition is a pure (mixing ratio $\delta = 0$) $E2$ (quadrupole) transition, and thus it is a so-called stretched transition. The latter is defined [326] to be a transition for which $j \xrightarrow{L=2} (j-2) \xrightarrow{L=2} (j-4) \xrightarrow{L=2} \cdots \xrightarrow{E2} 4 \xrightarrow{E2} 2 \xrightarrow{E2} 0$ (stretched quadrupole)[36], where L is the multipolarity of the transition, and j is the spin of the initial state.

Once the experimental intensities at each angle were determined for the $2_1^+ \rightarrow 0_1^+$ transition in ^{30}S, they were used to normalize the theoretical angular distribution $W(\theta)_{theo}$ for this transition obtained from equations (4.18) and (4.19), and by application of $\delta = 0$. For this process the coefficients B_2F_2 and B_4F_4 for the $2^+ \rightarrow 0^+$ transition were taken to be 0.7143 and -1.7143, respectively from Ref. [325] (p. 82). Therefore, the only parameters that were free to vary were the alignment factors α_2 and α_4. These coefficients are given in the literature for different σ/j values that vary from 0.1 to 2.

Thus, for each (α_2, α_4) pair the theoretical angular distribution was calculated at the same angles, for which the experimental relative yield was measured in the present work. An average normalization factor was thus obtained, and was used to normalize $W(\theta)_{theo}$ to the intensity at each angle. Then the $|W(\theta)^{norm}_{theor} - I_{exp}|/\delta I_{exp}$ was plotted against $\cos^2\theta$, where I_{exp} and δI_{exp} are the intensity and its associated uncertainty obtained from the data at the angle θ. Hence, the particular (α_2, α_4) pair, which yielded the

[36]Similarly, for a stretched dipole transition $L = |j_i - j_f| = 1$, where L, j_i and j_f are the transition's multipolarity and the spins of initial and final states, respectively.

minimum difference between $W(\theta)_{theo}$ and I_{exp}, was found. Finding this pair uniquely determines the parameter σ/j, where σ is the FWHM of the population parameter. The results for the $2_1^+ \rightarrow 0_1^+$ transition in ^{30}S are presented in Fig. 4.22 and Table 4.3.

Table 4.3: Results of the angular distribution studies for ^{30}S γ-rays observed in the present work. Energies are in keV. The reported uncertainties are in the last digit(s).

E_γ	$J_i^\pi \rightarrow J_f^\pi$	A_2/A_0 [a]	A_4/A_0 [a]	σ/j [b]	Radiation Mode	δ
2210.6(3) [c]	$2_1^+ \rightarrow 0_1^+$	0.4(2)	-0.0091(1800)	0.6	$E2$	0
1194.0(1) [d]	$2_2^+ \rightarrow 2_1^+$	0.38(25)	-0.14(22)	0.5	$M1$, $E2$	0.16(4)

[a] This value is normalized such that equation (4.21) is turned into $W_{exp}(\theta) = 1 + (A_2/A_0)\,P_2(\cos\theta) + (A_4/A_0)\,P_4(\cos\theta)$, which resembles equation (4.18), where $A_0 P_0(\cos\theta) = 1$.

[b] The attenuation factors corresponding to σ/j = 0.6 are $\alpha_2 = 0.41482$ and $\alpha_4 = 0.48393 \times 10^{-1}$, while those of σ/j = 0.5 are $\alpha_2 = 0.53784$ and $\alpha_4 = 0.95181 \times 10^{-1}$.

[c] $E_i \rightarrow E_f$: 2210.7(3) keV $\rightarrow$ g.s.

[d] $E_i \rightarrow E_f$: 3404.7(3) keV $\rightarrow$ 2210.7(3) keV.

- **The 1194-keV Transition of ^{30}S:**

From a comparison of the 1194-keV γ-ray corresponding to the $2_2^+ \rightarrow 2_1^+$ transition in ^{30}S to the mirror transition in ^{30}Si, it was assumed that this transition is a mixed $M1$, $E2$. Therefore, the analysis was not as simple as the above case because there is an additional free parameter – the mixing ratio δ – that should also be determined.

Some of the standard procedures for such a case is explained in detail on p. 53 and Appendix A in Ref. [332]. For our case, the coefficients A_2 and A_4 from equation (4.21) extracted from the experimental fit were first normalized by division by A_0, which was also extracted from that fit. Then, $W(\theta)_{theo}$ was calculated based on equations (4.18) and (4.19) for all values of σ/j, or equivalently for all (α_2, α_4) pairs that are given in the literature for this particular transition, i.e., $2^+ \rightarrow 2^+$ [329]. The mixing ratio, δ, was assumed to be a free parameter, and thus a pre-determined set of values not too far from the mixing ratio of the corresponding mirror transition given in Ref. [187] was assumed for δ, and this calculation was repeated for each value of δ. The parameters B_2F_2 and B_4F_4 were also constants given in the literature [325] (p. 82) for three sets of known $\lambda\lambda'$ for the $2^+ \rightarrow 2^+$ transition. Then, a χ^2 statistical test was performed with χ^2 defined by:

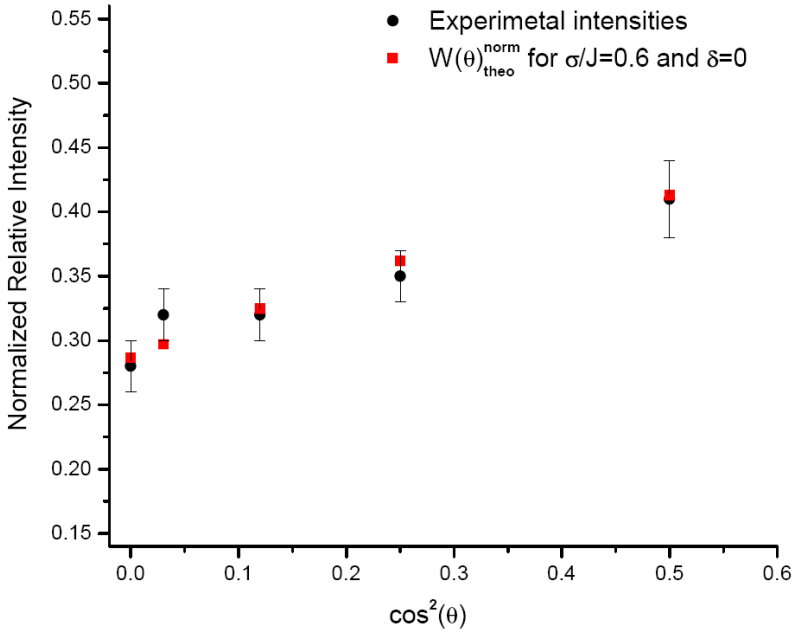

(a) The 2210.6-keV γ-ray transition from the $2_1^+ \rightarrow 0_1^+$ decay in ^{30}S.

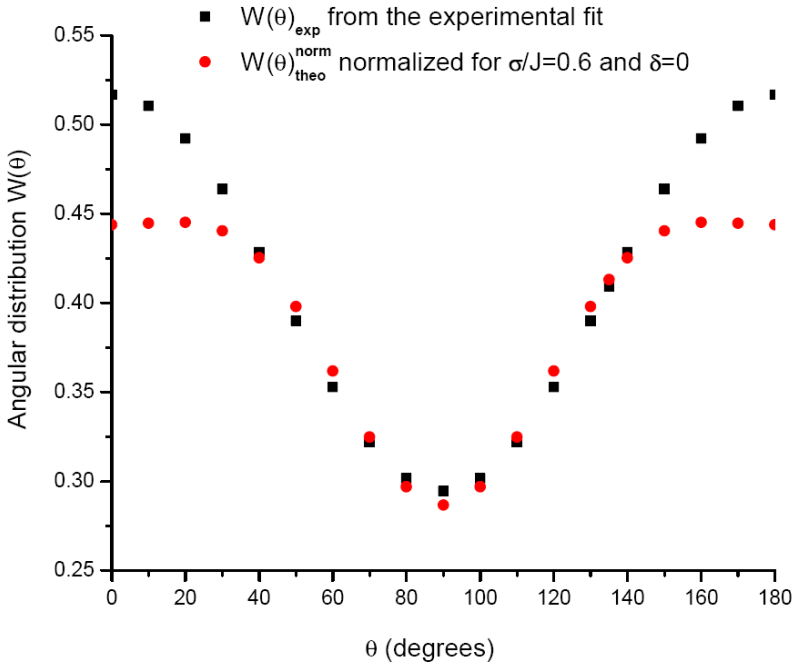

(b) The 2210.6-keV γ-ray transition from the $2_1^+ \rightarrow 0_1^+$ decay in ^{30}S.

Figure 4.22: (top) The plot of relative intensities measured from the areas under the 2210.6-keV peak in comparison with the theoretical angular distributions normalized to the data. The normalization is best performed for $\sigma/j = 0.6$. (bottom) The comparison between $W(\theta)^{norm}_{theo}$ and $W(\theta)_{exp}$. The latter is obtained from the fit given by equation (4.21). The agreement is good between the two curves for most of the angles. For those angles lower than 40° and higher than 150°, the $W(\theta)^{norm}_{theo}$ diverges due to the lack of data points for normalization at those angles.

$$\chi^2 = \left(\frac{A_2^{exp} - A_2^{theo}}{\delta A_2^{exp}}\right)^2 + \left(\frac{A_4^{exp} - A_4^{theo}}{\delta A_4^{exp}}\right)^2 \tag{4.24}$$

where A_i^{exp} parameters are normalized as discussed; and δA_i are the normalized (to δA_0) experimental uncertainties in A_i extracted from the fit given by equation (4.21).

χ^2 was subsequently plotted against $\arctan\delta$ (see Fig. 4.23). For the theoretical calculations δ in principle varies between $-\infty$ to $+\infty$, and thus it is customary to plot $\arctan\delta$ instead. A wide range around those mixing ratios which minimized χ^2 were then obtained[37]. Then χ^2 was again separately plotted only for the allowed ranges of $\arctan\delta$, and each range was fitted separately with a polynomial of the third degree that fitted the data the best to obtain the functional form of χ^2 with respect to δ. Then each of those functions were minimized by obtaining those δ's at which $\partial\chi^2/\partial\delta = 0$. Two resulting solutions corresponding to the mixing ratios and their uncertainties were then compared with the mixing ratio of the $2_2^+ \rightarrow 2_1^+$ mirror transition in ^{30}Si. The mixing ratio that was consistent with that of the mirror transition was then selected. The mixing ratio was thus determined and was kept constant.

Finally, the procedure that was described for the 2210.6-keV γ-ray was repeated for the 1194-keV γ-ray to determine the FWHM of its population parameter. The results are given in Figs. 4.23 and 4.24, and Table 4.3.

It should be noted that no special software was used to perform these calculations. A normal spreadsheet provided by Origin was adequate.

The described χ^2 method was also performed as a check for the 2210.6-keV transition, and the resulting mixing ratio was indeed zero, confirming the stretched $E2$ profile for that γ-ray transition.

The large uncertainties in the experimentally determined A_2/A_0 and A_4/A_0 (see Table 4.3) are mostly due to the low statistics in each peak in the γ-ray spectra. However, they are still consistent with the typical values expected for a stretched quadrupole with $\Delta j = 2$, where Δj is the spin of the initial state (2210.7 keV) minus that of the final state (ground state); and a mixed dipole + quadrupole with $\Delta j = 0$ for the transition from the 3404.7-keV state to the 2210.7-keV state [250, 333].

The mixing ratios obtained for the 1194-keV transition are 0.16(4) and 1.5(6). The

[37] A more realistic way to reject values that fall outside this interval is to find a confidence level.

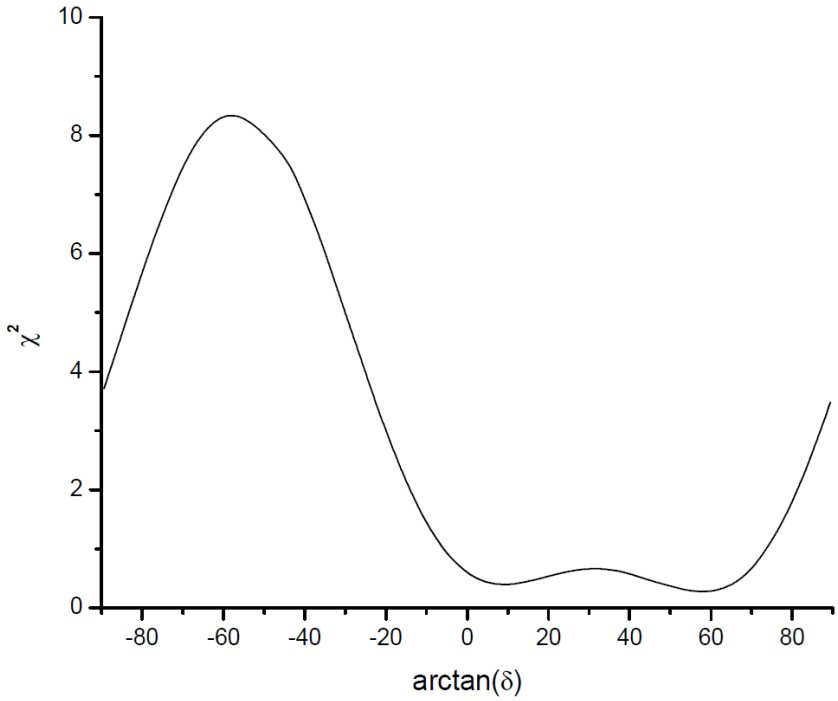

(a) χ^2 *vs.* arctan δ for the 1194-keV γ-ray.

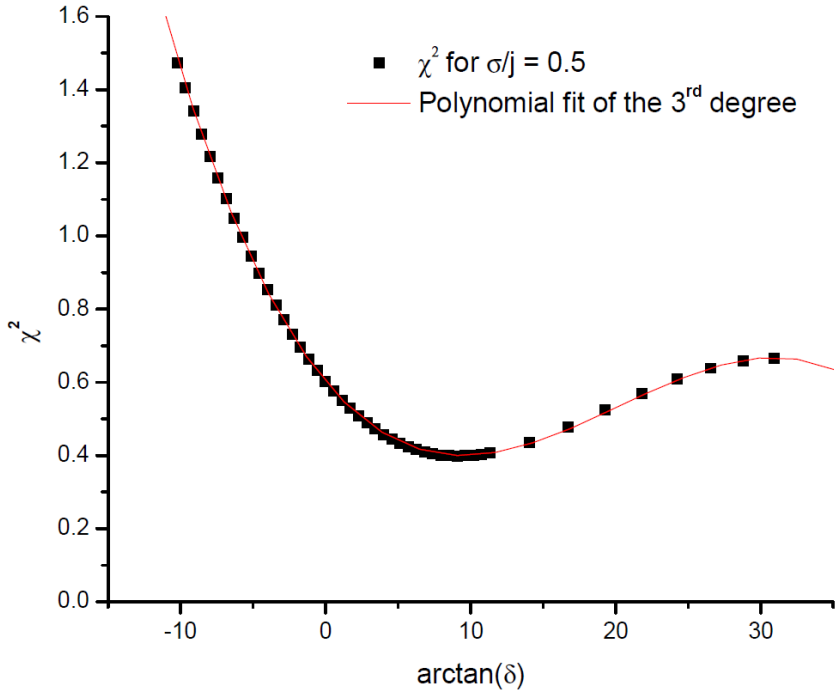

(b) χ^2 fit to find the best value of δ.

Figure 4.23: (top) χ^2 *vs.* arctan δ for the 1194-keV γ-rays de-exciting the 3404.7-keV excited state of ^{30}S. (bottom) A polynomial of the 3^{rd} degree fit for a selected portion of arctan δ, which minimizes χ^2.

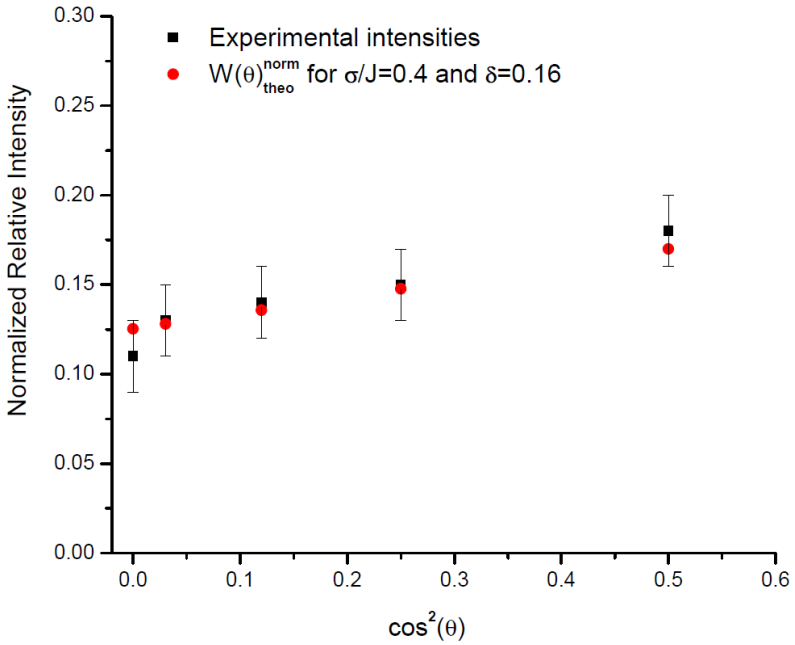

(a) The 1194-keV γ-ray transition from the $2_2^+ \rightarrow 2_1^+$ decay in ^{30}S.

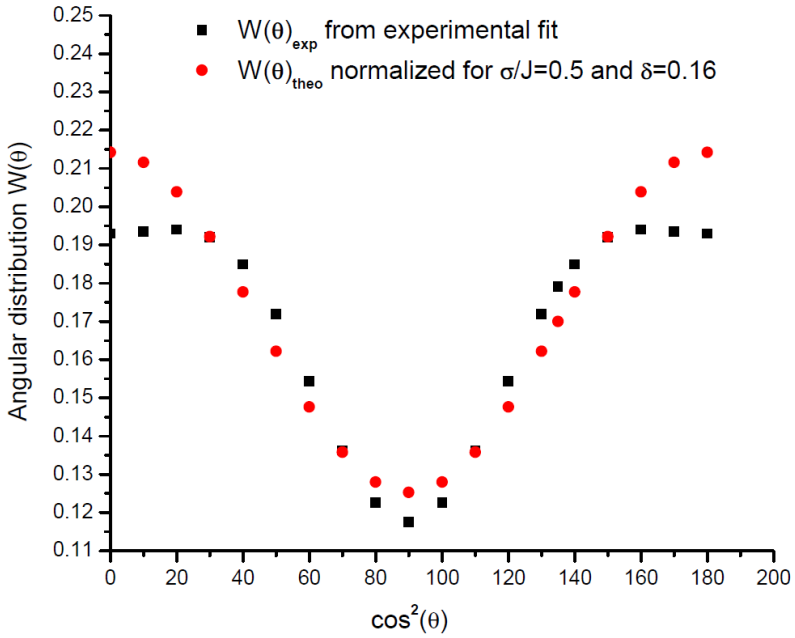

(b) The 1194-keV γ-ray transition from the $2_2^+ \rightarrow 2_1^+$ decay in ^{30}S.

Figure 4.24: (top) Comparison of relative intensities measured from the areas under the 1194-keV peak to the theoretical angular distributions normalized to the data. $\sigma/j = 0.5$ yields the best normalization. (bottom) The plot compares $W(\theta)^{norm}_{theo}$ and $W(\theta)_{exp}$. The latter is obtained from the fit given by equation (4.21). The agreement between the two curves is best for $\sigma/j = 0.4$; however, δ in that case is 0.04, which is not consistent with the mixing ratio of the mirror transition, Therefore, the next best value is $\sigma/j = 0.5$, which yields a mixing ratio consistent with that of the mirror transition. At low and high angles, the theoretical curve diverges dues to lack of normalization points.

former is consistent with the mixing ratio of $\delta = 0.18(5)$ for the mirror transition in ^{30}Si [187]. To confirm that we can reject the latter, the single particle $E2$ transition strength in Weisskopf unit ($B(E2; 2^+ \rightarrow 0^+)$) was determined as follows:

$$B(E2)(\text{in W.u.}) = \frac{9.527 \times 10^6\, BR}{E_\gamma^5\,(1+\alpha)\,A^{4/3}\,t_{1/2}} \tag{4.25}$$

where $t_{1/2}$ is the half-life of the state under consideration; A is the mass number; E_γ is in keV; α's are the internal conversion coefficients, which for this case are ignored as these coefficients increase with the atomic number and decrease by E_γ [250]; and BR is the branching ratio of the transition of interest.

The resulting $B(E2; 2^+ \rightarrow 0^+)$ single particle transition strength is 0.41. As a rule of thumb [250], when $B(E2; 2^+ \rightarrow 0^+)$ of a transition is larger than one, the corresponding state that emits the γ-ray of interest is a collective state for which the mixing ratio should be large. On the other hand, when $B(E2; 2^+ \rightarrow 0^+) < 1$ for a transition, the corresponding state is to a good approximation estimated as a single particle state that has a small mixing ratio. Since our estimated $B(E2; 2^+ \rightarrow 0^+)$ for the 1194-keV transition falls into the latter category, we concluded that the 3404.7-keV state is a single particle state.

One consideration is that for the sign of δ, we have followed Krane-Steffen convention [334] as opposed to that of Rose-Brink [335] in which the sign of the mixing ratio is reversed. The former is also accepted by the nuclear data evaluators working for the NNDC.

Finally, the A_0 coefficient from the experimental fit (equation (4.21)) is angle independent. Therefore, when corrected for the detection efficiency (ϵ_{int}) of each transition, the $A_0^{2_1^+ \rightarrow 0_1^+}/A_0^{2_2^+ \rightarrow 2_1^+}$ yields the angle integrated intensity of the $2_1^+ \rightarrow 0_1^+$ transition with respect to that of the $2_2^+ \rightarrow 2_1^+$ transition, i.e., $I_\gamma^{2_1^+ \rightarrow 0_1^+}/I_\gamma^{2_2^+ \rightarrow 2_1^+} = A_0^{2_1^+ \rightarrow 0_1^+}/A_0^{2_2^+ \rightarrow 2_1^+} \times \epsilon_{int}^{2_2^+ \rightarrow 2_1^+}/\epsilon_{int}^{2_1^+ \rightarrow 0_1^+}$. If the detector were positioned at 55° with respect to the beam, then the angle integrated intensities could also be determined from the areas under each peak corrected for the efficiency. Thus the results of these two methods could be compared with each other.

This is due to the fact that at $\theta = 55°$ (or equivalently 125°), $P_2(\cos\theta)$ vanishes based on equation (4.22). Thus, if the A_4 term is negligible and can be ignored, then $W_{theo}(\theta) =$

$A_0 P_0(\cos\theta) = 1$. This implies isotropic emission [1] (p. 603). Hence, if a narrow resonance is populated with well-defined quantum numbers, namely, no odd Legendre polynomials caused by interferences appear in equation (4.18), and the detector is positioned at 55°, then the absolute angle-integrated intensities are found by dividing measured intensities by the solid angle subtended by the detector, in addition to corrections for efficiencies, branching ratios, etc.

In our experiment, such a measurement was not performed, and therefore the intensities obtained from the A_0 coefficients will not be compared to the measured angle-dependent intensities listed in Table 4.2 on page 184.

4.3.3 Coincidence Measurements: γ-γ Angular Correlations

Dunworth [336] pointed out that the observation of two radiation quanta in coincidence with each other that are emitted from a single radiating system results in a correlation in their relative propagation directions. Such correlations are formulated in Refs. [337–340].

In the simplest case, when only one direction is observed and the other direction is assumed to be fixed, the correlation theory becomes the theory of angular distribution explained previously. Choosing a fixed direction in the space causes the magnetic substates of the state that emits the observed radiation to be weighted accordingly, and therefore the observed radiation is in general anisotropic [341].

Another simple case is the angular correlations between two successive γ-rays emitted in coincidence[38] from a single cascade (part (b) in Fig. 4.25). When both such γ-rays are observed, the theory becomes that of the so-called γ-γ DCO. Such γ-rays are emitted from oriented states. The beam carrying angular momentum $\mathscr{L}_1$ hits the target and makes the compound nucleus, which after some time (10^{-16} s) successively decays into an unobserved outgoing particle carrying away angular momentum $\mathscr{L}_2$ and to the initial state, which in turn is an excited state in the residual nucleus. The initial state is oriented due to the angular momentum that is brought in by the beam. This state then emits γ_1 radiation, which is observed at a particular angle. The intermediate state is thus also aligned because the first radiation is observed at a particular direction, indicating that

[38]The radiations do not necessarily need to be successive transitions, but for the latter case the theory is simpler.

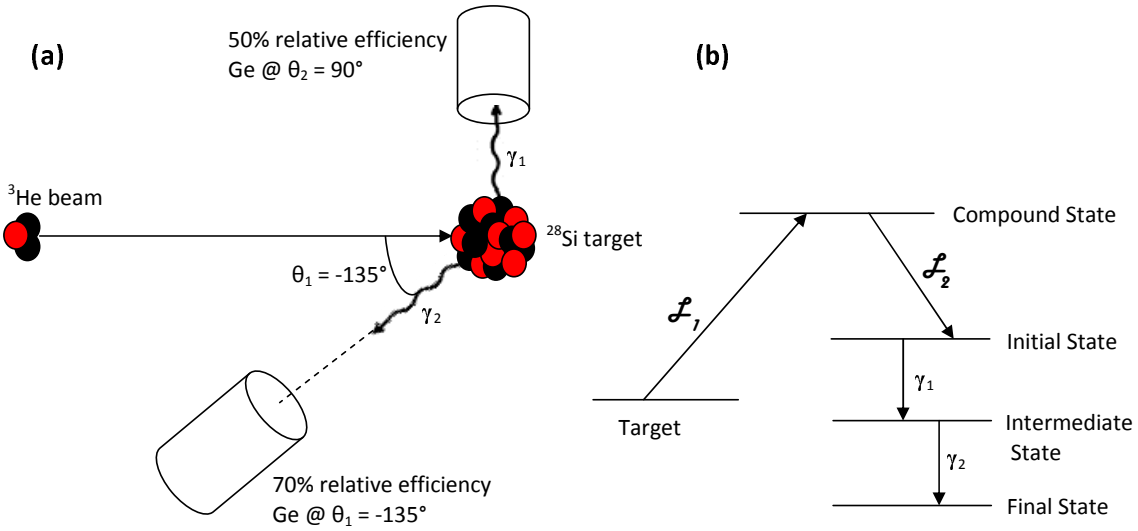

Figure 4.25: (left) Part (a) shows the schematic of the detectors setup for measuring the DCO ratios of γ-rays of ^{30}S. (right) Part (b) shows the energy level diagram of a reaction that is used for the γ-γ directional correlation measurements. For $\mathscr{L}_1$ and $\mathscr{L}_2$, see text.

a preferred direction in the space is singled out, which results in the intermediate state being oriented [1] (p. 601). Consequently, the second radiation γ_2 emitted by the aligned intermediate state also exhibits a non-isotropic intensity distribution with respect to the direction of observation of the first radiation.

In the cases when one of these states emits a γ-ray and the other emits a light particle instead, then particle-γ correlations can be observed. It is evident that for all such cases coincidence measurements are necessary. The theory of directional correlations is based on the assumption that the intermediate state does not cause any appreciable interaction as a result of spin couplings [341]. The aforementioned correlations depend on the spins of the states participating in the transitions, the FWHM of the population distributions of the initial and the intermediate states, as well as the multipolarities and mixing ratios of the γ-rays involved.

In our experiment, only γ-γ directional correlations were observed. The γ-ray polarization was not observed[39] and the beam was not polarized.

Experimentally it would be prohibitively long to determine a complete γ-γ directional correlations with data obtained at many angles. This is because the detection efficiency for coincidence measurements is much lower than that of the singles measure-

[39]Therefore, the backward and forward angles are identical [338] (p. 77).

ments. Therefore obtaining good statistics would require a long duration of time. Hence, coincidence measurements are performed in a reasonable length of time in what is essentially a two point (one angular pair with two detectors) angular correlation. The information obtained from such a measurement is not nearly as complete as one would obtain from a full angular correlation, but the simplicity of such a measurement makes it still useful.

To perform this two point angular correlation, we placed two Ge-detectors at angles 90° and -135° with respect to the beam axis during Phase II of the experiment, and measured the γ-γ coincidences. The information regarding the detectors geometries are already given in § 4.1.2. The angular correlations of ^{30}S γ-rays were then determined by measuring a ratio called the DCO ratio for each ^{30}S γ-ray that was observed at both angles. This ratio is defined as [342]:

$$R_{DCO} = \frac{W(\theta_2,\, \theta_1,\, \phi)}{W(\theta_1,\, \theta_2,\, \phi)} = \frac{I^{\gamma_2}_{\theta_1}\,(\mathrm{Gate}^{\gamma_1}_{\theta_2})}{I^{\gamma_2}_{\theta_2}\,(\mathrm{Gate}^{\gamma_1}_{\theta_1})} \tag{4.26}$$

where θ_1 and θ_2 are the angles with respect to the beam axis, at which detectors 1 and 2 are placed, respectively. A plane passes from the symmetry axis of each of these detectors together with the beam axis, and ϕ is the angle between those two planes. In our experiment both detectors and the beam were in the same plane, and thus $\phi = 0°$. γ_1 and γ_2 are two observed (in coincidence) transitions that are members of the same cascade. $W(\theta_2,\, \theta_1,\, \phi)$ is the probability that γ_2 is emitted into solid angle $d\Omega_1$ at the angle θ_1, and at the same time γ_1 is emitted into solid angle $d\Omega_2$ at the angle θ_2. This implies that γ_2 is measured by detector 1, while γ_1 is measured by detector 2. $W(\theta_1,\, \theta_2,\, \phi)$ is the reversed case. An exchange of the angles, or the gate and coincidence transitions will invert the ratio.

To understand the second fraction in equation (4.26), part (a) in Fig. 4.25 illustrates our reaction and the detectors' setup. We assume that θ_1 = -135°, and thus detector 1 is the Ge-detector with 70% relative efficiency. Similarly, the 50% relative efficiency Ge-detector is assumed to be detector 2 located at $\theta_2 = 90°$. Therefore, when a gate is set around γ_1 in the singles γ-ray spectrum measured by detector 2 at 90°, all those γ-rays that are in coincidence with γ_1 can be found in the coincidence spectrum measured by detector 1 at -135°. A particular γ-ray, e.g., γ_2, is then found in such a spectrum, and

its intensity is thus $I_{\theta_1}^{\gamma_2}$. The reverse case would then be finding γ_1 in the singles γ-ray spectrum but this time measured by detector 1 at -135°, and setting a gate around it to find the γ-rays including γ_2 in the coincidence spectrum measured by detector 2 at 90°. The intensity $I_{\theta_2}^{\gamma_2}$ is obtained this way. The ratio of the two intensities is R_{DCO}.

The aforementioned intensities are areas under the corresponding peaks corrected for the efficiency of the detector in which they are measured (see equation (4.8)). However, no finite solid angle correction is required because it is important that the intensities are measured at a particular angle and not in the full solid angle. In other words:

$$R_{DCO} = \frac{Y_{\gamma_2}^{-135^\circ}}{Y_{\gamma_2}^{90^\circ}} \frac{\epsilon_{\gamma_2}^{90^\circ}}{\epsilon_{\gamma_2}^{-135^\circ}} \frac{\epsilon_{\gamma_1}^{-135^\circ}}{\epsilon_{\gamma_1}^{90^\circ}} \tag{4.27}$$

where Y is the area or yield under each peak of interest, and ϵ is the intrinsic detector efficiency. The correction for detection efficiency of γ_1 (the gate transition) also matters because it affects the yield of this transition, and thus the yields of the γ-rays in the coincidence spectrum. An immediate conclusion is that this ratio could not be determined for the 1283.4-keV, 1405.1-keV, and 2599-keV γ-rays from the $3_1^+ \rightarrow 2_2^+$, $2_3^+ \rightarrow 2_2^+$ and $2_3^+ \rightarrow 2_1^+$ transitions in ^{30}S, respectively, because although there is evidence that they are observed at -135°, these transitions are very weak and the statistics under these peaks measured at -135° is too poor. Therefore, due to the poor peak-to-background ratio, a reasonable area could not be determined at -135° for these peaks.

The experimental DCO ratios of all other transitions of ^{30}S with reasonable peak-to-background ratios were determined by first setting a gate around the stretched quadrupole transition with 2210.6-keV energy ($2_1^+ \rightarrow 0_1^+$) observed in the singles γ-ray spectra at both angles to obtain the corresponding coincidence spectra. Then by fitting the peaks of interest in the coincidence spectra, the yields of all other transitions of ^{30}S were obtained. The yields were corrected for efficiencies as described. Therefore, from equation (4.27), the DCO rations were calculated, which are given in Table 4.4. To obtain the experimental DCO ratio of the 2210.6-keV transition, we could gate on the 1194-keV transition to get the yields of the 2210.6-keV γ-ray from the corresponding coincidence spectra at each angle. However, as mentioned before, this ratio is equivalent to the inverse of that of the 1194-keV γ-ray when the gate transition is the 2210.6-keV γ-ray, which was confirmed by following the procedure that was explained.

Table 4.4: The DCO ratios (R) for ^{30}S γ-rays observed in the present work. j_i, j_{in} and j_f are the spins of the initial, intermediate and final states, respectively. The uncertainties are in the last digit(s).

E_γ	$j_i \rightarrow j_{in} \rightarrow j_f$	σ/j	Radiation Mode	δ	R_{thoe}	R_{exp}
1194.0(1)	$2 \rightarrow 2 \rightarrow 0$	0.5[a]	$M1$, $E2$	0.16(4)[a]	1	0.92(4)
1456.5(3)	$0 \rightarrow 2 \rightarrow 0$	0.3[b]	$E2$	0[c]	1	0.94(9)
1466.2(3)	$1 \rightarrow 2 \rightarrow 0$	0.3[b]	$M1$, $E2$	-0.09(3)[d]	0.5	0.40(8)
2477.3(3)	$3 \rightarrow 2 \rightarrow 0$	0.3[b]	$M1$, $E2$	0.73(9)[d]	0.5	0.37(4)
2921.4(4)	$4 \rightarrow 2 \rightarrow 0$	0.3[b]	$E2$	0[b]	1	0.99(11)

[a]Determined experimentally from angular distribution measurements.
[b]See § 4.3.4.
[c]From selection rules.
[d]This mixing ratio belongs to the mirror transition (see Ref. [187]).

An attempt to calculate the theoretical DCO ratios via an updated version of a code called AngCor [343] compatible with GNU/Linux systems failed. This code was obtained via private communication with Dr. Krishichayan [344]. The theoretical formalism used in this code was carefully double checked. However, this code failed to reproduce the experimental DCO ratios obtained in the present work and a couple of test models found in the literature. The reason remains to be determined. Therefore, we have adopted the theoretical DCO ratios of Ref. [345] that are determined for general cases.

The interpretation of the data presented in Table 4.4 is the subject of discussion in the next section. The γ-ray energies mentioned below are already corrected for the corresponding recoil energies given in Table 4.2 on page 184.

4.3.4 Conclusions on ^{30}S γ-Ray Transitions

• ***The 2210.7-keV γ-ray:*** This transition corresponds to the decay of the 2210.7-keV state of ^{30}S to the ground state. The spin-parity of the 2210.7-keV state is already known to be $J^\pi = 2^+$ from various previous measurements, and our derived angular distribution parameters (see Table 4.3 on page 198) confirm this.

• ***The 1194-keV γ-ray:*** This transition corresponds to the decay of the 3404.7-keV state of ^{30}S to the 2210.7-keV state. The spin-parity of the 3404.7-keV state is already established to be $J^\pi = 2^+$ from various previous measurements, and our derived angular

distribution parameters (see Table 4.3 on page 198) most likely confirm this. Moreover, the experimental DCO ratio obtained from the present work for the $2_2^+ \rightarrow 2_1^+ \rightarrow 0_1^+$ cascade agrees with the theoretical ratio within 2σ-level. According to the prescriptions presented in Ref. [345] (p. iv), when the transition on which the gate is set (the 2210.7-keV transition in our case) is a stretched quadrupole transition connecting two states with $\Delta j = 2$ (where Δj is the difference in spins of the initial and final states), the theoretical DCO ratio is equal to unity if the transition of interest (for example the 1194-keV γ-ray) is either a stretched quadrupole itself (connecting two states with $\Delta j = 2$) or it is a pure dipole transition connecting two states with $\Delta j = 0$. Since we know that both the 3404.7-keV and 2210.7-keV states of ^{30}S are 2^+ states, Δj must be equal to 0 for the 1194-keV γ-ray, and based on the suggestions of Ref. [345], this transition must be a pure dipole. However, the fact that our experimental DCO ratio is slightly lower than the theoretically estimated value seems to imply that the 1194-keV transition is not a pure dipole, as is evident from the resulting $\delta = 0.16 \pm 0.04$ obtained from our angular distribution measurements. This result is in excellent agreement with the mixing ratio of 0.18 ± 0.05 [187] for the mirror transition in ^{30}Si. The fact that the mixing ratio we have obtained for the 1194-keV γ-ray is small indicates that this transition is almost a pure dipole transition (see equation (4.20)) that is roughly consistent with the conclusions we made above. Thus, we confirm that this state is the 2_2^+ state of ^{30}S.

• ***The 1456.5-keV γ-ray:*** This transition corresponds to the decay of the 3667.2-keV state of ^{30}S to the 2210.7-keV state. The experimental DCO ratio is consistent with unity, suggesting that the transition from the 3667.2-keV state to the 2210.7-keV state has the same multipolarity as that of the decay of the 2210.7-keV state to the ground state [342], i.e., a stretched quadrupole. This assumption implies that the 3667.2-keV state is the 0_2^+ state in ^{30}S, because from the mirror nucleus, no other possibilities are expected in this energy range. This assumption is confirmed by the theoretical DCO ratio that is obtained for the $0_2^+ \rightarrow 2_1^+ \rightarrow 0_1^+$ cascade. The alignment factor of $\sigma/j = 0.3$ is the default value, which is widely accepted in the literature for the cases where no experimental information is available for this parameter. That is why, for all other transitions we have assigned σ/j to be 0.3.

• ***The 1466.2-keV γ-ray:*** This transition corresponds to the decay of the 3676.9-keV state of ^{30}S to the 2210.7-keV state. Being very close in energy to the 3667.2-keV

state, the 3676.9-keV state must be the 1^+ member of the doublet, now that we have confirmed the former is the 0^+ member. Based on Ref. [345] and under the assumption that $\sigma/j = 0.3$, if the DCO ratio is ≈ 0.5, the transition is in general $\Delta j = 1$ (stretched dipole, i.e., pure $E1$ or $M1$). The experimental DCO ratio obtained for this case is consistent with the theoretical value at the 2σ level, which implies that the 3676.9-keV state is most likely the 1^+_1 state of ^{30}S. However, the $1^+_1 \rightarrow 2^+_1$ transition in the mirror nucleus is a mixed $M1$, $E2$ transition with a small mixing ratio of -0.09(3) [187]. This mixing ratio is small enough that the $M1$ transition dominates (see equation (4.20)), and we can perhaps say that the $1^+_1 \rightarrow 2^+_1$ in ^{30}Si is an almost pure dipole transition. We could not determine the mixing ratios of any of the transitions observed via our angular correlation measurements. Therefore, we have assigned the mixing ratio to be -0.09(3) for this transition in ^{30}S. In conclusion, we suggest $J^\pi = 1^+$ for the 3676.9-keV state of ^{30}S.

• ***The 2477.3-keV γ-ray:*** This transition corresponds to the decay of the 4688.1-keV state of ^{30}S to the 2210.7-keV state. From the results of our ^{32}S$(p,t)^{30}$S measurement, we expect the 4688.1-keV state to be the 3^+_1 state in ^{30}S. Moreover, the decay branches of this state also agree with those of the mirror state [285]. Our experimental DCO ratio is significantly different from 0.5, and thus based on the theory prescribed by Ref. [345], we expect that $\Delta j = 1$, and that this transition is a mixed $M1$, $E2$ transition. Therefore, the experimental DCO ratio also supplements the results obtained from our transfer reaction experiment regarding the spin of the 4688.1-keV state. We have adopted the mixing ratio of the mirror transition ($\delta = 0.73(9)$ [187]) for this γ-ray due to the lack of knowledge of its own mixing ratio.

• ***The 2599.1-keV γ-ray:*** This transition corresponds to the decay of the 4809.8-keV state of ^{30}S to the 2210.7-keV state, which is a very weak transition at -135°. Therefore, no experimental DCO ratio could be obtained for this transition. However, we have assigned a tentative $J^\pi = 2^+$ to the 4809.8-keV state of ^{30}S based on the results of our transfer reaction experiment and those mentioned in Ref. [285].

• ***The 2921.4-keV γ-ray:*** This transition is from the decay of the 5132.3-keV state to the 2210.7-keV state, and is one of the rare cases where the result of the theoretical calculation from AngCor is consistent with the experimental result, both of which are also consistent with the theoretical predictions given in Ref. [345] under the assumption

that the 5132.3-keV $\rightarrow$ 2210.7-keV $\rightarrow$ g.s. transition is a stretched quadrupole with $\Delta j = 2$. This indicates that the 5132.3-keV state is either the 4_1^+ state of ^{30}S or the 0_3^+ state. The former is much more probable, because a comparison with the mirror transitions in ^{30}Si reveals that the 4_1^+ level at 5279.37 keV in ^{30}Si decays with a 100% branch to the first excited 2_1^+ state [187], which is consistent with what we observe for the 5132.3-keV state in ^{30}S, as well as what was observed for the same state in Ref. [173]. If the latter state were the 0_3^+ state, based on its decay scheme in the mirror nucleus, we would have expected to observe other decay branches from this state with comparable strengths in addition to the 2921.4-keV γ-ray transition [187]. From these arguments, we tentatively assign $J^\pi = 4^+$ to the 5132.7-keV level of ^{30}S.

Having described both experiments performed to investigate some of the nuclear properties of ^{30}S that play an important role in determination of the $^{29}\mathrm{P}(p,\gamma)^{30}\mathrm{S}$ thermonuclear reaction rate, we new turn our attention to the calculation of this reaction rate and exploration of its impact on the silicon abundance ratios at the temperatures characteristic of explosive nucleosynthesis in novae.

Chapter 5

The ^{29}P$(p,\gamma)^{30}$S Reaction Rate and its Astrophysical Implications

Nuclear structure and nuclear dynamics play an important role in astrophysics. The occurrence (or non-occurrence) of a certain state at a given excitation energy can change the reaction rate by many orders of magnitude, and consequently the abundance of the elements involved may changed significantly.

As mentioned in the two previous chapters, we have observed an excited state in ^{30}S for the first time around 4.8 MeV. The existence of this level was previously predicted [149]. However, the predicted theoretical energy was uncertain by 40 keV. In our experiments, not only could we measure the energy of this state to within a few keV, but we also confirmed the existence of another previously known state around 4.7 MeV, and our measured energy for the latter state is constrained to better than 40% with respect to the previously measured value [150].

Both of these two states are above the proton threshold (4394.9 keV), and thus are considered to be resonances. The ^{29}P$(p,\gamma)^{30}$S reaction rate was predicted to be dominated by these two resonances at the temperature characteristic of explosive hydrogen burning in novae [149] ($T = 0.1 - 0.4$ GK). Therefore, it seemed necessary to determine the effects of these updated energies on the ^{29}P$(p,\gamma)^{30}$S reaction rate.

A summary of reaction rate formalism was given in Chapter 2. Here we present the required input and the results of the calculation of the ^{29}P$(p,\gamma)^{30}$S thermonuclear reaction rate based on the formalism given previously and the new state-of-the-art Monte Carlo

method which is explained in detail in Refs. [129, 134–136], and thus is not presented here again.

Lastly, the updated $^{29}\mathrm{P}(p,\gamma)^{30}\mathrm{S}$ thermonuclear reaction rate was used as an input to a particular stellar nucleosynthesis model of novae [68, 346] to determine the effect of this updated rate on the resultant silicon abundances produced by nova nucleosynthesis. Here we present the results of the latter calculation.

5.1 The ^{30}S Weighted Average Excitation Energies

We decided to investigate the rate of the $^{29}\mathrm{P}(p,\gamma)^{30}\mathrm{S}$ reaction in the temperature range characteristic of explosive hydrogen burning in novae, as well as type I X-ray bursts ($T = 0.1$ – 1.3 GK). The Gamow window for this temperature range spans $E_{cm} \approx 70$ – 1770 keV. The reaction rate is thus dominated by contributions from direct capture, as well as isolated and narrow $^{29}\mathrm{P} + p$ resonances corresponding to ^{30}S states with $4470 \lesssim E_x \lesssim 6000$ keV.

Prior to the calculation of the reaction rate, it is essential to know the energies of the excited states of ^{30}S in this range averaged over all independent measurements. The previous measurements are already described in Chapter 2, and the results are given in Tables 2.1 to 2.3 on pages 37 to 39.

Table 5.1 presents the results of our measurements on ^{30}S excitation energies below 6 MeV, and the corresponding spin/parities. The excited states whose energies are below 4.47 MeV also become important as shall be seen later in determination of the non-resonant contributions to the $^{29}\mathrm{P}(p,\gamma)^{30}\mathrm{S}$ reaction rate. The fifth and sixth columns in Table 5.1 respectively present the ^{30}S excitation energies averaged over all independent measurements, and the conclusions we have drawn on the spins and parities of ^{30}S states based on the results of all independent measurements including ours. The weighted average energies are calculated with the AveTools software. Those states that were used as internal calibration points in any of the measurements are not included in the calculation of the weighted average energies, as they are not considered to be independently measured. The last column in Table 5.1 presents the resonance energies corresponding to those states that are above the proton threshold ($Q = 4394.9$ keV).

Table 5.1: Energy levels of ^{30}S from this work for those excitation energies that are below 6 MeV. The states used as internal calibration points in our ^{32}S$(p,t)^{30}$S measurement are not shown here. The uncertainties are in the last digit(s).

Present Work ^{32}S$(p,t)^{30}$S		Present Work ^{28}Si(^{3}He, $n\gamma$)^{30}S		Weighted Average [a] (all measurements)		E_r (keV)[b]
E_x (keV)	J^π	E_x (keV)	J^π	E_x (keV)	J^π	
		g.s.		g.s.	0^+	
2208(3)		2210.7(3)	2^+	2210.6(3)	2^+	
		3404.7(3)	2^+	3403.6(6)	2^+	
		3667.2(4)	0^+	3667.0(5)	0^+	
3681(3)	$(1^+, 0^+)$	3676.9(4)	1^+	3677.0(4)	1^+	
4688(2)	3^+	4688.1(4)	3^+	4688.1(4)	3^+	293.2(8)
4812(2)	(2^+)	4809.8(5)		4809.8(6)	(2^+)	414.9(9)
	(4^+)[c]	5132.3(5)	(4^+)	5132.6(8)	(4^+)	737.7(11)
5225(2)	(0^+)			5221(2)	(0^+)	826(2)
5315(2)	$(3^-, 2^+)$			5314(4)	(3^-)[d]	919(4)
5393(2)	(3^+)			5391(2)	(3^+)	996(2)
5849(2)	$(1^-, 2^+, 4^+)$			5847(2)	$(2^+)^a$	1452(2)
5947(2)				5946(3)	$(4^+)^a$	1551(3)

[a] See text.

[b] $E_r = E_x - Q$, where E_r is the resonance energy, E_x is the weighted average excitation energy and Q is the proton threshold of the ^{29}P$(p,\gamma)^{30}$S reaction, which is 4394.9-keV. Those excitation energies for which no resonance energy is reported correspond to the bound states of ^{30}S.

[c] The corresponding energy (5136(2) keV) was used as internal calibration point, and is thus not reported here.

[d] This state is most likely the 5288(10) keV state observed by Yokota *et al.* [169], which was assigned to be the 3^-_1 state in ^{30}S.

When calculating the weighted average energies, one has to first correct for any possible consistent shift in energies of one or more measurements with respect to the other measurements. If for instance, all energies of a data set are consistently higher or lower than those of every other measurements by a difference larger than 2σ, then that single measurement has to first be re-calibrated with respect to a standard[1] data set [250]. Such consistent shifts were not observed in any of the data sets we used for ^{30}S excitation energies. Thus, none of the energies of the independent measurements were modified.

The J^π value of the 1452(2) keV resonance in ^{30}S is tentatively assigned to be 1^- in Ref. [150], but it is also mentioned in that reference that due to poor statistics for this

[1] This could be the most precise independent measurement, e.g., a γ-ray measurement.

particular resonance, $l = 2$ or 3 transfers are not excluded. Therefore, the corresponding J^π value for this resonance could also be 2^+ or 3^-. Since, the J^π value for the 996(2) keV resonance fits best with a 3^+ assignment, and we have assigned the 919(4) keV resonance to be the 3^-_1 state, we assigned the 1452(2) keV resonance to be the 2^+_4 state in ^{30}S.

The 1551(3) keV resonance has only been observed in the measurement of Ref. [180] and in our ^{32}S$(p,t)^{30}$S measurement. However, none of these measurements could assign a J^π value to this resonance. Therefore, from the results of a recent shell model calculation [283, 284] we noticed that the energies of the 4^+_2 states in ^{30}S and ^{30}Si (mirror nucleus) are almost identical to each other. The excitation energy of the 4^+_2 state in ^{30}Si is 5950.73(15) keV [187]. On the other hand, the weighted average energy between the result of Ref. [180] and our ^{32}S$(p,t)^{30}$S measurement for the corresponding state in ^{30}S is 5946(3) keV. Therefore, we concluded that this latter state is most likely the mirror to the 4^+_2 state in ^{30}Si at 5950.73(15) keV.

Now that the weighted average energies of ^{30}S are obtained, we proceed to the calculation of the ^{29}P$(p,\gamma)^{30}$S reaction rate.

5.2 The ^{29}P$(p,\gamma)^{30}$S Thermonuclear Reaction Rate

The reaction rate is calculated based on equation (2.3). The functional form of $\sigma(E)$ in this equation depends on the mechanism by which the ^{29}P$(p,\gamma)^{30}$S reaction takes place: non-resonant *vs.* resonant. In the former case, one has to determine the astrophysical S-factor, $S(E)$, from equation (2.10) to be able to calculate the reaction rate from equation (2.6). The resonant reaction rate, on the other hand, is calculated from equation (2.21) under the assumption that the resonances are narrow.

We begin the calculation of the ^{29}P$(p,\gamma)^{30}$S reaction rate with the non-resonant contribution, and describe how the S-factor is determined. We then proceed to the resonant contribution, and elaborate on the input required for its quantitative calculation.

5.2.1 Non-Resonant Reaction Rate Input

The non-resonant contribution to the ^{29}P$(p,\gamma)^{30}$S rate comes from the capture of a proton directly into the bound states of the compound nucleus ^{30}S (see Table 5.1). Direct capture reactions are explained in Chapter 2.

The astrophysical reaction of interest is:

$$^{29}P + p \rightarrow {}^{30}S + \gamma$$

The incoming proton has an intrinsic spin of $1/2$, and carries an initial orbital angular momentum L_i. ^{29}P is assumed to be in its ground state, which has $J^\pi = \frac{1}{2}^+$, and the radiation mode of the γ-ray could be, in terms of decreasing transition probability, $E1$, $M1$ or $E2$. The $M1$ and $E2$ contributions to the direct capture process are usually negligible compared to the $E1$ contributions [268]. Detailed calculations show that the $M1$ and $E2$ contributions amount to less than 0.1% of the dominant $E1$ contribution [347]. If however the $E1$ contribution is inhibited, then the $M1$ and $E2$ transitions may form the dominant contributions in the direct capture process [347].

In order to calculate the direct capture reaction rate, one has to first calculate the contribution of the direct capture to the astrophysical S-factor (called the direct capture S-factor) as a function of bombarding energy, which can then be integrated to give the non-resonant reaction rate.

The incoming proton can be directly captured into the ground state or any of the four bound states of ^{30}S. Each of these states has a well defined spin/parity given in Table 5.1. Therefore, the contribution of each of these bound states, as well as that of the ground state of ^{30}S, to the direct capture S-factor has to be separately calculated. This calculation was performed with a program obtained from Ref. [268] which is not publicly available.

Although the $M1$ transitions are negligible, the contribution of the ground state and each of the bound states of ^{30}S to the direct capture S-factor was calculated by separately taking into account the $E1$ and $M1$ nature of the transitions. $E2$ transitions were neglected. For each of these radiation modes, the L_i values and the orbital angular momenta L_f for the shell model orbitals, from which the proton is transferred, were calculated separately based on the momentum and parity conservation laws. These values are given in Table 5.2.

For those final states in ^{30}S that have more than one allowed value of L_i, the contributions of those final states to the direct capture S-factor were calculated for each of their L_i values, and then those contributions were added together at each proton bombarding

Table 5.2: Some of the required input for calculation of the direct capture S-factor for the ^{29}P + $p \rightarrow {}^{30}$S + γ direct capture reaction.

E_x (keV)	J^π	Radiation Mode				C^2S^a
		$E1$		$M1$		
		L_i	L_f	$L_i{}^b$	L_f	
0	0^+	1	0	2	0	0.90
2210.6(3)	2^+	1,3	2	2,4	2	0.732
3403.6(6)	2^+	1,3	2	2,4	2	0.124
3667.0(5)	0^+	1	0	2	0	0.70
3677.0(4)	1^+	1,3	0,2	2	0,2	0,0.733^c

[a] C^2 is the square of the isospin Clebsch-Gordan coefficient, which depends on the nuclear reaction. S is the spectroscopic factor defined in the text. The C^2S values are taken from Ref. [348].

[b] For $M1$ transitions, $L_i = 0$ is allowed for all J^π values. However, when $L_i = 0$, the resulting contribution to the S-factor is zero for all bombarding energies.

[c] The C^2S values for $L_f = 0$ and 2 are respectively zero and 0.733 (see Ref. [348]).

energy. The latter is defined by the user, and is one of the inputs to the program.

Each transition was then weighted by the corresponding spectroscopic factor to take into account the relative probability that the nucleons may arrange themselves into configurations such that the specific level of interest in ^{30}S, produced by direct proton capture, can be simulated as a ^{29}P core plus a single particle projectile (proton) orbiting around it. This probability is measured by a parameter called the spectroscopic factor denoted by S, which takes into account the nuclear structures of the initial and final nuclei [349]. In a reaction of the form $A + a \rightarrow B$, this factor is a measure of the overlap between the final state's wave function and the initial state's wave function [1] (p. 49), where the final state is B and the initial state is $A + a$.

No experimental information is available for the spectroscopic factors of ^{30}S states[2], and therefore such parameters were determined from those of the mirror states measured by Mackh *et al.* [348].

Finally, at each bombarding energy the weighted direct capture S-factor contributions from each state of ^{30}S were added together to derive the total direct capture S-factor as a function of proton bombarding energy for a particular radiation mode. The results of

[2] The spectroscopic factors can be obtained experimentally from single nucleon transfer reactions (see Ref. [349]).

Table 5.3: The direct capture S-factor for the $^{29}\mathrm{P}(p,\gamma)^{30}\mathrm{S}$ reaction for selected proton bombarding energies.

E^a (keV)	S-factor (keV·b) For $E1$	S-factor (keV·b) For $M1$	S-factor (keV·b) Total[b]
30	82.71332	0.33061	83.04393
60	81.87205	0.34290	82.21494
90	81.07711	0.35531	81.43242
120	80.32502	0.36786	80.69288
150	79.61114	0.38053	79.99167
180	78.93368	0.39333	79.32701
210	78.28655	0.40624	78.69278
240	77.66728	0.41928	78.08656
270	77.07571	0.43243	77.50814
300	76.50805	0.44571	76.95376
330	75.96186	0.45910	76.42096
360	75.43504	0.47260	75.90764
390	74.92771	0.48622	75.41393
420	74.43679	0.49996	74.93675
450	73.96235	0.51380	74.47615
480	73.50323	0.52776	74.03099
510	73.05571	0.54182	73.59753
540	72.62222	0.55600	73.17822
570	72.19975	0.57026	72.77001
600	71.78969	0.58465	72.37434
630	71.38793	0.59912	71.98706
660	70.99604	0.61371	71.60976
690	70.61258	0.62840	71.24098
720	70.23772	0.64318	70.88089
750	69.87048	0.65806	70.52854
780	69.51101	0.67304	70.18406
810	69.15865	0.68811	69.84677
840	68.81163	0.70329	69.51492
870	68.46923	0.71854	69.18777
900	68.13328	0.73389	68.86717
930	67.80294	0.74933	68.55227
960	67.47802	0.76485	68.24287
990	67.15640	0.78048	67.93688
1000	67.05022	0.78570	67.83592

[a]The proton bombarding energy.
[b]This is the sum of the two previous columns.

this calculation are presented in Table 5.3. It is evident that the $E1$ transitions do indeed dominate, and that the $M1$ contributions to the direct capture S-factor are negligible.

When the direct capture S-factor is determined, it is plotted *vs.* proton bombarding energy, and is fitted with a polynomial of the form given in equation (2.10) to determine the fit parameters, i.e., $S(0)$ (in keV·b), $S'(0)$ (in b) and $S''(0)$ (in b/keV). The direct capture S-factor and its fit are shown in Fig. 5.1.

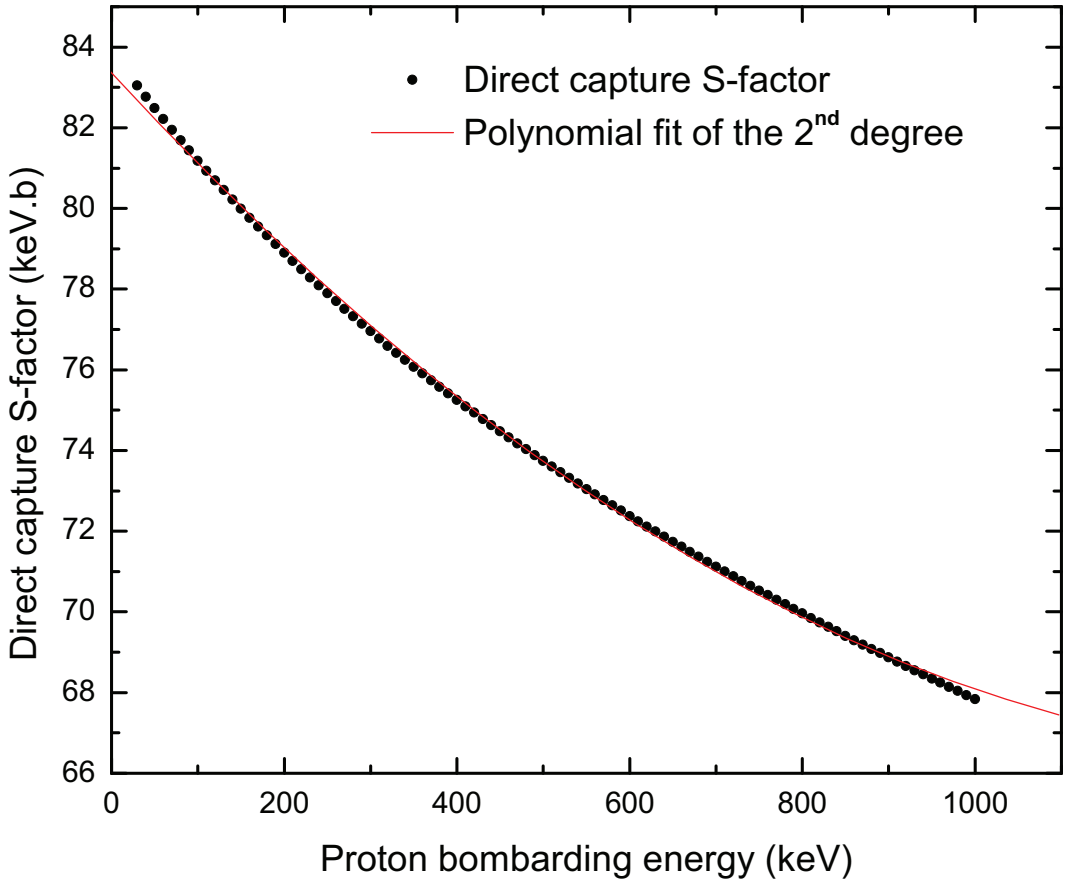

Figure 5.1: Total direct capture S-factor for the $^{29}\mathrm{P}(p,\gamma)^{30}\mathrm{S}$ reaction as a function of energy. This S-factor is a smooth decreasing function of energy. The red solid curve is the 2^{nd} degree polynomial fit. The numerical values are given in Table 5.3.

An uncertainty of 40% for the direct capture S-factor is adopted following the approach of Ref. [135]. From the fit parameters for the direct capture S-factor of the $^{29}\mathrm{P}(p,\gamma)^{30}\mathrm{S}$ reaction, we have:

$$S(E) \approx 7.9 \times 10^{+1} - 1.1 \times 10^{-2}\,E + \frac{1.3 \times 10^{-6}}{2}\,E^2 \tag{5.1}$$

The $S(E)$ in equation (5.1) generally indicates the total astrophysical S-factor as opposed to the direct capture S-factor. With increasing proton bombarding energy, the resonances in ^{30}S will eventually also become important, and the total astrophysical S-factor would then be the sum of the direct capture S-factor plus the contributions of the resonances to the astrophysical S-factor. This total astrophysical S-factor as seen in Fig. 5.2 is not a smooth varying function of energy anymore. Therefore, equation (5.1) is only valid for a certain range of bombarding energies because the fit parameters we obtained are only for the direct capture S-factor.

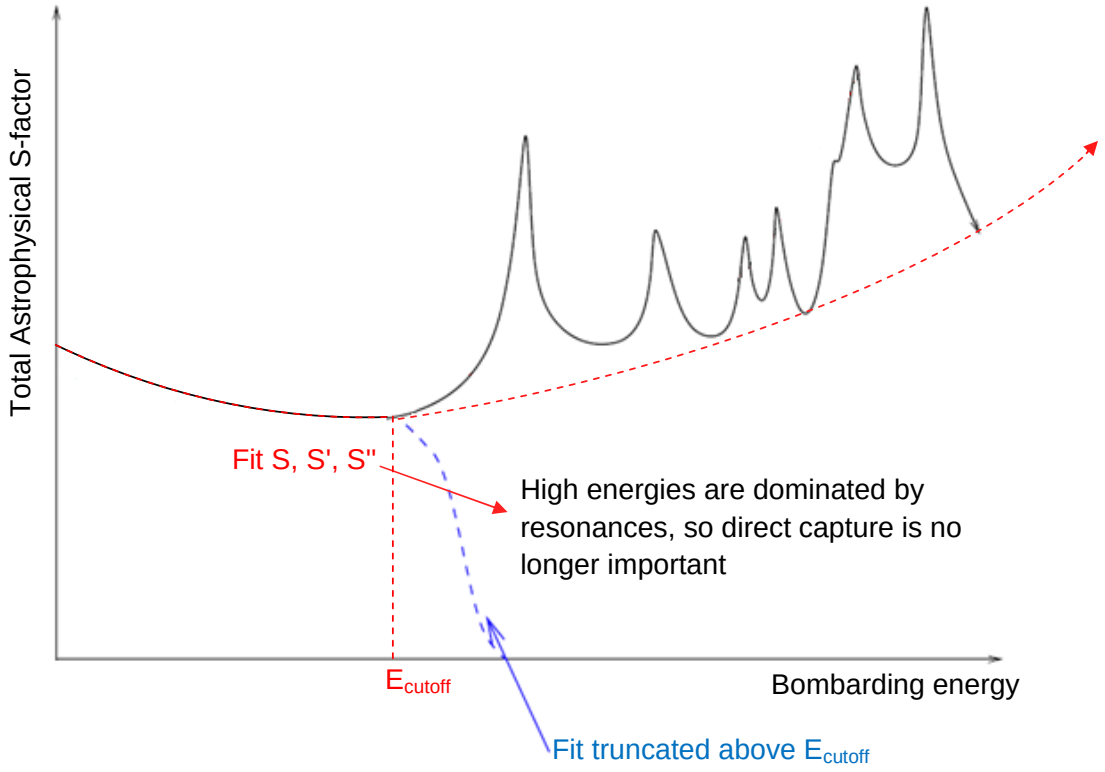

Figure 5.2: The total astrophysical S-factor as a function of bombarding energy. The cutoff energy is shown. The figure is obtained from Ref. [350].

Equation (5.1) becomes invalid for energies above the so-called cutoff energy, after which the direct capture S-factor deviates from the total astrophysical S-factor. The cutoff energy occurs at $\sim$ 1000 keV for the astrophysical reaction of interest to this work [135].

According to Ref. [135], the cutoff temperature (in GK) for this cutoff energy (in

MeV) is:

$$T_{9,\mathrm{cutoff}} = \sqrt{E^3_{\mathrm{cutoff}}}\,\frac{19.92}{\sqrt{(Z_pZ_t)^2\,\dfrac{m_pm_t}{m_p+m_t}}} = 1.3 \tag{5.2}$$

where T_9 is the temperature in units of GK; Z_p and Z_t are the atomic numbers for the projectile (proton) and the target (^{29}P), respectively; and m_p and m_t are the masses (in amu) of the projectile and the target, respectively.

The non-resonant reaction rate is multiplied by the following cutoff factor [129] to account for the region over which the S-factor expansion given by equation (5.1) becomes inaccurate:

$$f_{\mathrm{cutoff}} \approx \exp\left[-\left(\frac{T_9}{T_{9,\mathrm{cutoff}}}\right)^2\right] \tag{5.3}$$

5.2.2 Resonant Reaction Rate Input

To calculate the contributions of the resonances of ^{30}S to the reaction rate, one needs to know the resonance strengths (see equations (2.22) and (2.23)) corresponding to the resonances listed in Table 5.1. Thus, a theoretical estimation of the partial widths of each resonance is necessary because this information is not currently available experimentally.

We first describe the calculation of the γ-ray partial widths, Γ_γ, and then proceed to the proton partial widths Γ_p.

- **Calculation of the Partial γ-Ray Widths (Γ_γ's):**

The γ-ray partial widths corresponding to the resonances of ^{30}S have to be estimated from those of the associated mirror levels in ^{30}Si. The proton threshold in ^{30}Si, e.g., the Q-value of the $^{29}\mathrm{Al}(p,\gamma)^{30}\mathrm{Si}$ reaction, is 13.507 MeV [241]. Therefore, the mirror levels of interest in ^{30}Si are all bound states, and decay solely via γ-ray emission since no other decay channel is open for them. Hence, for the latter states the particle partial widths are zero, and thus:

$$\Gamma_{\mathrm{tot}} = \Gamma_{\gamma,\mathrm{tot}} = \frac{\hbar}{\tau} = \frac{\hbar\,\ln 2}{t_{1/2}} \tag{5.4}$$

where Γ_{tot} and $t_{1/2}$ are the total decay width and the half-life of each of the mirror levels in ^{30}Si, respectively. The total γ-ray width of each state in ^{30}Si is the sum of the partial γ-ray widths, each of which corresponds to a decay from that state to a specific low-lying level (see equation (4.10)). Each of these decay transitions has a branching ratio

and possibly a mixing ratio, which can be used together with the total γ-ray width to calculate the partial γ-ray widths corresponding to a state of interest in ^{30}Si as follows [1] (p. 54):

$$\Gamma_j(\overline{\omega'}L) = \frac{1}{1+\delta_j^2}\frac{B_j}{100}\Gamma_{\gamma,\text{tot}} \tag{5.5}$$

$$\Gamma_j(\overline{\omega}L+1) = \frac{\delta_j^2}{1+\delta_j^2}\frac{B_j}{100}\Gamma_{\gamma,\text{tot}} \tag{5.6}$$

where $\overline{\omega'}L$ and $\overline{\omega}L+1$ are the magnetic and electric transitions of multipolarity L, and $L+1$, respectively; B_j is the branching ratio; and δ_j is the mixing ratio defined in equation (4.20).

The half-lives, branching and mixing ratios of the levels of interest in ^{30}Si are all experimentally known and the information is given in Ref. [187]. The only exceptions are that some mixing ratios of the transitions of interest in ^{30}Si are not determined experimentally or theoretically. In those cases, we have assumed that such transitions are pure and the multipolarities are assumed to be the dominant multipolarity of the actual mixed transition.

The states of interest in ^{30}S however are resonances above the proton threshold, and thus decay via γ-ray emission, as well as proton emission. So for ^{30}S resonances:

$$\Gamma_{\text{tot}} = \Gamma_p + \Gamma_\gamma \tag{5.7}$$

The partial widths are energy dependent. Thus, to calculate the γ-ray partial widths of each of the ^{30}S states of interest, the individual corresponding partial γ-ray widths of the associated mirror levels in ^{30}Si have to be scaled to account for the differences in energies of the levels between each mirror pair, assuming similar decay branches and reduced transition probabilities. The scaling is performed by the following equation, which comes from the Weisskopf estimates given on page 51 of Ref. [1]:

$$\left(\frac{E'_\gamma}{E_\gamma}\right)^{2L+1} = \frac{\Gamma'_j}{\Gamma_j} \tag{5.8}$$

where L is multipolarity, and the primed parameters belong to ^{30}S and the other parameters belong to ^{30}Si. Once the partial γ-ray widths of each state of ^{30}S, Γ'_j, are calculated

based on the above equation, then they can be added together (see equation (4.10)) to obtain the total γ-ray width of that state given in equation (5.7). The results of this calculation are given in § 5.2.3.

For the 2_4^+ state in ^{30}Si, only an upper limit is known for its half-life. Hence, this method of calculation of the γ-ray partial width is not possible for the 2_4^+ state in ^{30}S. Therefore, we considered the 0.012 eV value based on Ref. [135] for the total γ-ray width of the 2_4^+ resonance in ^{30}S, and scaled this to account for the differences in energies of this resonance between our work and that of Ref. [135].

Following the procedure discussed in Ref. [135], the uncertainties in γ-ray widths are assumed to be 50%.

- **Calculation of Proton Widths (Γ_p's):**

The proton widths of the resonances of ^{30}S are estimated from the following formula, which is standard for their theoretical estimation [129]:

$$\Gamma_p = \frac{2\hbar^2}{\mu R^2} P_l C^2 S \theta_{sp}^2 \tag{5.9}$$

where μ is the reduced mass; R is the radius (in fm) of the entrance channel, defined as $R = r_0(A_p^{1/3} + A_t^{1/3})$ with $r_0 = 1.25$ fm, and A_p and A_t are the mass numbers of the projectile (proton) and the target (^{29}P), respectively; C^2 is the square of the isospin Clebsch-Gordan coefficient and S is the spectroscopic factor containing the information on nuclear structure; θ_{sp}^2 is the "observed" dimensionless reduced single-particle width for proton decay, as opposed to the "formal" width [351]; and P_l is the penetration factor, i.e., the probability that the proton will penetrate the Coulomb and centrifugal barriers. This factor is strongly energy dependent and can be computed precisely from Coulomb wave functions.

The penetrability factor for each resonance was calculated using numerically computed Coulomb wave functions and a radius parameter $r_0 = 1.25$ fm. These calculations were performed via a code obtained from Ref. [276]. For calculation of particle partial widths only the product of C^2S is of interest. These factors were determined from neutron spectroscopic factors of the mirror states measured with the ^{29}Si$(d,p)^{30}$Si reaction [348], which is a nucleon stripping reaction. The theoretical spectroscopic factor S does not distinguish between proton and neutron stripping. The isospin Clebsch-Gordan

coefficient C takes care of the fact that the stripped nucleon is either a proton or a neutron [349] (p. 148). The neutron structures of ^{29}Si and ^{30}Si (with 15 and 16 neutrons, respectively) are most likely similar to the proton structures of ^{29}P and ^{30}S (with 15 and 16 protons, respectively). Thus, there might be some similarities in the strengths to specific ^{30}S levels populated in the $^{29}\mathrm{P}(p,\gamma)^{30}\mathrm{S}$ reaction and the corresponding ^{30}Si levels populated in the $^{29}\mathrm{Si}(d,p)^{30}\mathrm{Si}$ reaction [352]. Moreover, the $^{29}\mathrm{Si}(d,p)^{30}\mathrm{Si}$ reaction is the mirror of the $^{29}\mathrm{P}(d,n)^{30}\mathrm{S}$ reaction, which could be used directly to experimentally determine the neutron spectroscopic factors of the ^{30}S states.

The mirror levels in ^{30}Si corresponding to the resonances of ^{30}S at 737.7-keV, 826-keV and 1551-keV were populated very weakly in the measurement of Ref. [348], and thus no C^2S values could be determined experimentally for these levels. Hence, an upper limit $C^2S \leq 0.01$ is adopted for these states, based on the sensitivity for the extraction of small spectroscopic factors in the measurement of Ref. [348].

Finally, the observed θ_{sp}^2 factors were estimated from equation (11) and Table 1 in Ref. [353]. The only exceptions were the 4^+ states corresponding to the resonances at 737.7-keV and 1551-keV. The reduced widths of these resonances could not be determined from the approach of Ref. [353], which is limited to single-particle states in the $sd-fp$ shells. Consequently, $\theta_{sp}^2 \leq 1$ is assumed for these states, which is an upper limit widely accepted in the literature when no value can be calculated.

Following the procedure of Ref. [135], the uncertainties in the proton widths were estimated to be 40%. The proton widths of the resonances of interest to this work are given in § 5.2.3.

5.2.3 The $^{29}\mathrm{P}(p,\gamma)^{30}\mathrm{S}$ Monte Carlo Rate Input File

The input file required for Monte Carlo calculation of the $^{29}\mathrm{P}(p,\gamma)^{30}\mathrm{S}$ reaction rate is given here. Each input row and its parameters are explained in Ref. [135], and thus we do not elaborate on these parameters here again. However, the γ-ray multipolarities, $L2$ factors, are considered to be unity for the $E1$ transitions that are dominant. The orbital angular momenta ($L1$ factors) for each resonance are computed by the momentum and parity conservation laws. Following the recommendation of Ref. [354], the fractional standard deviation in C^2S (`fracErr` parameter) is taken to be 0.4 for those nuclei with valence nucleons in the sd-shell. All resonances are considered to be narrow. The res-

onance parameters for all ^{30}S resonances of interest are known as relatively precisely as is possible from theoretical estimations, except the 1452-keV resonance for which only a rough γ-ray width is estimated. Therefore, the contributions of all resonances to the rate except that of the 1452-keV resonance can be calculated numerically by integrating over the shapes of the resonances to take into account their tails' contributions [268]. However, the contribution of the 1452-keV resonance must be calculated analytically [268] because the γ-ray width of this resonance is not well known, and neither is its shape. Hence, the `Int` parameter is unity for all resonances except for the 1452-keV resonance. The results of the calculation of the $^{29}\mathrm{P}(p,\gamma)^{30}\mathrm{S}$ reaction rate are given next.

Finally, in Ref. [135], the rates of most of the astrophysically important thermonuclear reactions have been calculated with the new Monte Carlo technique using 5000 samples. However, for our reaction rate there were 5% statistical fluctuations with the 5000 samples [350], so we used 10000 random samples instead.

```
29P(p,g)30S
********************************************************************************
1                       !  Zproj
15                      !  Ztarget
0                       !  Zexitparticle (only 2 channels are open)
1.007825                !  Aproj
28.98180                !  Atarget
0                       !  Aexitparticle
0.5                     !  Jproj
0.5                     !  Jtarget
0                       !  Jexitparticle
4394.9                  !  Projectile separation energy (keV)
0                       !  Exit particle separation energy
1.25                    !  Radius parameter R0 (fm)
2                       !  Gamma-ray channel number
********************************************************************************
1                       !  Minimum energy for numerical integration (keV)
10000                   !  Number of random samples
0                       !  = 0 for rate output at all temperatures
********************************************************************************
Nonresonant contribution
S(keVb)      S′(b)      S″(b/keV)      fracErr      Cutoff Energy(keV)
7.9e1        -1.1e-2    1.3e-6         0.4          1000.0
0.0          0.0        0.0            0.0          0.0
```

```
************************************************************************
Resonant contribution
Note:  G1 = entrance channel, G2 = exit channel, G3 = spectator channel (d-
oes not exist in our case) !  Ecm and Exf are in keV; wg and Gx are in eV !
Ecm    DEcm  wg  Dwg  J  G1     DG1     L1  G2     DG2     L2  G3  DG3  L3  Exf  Int
293.2  0.8   0   0    3  1.7e-5 6.8e-6  2   4.6e-3 2.3e-3  1   0   0    0   0.0  1
414.9  0.9   0   0    2  3.7e-3 1.5e-3  2   4.9e-3 2.5e-3  1   0   0    0   0.0  1
919.0  4.0   0   0    3  1.1e0  4.4e-1  3   9.7e-3 4.9e-3  1   0   0    0   0.0  1
996.0  2.0   0   0    3  2.8e0  1.1e0   2   1.9e-2 9.5e-3  1   0   0    0   0.0  1
1452.0 2.0   0   0    2  1.0e2  4.0e1   2   1.8e-2 9.0e-3  1   0   0    0   0.0  0
************************************************************************
Upper Limits of Resonances
Note:  PT is non-zero for upper limit partial widths
Note:  Number of upper limits < number of open channels
Ecm    DEcm Jr G1     DG1  L1  PT     G2     DG2    L2  PT G3 DG3 L3 PT Exf  Int
737.7  1.1  4  2.3e-4 0.0  4   0.0045 4.4e-3 2.2e-3 1   0  0  0   0  0  0.0  1
826.0  2.0  0  1.9e1  0.0  0   0.0045 6.5e-3 3.3e-3 1   0  0  0   0  0  0.0  1
1551.0 3.0  4  1.8e-1 0.0  4   0.0045 3.2e-2 1.6e-2 1   0  0  0   0  0  0.0  1
************************************************************************
Interference between Resonances
Note:  No broad resonances for this case, so no interferences exist here
Ecm   DEcm Jr  G1   DG1  L1  PT   G2   DG2  L2  PT   G3   DG3  L3  PT    Exf
!+-
0.0   0.0  0   0.0  0.0  0   0.0  0.0  0.0  0   0.0  0.0  0.0  0   0.0   0.0
0.0   0.0  0   0.0  0.0  0   0.0  0.0  0.0  0   0.0  0.0  0.0  0   0.0   0.0
************************************************************************
Comments:
1.  The Q-value is updated from the measurement of Ref.[140].
2.  The calculations of partial widths are explained in § 5.2.2.
```

5.2.4 The ^{29}P$(p,\gamma)^{30}$S Monte Carlo Rate

Prior to the publication of Refs. [129, 134–136], which introduced a new Monte Carlo method for reaction rate calculations with proper statistical interpretations, the uncertainties in thermonuclear reaction rates were calculated without any proper statistical treatments. The relationship between the uncertainty in each nuclear physics input and that of the resultant reaction rate was not straightforward, and no confidence level was derived for high and low limits of the rates.

The goal of the aforementioned references was to provide the probability density function for the total reaction rate at each temperature. Therefore, the Monte Carlo technique for calculation of the thermonuclear reaction rates still uses the formalism

given in Chapter 2; however, each nuclear physics input is given a probability density function [134], e.g., a Gaussian distribution for resonance energies; a lognormal distribution for the direct capture S-factor and partial widths; and a Porter-Thomas distribution for upper limit of partial widths. Then the total reaction rate (the sum of non-resonant and resonant contributions) and its uncertainty is estimated via a Monte Carlo technique[3] from a probability density function approximated by a lognormal distribution of the form [129]:

$$f(N_A<\sigma\upsilon>) = \frac{1}{\sigma\sqrt{2\pi}}\frac{1}{N_A<\sigma\upsilon>}e^{-\frac{[\ln(N_A<\sigma\upsilon>)-\mu]^2}{2\sigma^2}} \tag{5.10}$$

where $N_A<\sigma\upsilon>$ is the reaction rate in units of $\mathrm{cm^3\,s^{-1}\,mol^{-1}}$, and σ and μ are the width and location of the lognormal probability density function of the reaction rate, respectively.

From this distribution, the low, median and high rates are defined as the 16%, 50% and 84% quantiles of the cumulative reaction rate distribution, respectively [134]. Therefore, the low rate $= e^{\mu-\sigma}$, the median rate $= e^{\mu}$, and the high rate $= e^{\mu+\sigma}$, such that 68% of the probability distribution is covered by the boundaries determined by the low and high rates [134].

The uncertainty in the reaction rate is calculated from e^{σ}, which is also a measure of the shape of the probability distribution [134]: if $\sigma < 0.1$, the reaction rate probability density function is approximated by a Gaussian function; whereas a $\sigma > 0.1$ indicates that the reaction rate probability density function is a skewed lognormal distribution.

To measure how well the Monte Carlo reaction rate is approximated by the lognormal distribution given in equation (5.10), an Anderson-Darling test statistic [134] (A-D statistic in Table 5.4) is calculated. This statistical test shows whether or not there is evidence that a given sample of data did not arise from a given probability distribution [355]. If the value of A-D statistic is less than 1, then the approximation given in equation (5.10) suits the probability density function of the total reaction rate. If, on the other hand, the A-D statistic is ≈ 1 or larger, then the reaction rate probability density function is not lognormal. However, even in those cases as claimed by Iliadis *et al.* [134], parameters σ and μ still define a lognormal distribution of the same expectation value and variance

[3]The details of this method are provided in Ref. [134]

Table 5.4: Total Monte Carlo rate for the $^{29}\mathrm{P}(p,\gamma)^{30}\mathrm{S}$ thermonuclear reaction.

T (GK)	Low Rate	Median Rate	High Rate	lognormal μ	lognormal σ	A-D Statistic
0.010	5.06×10^{-42}	7.38×10^{-42}	1.08×10^{-41}	$-9.471\times10^{+01}$	3.85×10^{-01}	2.79×10^{-01}
0.011	1.93×10^{-40}	2.86×10^{-40}	4.19×10^{-40}	$-9.106\times10^{+01}$	3.90×10^{-01}	2.75×10^{-01}
0.012	4.88×10^{-39}	7.19×10^{-39}	1.06×10^{-38}	$-8.783\times10^{+01}$	3.88×10^{-01}	4.13×10^{-01}
0.013	8.95×10^{-38}	1.31×10^{-37}	1.91×10^{-37}	$-8.493\times10^{+01}$	3.82×10^{-01}	1.54×10^{-01}
0.014	1.20×10^{-36}	1.77×10^{-36}	2.59×10^{-36}	$-8.232\times10^{+01}$	3.83×10^{-01}	3.97×10^{-01}
0.015	1.29×10^{-35}	1.88×10^{-35}	2.74×10^{-35}	$-7.996\times10^{+01}$	3.82×10^{-01}	2.19×10^{-01}
0.016	1.12×10^{-34}	1.64×10^{-34}	2.42×10^{-34}	$-7.779\times10^{+01}$	3.85×10^{-01}	3.83×10^{-01}
0.018	5.17×10^{-33}	7.58×10^{-33}	1.11×10^{-32}	$-7.396\times10^{+01}$	3.86×10^{-01}	2.31×10^{-01}
0.020	1.41×10^{-31}	2.06×10^{-31}	3.01×10^{-31}	$-7.066\times10^{+01}$	3.85×10^{-01}	4.58×10^{-01}
0.025	1.04×10^{-28}	1.54×10^{-28}	2.27×10^{-28}	$-6.404\times10^{+01}$	3.87×10^{-01}	4.34×10^{-01}
0.030	1.62×10^{-26}	2.36×10^{-26}	3.49×10^{-26}	$-5.901\times10^{+01}$	3.88×10^{-01}	6.71×10^{-01}
0.040	2.49×10^{-23}	3.69×10^{-23}	5.38×10^{-23}	$-5.166\times10^{+01}$	3.83×10^{-01}	5.38×10^{-01}
0.050	4.64×10^{-21}	6.80×10^{-21}	9.90×10^{-21}	$-4.644\times10^{+01}$	3.83×10^{-01}	2.27×10^{-01}
0.060	2.47×10^{-19}	3.58×10^{-19}	5.33×10^{-19}	$-4.247\times10^{+01}$	3.87×10^{-01}	9.79×10^{-01}
0.070	6.05×10^{-18}	8.81×10^{-18}	1.28×10^{-17}	$-3.927\times10^{+01}$	3.77×10^{-01}	3.43×10^{-01}
0.080	1.41×10^{-16}	1.88×10^{-16}	2.49×10^{-16}	$-3.621\times10^{+01}$	2.87×10^{-01}	3.18×10^{-01}
0.090	5.33×10^{-15}	7.34×10^{-15}	1.03×10^{-14}	$-3.254\times10^{+01}$	3.32×10^{-01}	$1.63\times10^{+00}$
0.100	1.66×10^{-13}	2.39×10^{-13}	3.47×10^{-13}	$-2.906\times10^{+01}$	3.74×10^{-01}	4.86×10^{-01}

Continued on the next page

Table 5.4 – continued from the previous page

T (GK)	Low Rate	Median Rate	High Rate	lognormal μ	lognormal σ	A-D Statistic
0.110	3.07×10^{-12}	4.45×10^{-12}	6.52×10^{-12}	$-2.614\times10^{+01}$	3.82×10^{-01}	5.51×10^{-01}
0.120	3.53×10^{-11}	5.11×10^{-11}	7.49×10^{-11}	$-2.369\times10^{+01}$	3.83×10^{-01}	5.72×10^{-01}
0.130	2.77×10^{-10}	4.01×10^{-10}	5.87×10^{-10}	$-2.163\times10^{+01}$	3.83×10^{-01}	5.74×10^{-01}
0.140	1.61×10^{-09}	2.33×10^{-09}	3.41×10^{-09}	$-1.987\times10^{+01}$	3.82×10^{-01}	5.54×10^{-01}
0.150	7.37×10^{-09}	1.07×10^{-08}	1.56×10^{-08}	$-1.835\times10^{+01}$	3.80×10^{-01}	5.24×10^{-01}
0.160	2.79×10^{-08}	4.02×10^{-08}	5.87×10^{-08}	$-1.703\times10^{+01}$	3.78×10^{-01}	4.89×10^{-01}
0.180	2.56×10^{-07}	3.66×10^{-07}	5.29×10^{-07}	$-1.482\times10^{+01}$	3.69×10^{-01}	4.60×10^{-01}
0.200	1.53×10^{-06}	2.16×10^{-06}	3.07×10^{-06}	$-1.304\times10^{+01}$	3.55×10^{-01}	6.94×10^{-01}
0.250	4.23×10^{-05}	5.65×10^{-05}	7.67×10^{-05}	$-9.775\times10^{+00}$	3.01×10^{-01}	$2.27\times10^{+00}$
0.300	4.42×10^{-04}	5.70×10^{-04}	7.39×10^{-04}	$-7.467\times10^{+00}$	2.58×10^{-01}	6.29×10^{-01}
0.350	2.53×10^{-03}	3.23×10^{-03}	4.14×10^{-03}	$-5.733\times10^{+00}$	2.44×10^{-01}	3.60×10^{-01}
0.400	9.65×10^{-03}	1.24×10^{-02}	1.59×10^{-02}	$-4.391\times10^{+00}$	2.48×10^{-01}	3.74×10^{-01}
0.450	2.76×10^{-02}	3.56×10^{-02}	4.61×10^{-02}	$-3.333\times10^{+00}$	2.57×10^{-01}	5.07×10^{-01}
0.500	6.40×10^{-02}	8.30×10^{-02}	1.09×10^{-01}	$-2.484\times10^{+00}$	2.66×10^{-01}	7.01×10^{-01}
0.600	2.23×10^{-01}	2.93×10^{-01}	3.88×10^{-01}	$-1.222\times10^{+00}$	2.78×10^{-01}	8.37×10^{-01}
0.700	5.35×10^{-01}	7.09×10^{-01}	9.43×10^{-01}	-3.389×10^{-01}	2.84×10^{-01}	8.72×10^{-01}
0.800	$1.02\times10^{+00}$	$1.35\times10^{+00}$	$1.80\times10^{+00}$	3.070×10^{-01}	2.87×10^{-01}	9.08×10^{-01}
0.900	$1.67\times10^{+00}$	$2.21\times10^{+00}$	$2.95\times10^{+00}$	7.992×10^{-01}	2.87×10^{-01}	$1.01\times10^{+00}$
1.000	$2.47\times10^{+00}$	$3.26\times10^{+00}$	$4.34\times10^{+00}$	$1.189\times10^{+00}$	2.83×10^{-01}	$1.20\times10^{+00}$

Continued on the next page

Table 5.4 – continued from the previous page

T (GK)	Low Rate	Median Rate	High Rate	lognormal μ	lognormal σ	A-D Statistic
1.250	$5.14\times10^{+00}$	$6.67\times10^{+00}$	$8.71\times10^{+00}$	$1.903\times10^{+00}$	2.64×10^{-01}	$1.77\times10^{+00}$
1.500	$8.85\times10^{+00}$	$1.12\times10^{+01}$	$1.43\times10^{+01}$	$2.419\times10^{+00}$	2.39×10^{-01}	$1.07\times10^{+00}$
1.750	$1.36\times10^{+01}$	$1.70\times10^{+01}$	$2.12\times10^{+01}$	$2.830\times10^{+00}$	2.22×10^{-01}	5.42×10^{-01}
2.000	$1.91\times10^{+01}$	$2.38\times10^{+01}$	$2.94\times10^{+01}$	$3.168\times10^{+00}$	2.16×10^{-01}	3.68×10^{-01}
2.500	$3.18\times10^{+01}$	$3.96\times10^{+01}$	$4.95\times10^{+01}$	$3.681\times10^{+00}$	2.20×10^{-01}	8.45×10^{-01}
3.000	$(4.51\times10^{+01})$	$(5.67\times10^{+01})$	$(7.12\times10^{+01})$	$(4.037\times10^{+00})$	(2.28×10^{-01})	
3.500	$(5.98\times10^{+01})$	$(7.51\times10^{+01})$	$(9.43\times10^{+01})$	$(4.319\times10^{+00})$	(2.28×10^{-01})	
4.000	$(7.52\times10^{+01})$	$(9.44\times10^{+01})$	$(1.19\times10^{+02})$	$(4.548\times10^{+00})$	(2.28×10^{-01})	
5.000	$(1.05\times10^{+02})$	$(1.32\times10^{+02})$	$(1.65\times10^{+02})$	$(4.881\times10^{+00})$	(2.28×10^{-01})	
6.000	$(1.34\times10^{+02})$	$(1.69\times10^{+02})$	$(2.12\times10^{+02})$	$(5.127\times10^{+00})$	(2.28×10^{-01})	
7.000	$(1.62\times10^{+02})$	$(2.03\times10^{+02})$	$(2.55\times10^{+02})$	$(5.314\times10^{+00})$	(2.28×10^{-01})	
8.000	$(1.88\times10^{+02})$	$(2.36\times10^{+02})$	$(2.96\times10^{+02})$	$(5.462\times10^{+00})$	(2.28×10^{-01})	
9.000	$(2.12\times10^{+02})$	$(2.66\times10^{+02})$	$(3.34\times10^{+02})$	$(5.585\times10^{+00})$	(2.28×10^{-01})	
10.000	$(2.40\times10^{+02})$	$(3.01\times10^{+02})$	$(3.78\times10^{+02})$	$(5.707\times10^{+00})$	(2.28×10^{-01})	

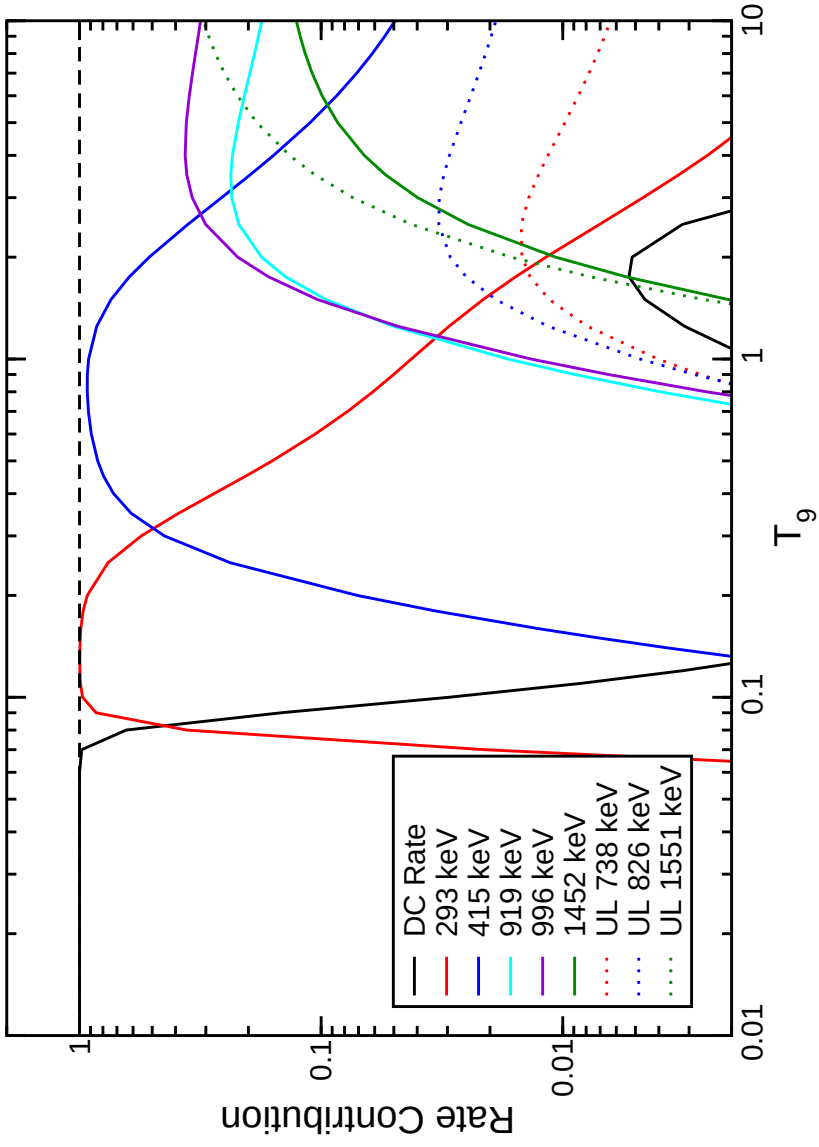

Figure 5.3: The Monte Carlo rate for the thermonuclear $^{29}\mathrm{P}(p,\gamma)^{30}\mathrm{S}$ reaction as a function of temperature. Abbreviations are as follows: DC: Direct Capture; UL: Upper Limit. The latter is used for those resonances, for which the particle partial width is estimated to be an upper limit. The 293.2-keV resonance controls the rate over the temperature range of $0.08 < T \leq 0.3$ GK. The new 414.9-keV resonance, in turn, dominates the rate from 0.35 to 2 GK. The 996-keV resonance becomes important at temperatures higher than 2 GK, which are beyond the astrophysical temperature range of interest to this work. The other resonances, including those for which only an upper limit (UL) particle partial width is known (see § 5.2.3), do not contribute significantly to the $^{29}\mathrm{P}(p,\gamma)^{30}\mathrm{S}$ total rate at the temperature range of interest ($0.1 \leq T \leq 1.3$ GK).

as the actual Monte Carlo probability density function.

Here we present the results of the calculation of the ^{29}P$(p,\gamma)^{30}$S thermonuclear reaction rate via the Monte Carlo technique using a code called RatesMC. This calculation and the results given in this section were kindly carried out by Dr. Richard Longland [350].

Since, as shown in Table 5.1, we have only taken into account the ^{30}S states below 6 MeV, our resultant total reaction rate would eventually be calculated with zero cross section at high energies corresponding to high temperatures. This is because the experimental input is truncated at 6 MeV. Therefore, there exists a temperature denoted by $T_{\rm match}$ [134], above which the nuclear physics input is insufficient to calculate a reliable reaction rate. For our case, this temperature was found to be 3 GK [350]. The reaction rate above 3 GK was therefore obtained as follows: the theoretical ^{29}P$(p,\gamma)^{30}$S rate as a function of temperature was calculated based on the Hauser-Feshbach statistical model [356] using the NONSMOKER code [357]. Then, these rates were scaled and normalized to the experimental Monte Carlo rate at $T = T_{\rm match} = 3$ GK. Such renormalized rates (shown in parenthesis in Table 5.4) then provide the extrapolated rates at temperatures beyond $T_{\rm match}$. In this case, no A-D statistic is provided.

The numerical values for the Monte Carlo rate corresponding to the ^{29}P$(p,\gamma)^{30}$S thermonuclear reaction are given in Table 5.4.

Fig. 5.3 compares the contribution of the direct capture rate (DC Rate), as well as that of each of the resonances listed in Table 5.1, to the total ^{29}P$(p,\gamma)^{30}$S thermonuclear reaction rate. Fig. 5.3 shows which resonances play major roles in determination of the ^{29}P$(p,\gamma)^{30}$S total rate. From this figure it is evident that the direct capture rate (DC Rate) dominates the total rate for T $\leq$ 0.08 GK, whereas at higher temperatures characteristic of explosive nucleosynthesis in novae the total reaction rate is dominated by a single 3^+_1 resonance at 293.2 keV from 0.09 – 0.3 GK. The new 414.9-keV resonance with $J^\pi = (2^+_3)$ is the main contributor to the total rate from 0.35 GK to 2 GK, which covers the whole range of interest for explosive nucleosynthesis in type I X-ray bursts.

Fig. 5.4 compares our Monte Carlo rate for the ^{29}P$(p,\gamma)^{30}$S reaction with that of Ref. [134], where the energy of the 2^+_3 state of ^{30}S was assumed to be 4888(40) keV from a theoretical estimation based on the IMME. Both rates that are compared on this figure are calculated based on the Monte Carlo technique; however, since for our rate the energy of the resonance corresponding to the 2^+_3 state of ^{30}S is determined experimentally, its

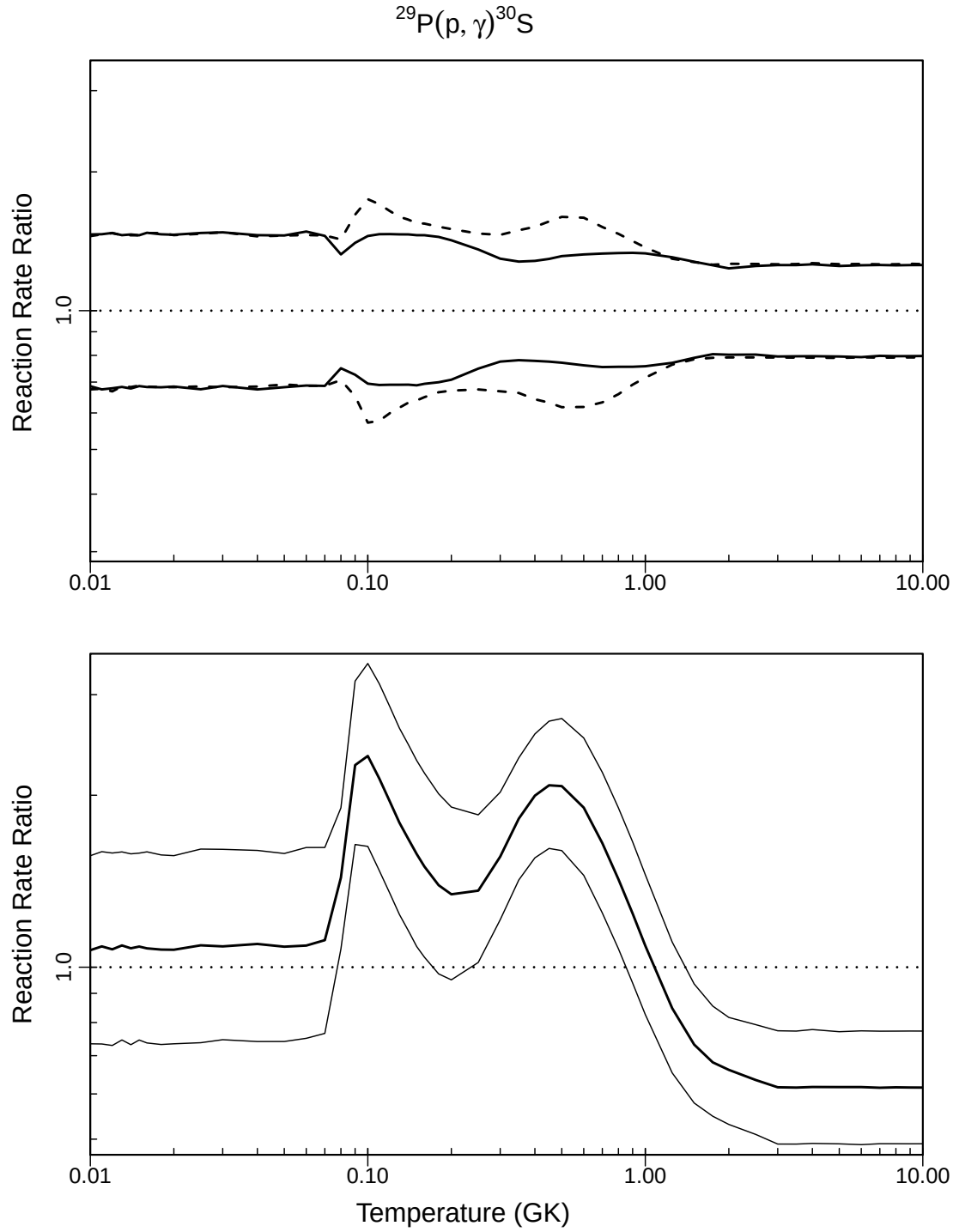

Figure 5.4: (top) The uncertainty bands corresponding to $N_A < \sigma\upsilon >_{\rm high}/N_A < \sigma\upsilon >_{\rm median}$ and $N_A < \sigma\upsilon >_{\rm low}/N_A < \sigma\upsilon >_{\rm median}$ from our Monte Carlo rate (solid lines) compared to those of Ref. [134] (dashed lines). Clearly the uncertainties in our rate are smaller than those of Ref. [134]. (bottom) The ratio of our Monte Carlo low (lower thin line), median (middle tick line) and high (upper thin line) rates to the Monte Carlo median rate of Ref. [134]. Our median rate is 2.3 times larger than the median rate of Ref. [134] at $T = 0.1$ GK.

uncertainty of 0.9 keV is reduced by a factor of 44.4 with respect to the theoretical estimation of 40 keV considered in Ref. [134]. Furthermore, the 2-keV uncertainty in the energy of the resonance corresponding to the 3_1^+ state in ^{30}S measured in this work is also reduced by 40% with respect to the 5 keV measured in Ref. [150] that is used to derive the rate in Ref. [134].

Therefore, as these two resonances together dominate the total rate over $0.08 < T \leq 2$ GK, the reductions in their associated uncertainties also reduce the uncertainty in the total reaction rate (see the top panel in Fig. 5.4 on page 233). For instance, at $T = 0.1$ GK, where the uncertainty in both our rate and that of Ref. [134] is maximum, the ratio of the $N_A < \sigma\upsilon >_{\rm high}/N_A < \sigma\upsilon >_{\rm low}$ from our Monte Carlo rate is 72% smaller than that of the Monte Carlo rate reported in Ref. [134].

In addition, the reduction in the measured energies of these two resonances from the present work causes our median rate to be up to 2.3 times larger (at $T_9 = 0.1$) than that of Ref. [134] (see bottom panel in Fig. 5.4) and up to 11.5 times larger (at $T_9 = 0.1$) than the recommended rate of Ref. [149] (see Fig. 5.5). For calculation of the latter rate, the energies of both of the two astrophysically important resonances (corresponding to the 3_1^+ and 2_3^+ states in ^{30}S) were determined theoretically based on the IMME since none of these resonances were observed at the time. Also, the latter rate was not computed from the new Monte Carlo technique, and was solely based on the analytical formalism presented in Chapter 2.

Figs. 5.6 to 5.11 show the present Monte Carlo reaction rate probability density functions (in red), together with their lognormal approximations (in black) for all temperatures in units of GK. The latter distributions are calculated based on equation (5.10) together with the lognormal parameters μ and σ that are listed in columns 5 and 6 in Table 5.4. The temperatures given in the top right corner of the last series of figures cover the astrophysical temperature range of interest in Red Giant stars, AGB stars, classical novae, massive stars and type I X-ray bursts.

Each panel in Figs. 5.6 to 5.11 displays the temperature T and the Anderson-Darling test statistic, A-D. To interpret these figures, when the parameter A-D is less than 1, the Monte Carlo probability density distribution shown by the red curve follows the lognormal distribution shown by the black curve. At each temperature the lognormal parameter σ listed in column 6 in Table 5.4 shows the corresponding factor uncertainty

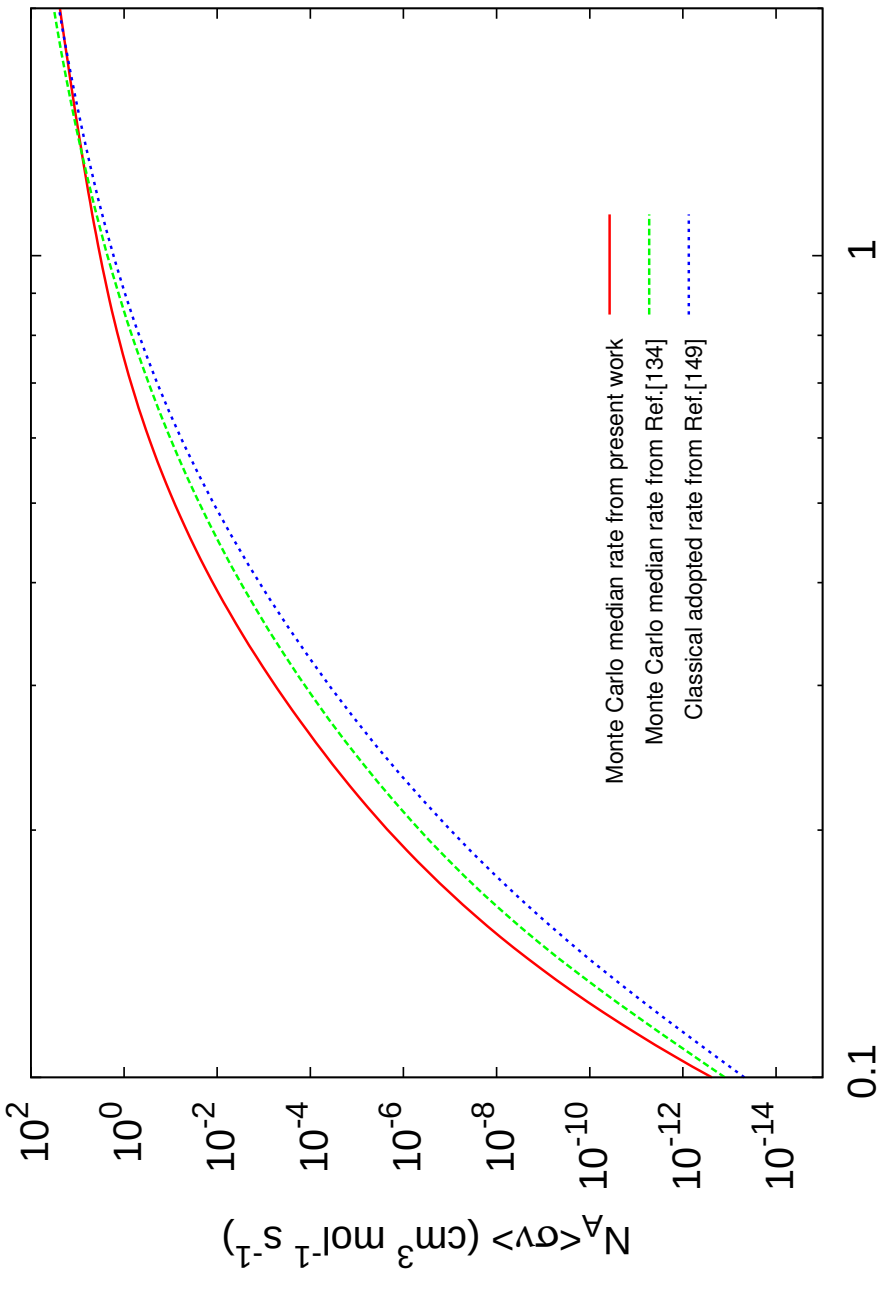

Figure 5.5: Comparison of the Monte Carlo median rates from the present work and Ref. [134] with the recommended "classical" rate from Ref. [149] over the range of temperatures of interest to novae and type I X-ray bursts. The last rate was not computed from the Monte Carlo method. Our present rate is higher than those of Ref. [134] and Ref. [149] at $T = 0.1$ GK by at most a factor of 2.3 and 11.5, respectively. This is due mainly to new measured energies for the two important levels near $E_x = 4.7 - 4.8$ MeV.

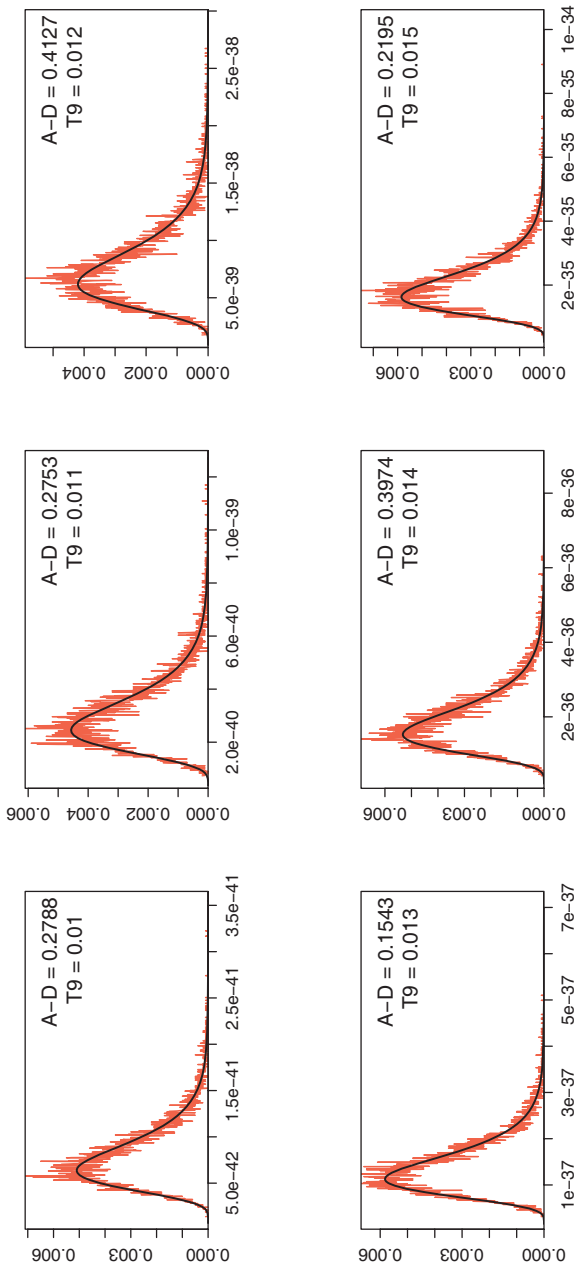

Figure 5.6: Total reaction rate probability density function for the $^{29}\mathrm{P}(p,\gamma)^{30}\mathrm{S}$ reaction. The y-axes are probability in arbitrary units, while the x-axes are reaction rates in units of $\mathrm{cm}^3\,\mathrm{mol}^{-1}\,\mathrm{s}^{-1}$. The red histograms are obtained from the Monte Carlo method with 10000 samples. The black curves depict the lognormal distributions calculated from the μ and σ parameters listed in Table 5.4 and based on equation (5.10). The temperature (in GK) and the Anderson-Darling statistics (A-D) parameter are given for each panel.

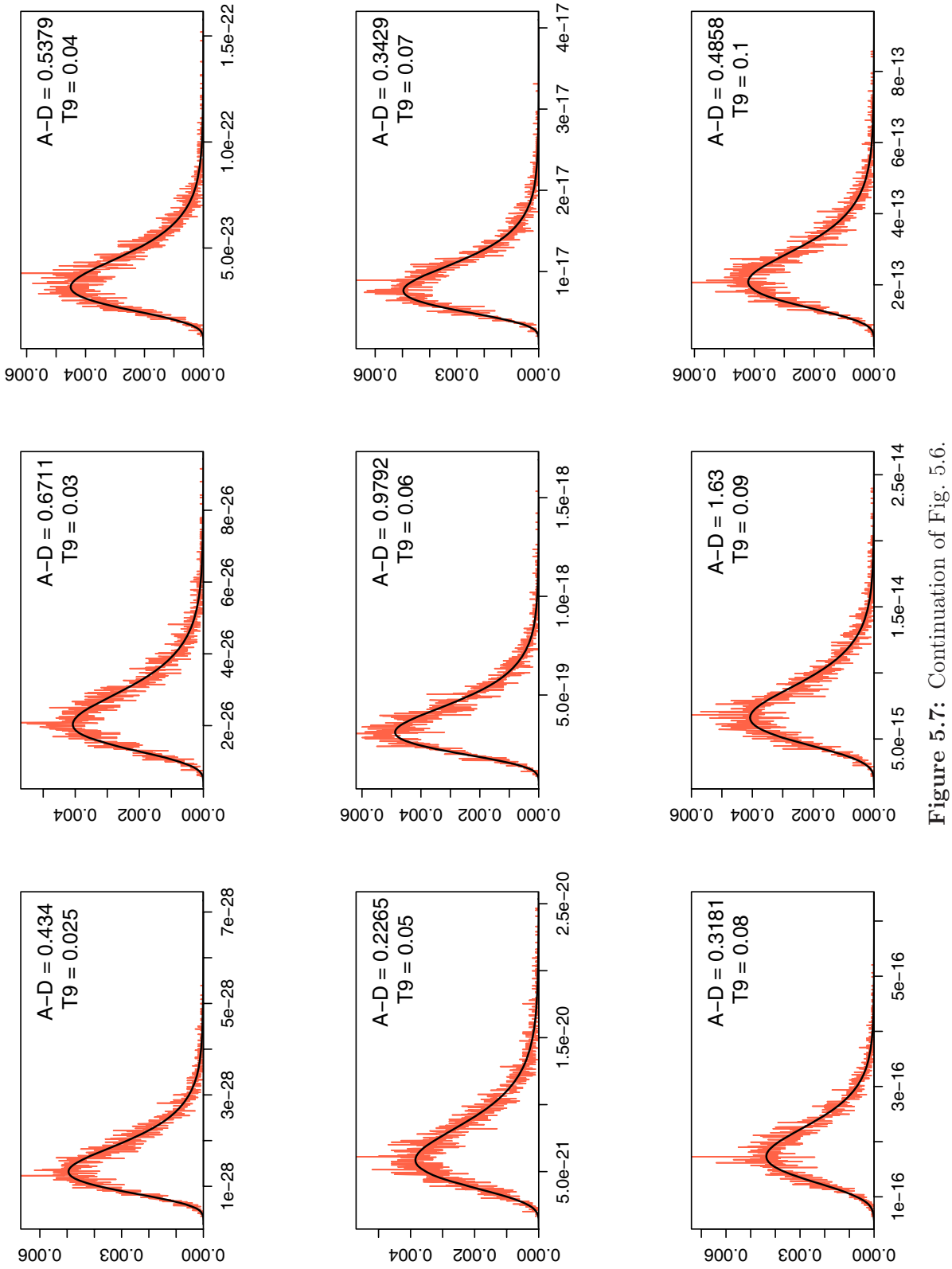

Figure 5.7: Continuation of Fig. 5.6.

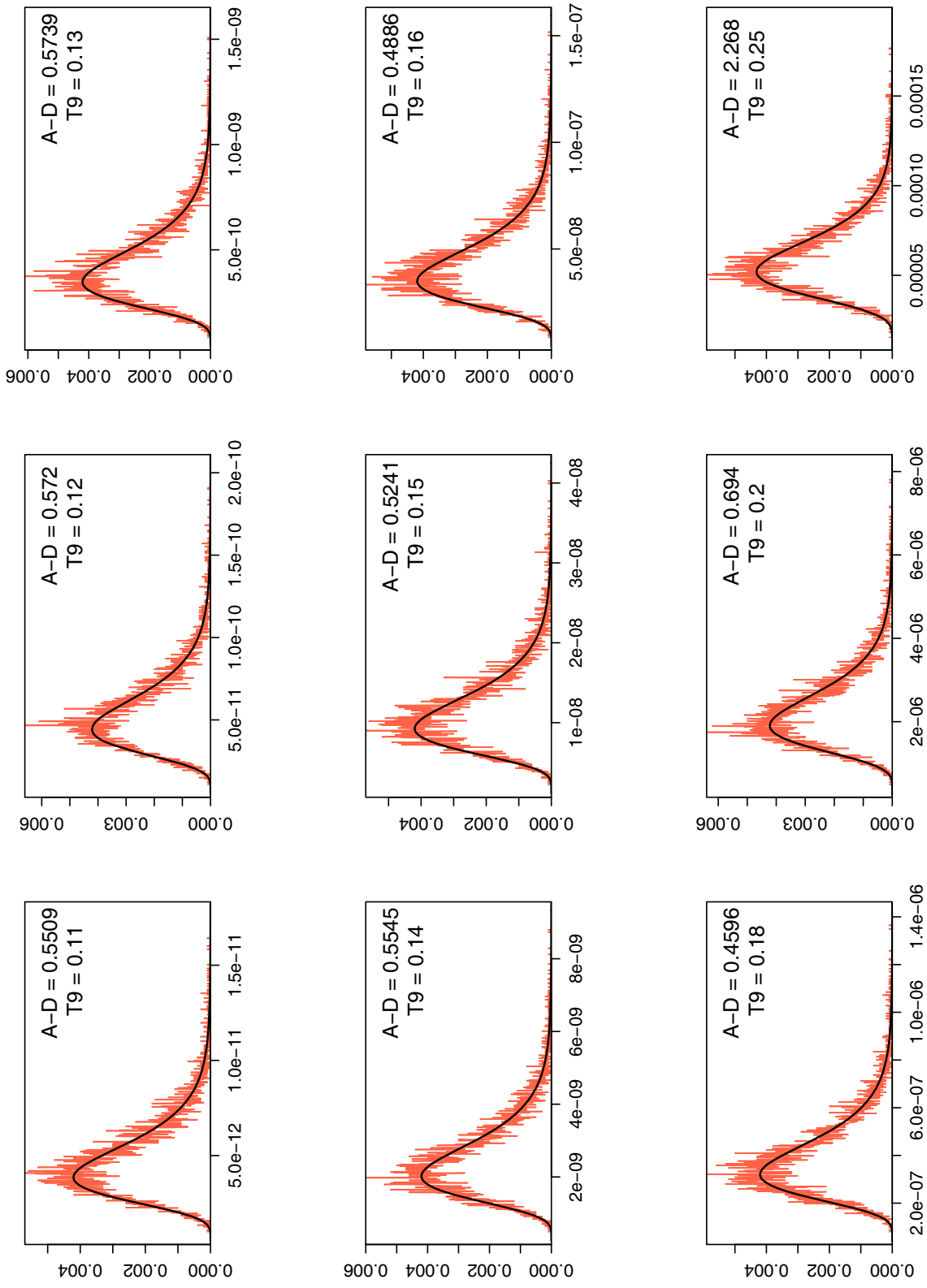

Figure 5.8: Continuation of Fig. 5.6.

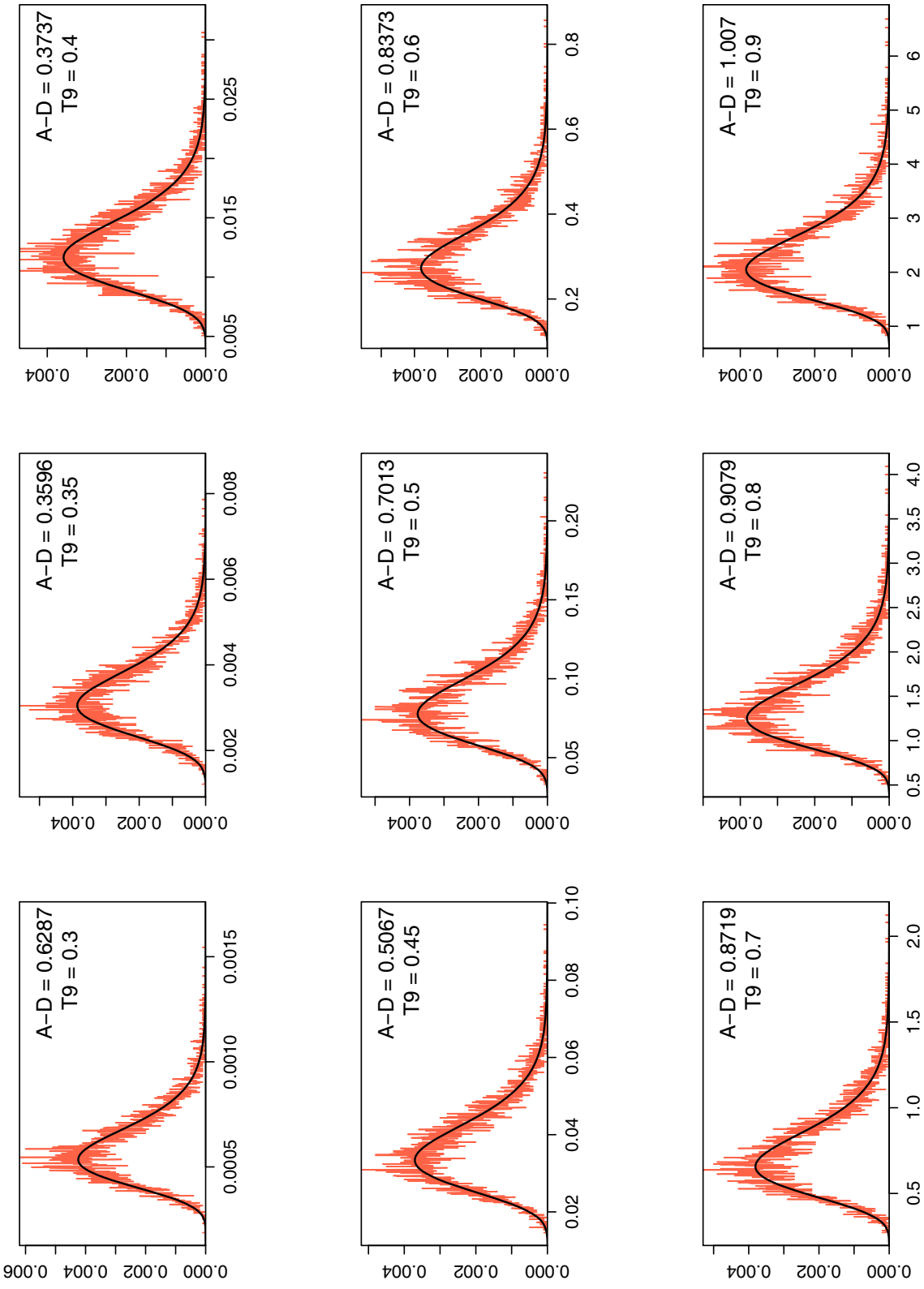

Figure 5.9: Continuation of Fig. 5.6.

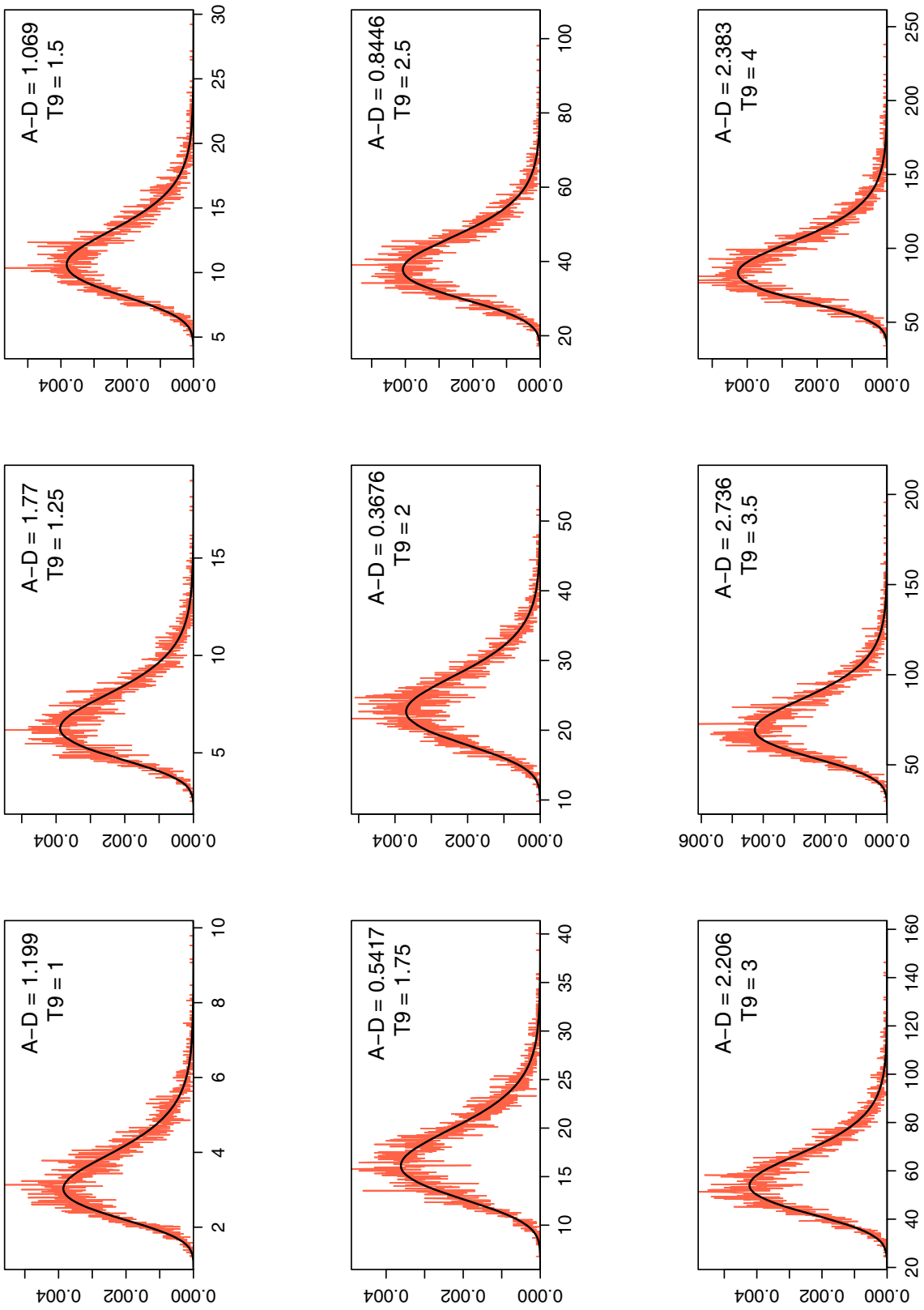

Figure 5.10: Continuation of Fig. 5.6.

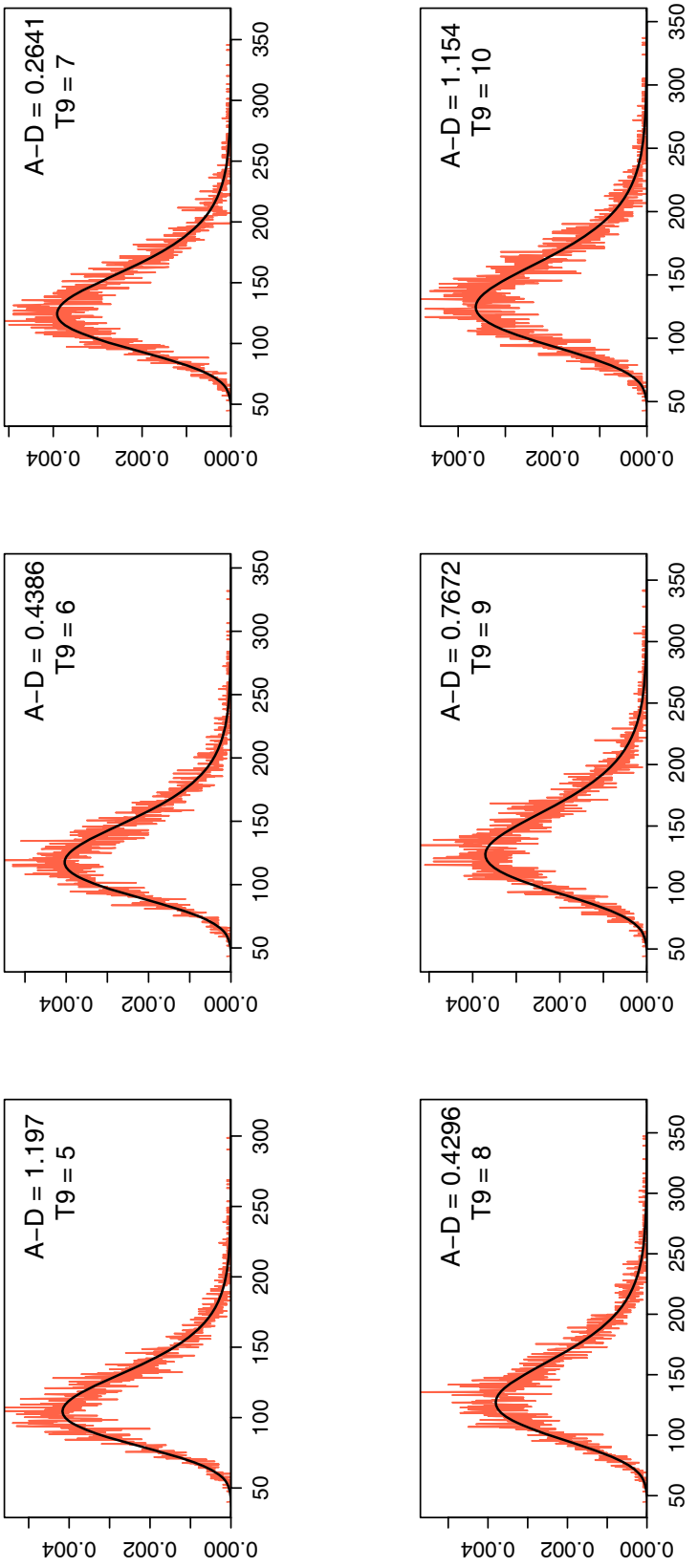

Figure 5.11: Continuation of Fig. 5.6.

e^{σ}, which in turn determines whether or not the distribution is skewed[4]. At low temperatures, where the direct capture rate dominates the total rate, the A-D parameter is a small number less than one, which indicates that since the input direct capture S-factor is associated with a lognormal probability distribution, the total output rate also follows the lognormal probability distribution. At higher temperatures, where the resonances start to dominate the rate, the A-D parameter becomes larger while σ remains a small number. This means that the Monte Carlo probability distributions (the red curves) are weakly skewed or even symmetric. Thus, the black curves are nearly Gaussian. This is because the input narrow resonances that dominate the total rate are each given a Gaussian distribution function. So the total reaction rate probability density tends toward a Gaussian function.

Finally, the present Monte Carlo rate for the $^{29}\mathrm{P}(p,\gamma)^{30}\mathrm{S}$ reaction, as well as all other reaction rates discussed here are all appropriate only for bare nuclei that are detached from their electrons. Therefore, no electron screening (discussed in Chapter 2) is taken into account. Moreover, we have assumed that ^{29}P is in its ground state; however, at stellar environments, due to the very high temperatures involved, these nuclei could be thermally excited and such excited states may also participate in the nuclear burning processes. Therefore, the rate of this reaction in the actual stellar environments is enhanced. Such stellar enhancement factors are estimated via nuclear reaction models, e.g., the Hauser-Feshbach model [358], because in the laboratory we cannot directly measure the cross sections when the targets are excited. The reaction rates discussed here must then be multiplied by the appropriate stellar enhancement factor at each temperature to obtain a better estimation of the actual reaction rate as it happens in stars.

5.3 Isotopic Abundances in Nova Ejecta

In Chapter 2, we emphasized that the $^{29}\mathrm{P}(p,\gamma)^{30}\mathrm{S}$ reaction is thought to directly affect the silicon isotopic ratios in nova ejecta, influences the synthesis of some elements heavier than silicon, and becomes important in the nucleosynthesis of type I X-ray bursts. This last effect was not examined in the present work. Thus, future work is required to shed light on this issue.

However, to investigate the impact of the updated rate of the $^{29}\mathrm{P}(p,\gamma)^{30}\mathrm{S}$ reaction

[4]A factor uncertainty larger than 1 means the distribution is skewed [134].

on the silicon isotopic abundances as well as the heavier elements resulting from classical nova nucleosynthesis in the temperature range of $0.1 \leq T \leq 0.4$ GK, Prof. Jordi José [359] has kindly computed three different models of nova outbursts, with identical input physics except for the specific choice of the $^{29}\mathrm{P}(p,\gamma)^{30}\mathrm{S}$ rate adopted.

5.3.1 Simulations

The models are computed with a code called SHIVA, which is in the Lagrangian formulation and is a one-dimensional spherically symmetric hydrodynamic and implicit code that simulates a nova outburst from the onset of the accretion to the explosion and the ejection of the nova ejecta. The detailed information about this code is provided in Refs. [68, 346]. The hydrodynamic code is coupled directly to the reaction network. Thus, it is a more complete simulation than the post-processing nucleosynthesis simulation used in Refs. [148, 150]. The latter simulation requires as input the structure of the star as a function of time, and the initial abundances and reaction rates. Then, the abundances of elements produced in the star are recalculated as a function of time and the star's interior mass. This approach is often used when the variation in the reaction rate of interest and the energy liberated from the other reactions do not appreciably change the nuclear energy generation nor, therefore, the temperature and density history of the explosion. Therefore, in post-processing nucleosynthesis simulations the nucleosynthesis is decoupled from the hydrodynamics of the outburst. The post-processing nucleosynthesis simulation is much simpler and less time consuming than the full hydrodynamic simulations.

The full hydrodynamic simulation code used in the present work is one of the best and most complete 1D codes that are available today. The advantage of our present simulations is that the important effect of convection on the final nova abundances is taken into account, since the reaction network is coupled directly to the hydrodynamics. As pointed out in Ref. [68], the material is dredged up on short timescales from the hottest hydrogen-burning region to the surface of the WD by convective mixing processes. Thus the ejected abundances of fragile nuclei that would have been destroyed if they had not been carried to higher and cooler layers, are increased. Therefore, our calculations are suitable for defining absolute isotopic abundances resulting from nova nucleosynthesis. It must be emphasized that the absolute abundances observed in nova ejecta or in presolar

grains from novae provide strong constraints for nova simulations because nuclear reactions are very sensitive to temperature. While direct spectroscopic observations reveal the elemental, and thus atomic, abundance patterns, which do not pose very strict limits on nova models [71], a much more precise set of constraints can be obtained if information on specific isotopic abundances are available.

For the full hydrodynamic simulations performed for this work, thermodynamic profiles are taken from those of hydrodynamical simulations of Ref. [68] for an extreme ONe nova with an underlying WD, whose mass is assumed to be 1.35 $M_{\odot}$. This particular WD is used because being less massive and therefore cooler, a CO WD shows limited activity in the Si-Ca mass region [71]. Thus the nucleosynthesis of silicon isotopes in the CO novae, with even the most massive underlying WDs, is negligible.

In all three models, an accretion at a rate of $\dot{M}_{\rm acc} = 2 \times 10^{-10}\,M_{\odot}$/yr of solar-like matter that is enriched with 50% of the WD core material onto the 1.35 $M_{\odot}$ ONe WD is assumed. This is to mimic the unknown mechanism responsible for the enhancement in metals, which ultimately powers the explosion [71]. The initial abundances of some isotopes used for the present simulations are given in Ref. [71].

In addition to thermodynamics, a reaction rate network including 370 nuclear reactions involving 117 isotopes ranging from ^{1}H to ^{48}Ti is used. Reaction rates are taken from the compilation of Ref. [134] with additional reactions taken from Prof. Iliadis' 2005 reaction rate library[5] [359]. The only exception is the $^{29}\mathrm{P}(p,\gamma)^{30}\mathrm{S}$ reaction, which is taken (one at a time for each of the three models) from the present work, as well as the rates reported in Refs. [134, 149].

These rates are corrected for the stellar enhancement factors discussed previously. Therefore, the impact of the stellar rate of the $^{29}\mathrm{P}(p,\gamma)^{30}\mathrm{S}$ reaction on nova nucleosynthesis was compared for the three different reported rates: the recommended "classical" rate from Ref. [149], hereafter model A; the median Monte Carlo rate from Ref. [134], hereafter model B; and the high Monte Carlo rate from this work, hereafter model C.

The high rate from this work is used as opposed to the median rate, because we wish to study the highest possible effect of the new rate on the abundances of elements synthesized in novae. While the median rate from the present work is 2.3 times larger than that of Ref. [134] (see bottom panel in Fig. 5.4) at $T = 0.1$ GK, the high rate from

[5]This library is not available online.

the present work is a factor of 3.5 larger at the same temperature.

The differences in these three rates arise from the input energies and their associated uncertainties of two resonances corresponding to the 3_1^+ and 2_3^+ states of ^{30}S. For the rate in Ref. [149], none of these resonances was observed, and thus their energies were predicted from the IMME and their uncertainties each amounted to 40 keV. For the rate of Ref. [134], only the 3_1^+ resonance had been observed, and thus the energy of the other resonance was still uncertain by 40 keV. Since the latter resonance dominates the rate at $T > 0.3$ GK, the Monte Carlo median rate of Ref. [134] differs very little from the classical recommended rate of Ref. [149], as a result of using the same theoretically predicted energy and its uncertainty for this resonance (see Fig. 5.5). Finally, in the present work, not only was the 2_3^+ resonance observed, but our higher energy resolution measurements helped reduce the uncertainty in the 3_1^+ resonance by 40% with respect to that used in Ref. [134].

5.3.2 Results

The resulting mean (in mass fractions), mass-averaged abundances in the ejected envelope shells for models A to C are given in Tables 5.5 to 5.7, respectively. A mass averaging process assigns different weights to individual shells of the underlying WD [71]. The total ejected envelope mass for all three models is 9.043×10^{27} g (equivalent to 4.55×10^{-6} $M_\odot$).

It should be noted that ^{26}Al has 5 different isotopes: $^{26}\mathrm{Al}_{g.s.}$, ^{26m}Al, ^{26a}Al, ^{26b}Al and ^{26c}Al. These isotopes indicate the ground state, the meta stable isomeric state, and three other additional isomers, respectively. The last three isomers are not relevant at all for nova conditions but may have some influence at higher temperatures [359].

The interpretation of the results is surprising: with respect to models A and B, model C shows very limited impact on the yields of the silicon isotopes synthesized in the particular nova outbursts used for these models. Changes of the order of 3.5 – 17 at $T = 0.1$ GK in the $^{29}\mathrm{P}(p,\gamma)^{30}\mathrm{S}$ rate[6] has only decreased[7] the ^{30}P (the product of ^{30}S

[6] At $T = 0.1$ GK, the $^{29}\mathrm{P}(p,\gamma)^{30}\mathrm{S}$ rate in model C is a factor of 17 and 3.5 times larger than those in models A and B, respectively.

[7] The percentage differences mentioned here are defined to be: [(new value − old value) ÷ old value] × 100%, where the "new value" is an isotopic abundance (or a Si isotopic abundance ratio with respect to the abundance of ^{28}Si) resulting from model C, and the "old values" are those resulting from models A or B, whichever gives a higher percentage difference.

Table 5.5: Model A: the mean composition (in mass fractions) of the ejecta of a nova outburst with an underlying 1.35 $M_{\odot}$ ONe WD. The listed isotopic abundances are computed using a network of reactions, all of which are taken from reaction rate libraries (see text) except that of the ^{29}P$(p,\gamma)^{30}$S reaction, which is here the recommended classical rate of Ref. [149].

Nucleus	Yield	Nucleus	Yield	Nucleus	Yield	Nucleus	Yield	Nucleus	Yield
^{1}H	2.34×10^{-01}	^{2}H	9.51×10^{-19}	^{3}H	1.48×10^{-23}	^{3}He	7.12×10^{-09}	^{4}He	2.51×10^{-01}
^{6}Li	5.36×10^{-27}	^{7}Li	3.27×10^{-10}	^{7}Be	1.71×10^{-06}	^{8}B	2.27×10^{-23}	^{9}Be	3.25×10^{-32}
^{9}C	1.26×10^{-31}	^{10}B	1.06×10^{-24}	^{11}B	6.68×10^{-10}	^{11}C	6.29×10^{-10}	^{12}C	2.21×10^{-02}
^{12}N	5.88×10^{-33}	^{13}C	1.12×10^{-02}	^{13}N	4.36×10^{-03}	^{13}O	1.30×10^{-34}	^{14}N	5.47×10^{-02}
^{14}O	1.24×10^{-06}	^{15}N	1.07×10^{-01}	^{15}O	1.55×10^{-04}	^{16}O	6.03×10^{-03}	^{17}O	4.05×10^{-02}
^{17}F	2.28×10^{-08}	^{18}O	6.84×10^{-06}	^{18}F	4.34×10^{-05}	^{18}Ne	1.39×10^{-30}	^{19}F	1.19×10^{-06}
^{19}Ne	3.42×10^{-24}	^{20}Ne	1.46×10^{-01}	^{20}Na	2.00×10^{-34}	^{21}Ne	4.08×10^{-05}	^{21}Na	6.75×10^{-17}
^{21}Mg	2.10×10^{-34}	^{22}Ne	3.13×10^{-05}	^{22}Na	5.59×10^{-04}	^{22}Mg	2.20×10^{-34}	^{23}Na	3.44×10^{-03}
^{23}Mg	1.25×10^{-24}	^{23}Al	2.30×10^{-34}	^{24}Mg	8.58×10^{-05}	^{24}Al	2.40×10^{-34}	^{25}Mg	2.24×10^{-03}
^{25}Al	1.53×10^{-31}	^{25}Si	2.50×10^{-34}	^{26}Mg	1.49×10^{-04}	^{26c}Al	2.60×10^{-34}	^{26b}Al	2.60×10^{-34}
^{26m}Al	2.63×10^{-24}	^{26}Al$_{g.s.}$	4.54×10^{-04}	^{26a}Al	2.60×10^{-34}	^{26}Si	2.60×10^{-34}	^{27}Al	3.01×10^{-03}
^{27}Si	5.08×10^{-28}	^{27}P	2.70×10^{-34}	^{28}Si	3.08×10^{-02}	^{28}P	2.80×10^{-34}	^{29}Si	2.38×10^{-03}
^{29}P	4.05×10^{-31}	^{29}S	2.90×10^{-34}	^{30}Si	1.54×10^{-02}	^{30}P	2.16×10^{-05}	^{30}S	3.00×10^{-34}
^{31}P	8.71×10^{-03}	^{31}S	9.36×10^{-34}	^{31}Cl	3.10×10^{-34}	^{32}S	5.27×10^{-02}	^{32}Cl	3.20×10^{-34}
^{32}Ar	3.20×10^{-34}	^{33}S	8.02×10^{-04}	^{33}Cl	2.87×10^{-29}	^{33}Ar	3.30×10^{-34}	^{34}S	3.63×10^{-04}
^{34}Cl	3.40×10^{-34}	^{34}Ar	3.40×10^{-34}	^{35}S	3.50×10^{-34}	^{35}Cl	3.85×10^{-04}	^{35}Ar	7.81×10^{-34}
^{35}K	3.50×10^{-34}	^{36}S	3.60×10^{-34}	^{36}Cl	1.52×10^{-33}	^{36}Ar	5.14×10^{-05}	^{36}K	3.60×10^{-34}
^{36}Ca	3.60×10^{-34}	^{37}Cl	1.39×10^{-07}	^{37}Ar	1.43×10^{-04}	^{37}K	3.70×10^{-34}	^{37}Ca	3.70×10^{-34}
^{38}Ar	2.19×10^{-05}	^{38}K	2.21×10^{-06}	^{38}Ca	3.80×10^{-34}	^{39}Ar	3.90×10^{-34}	^{39}K	5.96×10^{-06}
^{39}Ca	3.90×10^{-34}	^{40}Ar	4.00×10^{-34}	^{40}K	4.81×10^{-34}	^{40}Ca	3.06×10^{-05}	^{40}Sc	4.00×10^{-34}
^{41}K	6.34×10^{-19}	^{41}Ca	1.99×10^{-09}	^{41}Sc	4.10×10^{-34}	^{42}Ca	4.87×10^{-11}	^{42}Sc	4.20×10^{-34}
^{42}Ti	4.20×10^{-34}	^{43}Ca	7.41×10^{-14}	^{43}Sc	9.94×10^{-13}	^{43}Ti	4.30×10^{-34}	^{44}Ca	1.25×10^{-18}
^{44}Sc	1.82×10^{-17}	^{44}Ti	3.84×10^{-15}	^{45}Sc	2.80×10^{-21}	^{45}Ti	2.88×10^{-20}	^{46}Ti	1.89×10^{-25}
^{47}Ti	4.70×10^{-34}	^{48}Ti	4.80×10^{-34}						

Table 5.6: Model B: the mean composition (in mass fractions) of the ejecta of a nova outburst with an underlying 1.35 $M_{\odot}$ ONe WD. The listed isotopic abundances are computed using a network of reactions, all of which are taken from reaction rate libraries (see text) except that of the ^{29}P$(p,\gamma)^{30}$S reaction, which is here the median Monte Carlo rate of Ref. [134].

Nucleus	Yield	Nucleus	Yield	Nucleus	Yield	Nucleus	Yield	Nucleus	Yield
^{1}H	2.34×10^{-01}	^{2}H	9.51×10^{-19}	^{3}H	1.47×10^{-23}	^{3}He	7.10×10^{-09}	^{4}He	2.51×10^{-01}
^{6}Li	5.36×10^{-27}	^{7}Li	3.24×10^{-10}	^{7}Be	1.71×10^{-06}	^{8}B	2.45×10^{-23}	^{9}Be	4.66×10^{-32}
^{9}C	1.41×10^{-31}	^{10}B	2.79×10^{-25}	^{11}B	6.63×10^{-10}	^{11}C	6.31×10^{-10}	^{12}C	2.21×10^{-02}
^{12}N	6.60×10^{-33}	^{13}C	1.12×10^{-02}	^{13}N	4.41×10^{-03}	^{13}O	1.30×10^{-34}	^{14}N	5.47×10^{-02}
^{14}O	1.35×10^{-06}	^{15}N	1.07×10^{-01}	^{15}O	1.63×10^{-04}	^{16}O	6.05×10^{-03}	^{17}O	4.05×10^{-02}
^{17}F	2.52×10^{-08}	^{18}O	6.80×10^{-06}	^{18}F	4.35×10^{-05}	^{18}Ne	1.66×10^{-30}	^{19}F	1.20×10^{-06}
^{19}Ne	4.26×10^{-24}	^{20}Ne	1.46×10^{-01}	^{20}Na	2.00×10^{-34}	^{21}Ne	4.08×10^{-05}	^{21}Na	8.61×10^{-17}
^{21}Mg	2.10×10^{-34}	^{22}Ne	3.15×10^{-05}	^{22}Na	5.59×10^{-04}	^{22}Mg	2.20×10^{-34}	^{23}Na	3.44×10^{-03}
^{23}Mg	1.36×10^{-24}	^{23}Al	2.30×10^{-34}	^{24}Mg	8.49×10^{-05}	^{24}Al	2.40×10^{-34}	^{25}Mg	2.24×10^{-03}
^{25}Al	1.70×10^{-31}	^{25}Si	2.50×10^{-34}	^{26}Mg	1.49×10^{-04}	^{26c}Al	2.60×10^{-34}	^{26b}Al	2.60×10^{-34}
^{26m}Al	2.88×10^{-24}	^{26}Al$_{g.s.}$	4.54×10^{-04}	^{26a}Al	2.60×10^{-34}	^{26}Si	2.60×10^{-34}	^{27}Al	3.01×10^{-03}
^{27}Si	5.73×10^{-28}	^{27}P	2.70×10^{-34}	^{28}Si	3.08×10^{-02}	^{28}P	2.80×10^{-34}	^{29}Si	2.39×10^{-03}
^{29}P	4.53×10^{-31}	^{29}S	2.90×10^{-34}	^{30}Si	1.54×10^{-02}	^{30}P	2.26×10^{-05}	^{30}S	3.00×10^{-34}
^{31}P	8.73×10^{-03}	^{31}S	1.87×10^{-33}	^{31}Cl	3.10×10^{-34}	^{32}S	5.27×10^{-02}	^{32}Cl	3.20×10^{-34}
^{32}Ar	3.20×10^{-34}	^{33}S	8.01×10^{-04}	^{33}Cl	3.20×10^{-29}	^{33}Ar	3.30×10^{-34}	^{34}S	3.63×10^{-04}
^{34}Cl	4.16×10^{-34}	^{34}Ar	3.40×10^{-34}	^{35}S	3.50×10^{-34}	^{35}Cl	3.85×10^{-04}	^{35}Ar	1.73×10^{-33}
^{35}K	3.50×10^{-34}	^{36}S	3.60×10^{-34}	^{36}Cl	1.52×10^{-33}	^{36}Ar	5.14×10^{-05}	^{36}K	3.60×10^{-34}
^{36}Ca	3.60×10^{-34}	^{37}Cl	1.39×10^{-07}	^{37}Ar	1.44×10^{-04}	^{37}K	3.70×10^{-34}	^{37}Ca	3.70×10^{-34}
^{38}Ar	2.19×10^{-05}	^{38}K	2.25×10^{-06}	^{38}Ca	3.80×10^{-34}	^{39}Ar	3.90×10^{-34}	^{39}K	5.96×10^{-06}
^{39}Ca	3.90×10^{-34}	^{40}Ar	4.00×10^{-34}	^{40}K	4.81×10^{-34}	^{40}Ca	3.06×10^{-05}	^{40}Sc	4.00×10^{-34}
^{41}K	6.30×10^{-19}	^{41}Ca	1.99×10^{-09}	^{41}Sc	4.10×10^{-34}	^{42}Ca	4.88×10^{-11}	^{42}Sc	5.84×10^{-34}
^{42}Ti	4.20×10^{-34}	^{43}Ca	7.39×10^{-14}	^{43}Sc	9.97×10^{-13}	^{43}Ti	4.30×10^{-34}	^{44}Ca	1.25×10^{-18}
^{44}Sc	1.83×10^{-17}	^{44}Ti	3.85×10^{-15}	^{45}Sc	2.80×10^{-21}	^{45}Ti	2.90×10^{-20}	^{46}Ti	1.90×10^{-25}
^{47}Ti	4.70×10^{-34}	^{48}Ti	4.80×10^{-34}						

Table 5.7: Model C: the mean composition (in mass fractions) of the ejecta of a nova outburst with an underlying 1.35 $M_{\odot}$ ONe WD. The listed isotopic abundances are computed using a network of reactions, all of which are taken from reaction rate libraries (see text) except that of the ^{29}P$(p,\gamma)^{30}$S reaction, which is here the high Monte Carlo rate of the present work.

Nucleus	Yield	Nucleus	Yield	Nucleus	Yield	Nucleus	Yield	Nucleus	Yield
^{1}H	2.34×10^{-01}	^{2}H	9.51×10^{-19}	^{3}H	1.52×10^{-23}	^{3}He	7.34×10^{-09}	^{4}He	2.51×10^{-01}
^{6}Li	5.36×10^{-27}	^{7}Li	3.25×10^{-10}	^{7}Be	1.71×10^{-06}	^{8}B	2.36×10^{-23}	^{9}Be	5.56×10^{-32}
^{9}C	1.34×10^{-31}	^{10}B	6.68×10^{-25}	^{11}B	6.65×10^{-10}	^{11}C	6.30×10^{-10}	^{12}C	2.21×10^{-02}
^{12}N	6.19×10^{-33}	^{13}C	1.12×10^{-02}	^{13}N	4.40×10^{-03}	^{13}O	1.30×10^{-34}	^{14}N	5.47×10^{-02}
^{14}O	1.31×10^{-06}	^{15}N	1.07×10^{-01}	^{15}O	1.61×10^{-04}	^{16}O	6.09×10^{-03}	^{17}O	4.05×10^{-02}
^{17}F	2.44×10^{-08}	^{18}O	6.81×10^{-06}	^{18}F	4.35×10^{-05}	^{18}Ne	1.54×10^{-30}	^{19}F	1.19×10^{-06}
^{19}Ne	4.01×10^{-24}	^{20}Ne	1.46×10^{-01}	^{20}Na	2.00×10^{-34}	^{21}Ne	4.08×10^{-05}	^{21}Na	8.08×10^{-17}
^{21}Mg	2.10×10^{-34}	^{22}Ne	3.17×10^{-05}	^{22}Na	5.59×10^{-04}	^{22}Mg	2.20×10^{-34}	^{23}Na	3.44×10^{-03}
^{23}Mg	1.30×10^{-24}	^{23}Al	2.30×10^{-34}	^{24}Mg	8.77×10^{-05}	^{24}Al	2.40×10^{-34}	^{25}Mg	2.24×10^{-03}
^{25}Al	1.60×10^{-31}	^{25}Si	2.50×10^{-34}	^{26}Mg	1.49×10^{-04}	^{26c}Al	2.60×10^{-34}	^{26b}Al	2.60×10^{-34}
^{26m}Al	2.76×10^{-24}	^{26}Al$_{g.s.}$	4.53×10^{-04}	^{26a}Al	2.60×10^{-34}	^{26}Si	2.60×10^{-34}	^{27}Al	3.00×10^{-03}
^{27}Si	5.35×10^{-28}	^{27}P	2.70×10^{-34}	^{28}Si	3.08×10^{-02}	^{28}P	2.80×10^{-34}	^{29}Si	2.24×10^{-03}
^{29}P	4.25×10^{-31}	^{29}S	2.90×10^{-34}	^{30}Si	1.51×10^{-02}	^{30}P	2.19×10^{-05}	^{30}S	3.00×10^{-34}
^{31}P	8.61×10^{-03}	^{31}S	9.35×10^{-34}	^{31}Cl	3.10×10^{-34}	^{32}S	5.30×10^{-02}	^{32}Cl	3.20×10^{-34}
^{32}Ar	3.20×10^{-34}	^{33}S	8.17×10^{-04}	^{33}Cl	3.03×10^{-29}	^{33}Ar	3.30×10^{-34}	^{34}S	3.71×10^{-04}
^{34}Cl	3.40×10^{-34}	^{34}Ar	3.40×10^{-34}	^{35}S	3.50×10^{-34}	^{35}Cl	3.95×10^{-04}	^{35}Ar	7.88×10^{-34}
^{35}K	3.50×10^{-34}	^{36}S	3.60×10^{-34}	^{36}Cl	1.52×10^{-33}	^{36}Ar	5.29×10^{-05}	^{36}K	3.60×10^{-34}
^{36}Ca	3.60×10^{-34}	^{37}Cl	1.40×10^{-07}	^{37}Ar	1.47×10^{-04}	^{37}K	3.70×10^{-34}	^{37}Ca	3.70×10^{-34}
^{38}Ar	2.21×10^{-05}	^{38}K	2.27×10^{-06}	^{38}Ca	3.80×10^{-34}	^{39}Ar	3.90×10^{-34}	^{39}K	5.96×10^{-06}
^{39}Ca	3.90×10^{-34}	^{40}Ar	4.00×10^{-34}	^{40}K	4.81×10^{-34}	^{40}Ca	3.06×10^{-05}	^{40}Sc	4.00×10^{-34}
^{41}K	6.30×10^{-19}	^{41}Ca	1.98×10^{-09}	^{41}Sc	4.10×10^{-34}	^{42}Ca	4.86×10^{-11}	^{42}Sc	4.20×10^{-34}
^{42}Ti	4.20×10^{-34}	^{43}Ca	7.34×10^{-14}	^{43}Sc	9.89×10^{-13}	^{43}Ti	4.30×10^{-34}	^{44}Ca	1.24×10^{-18}
^{44}Sc	1.81×10^{-17}	^{44}Ti	3.81×10^{-15}	^{45}Sc	2.77×10^{-21}	^{45}Ti	2.86×10^{-20}	^{46}Ti	1.87×10^{-25}
^{47}Ti	4.70×10^{-34}	^{48}Ti	4.80×10^{-34}						

β^+-decay) abundance by at most 3% (with respect to that obtained from model B). Such a small effect therefore is not expected to significantly change the abundance of ^{30}Si from the β^+-decay of ^{30}P. Similarly, the higher rate of destruction of ^{29}P through proton capture in model C has reduced the abundance of this isotope by at most 6% (with respect to that obtained from model B), which is again not sufficiently large to significantly change the abundance of the product of ^{29}P β^+-decay, ^{29}Si.

Regarding the abundances of the heavier isotopes mentioned in § 2.4.1, model C again shows limited impact (with respect to models A and B), which vary from a 1.4% decrease to at most a 2.9% increase in the abundances of ^{31}P and ^{36}Ar, respectively. The highest change observed is in the abundance of ^{31}S: model C shows a 50% decrease with respect to model B. This is expected since the destruction of ^{30}P is favored by β^+-decay as opposed to a proton capture reaction leading to ^{31}S [71]. Also, as pointed out previously, with respect to model B, model C results in a reduction of ^{30}P by 3%.

The measured silicon isotopic ratios are usually expressed as [71]:

$$\delta\left(\frac{^{29,30}\mathrm{Si}}{^{28}\mathrm{Si}}\right) = \left[\left(\frac{^{29,30}\mathrm{Si}}{^{28}\mathrm{Si}}\right)_{\mathrm{ejecta}} / \left(\frac{^{29,30}\mathrm{Si}}{^{28}\mathrm{Si}}\right)_{\odot} - 1\right] \times 1000 \tag{5.11}$$

where δ represents deviations from solar abundances in permil [71], and the numerical values for the solar silicon isotopic ratios are (see Fig. 6.2 on p. 130 of Ref. [33]): $(^{29}\mathrm{Si}/^{28}\mathrm{Si})_{\odot} = 0.0506$ and $(^{30}\mathrm{Si}/^{28}\mathrm{Si})_{\odot} = 0.0334$.

From the classical nova simulations performed in the present work, such ratios are computed for models A, B and C. The results are shown in Table 5.8. Also shown are some SiC presolar grains with proposed classical nova paternity, whose ^{29}Si/^{28}Si and ^{30}Si/^{28}Si ratios have been measured [99].

As seen in Table 5.8, the theoretically predicted δ-values are much larger than the measured counterparts. Overall, however, regardless of the $^{29}\mathrm{P}(p,\gamma)^{30}\mathrm{S}$ reaction rate used, the ^{29}Si/^{28}Si ratio in the ejecta resulting from the simulations is only slightly higher (1.4 – 1.5 times larger) than the solar value. By using equation (5.11) and the measured $\delta(^{29}\mathrm{Si}/^{28}\mathrm{Si})$ values given in Table 5.8, we obtain a ^{29}Si/^{28}Si ratio measured in presolar grains that varies between a factor of 0.9 – 1.1 times the solar ratio, and thus is again only slightly higher than the solar value. Therefore, the simulated signatures are qualitatively consistent with the ^{29}Si/^{28}Si ratios measured in presolar grains identified

Table 5.8: Deviations (in permil) from solar abundances in simulated and measured nova silicon isotopic abundances. Models A to C are explained in the text, and are obtained from hydrodynamic simulations of classical nova outbursts. The measured values (the first four rows) are for those SiC presolar grains reported in Ref. [71, 99].

Grain	$\delta(^{29}Si/^{28}Si)$ (‰)	$\delta(^{30}Si/^{28}Si)$ (‰)	Hydrodynamic Model
AF15bB-429-3	28 ± 30	1118 ± 44	
AF15bC-126-3	-105 ± 17	237 ± 20	
KJGM4C-100-3	55 ± 5	119 ± 6	
KJGM4C-311-6	-4 ± 5	149 ± 6	
	527.1	13970	A
	533.5	13970	B
	437.3	13678	C

to have a nova origin. In other words, the simulated and measured δ-values both show enhancements in the same direction (qualitative agreement).

On the other hand, the $^{30}Si/^{28}Si$ ratio in the ejecta resulting from the simulations is much higher ($\sim$ 15 times larger) than the solar value, such that the classical nova ejecta resulting from the hydrodynamic models are significantly enriched in ^{30}Si. The $^{30}Si/^{28}Si$ ratio obtained[8] in presolar grains, however, varies between a factor of 1.1 – 2.1 times the solar ratio. Hence, both the simulated and the measured $^{30}Si/^{28}Si$ ratios are higher than the solar value but the models predict $^{30}Si/^{28}Si$ excesses much larger than those observed in nova-grain candidates. Therefore, the simulated and measured values again are in qualitative agreement with each other, i.e., enhancement in the same direction, but the magnitudes of the enhancements are not in agreement.

In order for the models to predict the $^{30}Si/^{28}Si$ ejecta ratio that quantitatively (enhancements in the same direction and of the same magnitude) matches the grain data, one has to assume a mixing process between material newly synthesized in the nova outburst and more than 10 times as much unprocessed, isotopically close to solar, material before the process of grain formation [71]. The details of the ejecta dilution and the grain formation processes are still unknown.

[8] Via using equation (5.11) and the measured $\delta(^{30}Si/^{28}Si)$ values given in Table 5.8.

In addition to invoking the mixing with solar composition material, increasing the $^{30}\mathrm{P}(p,\gamma)^{31}\mathrm{S}$ reaction rate [230] also helps to reduce the $^{30}\mathrm{Si}/^{28}\mathrm{Si}$ ratio by moving the nucleosynthesis flow away from $^{30}\mathrm{P}$ toward the heavier isotopes. A decrease in the abundance of $^{30}\mathrm{P}$ consequently reduces that of $^{30}\mathrm{Si}$ produced from $^{30}\mathrm{P}(\beta^+)^{30}\mathrm{Si}$. The $^{30}\mathrm{P}(p,\gamma)^{31}\mathrm{S}$ reaction rate is still uncertain [360]. By reducing the uncertainty in this rate, one can better constrain the nova model predictions, which in turn would also constrain the requirements for the aforementioned dilution process.

As shown in Table 5.8, with respect to models A and B, model C shows a 17% and 18% decrease in $\delta(^{29}\mathrm{Si}/^{28}\mathrm{Si})$, respectively. In addition, model C results in a $\delta(^{30}\mathrm{Si}/^{28}\mathrm{Si})$ which is decreased by 2.1% with respect to those obtained from models A and B. Thus, our more constrained $^{29}\mathrm{P}(p,\gamma)^{30}\mathrm{S}$ rate has reduced the silicon isotopic abundance ratios which are overly estimated in the simulations.

In comparison with the high Monte Carlo rate from the present work, the median and low Monte Carlo rates also obtained in the present work show smaller variations with respect to the rates of Refs. [134, 149]. Therefore, we did not continue our investigation of the effects of these rates on the nova yields.

As a conclusion, we have however eliminated the factor-of-three variation in silicon isotopic abundances obtained in Ref. [148] because the uncertainty in our rate has been significantly reduced relative to the range used in the aforementioned sensitivity study. In addition, we have used a full hydrodynamic simulation which is far more realistic and accurate than the post-processing nucleosynthesis simulation performed in the aforementioned sensitivity study [148]. Furthermore, the reaction rate library used in the present work includes reactions whose rates are calculated based on the new Monte Carlo method, and are thus updated with respect to those used in Ref. [148]. These factors also imply that the present nova calculations can be compared with more reliability to the isotopic ratios measured in presolar grains of potential nova paternity.

Chapter 6

Summary and Conclusions

The structure of proton unbound ^{30}S states plays a significant role in the determination of the ^{29}P$(p,\gamma)^{30}$S reaction rate, which influences explosive hydrogen burning in classical novae and type I X-ray bursts.

The ^{29}P$(p,\gamma)^{30}$S reaction rate at the temperature range of interest to novae and type I X-ray bursts had been predicted [149] to be dominated by two low energy resonances just above the proton threshold (4394.9(7) keV, determined from the recent measurement of Ref. [140]) corresponding to two excited states in ^{30}S at $E_x \approx 4.7$ – 4.8 MeV, whose J^π values were determined [149] to be 3^+ and 2^+, respectively. At the time of this prediction, both of these resonances were still unobserved, and thus their energies and the corresponding uncertainties were obtained [149] via theoretical predictions from the isobaric multiplet mass equation.

Such theoretical predictions, however, could only determine the energies of those two astrophysically important resonances with uncertainties of 40 keV. Therefore, since the reaction rate depends exponentially on the resonance energy, 40 keV uncertainty in the resonances' energies translated into up to 3 orders of magnitude of uncertainty in the reaction rate [149].

In a measurement [150] to investigate the nuclear level structure of ^{30}S via the two-nucleon transfer reaction ^{32}S$(p,t)^{30}$S, a tentatively assigned 3^+ level was observed at E_x = 4704(5) keV. The 2^+ level, on the other hand, remained unobserved.

We have also performed a similar experiment to study the level structure of ^{30}S via the ^{32}S$(p,t)^{30}$S reaction but with an energy resolution that is a factor of 3 better than

that of Ref. [150]. In order to reduce the background produced by our CdS target, we have fabricated a ^{32}S implanted target, whose ^{32}S content is the highest to date, and which reduced the background by about a factor of 2. As a result of these experiments, the energy of the 3^+ level is now determined to be 4688(2) keV, which is inconsistent with that of Ref. [150]. Moreover, for the first time, we have observed a new level in ^{30}S just above the proton threshold at 4812(2) keV. To confirm the existence of this level and its energy, as well as to determine the energy of the 3^+ level via another method, we also performed a high energy resolution in-beam γ-ray spectroscopy using the ^{28}Si(^{3}He, $n\gamma$)^{30}S reaction.

In the latter experiment, we constructed the energy of the 3^+ level from its γ-decays to the first and the second excited states in ^{30}S. The resulting energy is determined to be 4688.1(4) keV, which is consistent with our measurement from the ^{32}S$(p,t)^{30}$S experiment. Both of our results for the energy of this state from two measurements with completely different methods are consistent with each other, and yet inconsistent with the result of the measurement of Bardayan *et al.* [150]. Therefore, we concluded that the energy of 4704(5) keV measured in Ref. [150] differs from ours most likely due to poor statistics and energy resolution of the measurement in Ref. [150]. Furthermore, the energy of the 2^+ level from the in-beam γ-ray spectroscopy experiment is determined to be 4809.8(5) keV, which is also in good agreement with our result from the ^{32}S$(p,t)^{30}$S experiment.

From both of our experiments, we strongly suggest that the 4688-keV state has $J^\pi = 3^+$; however, the $J^\pi = 2^+$ assignment for the 4809.8-keV level still remains as tentative.

The rate of the ^{29}P$(p,\gamma)^{30}$S reaction at the temperature range of 0.1 GK to 1.3 GK corresponding to novae and type I X-ray bursts' nucleosynthesis was then recalculated via the new state-of-the-art Monte Carlo technique. This rate is indeed dominated by these two resonances at the temperature range of interest. The resonance energies corresponding to these two astrophysically important states in ^{30}S are now determined experimentally, and with significantly better precision than before. This achievement, in turn, has further substantially reduced the uncertainty in the rate of the ^{29}P$(p,\gamma)^{30}$S reaction.

Lastly, the impact of the ^{29}P$(p,\gamma)^{30}$S reaction rate on the abundances of the elements synthesized in novae was investigated. The surprising results for the effect of the new and

more constrained reaction rate on the silicon isotopic yields suggest that this reaction rate has limited impact on the silicon isotopic abundance ratios in nova ejecta calculated from hydrodynamic models as opposed to post-processing calculations.

This study also shows that the ^{29}Si/^{28}Si and ^{30}Si/^{28}Si ratios predicted by classical nova models follow the same trend as those measured in SiC presolar grains of possible nova paternity. While the former ratio predicted by the models is roughly qualitatively consistent with the measured ratio, the models predict a ^{30}Si/^{28}Si ratio that is much larger than the measured value. In order to obtain a ^{30}Si/^{28}Si ratio that is in quantitative agreement with the measured value, one has to understand better the mixing process between the nova ejecta material and the unprocessed material with solar abundances. Also, the grain formation process as well as the rate of $^{30}\mathrm{P}(p,\gamma)^{31}\mathrm{S}$ reaction have to be constrained better.

For future work, it will be worthwhile to investigate the impact of this most updated rate and its uncertainty on the yields of the elements synthesized in type I X-ray bursts to examine what impact this rate may have on the abundance of ^{30}S as an important rp-process waiting point. A significant change in the abundance of ^{30}S may potentially change the properties of the burst, e.g., the light curve structure and energy generation.

Although the previously unobserved astrophysically important resonances of ^{30}S are now experimentally known, the nuclear structure of this nucleus is still far from being understood. Most of the resonances of this nucleus, even the lowest-lying ones, have either unknown or tentatively assigned spin-parities. The half-lives, transition modes, mixing ratios, spectroscopic factors, resonance strengths, γ-ray and proton partial widths are not measured. Therefore, it is worthwhile to try to constrain these values by a direct $^{29}\mathrm{P}(p,\gamma)^{30}\mathrm{S}$ measurement, which requires the development of an intense ^{29}P radioactive ion beam.

Also, the spin-parities of the states of ^{30}S can be determined better theoretically via the isobaric multiplet mass equation. However, this method is currently unreliable (as shown in Chapter 3) because the analog states in ^{30}P also have unknown or tentatively assigned spin-parities. Thus, if such properties of the levels of ^{30}P are constrained better, this in turn will help with the determination of those of ^{30}S.

Appendix A

Fabrication of ^{32}S Implanted Targets

In Chapter 3, we mentioned that one of the targets, used for the $^{32}\mathrm{S}(p,t)^{30}\mathrm{S}$ two-nucleon transfer measurement, was a ^{32}S implanted into isotopically pure ^{12}C target. Here we describe the implantation process, as well as a RBS measurement that was performed (after the experiment at WNSL) to measure the areal density and absolute depth distribution of the implanted ^{32}S ions within the isotopically pure ^{12}C foil.

^{32}S implanted targets have been made previously [361]; however, the ^{32}S areal density achieved during our implantations, and the implantation time required per fabrication of each of our implanted targets, are respectively the largest and the shortest to date. This indicates that we have been able to make cheaper targets whose ^{32}S content are the largest so far.

It should be mentioned that all the pre- and post-implantation analysis regarding the required implantation dose at each incident energy and the analysis of the RBS measurement were kindly performed by Prof. W. N. Lennard from the UWO. Thus, this appendix does not include the details of the analysis. This work was partially funded by NSERC under *Discovery* Grant No. R0941, and is published in Ref. [362].

A.1 Introduction

As mentioned in Chapter 3, our CdS target used for the $^{32}S(p,t)^{30}S$ experiment yielded a large background counts/channel, which was attributed to the unwanted isotopes in that target.

To obtain a cleaner triton spectra from the $^{32}S(p,t)^{30}S$ reaction, we decided to fabricate a number of implanted targets. To reduce the number of unwanted isotopes, we implanted ^{32}S into isotopically pure ^{12}C foils, produced by ACF-Metals company [219]. Carbon foils are the most common substrates to support those targets made by evaporation or implantation of another material, and are frequently used in nuclear physics experiments.

The isotopically pure ^{12}C foils used for our purposes were enriched in ^{12}C by 99.9% [363], and were made via electron-beam evaporation onto 25-mm $\times$ 75-mm conventional glass slides [364].

These foils are more fragile than the natural carbon foils (made via arc evaporation) and usually have more pinholes in them [363]. Therefore, they are correspondingly more prone to breakage during the processes of floatation or mounting on the frame, as well as in and out of vacuum. These foils also absorb moisture significantly. Therefore, if the foils are not stored with desiccants such as silica gel or under vacuum as soon as they are received, the moisture in the air contaminates them with oxygen, and causes them to curl and blister while they are on the glass slide (see Fig. A.1).

Such blisters cause the foil to be somewhat detached from the glass slide, and thus during the floatation, the foil frequently cracks where it has curled, and as a result it may tear. Furthermore, when such foils with blistered areas are put under vacuum, there is a great chance that during the first few seconds of rapid depressurization the foil tears when the air behind those areas is sucked suddenly by the pump.

The carbon foils we used for the implantation had original areal densities[1] of (40 – 61) $\pm$ 10% μg/cm^2.

For our purposes, where the differential cross sections of the states of interest in ^{30}S are too low (a few μb/sr, see Chapter 3), it was crucial that the areal density of the ^{32}S content of the implanted target be as large as possible, because otherwise the low

[1] Areal density in units of g/cm^2 is equal to $\rho \times \Delta x$, where ρ is the density in g/cm^3 and Δx is the target thickness in cm.

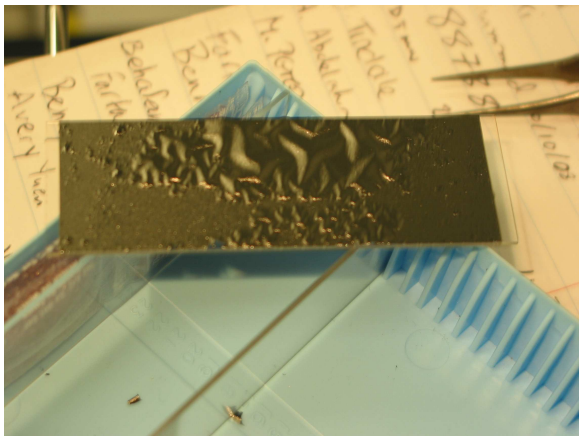

Figure A.1: The figure shows a non-implanted isotopically pure ^{12}C foil on a glass slide, when not kept under vacuum. The absorbed moisture causes the foil to be detached from the glass slide, and to blister.

target thickness would have imposed a problem of prohibitively long beamtime which would have been required for the measurements of the cross sections while obtaining a reasonable statistics at each spectrograph angle at WNSL.

On the other hand, with increasing implantation fluence (dose) the composition of the target changes [365]. Sputtering of the implanted ions (^{32}S in our case) increases, while sputtering of substrate atoms (^{12}C in our case) decreases [365]. Therefore, for all implanted targets no matter how long the substrate is irradiated, there is always a limit on how much of the desired ions could be implanted at a certain depth. Because with increasing implantation fluence, the target is sputtered, i.e., both the implanted ions and the substrate atoms will be lost, and ultimately a stationary concentration level will be reached where the amount of the implanted ions is equal to the amount of identical ions being sputtered. In other words, a saturation limit will be reached[2]. Furthermore, sputtering is not the only limitation: there is also diffusion, segregation and radiation damage to the carbon crystals due to the heat generated per unit area via irradiation by the sulfur ions [365].

As an example of the latter, 50-keV ^{32}S ions with a beam intensity per unit area of

[2]A very simple estimate of the saturation concentration is obtained from: saturation level = (low-fluence sputtered yield)$^{-1}$ [365].

250-μA/cm^2 raises the average temperature of the ^{12}C foil in vacuum by:

$$\frac{P}{A} = \frac{E\,I}{A} = \epsilon\,\sigma\,\left(T^4 - T_0^4\right) \Rightarrow T = 165^{\circ}\text{C} \tag{A.1}$$

where P/A is the power deposited by the ^{32}S beam per unit area; E is the beam energy (in eV); I is the beam intensity (in Amp); A is the area (in cm^2) on which the beam is scanned in a raster way, and here we have assumed that $A = 100$ cm^2; ϵ is the emissivity, which is 0.75 for carbon [366]; σ is the Stefan constant, and is equal to 5.6704 $\times$ 10^{-12} W/cm^2/K^4; T is the foil temperature (in K) after being irradiated by the beam; and T_0 = 293 K is the room temperature.

Such a thermal energy can only be exchanged in vacuum from the foil to the surrounding areas by thermal radiation. The Stefan-Boltzmann law given above links the thermal power radiative density to the average temperature of the foil (T) and that of the surrounding world (T_0). This formula only provides an underestimated value for the sample's temperature when the radiative power density is in equilibrium with the power deposited by the beam per unit area (P/A). The instantaneous foil's temperature can reach a much higher value because of the low volume to area ratio of the ^{12}C films we had [366]. However, the temperature stays far below 3000 °C at which point the carbon starts to sublime[3].

When the beam is scanned over high frequencies (1 kHz), our thin ^{12}C films would not average the temperature enough over the scan periods and the film's instantaneous temperature would change too rapidly over the unit area, causing a lot of thermal stress cycling over the time it takes to reach the desired implantation dose. The very small thermal time constant of the self-supported ^{12}C films [366] therefore causes the films' temperature variations to pose a significant problem if the deposited power per unit area is too high, e.g., the beam intensity per unit area is too high.

The other technical difficulties with the implantation process apart from those mentioned above are: the rupture risks resulting from the internal surface stresses build-up from sulphur intercalation into carbon, which causes the bombarded area of the foil to shrink[4], pulling in the material from the surrounding foil regions, and forming radial stress lines from the edge of the beam spot to the target frame [367]; as well as surface

[3]Carbon foils do not melt [366].

[4]This risk increases with the deposited power per unit area during implantation.

ion damages as a result of the Coulomb forces from charge build-up, since the carbon foils are not conductive enough. Such difficulties exist regardless of how the implanted targets are fabricated. However, a thin gold coating would probably decrease the latter risks. Also, it has been found empirically [367, 368] that initial exposure to an intense photographic strobe light may delay the onset of foil rupture through foil slackening.

After investigating all these challenges, it was decided that our ^{12}C films could be best implanted with ^{32}S ions via a de-focalized beam at lower beam currents to minimize the thermally induced mechanical stresses that seemed to be the most significant challenge involved. However, the lower the beam intensity, the longer the time it takes to implant each sample with the desired dose[5].

We had two choices for the location of the fabrication of our ^{32}S implanted target: the Tandetron Accelerator Laboratory at the UWO and the Laboratory of Micro- and Nano-fabrication at Institut National de la Recherche Scientifique Énergie, Matériaux et Télécommunications (INRS-EMT) at Université d'avant-garde in Québec.

The latter laboratory has an ion implanter, which provides very high ^{32}S beam currents (250 μA). The beam is scanned on the target with scanning frequencies of about 1 kHz horizontally and 117 Hz vertically [366]. As mentioned previously, this would pose a serious problem due to the thermal damages via thermally induced mechanical stresses caused by the instantaneous thermal load of the beam to the implanted target during its fabrication, and the very large number of the beam cycling.

Thus, we fabricated our implanted targets in the former laboratory, which was particularly chosen because the ^{32}S beam intensity that could be provided is not too high, the overall cost is lower even though the beam intensity is also lower and the laboratory is close to McMaster University, and thus the risk of the target foils getting damaged due to transportation is significantly decreased.

A.2 Tandetron Accelerator Laboratory at the UWO

The implantation was performed in the Tandetron Accelerator Laboratory at the UWO, where a T-shaped high current 1.7 MV (maximum terminal voltage) tandetron

[5]The relation is: $t = n\,e/I$, where t is time in sec, n is number of incident ions, e is the electronic charge and I is the beam intensity in Amperes.

accelerator, manufactured by General Ionex Corporation [369], accelerates ion beams of various non-radioactive elements (except the noble gases and a few others) provided by a dual source injecting system: a duo-plasmatron (for production of hydrogen and helium beams) and a negative sputtering ion source similar to the ones described in Chapters 3 and 4.

The tandetron accelerators are compact state-of-the-art tandem accelerators designed to produce a few tens of keV to several MeV ion beams, while operating in a normal laboratory environment. These rather small accelerators provide three types of beam currents: medium currents, "medium currents plus" and high currents [370]. Unlike the other tandem accelerators that are coupled to a Van de Graaff accelerator as described previously, the terminal voltage of the tandetron accelerators is provided by a parallel-fed Cockroft-Walton[6] high voltage power supply [371, 372] that is coupled to the tandem accelerator perpendicular to the accelerator tubes. This type of power supply is a purely electronic device. Therefore, no Pelletron chain is required and this makes the tandetrons terminal voltage much more stable, reliable and less prone to voltage fluctuation caused by the moving parts inside the pressure vessel. Also, the pressure tank does not need to be opened regularly for frequent maintenance [369].

Moreover, the beam energy resolution of the tandetron accelerator is superior to those of other types of tandem accelerators. Finally, a device called the Q-snout lens is used in the entrance of the low energy end of the acceleration tube, which eliminates the need of the pre-acceleration stage by an injector system [369].

The layout of the Tandetron Accelerator Laboratory at the UWO is shown in Fig. A.2. The tandetron accelerator at the UWO is a single-ended machine, i.e., there is no stripper foil or gas being used in the terminal. Hence, unlike the two tandems described in previous chapters, which have two acceleration stages for the negatively- and positively-charged beam prior to and after the terminal, respectively, this machine works in acceleration-deceleration mode. The beam remains negatively charged throughout the acceleration tube, and thus is accelerated towards the positive terminal located in the middle of the acceleration tube, and decelerated away from the terminal in the second stage.

Using compounds that have sulfur in the gas phase, e.g., H_2S or SO_2 gases, together with the duo-plasmatron ion source are in practice frequently troublesome as the H_2S

[6]See Ref. [123] (p. 204).

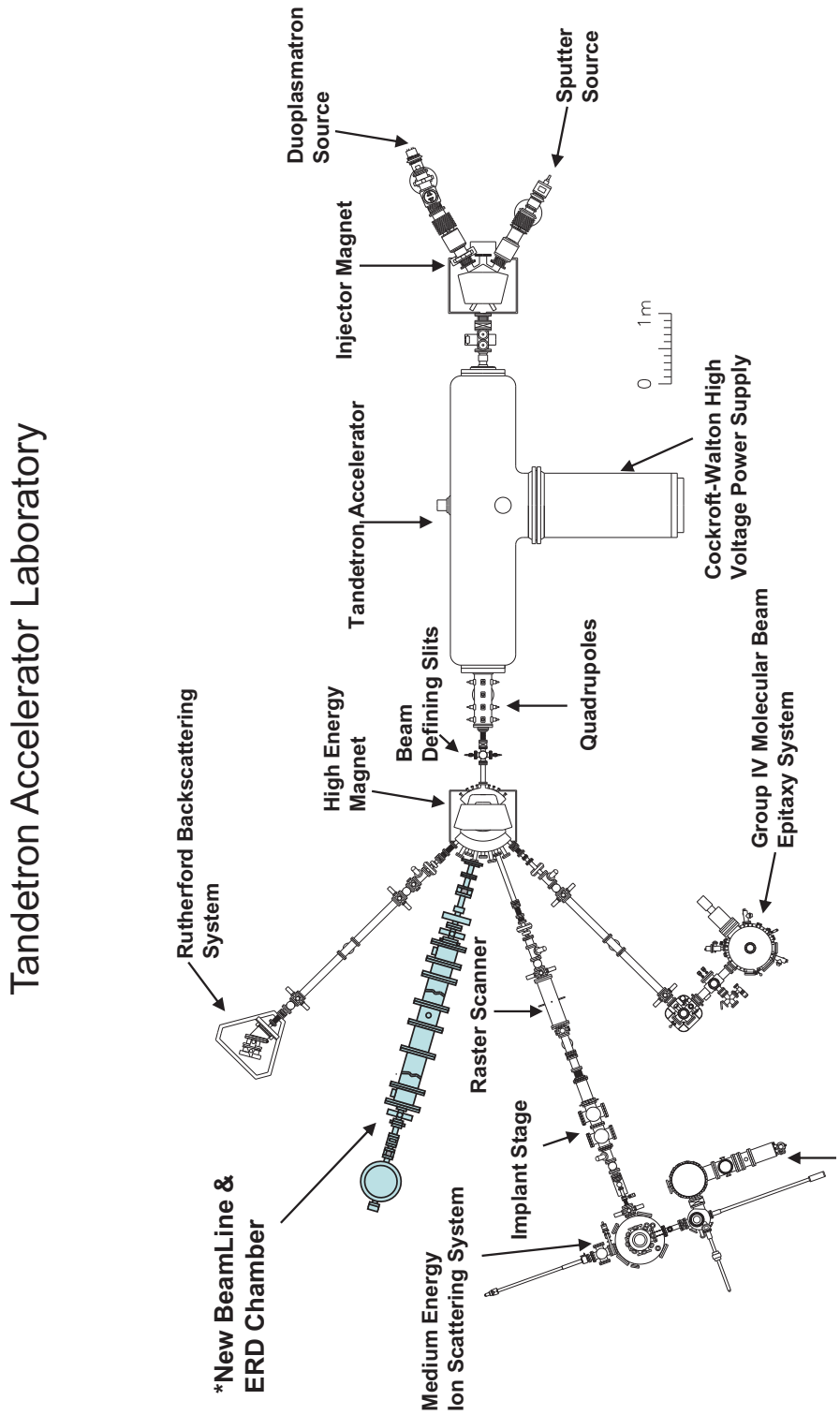

Figure A.2: Schematic diagram of the Tandetron Accelerator Laboratory at the UWO. For the present work, we used the implantation and the RBS beam lines. The figure was obtained from Mr. Jack Hendriks.

gas is not only corrosive but it has a tendency to decompose into elemental sulfur which condenses and blocks apertures in the ion source [195]. SO_2 gas, on the other hand, is an oxidizing gas at high temperatures, and thus it may get involved in a chemical reaction with the molybdenum plasma chamber of the duo-plasmatron ion source which is maintained at 1200 °C. We thereby did not use the duo-plasmatron ion source. Instead, we made use of the negative sputtering ion source to fabricated our implanted targets.

Sulfur has a low melting point (115.21 °C) and an extremely high vapor pressure (1 Pa at 375 K). Therefore, the elemental sulfur is unsuitable [206] for use as the material contained in the cathode cone in the sputtering ion source because even when the cathode is kept cooled to avoid elemental sulfur from being melted by the heat generated via bombardment of Cs^+ ions in the ion source, it will sublime in vacuum under the Cs bombardment. We therefore used a metallic natural iron sulfide (FeS with melting point of 1195 °C) with natural sulfur content, from which 95.02% is ^{32}S, as the cathode material in the negative sputtering ion source.

A beam of $^{32}S^-$ ions was produced using the negative sputtering ion source. The ion extraction voltage of the ion source is up to 20 kV and the tungsten plate in the source is kept at -8 kV.

Since the cathode material of the ion source contained natural sulfur, our beam contained all stable isotopes of sulfur, i.e., ^{32}S, ^{33}S, ^{34}S and ^{36}S. This cocktail beam then passed through the injector magnet, whose mass resolution of 1/190 is adequate to completely resolve ^{32}S from the other unwanted isotopes. The $^{32}S^-$ beam was then accelerated and decelerated with the tandetron accelerator to energies in the range of 50 – 100 keV (maximum tandem terminal voltage used was 0.5 MV).

To obtain an overall "high"[7] areal density of ^{32}S implanted ions, the most effective implantation procedure was to vary the beam energy in steps to change the location of the implantation and the depth profile of the implanted ions, therefore avoiding saturation; and to simultaneously change the implantation dose (or the beam current) to keep the power/area constant. In this way, we could obtain an overall higher ^{32}S equivalent thickness.

The beam was then deflected by -20° via the switching magnet (high energy magnet in

[7]With implanted targets, one would most likely never obtain more than a few $\mu g/cm^2$ for the areal density of the implanted ions.

Fig. A.2) into the dedicated ion implantation beamline. This beam was electrostatically rastered over a circular surface of a Ta collimator of area 1.13 cm^2. This is a standard way of implanting ions to produce a uniform implantation distribution by utilizing an over-sweeping procedure. The rastering was achieved by applying non-harmonically related triangular waveforms to the X and Y deflection plates located upstream of the implantation chamber. The raster scan unit has horizontal frequency of 517 Hz and vertical frequency of 64 Hz.

A.3 The Ion Implantation Procedure

Part of the 61 ± 6.1 $\mu g/cm^2$ ^{12}C foil was first cut and floated off the glass slide (parting agent: NaCl) using distilled water. This foil was then exposed to an intense photographic flash light from a camera located 10 cm away, and was mounted on the designated metallic target frame mounted in turn on a Ni block target holder to provide beam current integration. This assembly was located inside an electron-suppressed screened cage, and was kept under vacuum maintained at a pressure of $P < 10^{-7}$ Torr to minimize impurities, including ^{13}C contamination from residual hydrocarbons in the beamline. The Ni block was not cooled since it is found that the cooled frame adds no particular advantage [367]. After approximately an hour of irradiation of this foil with $\approx$ 4-μA 100-keV $^{32}S^-$ ions, the foil ruptured. This could be avoided by decreasing the beam current to the range of enA; however, decreasing the beam intensity is undesirable because it increases the implantation time, and therefore causes the target to cost more. Thus, all targets were fabricated while the ^{12}C foils were still mounted on the glass slides, and the implanted foils (targets) were then subsequently floated off the glass slides using distilled water.

Therefore, for all subsequent implantations a whole glass slide was mounted on the Ni block. To avoid serious thermal damage to the foils, the beam current was limited to values less than 4 μA. The recorded beam ($E_{\text{beam}} = 100$ keV) current was ~ 1.3 μA when the sweeping system was operating. The local beam current density was ~ 25 $\mu A/cm^2$ based on the $\sim 4 \times 4$ mm^2 dimensions of the focused particle flux. Thus, the power deposited per unit area was ~ 2.5 watts/cm^2. For the lowest energy, i.e. 50 keV, the maximum beam current on target was ≈ 0.45 μA due to reduced transmission of such a beam through the accelerator. Therefore, we could not keep the deposited power/area

constant by increasing the beam intensity, while decreasing the beam energy. However, we still managed to keep the power/area constant by changing the implantation dose at each incident energy such that the times required to implant the desired doses differed from each other.

Four implanted targets were made this way with nominal total implantation fluences of $(1.92 - 2.01) \times 10^{17}$ ions/cm^2, which are equivalent[8] to $10.2 - 10.7$ μg/cm^2, respectively. The absolute dose calculated from measuring the beam current via the beam current integration system was found to be reliable (from previous implantations at the same laboratory) to within 5%.

For two of the targets, hereafter targets 1 and 2, the incident ^{32}S beam energies were chosen to be 50, 70, 80 and 100 keV with respective individual implanted fluences (in units of 10^{17} ions/cm^2) of 0.38, 0.29, 0.29 and 1.05 (for target 1), and 0.36, 0.28, 0.28 and 1.0 (for target 2). Therefore, the total implanted dose achieved was 2.01×10^{17} ions/cm^2 ≈ 10.7 μg/cm^2 (for target 1) and 1.92×10^{17} ions/cm^2 ≈ 10.2 μg/cm^2 (for target 2). The thicknesses of the ^{12}C substrates for both these targets were 40 ± 4 μg/cm^2. As an example, the depth distribution of ^{32}S ions in the ^{12}C foil for target 1 is shown in Fig. A.3a. Target 1 got destroyed due to a pump failure during our experiment in WNSL.

For the other two targets, hereafter targets 3 & 4, on the other hand, the incident beam energy varied between 60 – 100 keV with increments of 10 keV, and individual implanted fluences were 0.23, 0.33, 0.33, 0.33 and 0.76 (in units of 10^{17} ions/cm^2), respectively. The thicknesses of the ^{12}C substrates of these latter targets were 53 ± 5 and 61 ± 6 μg/cm^2, respectively. The total implantation fluence was thus 1.98×10^{17} ions/cm^2 ≈ 10.5 μg/cm^2 for the latter targets. Varying the implantation fluence at each incident energy yielded a Gaussian and symmetric concentration profile based on simulations using the SRIM software [320] (see Fig. A.3b). In Fig. A.3, the ordinates are obtained by division of the total implanted dose in units of ions/cm^2 by the thickness of the total ^{32}S content of the target in cm. The latter is obtained by the division of the total areal density of ^{32}S in units of μg/cm^2 by the density of ^{32}S, which is assumed to be equal to that of the natural sulfur (2.0686 g/cm^3).

From simulations with the SRIM software [320], the sputtering yields corresponding

[8]The formula is: $T = (t\,N_A)/A$, where T is the implanted thickness in units of (# of ions)/cm^2, t is the implanted thickness in units of g/cm^2, N_A is Avogadro's number, and A is the atomic mass of the implanted ions.

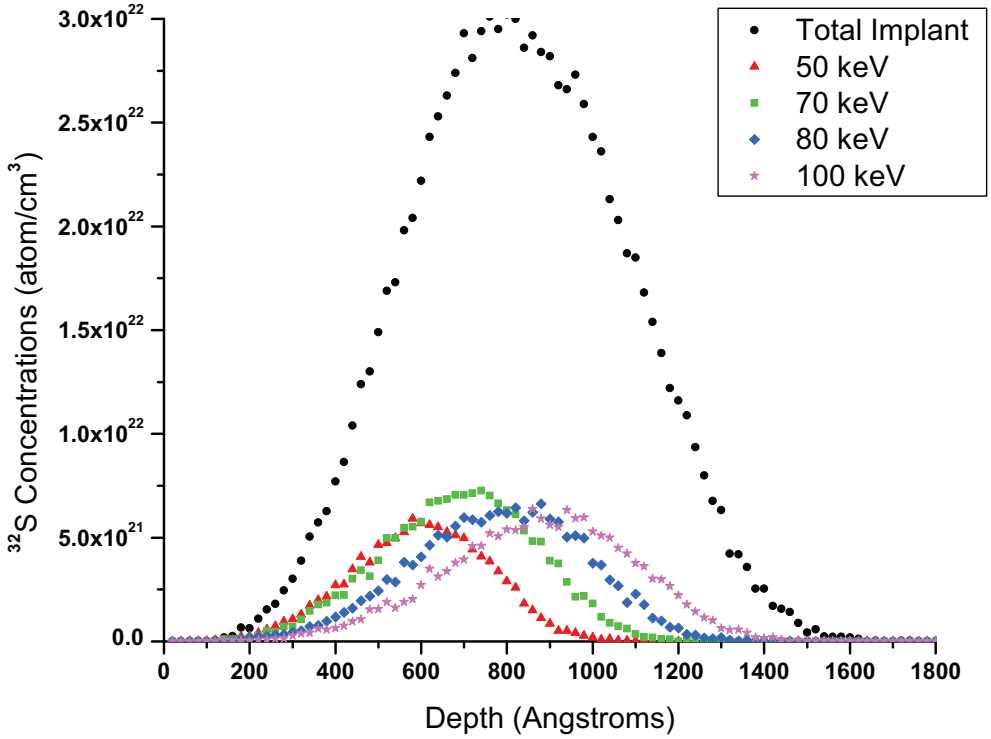

(a) Target 1

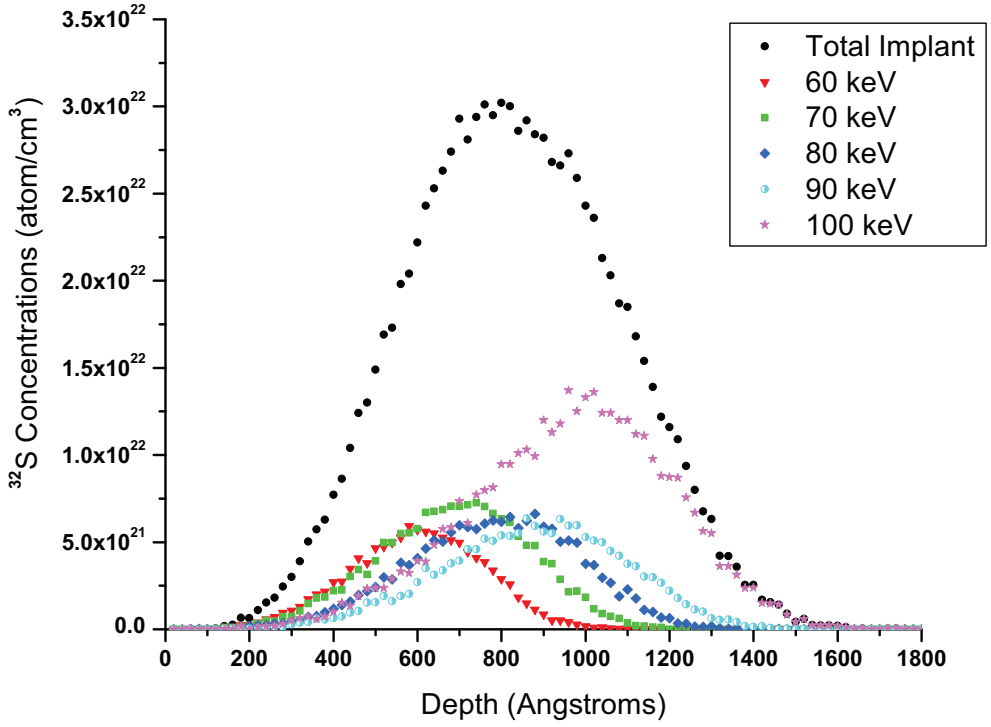

(b) Target 3

Figure A.3: Depth profiles for ^{32}S ions with different incident energies into ^{12}C foils. Each depth distribution is weighted by the implantation fluence at that energy.

to ^{32}S ions were estimated to be $Y_s = 0.79 - 0.57$ atom per incident ion for the incident beam energy range of 50 – 100 keV, respectively. Thus, the sputtering yield decreases with increasing energy. On the other hand, the sputtering yield corresponding to ^{12}C decreases with decreasing energy, and for the incident energy of 50 – 100 keV, $Y_c = (0.20 - 0.70) \times 10^{17}$ atoms/cm^2, respectively. Thus, the total amount of ^{12}C sputtered is found to be ≈ 2.5 μg/cm^2. Using the natural carbon's density of 2.253 g/cm^3 for ^{12}C, the equivalent thickness corresponding to 2.5 μg/cm^2 is 110 Å, which corresponds to near surface regions of the ^{12}C foil, and would therefore result in a negligible loss ($< 0.3\%$) of the implanted species since little implanted ^{32}S dose is found in this region (see Fig. A.4). It is worth noting that there are some empirical formulas for calculating the sputtering yields, which can be found in Refs. [373–375]. Ref. [375] provides reliable estimates (to within 20% [365]) for sputtering yields as long as the beam energy is in the keV region [365].

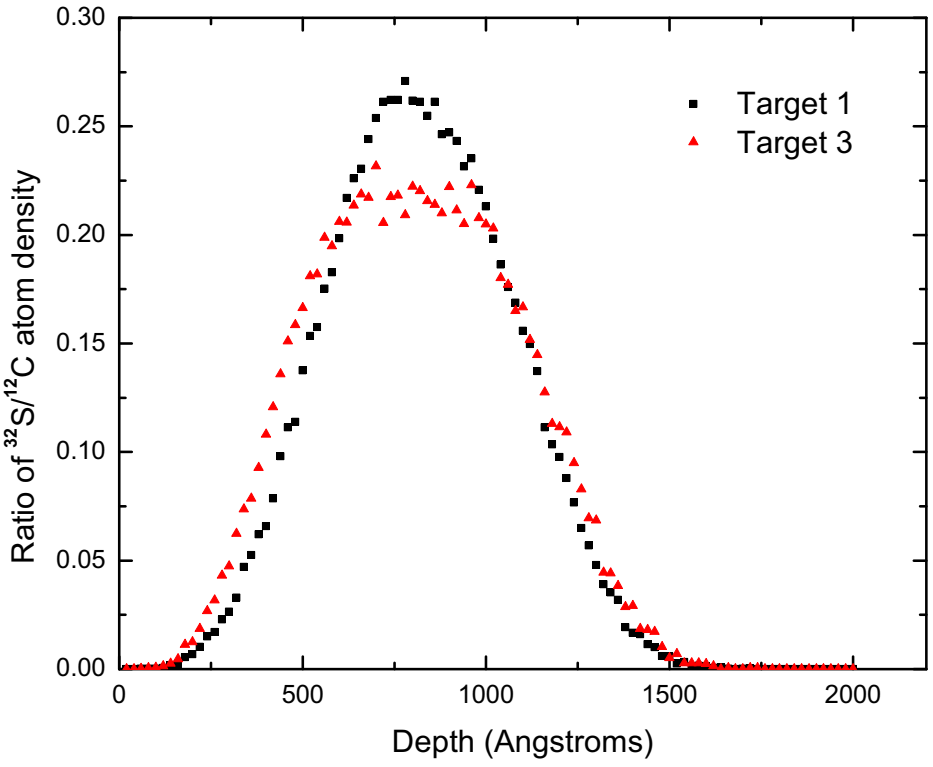

Figure A.4: The simulated (via SRIM software [320]) atom density of ^{32}S relative to that of ^{12}C for targets 1 and 3 fabricated at the Tandetron Accelerator Laboratory at the University of Western Ontario.

With regard to the saturation dose that could be achieved for the S-in-C system, we observe that at the maximum, the [^{32}S]:[^{12}C] ratio is ≈ 0.27, which occurs at a depth of ~ 18 μg/cm^2 (see Fig. A.4).

Each 25-mm $\times$ 75-mm conventional glass slide which did not show traces of blisters produced by moisture that was absorbed by the ^{12}C foil, resulted in two implanted targets for us. The fabrication of each of our ^{32}S implanted targets took 7 hours only. This implantation time is much less than that of those sulfur implanted targets fabricated by Kutt *et al.* [376], Fifield*et al.* [377], Vouzoukas *et al.* [378] and Wrede *et al.* [361], where the implantation of one sample took more than one day. Also, in comparison with the aforementioned sulfur implanted targets, the equivalent target thicknesses achieved for our targets are far superior than those mentioned previously. Moreover, our fragile self-supporting implanted targets survived a number of mounting and de-mounting procedures in and out of vacuum during the course of a number of experiments performed at WNSL and elsewhere.

After target 1 got destroyed, we used target 3 in our subsequent experiment with the implanted target at WNSL. The current integration system proved to be reliable; however, to measure the areal density and absolute depth distribution of the implanted ^{32}S atoms within the ^{12}C substrate of target 3, we transported this target back to the tandetron laboratory to perform a RBS measurement.

A.4 Rutherford Backscattering Spectrometry

The RBS measurements are useful tools[9] that are widely used for near-surface layer analysis of solids. A target is bombarded with ions (usually protons or α-particles) with incident energy of a few MeV, and the energy of the backscattered projectiles is recorded with an energy sensitive detector, typically a solid state detector, located at backscattering angles of typically 150° – 170°.

RBS allows for the quantitative determination of the elemental composition of a sample material and depth profiling of individual elements. It is very sensitive (on the order of ppm) for detecting heavier elements on lighter substrates when a projectile with low

[9]Ref. [379] is recommended for understanding the theory of the RBS measurements and their modern applications.

incident energy impacts such targets. However, the drawback of the RBS measurements is its low sensitivity to detection of lighter elements on heavier substrates [380]. Since the RBS experiments are in fact elastic scattering of protons or ^{4}He particles, they are non-destructive and do not alter the chemical structure of the sample. However, the name "Rutherford backscattering" is badly selected as these experiments could include scattering with non-Rutherford cross sections[10], as well as backward and forward scattering angles. Perhaps the first RBS measurement used as a tool for material analysis was performed by Rubin *et al.* [381]. However, originally Lord Ernest Rutherford of Nelson used the backscattering of α-particles from a gold film in 1911 to probe the structure of the atom.

To perform the RBS experiment on target 3, following its application in our nuclear physics experiment at WNSL, a $^4He^+$ beam was produced by the duo-plasmatron ion source at the tandetron laboratory at the UWO, and was accelerated to 1.5 MeV via the tandetron accelerator. This beam then impinged on target 3, which was located on the same plane as the beam and at 0° with respect to the beam axis. The elastically scattered ^{4}He ions were detected in a Si surface barrier detector with energy resolution of 11 keV positioned at the scattering angle of 170° such that the solid angle subtended by the detector was 2.3144 msr. The scattering geometry was defined by the Cornell geometry [380]. The advantages achieved by this geometry are a large scattering angle which provides optimized mass resolution; and large grazing incident and exit angles which optimize depth resolution [380].

A thick ($\approx$ 13 μm) mylar ($C_{10}H_8O_4$) backing foil was placed behind target 3 to stop the ^{4}He beam. To calibrate the solid angle and the detector's energy dispersion, we employed a reference target containing a precisely known fluence of ^{209}Bi atoms (specifically $(4.85 \pm 0.10) \times 10^{15}$ atoms/cm^2) implanted at 35 keV into amorphous Si to a depth of $\approx$ 20 nm.

The total RBS spectrum is shown in Fig. A.5. The sulfur peak and its background baseline were fitted by a Gaussian function and a linear polynomial, respectively, to extract the background-subtracted area under the sulfur peak. The pure ^{12}C peak corresponding to the ^{12}C content of target 3 was also extracted by subtracting the background

[10]Cross sections become non-Rutherford if nuclear forces get involved, i.e., at high incident energies and scattering angles, and for lighter substrates. At low incident beam energies, the departures from Rutherford cross sections are caused by partial electron screening of the nuclear charges [379] (Chapter 4).

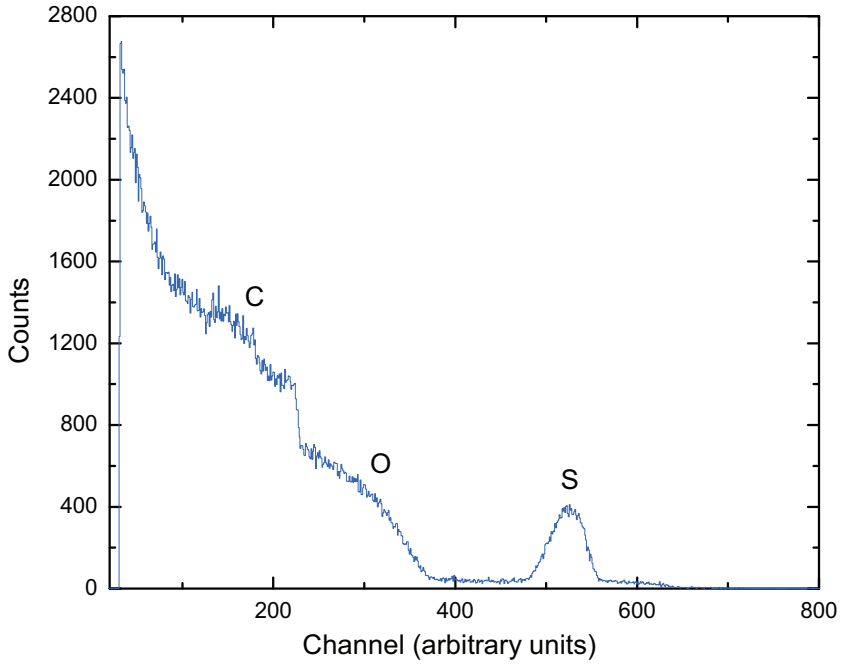

Figure A.5: The spectrum from the RBS measurement on the ^{32}S implanted target 3. The peaks corresponding to the sulfur and carbon contents of the implanted target are shown. The oxygen peak corresponds to the oxygen content of the mylar foil placed under target 3.

RBS spectrum measured on a non-implanted ^{12}C foil, identical to the one used as the backing of target 3, normalized to that of the spectrum obtained by target 3. These two residual spectra were then added together to produce one spectrum containing only two peaks corresponding to the ^{12}C and ^{32}S contents of target 3. This spectrum was then simulated using the SIMNRA simulation software package [382] with 12 layers of ^{12}C and ^{32}S with different concentrations and thicknesses for each layer. These latter parameters were varied until the simulated spectrum visually fitted the spectrum obtained from the RBS measurement (see Fig. A.6).

For the simulations, the values of the stopping power of ^{4}He in carbon were taken from Ref. [383].

In Fig. A.6, the carbon region of the spectrum below channel 230 is somewhat noisy due to the need to subtract that yield arising from the underlying mylar. Nevertheless, the large ^{32}S atom density in the ^{12}C-foil is evident from the dip in the spectrum around channel 180. The ^{32}S region of the spectrum ($\approx$ channel 480 – 560) is well separated from lower-Z features. The smooth curve is the result of fitting by SIMNRA [382].

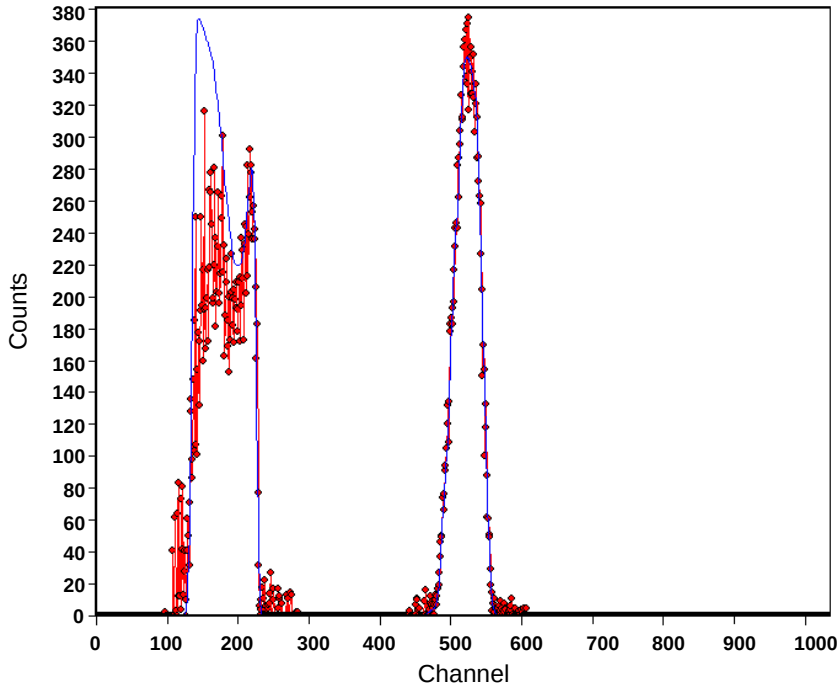

Figure A.6: RBS spectrum corresponding only to the ^{12}C and ^{32}S contents of target 3. The blue curve is the simulated fit resulting from a SIMNRA [382] simulation to the experimental data (red dots connected by red lines). The higher energy peak corresponds to ^{4}He ions scattered from the implanted ^{32}S atoms, and the lower energy region shows the yield of ^{4}He-ions scattered off ^{12}C.

As a result of the SIMNRA simulation, the total ^{12}C and ^{32}S thicknesses are determined to be 55.9 $\pm$ 5.6 μg/cm^2 and 10.4 $\pm$ 0.4 μg/cm^2, respectively.

This target thus proved that the implanted ^{32}S ions remained in the ^{12}C foil because the areal density of 10.4 $\pm$ 0.4 μg/cm^2 for the content of ^{32}S, measured (via RBS experiment) a few months after the implantation, can be expressed as (1.96 $\pm$ 0.08) $\times$ 10^{17} ions/cm^2, which is in excellent agreement with the total nominal implanted dose of (1.98 $\pm$ 0.10) $\times$ 10^{17} ions/cm^2, equivalent to 10.5 $\pm$ 0.5 μg/cm^2, measured via the beam current integrator during the implantation. Therefore, the ^{32}S species is stably locked into the ^{12}C lattice, and the irradiation of the ^{32}S species via the 34.5-MeV proton beam at WNSL and the depressurization of the implanted target by the high vacuum imposed on this target did not cause the removal of these atoms from the implanted target. This may be due to the rather high (with respect to the noble gases or other elements) energy required to form separated neutral atoms in their ground electronic state from the solid containing them (for natural sulfur: U_s = 2.85 eV/atom at 0 K and 1 atm [384]).

An attempt to also measure via ellipsometry [385] the areal density and depth profile of individual elements contained in target 3 failed because the target had an opaque and a curly surface, which was not appropriate for this technique.

Finally, the principal sources of contamination for target 3 are Si together with the possibility of traces of the parting agent (NaCl) present on the underlying glass slide. The latter are either released due to the heat generated by the ^{32}S beam during the implantation while the foil was still attached to the glass slide, or in the distilled water during floatation process. Neither the RBS spectrum nor the data obtained during the experiment performed at WNSL show no evidence for the presence of Na or Cl in the implanted target, although the RBS sensitivity for these elements is not high. We thus present a very conservative upper limit of 0.2 μg/cm^2 for Na and Cl impurities. No significant contamination was observed in the carbon foil alone from the RBS measurement on a identical piece of non-implanted ^{12}C foil. The silicon contamination was due to migration of silica dust from the silica gel, which was not removed from the chamber containing target 3. Therefore, the silica gel together with target 3 were stored under vacuum. The RBS measurement could not detect the amount of silicon contamination due to the proximity of Si to S in mass. However, as explained in Chapter 3, the equivalent areal density of Si contamination was determined from the two nucleon transfer experiment performed at WNSL to be 1.0 $\pm$ 0.5 μg/cm^2.

Bibliography

[1] C. Iliadis, *Nuclear Physics of Stars* (Wiley-VCH, Weinheim, 2007).

[2] S. Chandrasekhar, Philosophical Magazine Ser. 7 (Suppl.) **11**, 592 (1931), (this reference is reproduced in S. Chandrasekhar, J. Astrophys. Astron. **15**, 105 (1994)).

[3] W. J. Luyten, Publ. Astron. Soc. Pac. **34**, 156 (1922).

[4] W. J. Luyten, Publ. Astron. Soc. Pac. **34**, 54 (1922).

[5] W. J. Luyten, Publ. Astron. Soc. Pac. **34**, 132 (1922).

[6] W. J. Luyten, Publ. Astron. Soc. Pac. **34**, 356 (1922).

[7] A. S. Eddington, Mon. Not. R. Astron. Soc. **84**, 308 (1924).

[8] J. B. Holberg, Bull. Am. Astron. Soc. **37**, 1503 (2005).

[9] W. Bednarek and J. Pabich, Mon. Not. R. Astron. Soc. **411**, 1701 (2010).

[10] H. Ritter, Mem. Soc. Astron. It. **1**, 1 (2008).

[11] S. Chandrasekhar, Astrophys. J. **74**, 81 (1931).

[12] M. Kilic, K. Z. Stanek, and M. H. Pinsonneault, Astrophys. J. **671**, 761 (2007).

[13] S. Mereghetti, A. Tiengo, P. Esposito, N. L. Palombara, G. L. Israel, and L. Stella, AIP Conf. Proc. **1248**, 85 (2010).

[14] M. H. van Kerkwijk, P. Bergeron, and S. R. Kulkarni, Astrophys. J. **467**, L89 (1996).

[15] P. J. Callanan, P. M. Garnavich, and D. Koester, Mon. Not. R. Astron. Soc. **298**, 207 (1998).

[16] J. Liebert, P. Bergeron, D. Eisenstein, H. C. Harris, S. J. Kleinman, A. Nitta, and J. Krzesiński, Astrophys. J. **606**, L147 (2004).

[17] A. Kawka and S. Vennes, Astron. & Astrophys. **506**, L25 (2009).

[18] C. C. Dahn, P. Bergeron, J. Liebert, H. C. Harris, B. Canzian, S. K. Leggett, and S. Boudreault, Astrophys. J. **605**, 400 (2004).

[19] S. O. Kepler, S. J. Kleinman, A. Nitta, D. Koester, B. G. Castanheira, O. Giovannini, A. F. M. Costa, and L. Althaus, Mon. Not. R. Astron. Soc. **375**, 1315 (2007).

[20] M. Kilic, C. A. Prieto, W. R. Brown, and D. Koester, Astrophys. J. **660**, 1451 (2007).

[21] R. W. Brown, M. Kilic, C. A. Prieto, and S. J. Kenyon, Astrophys. J. **723**, 1072 (2010).

[22] M. Kilic, W. R. Brown, C. A. Prieto, S. J. Kenyon, and J. A. Panei, Astrophys. J. **716**, 122 (2010).

[23] S. Vennes and A. Kawka, Mon. Not. R. Astron. Soc. **389**, 1367 (2008).

[24] D. J. Eisenstein, J. Liebert, H. C. Harris, S. J. Kleinman, A. Nitta, N. Silvestri, S. A. Anderson, J. C. Barentine, H. J. Brewington, J. Brinkmann, et al., Astrophys. J. Suppl. Ser. **167**, 40 (2006).

[25] *Sloan Digital Sky Survey*, website: `http://www.sdss.org/`.

[26] R. N. Boyd, *An Introduction to Nuclear Astrophysics* (The University of Chicago Press, 2008).

[27] C. Plinius Secundus, *Naturae Historia* (written around 77 - 79 AD), Vol. 2, Chapter XXIV.

[28] C. Plinius Secundus (Pliny the Elder), *The Natural History of Pliny*, (H. G. Bohn, London, (1855)), J. Bostock and H. T. Riley, trans. and eds.

[29] M. F. Walker, Publ. Astron. Soc. Pac. **66**, 230 (1954).

[30] R. P. Kraft, *Advances in Astronomy and Astrophysics* (New York and London: Academic Press, 1963), Vol. 2, Z. Kopal, ed., p. 43.

[31] R. P. Kraft, Astrophys. J. **139**, 457 (1964).

[32] E. Hubble, *The Realm Of The Nebulae* (London: Humphrey Milford, Oxford University Press, 1936), Chapter IV.

[33] M. F. Bode and A. Evans, eds., *Classical Novae* (Cambridge University Press, 2008), 2^{nd} Edn.

[34] R. E. Williams, M. Hamuy, M. M. Phillips, S. R. Heathcote, L. Wells, and M. Navarrete, Astrophys. J. **376**, 721 (1991).

[35] R. E. Williams, Astron. J. **104**, 725 (1992).

[36] R. E. Williams, M. M. Phillips, and M. Hamuy, Astrophys. J. Suppl. Ser. **90**, 297 (1994).

[37] R. E. Williams, Astrophys. J. **426**, 279 (1994).

[38] F. V. Sirotkin and W.-T. Kim, Astrophys. J. **721**, 1356 (2010).

[39] C. Knigge, I. Baraffe, and J. Patterson, Astrophys. J. Suppl. Ser. **194**, 28 (2011).

[40] F. Verbunt, Mon. Not. R. Astron. Soc. **209**, 227 (1984).

[41] B. Paczyński, Acta Astron. **17**, 287 (1967).

[42] F. Verbunt and C. Zwaan, Astron. & Astrophys. **100**, L7 (1981).

[43] J. Smak, Phys. Rep. **311**, 331 (1999).

[44] M. R. Schreiber and B. T. Gänsicke, Astron. & Astrophys. **406**, 305 (2003).

[45] B. P. Gerasimovič, Astron. Nachr. **251**, 255 (1934).

[46] C. Payne-Gaposchkin, *Variable Stars and Galactic Structure* (The Athlone Press, London, 1954).

[47] B. Warner, Mon. Not. R. Astron. Soc. **160**, 35P (1972).

[48] H. C. Ford, Astrophys. J. **219**, 595 (1978).

[49] G. T. Bath and G. Shaviv, Mon. Not. R. Astron. Soc. **183**, 515 (1978).

[50] M. F. Bode, Astron. Nachr. / AN **331**, 160 (2010).

[51] W. Liller and B. Mayer, Publ. Astron. Soc. Pac. **99**, 606 (1987).

[52] R. Ciardullo, P. Tamblyn, G. H. Jacoby, H. C. Ford, and R. E. Williams, Astrophys. J. **99**, 1079 (1990).

[53] A. W. Shafter, Astrophys. J. **487**, 226 (1997).

[54] A. W. Shafter, *Classical Nova Explosions: International Conference on Classical Nova Explosions*, Sitges, Spain, M. Hernanz and J. José, eds., (Melville, New York: AIP), AIP Conf. Proc. **637**, 462 (2002).

[55] M. J. Darnley, M. F. Bode, E. J. Kerins, A. M. Newsam, J. An, P. Baillon, V. Belokurov, S. C. Novati, B. J. Carr, M. Cr*ézé*, et al., Mon. Not. R. Astron. Soc. **369**, 257 (2006).

[56] B. Paczyński, Acta Astron. **15**, 197 (1965).

[57] W. A. Fowler, Astrophys. J. **127**, 551 (1958).

[58] A. G. W. Cameron, Ann. Rev. Nucl. Sci. **8**, 299 (1958).

[59] E. G. Adelberger, S. M. Austin, J. N. Bahcall, A. B. Balantekin, G. Bogaert, L. S. Brown, L. Buchmann, F. E. Cecil, A. E. Champagne, L. de Braeckeleer, et al., Rev. Mod. Phys. **70**, 1265 (1998).

[60] M. Wiescher, J. Görres, E. Uberseder, G. Imbriani, and M. Pignatari, Ann. Rev. Nucl. Part. Sci. **60**, 381 (2010).

[61] J. José and M. Hernanz, Eur. Phys. J. A **27**, s01, 107 (2006).

[62] J. Casanova, J. José, E. García-Berro, A. Calder, and S. N. Shore, Astron. & Astrophys. **513**, L5 (2010).

[63] J. José, M. Hernanz, E. García-Berro, and P. Gil-Pons, in *Proceedings of the International Symposium on Nuclear Astrophysics-Nuclei in the Cosmos-IX* (CERN, Geneva, Switzerland, 2006), PoS(NIC-IX)034.

[64] A. R. Hyland and G. Neugebauer, Astrophys. J. **160**, L177 (1970).

[65] S. L. Geisel, D. E. Kleinmann, and F. J. Low, Astrophys. J. **161**, L101 (1970).

[66] R. J. Strope, B. E. Schaefer, and A. A. Henden, Astrophys. J. **140**, 34 (2010).

[67] R. González-Riestra, M. Orio, and J. Gallagher, Astron. Astrophys. Suppl. Ser. **129**, 23 (1998).

[68] J. José and M. Hernanz, Astrophys. J. **494**, 680 (1998).

[69] S. Starrfield, W. M. Sparks, J. W. Truran, and M. C. Wiescher, Astrophys. J. Suppl. Ser. **127**, 485 (2000).

[70] R. D. Gehrz, J. W. Truran, R. E. Williams, and S. Starrfield, Publ. Astron. Soc. Pac. **110**, 3 (1998).

[71] J. José, M. Hernanz, S. Amari, K. Lodders, and E. Zinner, Astrophys. J. **612**, 414 (2004).

[72] A. C. Alexakis, A. C. Calder, A. Heger, E. F. Brown, L. J. Dursi, J. W. Truran, R. Rosner, D. Q. Lamb, F. X. Timmes, B. Fryxell, et al., Astrophys. J. **602**, 931 (2004).

[73] A. Kovetz and D. Prialnik, Astrophys. J. **291**, 812 (1985).

[74] M. Y. Fujimoto, Astrophys. J. **257**, 752 (1982).

[75] M. Y. Fujimoto, Astrophys. J. **257**, 767 (1982).

[76] J. MacDonald, Astrophys. J. **267**, 732 (1983).

[77] J. José, E. García-Berro, M. Hernanz, and P. Gil-Pons, Astrophys. J. **662**, L103 (2007).

[78] A. Evans, Astrophys. Space Sci. **275**, 131 (2001).

[79] S. Starrfield, J. W. Truran, W. M. Sparks, and G. S. Kutter, Astrophys. J. **176**, 169 (1972).

[80] A. Kercek, W. Hillebrandt, and J. W. Truran, Astron. & Astrophys. **345**, 831 (1999).

[81] S. A. Glasner, E. Livne, and J. W. Truran, Astrophys. J. **625**, 347 (2005).

[82] R. S. Lewis, M. Tang, J. F. Wacker, E. Anders, and E. Steel, Nature **326**, 160 (1987).

[83] T. Bernatowicz, G. Fraundorf, T. Ming, E. Anders, B. Wopenka, E. Zinner, and P. Fraundorf, Nature **330**, 728 (1987).

[84] *Presolar Grains in Meteorites*, website: `http://www.dtm.ciw.edu/users/nittler/psg_main.html`.

[85] S. Amari, E. Zinner, and R. S. Lewis, Astrophys. J. **517**, L59 (1999).

[86] J. José and M. Hernanz, Meteor. Planet. Sci. **42**, 1135 (2007).

[87] E. Zinner, Ann. Rev. Earth Planet. Sci. **26**, 147 (1998).

[88] D. B. McLaughlin, Publ. Am. Astron. Soc. **8**, 145 (1935).

[89] O. C. Wilson and P. W. Merrill, Publ. Astron. Soc. Pac. **47**, 53 (1935).

[90] S. N. Shore and R. D. Gehrz, Astron. & Astrophys. **417**, 695 (2004).

[91] M. A. J. Snijders, T. J. Batt, P. F. Roche, M. J. Seaton, D. C. Morton, T. A. T. Spoelstra, and J. C. Blades, Mon. Not. R. Astron. Soc. **228**, 329 (1987).

[92] S. N. Shore, S. Starrfield, R. González-Riestra, P. H. Hauschildt, and G. Sonnenorn, Nature **369**, 539 (1994).

[93] R. D. Gehrz, Ann. Rev. Astron. Astrophys. **26**, 377 (1988).

[94] R. D. Gehrz, *Classical Nova Explosions: International Conference on Classical Nova Explosions*, Sitges, Spain, M. Hernanz and J. José, eds., (Melville, New York: AIP), AIP Conf. Proc. **637**, 198 (2002).

[95] J. H. Reynolds and G. Turner, J. Geo. Phys. Res. **69**, 3263 (1964).

[96] D. C. Black and R. O. Pepin, Earth Planet. Sci. Lett. **36**, 377 (1969).

[97] S. Amari, R. S. Lewis, and E. Anders, Geochim. Cosmochim. Acta **59**, 1411 (1995).

[98] S. Amari, X. Gao, L. R. Nittler, E. Zinner, J. José, M. Hernanz, and R. S. Lewis, Astrophys. J. **551**, 1065 (2001).

[99] S. Amari, New Astron. Rev. **46**, 519 (2002).

[100] H.-T. Janka, in *Young Neutron Stars and Their Environments IAU Symposium* **218**, 3 (2004), F. Camilo and B. M. Gaensler, eds.

[101] L. D. Landau, Phys. Z. Sowjetunion **1**, 285 (1932).

[102] W. Baade and F. Zwicky, Phys. Rev. **45**, 138 (1934).

[103] J. R. Oppenheimer and G. M. Volkoff, Phys. Rev. **55**, 374 (1939).

[104] R. C. Tolman, Phys. Rev. **55**, 364 (1939).

[105] J. E. Trümper, Prog. Part. Nucl. Phys. **66**, 674 (2011).

[106] D. M. Kahl, Master's thesis, McMaster University, Canada (2008).

[107] S. E. Thorsett and D. Chakrabarty, Astrophys. J. **512**, 288 (1999).

[108] P. C. C. Freire, S. M. Ransom, S. Begin, I. H. Stairs, J. W. T. Hessels, L. H. Frey, and F. Camilo, Astrophys. J. **675**, 670 (2008).

[109] P. B. Demorest, T. Pennucci, S. M. Ransom, M. S. E. Roberts, and J. W. T. Hessels, Nature **467**, 1082 (2010).

[110] S. Gandoli, J. Carlson, and S. Reddy, *The Maximum Mass and Radius of Neutron Stars and the Nuclear Symmetry Energy*, arXiv:1101.1921v1 [nucl-th] (2011).

[111] C. M. Zhang, H. X. Yin, Y. Kojima, H. K. Chang, R. X. Xu, X. D. Li, B. Zhang, and B. Kiziltan, Mon. Not. R. Astron. Soc. **374**, 232 (2007).

[112] N. A. Webb and D. Barret, Astrophys. J. **671**, 727 (2007).

[113] T. Güver, P. Wroblewski, L. Camarota, and F. Ozel, Astrophys. J. **719**, 1807 (2010).

[114] A. W. Steiner, J. M. Lattimer, and E. F. Brown, Astrophys. J. **722**, 33 (2010).

[115] M. Kutschera, Acta Phys. Pol. B **29**, 25 (1998).

[116] S. E. Woosley, A. Heger, A. Cumming, R. D. Hoffman, J. Pruet, T. Rauscher, J. L. Fisker, H. Schatz, B. A. Brown, and M. Wiescher, Astrophys. J. Suppl. Ser. **151**, 75 (2004).

[117] J. L. Fisker, H. Schatz, and F.-K. Thielemann, Astrophys. J. Suppl. Ser. **174**, 261 (2008).

[118] H. Schatz, A. Aprahamian, V. Barnard, L. Bildsten, A. Cumming, M. Ouellette, T. Rauscher, F.-K. Thielemann, and M. Wiescher, Phys. Rev. Lett. **86**, 3471 (2001).

[119] V.-V. Elomaa, G. K. Vorobjev, A. Kankainen, L. Batist, S. Eliseev, T. Eronen, J. Hakala, A. Jokinen, I. D. Moore, Y. N. Novikov, et al., Phys. Rev. Lett. **102**, 252501 (2009).

[120] R. Kippenhahn and A. Weigert, *Stellar Structure and Evolution* (Springer-Verlag, 1994), corrected 3^{rd} Edn., Part III, p. 152.

[121] G. V. Gamow, Z. Phys. **51**, 204 (1928).

[122] D. D. Clayton, *Principles of Stellar Evolution and Nucleosynthesis* (The University of Chicago Press, 1983), 2^{nd} Edn., Chapter 4.

[123] C. E. Rolfs and W. S. Rodney, *Cauldrons in the Cosmos* (The University of Chicago Press, 1988).

[124] M. Schwarzschild, *Structure and Evolution of the Stars* (Princeton University Press, 1958).

[125] I. J. Thompson and F. M. Nunes, *Nuclear Reactions for Astrophysics* (Cambridge University Press, 2009).

[126] K. S. Krane, *Introductory Nuclear Physics* (John Wiley & Sons, Inc., 1988), 1^{st} Edn., Chapter 11.

[127] N. K. Glendenning, *Direct Nuclear Reactions* (World Scientific Publishing Co. Pte. Ltd., 2004).

[128] H. E. Mitler, Astrophys. J. **212**, 513 (1977).

[129] R. Longland, C. Iliadis, A. E. Champagne, J. R. Newton, C. Ugalde, A. Coc, and R. Fitzgerald, Nucl. Phys. A **841**, 1 (2010).

[130] W. A. Fowler, G. R. Caughlan, and B. A. Zimmerman, Annu. Rev. Astron. Astrophys. **5**, 525 (1967).

[131] G. R. Satchler, *Introductions to Nuclear Reactions* (Macmillan Education LTD., 1990), 2^{nd} Edn.

[132] G. Breit and E. Wigner, Phys. Rev. **49**, 519 (1936).

[133] G. Breit, *Theory of Resonance Reactions, in: Handbuch der Physik XLI/1* (Springer, Berlin, Heidelberg, 1959).

[134] C. Iliadis, R. Longland, A. E. Champagne, A. Coc, and R. Fitzgerald, Nucl. Phys. A **841**, 31 (2010).

[135] C. Iliadis, R. Longland, A. E. Champagne, and A. Coc, Nucl. Phys. A **841**, 251 (2010).

[136] C. Iliadis, R. Longland, A. E. Champagne, and A. Coc, Nucl. Phys. A **841**, 323 (2010).

[137] E. E. Salpeter, Australian J. Phys. **7**, 373 (1954).

[138] S. Ichimaru, Rev. Mod. Phys. **54**, 1017 (1982).

[139] S. Ichimaru and K. Utsumi, Astrophys. J. **278**, 382 (1984).

[140] J. Souin, P. Ascher, L. Audirac, J. *Äystö*, B. Blank, V.-V. Elomaa, T. Eronen, J. Giovinazzo, J. Hakala, A. Jokinen, et al., Eur. J. phys. A **47**, 40 (2011).

[141] D. Galaviz, A. M. Amthor, D. Bazin, B. A. Brown, A. Cole, T. Elliot, A. Estrade, Z. F*ülö*p, A. Gade, T. Glasmacher, et al., J. Phys. G: Nucl. Part. Phys. **35**, 014030 (2008).

[142] R. G. Johnson, L. F. Chase, and W. L. Imhof, Bull. Am. Phys. Soc. **5**, 406 (1960).

[143] E. L. Robinson, J. I. Rhode, and O. E. Johnson, Phys. Rev. **122**, 879 (1961).

[144] G. Frick, A. Gallmann, D. E. Alburger, D. H. Wilkinson, and J. P. Coffin, Phys. Rev. **132**, 2169 (1963).

[145] S. Starrfield, C. Iliadis, W. R. Hix, F. X. Timmes, and W. M. Sparks, AIP Conf. Proc. **891**, 364 (2007).

[146] Private Communication from Daniel T. Irvine: Department of Physics & Astronomy, McMaster University, Canada.

[147] J. José, A. Coc, and M. Hernanz, Astrophys. J. **560**, 897 (2001).

[148] C. Iliadis, A. E. Champagne, J. José, S. Starrfield, and P. Tupper, Astrophys. J. Suppl. Ser. **142**, 105 (2002).

[149] C. Iliadis, J. M. D'Auria, S. Starrfield, W. J. Thompson, and M. Wiescher, Astrophys. J. Suppl. Ser. **134**, 151 (2001).

[150] D. W. Bardayan, J. C. Blackmon, R. P. Fitzgerald, W. R. Hix, K. L. Jones, R. L. Kozub, J. F. Liang, R. J. Livesay, Z. Ma, L. F. Roberts, et al., Phys. Rev. C **76**, 045803 (2007).

[151] H. S. Wilson, R. W. Kavanagh, and F. M. Mann, Phys. Rev. C **22**, 1696 (1980).

[152] F.-K. Thielemann, K. L. Kratz, B. Pfeiffer, T. Rauscher, L. V. Wormer, and M. C. Wiescher, Nucl. Phys. A **570**, 329c (1994).

[153] C. Wrede, J. A. Caggiano, J. A. Clark, C. M. Deibel, A. Parikh, and P. D. Parker, Phys. Rev. C **79**, 045808 (2009).

[154] J. L. Fisker, F.-K. Thielemann, and M. Wiescher, Astrophys. J. **608**, L61 (2004).

[155] J. José, F. Moreno, A. Parikh, and C. Iliadis, Astrophys. J. Suppl. Ser. **189**, 204 (2010).

[156] M. Wiescher and J. Görres, Z. phys. A. **329**, 121 (1988).

[157] W. R. McMurray, P. V. D. Merwe, and I. J. V. Heerden, Nucl. Phys. A **92**, 401 (1967).

[158] R. G. Miller and R. W. Kavanagh, Nucl. Phys. A **94**, 261 (1967).

[159] D. J. Frantsvog, A. R. Kunselman, and R. L. Wilson, Phys. Rev. C **25**, 770 (1982).

[160] W. R. McMurray, P. V. D. Merwe, and I. J. V. Heerden, Phys. Lett. **18**, 319 (1965).

[161] W. G. Davies, J. C. Hardy, D. J. Skyrme, D. G. Montague, K. Ramavataram, and T. A. Hodges, Rutherford Laboratory Report No. RHEL/R (1967), (unpublished).

[162] P. H. Barker, N. Drysdale, and W. R. Phillips, Proc. Phys. Soc. **91**, 587 (1967).

[163] M. Hagen, K. H. Maier, and R. Michaelsen, Phys. Lett. B **26**, 432 (1968).

[164] M. B. Greenfield and C. R. Bingham, Phys. Rev. C **6**, 1756 (1972).

[165] R. Bass, U. Friedland, B. Hubert, H. Nann, and A. Reiter, Nucl. Phys. A **198**, 449 (1972).

[166] A. Kogan and P. R. Bevington, J. Phys. G: Nucl. Phys. **1**, 422 (1975).

[167] W. Bohne, K. D. Büchs, H. Fuchs, K. Grabisch, D. Hilscher, U. Jahnke, H. Kluge, T. G. Masterson, and H. Morgenstern, Nucl. Phys. A **378**, 525 (1982).

[168] R. A. Paddock, Phys. Rev. C **5**, 485 (1972).

[169] H. Yokota, K. Fujioka, K. Ichimaru, Y. Mihara, and R. Chiba, Nucl. Phys. A **383**, 298 (1982).

[170] L. Kraus, A. Boucenna, I. Linck, B. Lott, R. Rebmeister, N. Schulz, and J. C. Sens, Phys. Rev. C **37**, 2529 (1988).

[171] M. Bini, P. G. Bizzeti, A. M. Bizzeti-Sona, M. Mando, and P. R. Maurenzig, Lett. Nuovo Cimento **3**, 235 (1970).

[172] J. M. G. Caraça, R. D. Gill, A. J. Cox, and H. J. Rose, Nucl. Phys. A **193**, 1 (1972).

[173] E. Kuhlmann, W. Albrecht, and A. Hoffmann, Nucl. Phys. A **213**, 82 (1973).

[174] T. K. Alexander, G. C. Ball, J. S. Forster, W. G. Davies, and I. V. Mitchell, Phys. Rev. Lett. **49**, 438 (1982).

[175] Y. Blumenfeld, E. Khan, F. Maréchal, and T. Suomijärvi, Acta Phys. Hung. N. S. **12**, 265 (2000).

[176] Y. Blumenfeld, E. Khan, F. Maréchal, and T. Suomijärvi, Pramana - J. Phys. **57**, 493 (2001).

[177] E. Khan, T. Suomij*ddotar*vi, Y. Blumenfeld, N. V. Giai, N. Alamanos, F. Auger, E. Bauge, D. Beaumel, J. P. Delaroche, P. Delbourgo-Salvador, et al., Nucl. Phys. A **694**, 103 (2001).

[178] P. D. Cottle, Z. Hu, B. V. Pritychenko, J. A. Church, M. Fauerbach, T. Glasmacher, R. W. Ibbotson, K. W. Kemper, L. A. Riley, H. Scheit, et al., Phys. Rev. Lett. **88**, 172502 (2002).

[179] L. Axelsson, J. *Äystö*, M. J. G. Borge, L. M. Fraile, H. O. U. Fynbo, A. Honkanen, P. Hornshj, A. Jokinen, B. Jonson, P. O. Lipas, et al., Nucl. Phys. A **634**, 475 (1998).

[180] H. O. U. Fynbo, M. J. G. Borge, L. Axelsson, J. *Äystö*, U. C. Bergmann, L. M. Fraile, A. Honkanen, P. Hornshj, Y. Jading, A. Jokinen, et al., Nucl. Phys. A **677**, 38 (2000).

[181] H. O. U. Fynbo, M. J. G. Borge, L. Axelsson, J. *Äystö*, U. C. Bergmann, L. M. Fraile, A. Honkanen, P. Hornshj, Y. Jading, A. Jokinen, et al., Nucl. Phys. A **701**, 394c (2002).

[182] D. Galaviz, A. M. Amthor, D. Bazin, B. A. Brown, A. Cole, T. Elliot, A. Estrade, Z. F*ülö*p, A. Gade, T. Glasmacher, et al., in *Proceedings of Science: International Symposium on Nuclear Astrophysics – Nuclei in the Cosmos – IX* (CERN, Geneva, Switzerland, 2006), PoS(NIC-IX)099.

[183] J. M. Figueira, et al., ATLAS Proposal No. 1242, Argonne National Laboratory (2008), (unpublished).

[184] S. O'Brien, T. Adachi, G. P. A. Berg, M. Couder, M. Dozono, H. Fujita, Y. Fujita, J. Görres, K. Hatanaka, D. Ishikawa, et al., AIP Conf. Proc. **1090**, 288 (2009).

[185] D. Galaviz, A. M. Amthor, D. Bazin, A. D. Becerril, B. A. Brown, A. A. Chen, A. Cole, J. M. Cook, T. Elliot, A. Estrade, et al., J. Phys.: Conf. Ser. **202**, 012009 (2010).

[186] *National Nuclear Data Center*, NuDat 2.5, Nucleus: ^{30}S, website: `http://www.nndc.bnl.gov/nudat2/getdataset.jsp?nucleus=30S&unc=nds`.

[187] M. S. Basunia, Nucl. Data Sheets **111**, 2331 (2010).

[188] W. P. Tan, S. Almaraz, A. Aprahamian, B. Bucher, J. Görres, H. Mach, M. Wiescher, C. Brune, Z. Heinen, and T. Massey, Nucl. Phys. A **834**, 679c (2010).

[189] G. Doucas and H. R. M. Hyder, Nucl. Instr. Meth. **119**, 413 (1974).

[190] C. Lejeune and J. Aubert, *Applied Charged Particle Optics* (Academic Press, New York, 1980), Part A: Advances in Electronics and Electron Physics, A. Septier, ed., p. 159.

[191] P. W. Hawkes, ed., *Advances in Electronics and Electron Physics* (Academic Press, Inc., London, 1989), Vol. 76, p. 57 & 70.

[192] R. G. Wilson and G. R. Brewer, *Ion Beams* (Malabar: Krieger, 1973).

[193] R. Middleton and C. T. Adams, Nucl. Instr. Meth. **118**, 229 (1974).

[194] R. Middleton and C. T. Adams, Nucl. Instr. Meth. **118**, 329 (1974).

[195] R. Middleton, Nucl. Instr. Meth. **122**, 35 (1974).

[196] D. A. Bromley, ed., *Treatise on Heavy-Ion Science* (Plenum Press, New York and London, 1985), Vol. 7, Chapter 2.

[197] V. E. Krohn, J. Appl. Phys. **33**, 3523 (1962).

[198] R. Middleton and C. T. Adams, University of Pennsylvania, Department of Physics Report (July 1973).

[199] G. Hortig, P. Mokler, and M. Müller, Z. Phys. **210**, 312 (1968).

[200] K. Brand, Nucl. Instr. Meth. **141**, 519 (1977).

[201] K. Brand, in *Proceedings of the Third Conference on Electrostatic Accelerator Technology* (1981), (IEEE-81-CH1639-4), p. 205.

[202] G. T. Caskey, A. D. Ross, H. T. Richards, and H. V. Smith, Nucl. Instr. Meth. **157**, 1 (1978).

[203] J. H. Billen and H. T. Richards, Proc. of SNEAP, Oak Ridge (1978), p. 137.

[204] R. Middleton, Proc. of SNEAP, Oak Ridge (1978), p. 114.

[205] R. Middleton, Proc. of SNEAP, University of Wisconsin (1980).

[206] R. Middleton, *A Negative-Ion Cookbook* (1989), website: `http://www.pelletron.com/cookbook.pdf`.

[207] *Wright Nuclear Structure Laboratory: Tandem Specifications*, website: `http://wnsl.physics.yale.edu/operations_specs.html`.

[208] *Wright Nuclear Structure Laboratory*, website: `http://wnsl.physics.yale.edu/aboutus_history.html`.

[209] R. Hellborg, *Electrostatic Accelerators: Fundamentals and Applications* (Springer-Verlag, 2005), p. 49–63.

[210] H. R. M. Hyder, J. Baris, C. E. L. Gingell, C. McKay, P. D. Parker, and D. A. Bromley, Nucl. Instr. Meth. Phys. Res. A **268**, 285 (1988).

[211] R. G. Herb, Nucl. Instr. Meth. **122**, 267 (1974).

[212] M. Imai, M. Sataka, K. Kawatsura, K. Takahiro, K. Komaki, H. Shibata, H. Sugai, and K. Nishio, Nucl. Instr. Meth. Phys. Res. B **267**, 2675 (2009).

[213] Y. Sato, A. Kitagawa, M. Muramatsu, T. Murakami, S. Yamada, C. Kobayashi, Y. Kageyama, T. Miyoshi, H. Ogawa, H. Nakabushi, et al., Nucl. Instr. Meth. Phys. Res. B **201**, 571 (2003).

[214] Private Communication from David M. Kahl: Center for Nuclear Study (CNS), the University of Tokyo, Japan.

[215] K. Shima, S. Ishii, T. Takahashi, and I. Sugai, Nucl. Instr. Meth. Phys. Res. A **460**, 233 (2001).

[216] A. R. Parikh, Ph.D. thesis, Yale University, USA (2007).

[217] J. C. Overley, P. D. Parker, and D. A. Bromley, Nucl. Instr. Meth. **68**, 61 (1969).

[218] *Lebow Company*, 5960 Mandarin Ave., Goleta, California, 93117 USA.

[219] *ACF-Metals, the Arizona Carbon Foil Co., Inc.*, 2239 E. Kleindale Road, Tucson, Arizona, 85719-2440 USA, website: `http://www.techexpo.com/firms/acf-metl.html`.

[220] W. W. Buechner, C. P. Browne, H. A. Enge, M. Mazari, and C. D. Buntschuh, Phys. Rev. **95**, 609 (1954).

[221] W. W. Buechner, M. Mazari, and A. Sperduto, Phys. Rev. **101**, 188 (1956).

[222] C. P. Browne and W. W. Buechner, Rev. Sci. Instr. **27**, 899 (1956).

[223] H. A. Enge, Rev. Sci. Instr. **35**, 278 (1964).

[224] H. A. Enge, Nucl. Instr. Meth. **28**, 119 (1964).

[225] R. Lewis, Ph.D. thesis, Yale University, USA (2005).

[226] J. E. Spencer and H. A. Enge, Nucl. Instr. Meth. **49**, 181 (1967).

[227] H. A. Enge, Nucl. Instr. Meth. **162**, 161 (1979).

[228] S. Das and N. Sarma, Nucl. Instr. Meth. **95**, 213 (1971).

[229] H. A. Enge, Nucl. Instr. Meth. **187**, 1 (1981).

[230] C. L. H. Wrede, Ph.D. thesis, Yale University, USA (2008).

[231] Private Communication from Dr. Jason A. Clark: Argonne National Laboratory, USA.

[232] O. Frisch, British Atomic Energy Report **BR-49** (1944).

[233] C. M. Deibel, Ph.D. thesis, Yale University, USA (2008).

[234] W. R. Leo, *Techniques for Nuclear and Particle Physics Experiments* (Springer-Verlag, Berlin, Heidelberg, 1994), 2^{nd} revised Edn.

[235] G. F. Knoll, *Radiation Detection and Measurement* (John Wiley & Sons, Inc., 2000), 3^{rd} Edn., p. 347.

[236] *JRelKin: Relativistic Kinematics Software*, website: `http://wnsl.physics.yale.edu/astro/software/index.html`.

[237] K. B. Swartz, D. W. Visser, and J. M. Baris, Nucl. Instr. Meth. Phys. Res. A **463**, 354 (2001), website: `http://jam-daq.wiki.sourceforge.net/`.

[238] *Det: Particle ID Simulating Software*, website: `http://wnsl.physics.yale.edu/astro/software/index.html`.

[239] *Plotter: Position Simulating Software*, website: `http://wnsl.physics.yale.edu/astro/software/index.html`.

[240] *Igor Pro, WaveMetrics, Inc.*, P.O. Box 2088, Lake Oswego, Oregon, 97035 USA (2003), website: `http://www.wavemetrics.com/`.

[241] G. Audi, A. H. Wapstra, and C. Thibault, Nucl. Phys. A **729**, 337 (2003).

[242] A. Matic, A. M. V. D. Berg, M. N. Harakeh, H. J. Wörtche, G. P. A. Berg, M. Couder, J. Görres, P. LeBlanc, S. O'Brien, M. Wiescher, et al., Phys. Rev. C **82**, 025807 (2010).

[243] D. Seweryniak, P. J. Woods, M. P. Carpenter, T. Davinson, R. V. F. Janssens, D. G. Jenkins, T. Lauritsen, C. J. Lister, J. Shergur, S. Sinha, et al., Phys. Rev. C **75**, 062801 (2007).

[244] Y. Parpottas, S. M. Grimes, S. A. Quraishi, C. R. Brune, T. N. Massey, J. E. Oldendick, A. Salas, and R. T. Wheeler, Phys. Rev. C **70**, 065805 (2004).

[245] J. A. Caggiano, W. Bradfield-Smith, R. Lewis, P. D. Parker, D. W. Visser, J. P. Greene, K. E. Rehm, D. W. Bardayan, and A. E. Champagne, Phys. Rev. C **65**, 055801 (2002).

[246] D. W. Bardayan, J. C. Blackmon, A. E. Champagne, A. K. Dummer, T. Davinson, U. Greife, D. Hill, C. Iliadis, B. A. Johnson, R. L. Kozub, et al., Phys. Rev. C **65**, 032801(R) (2002).

[247] R. A. I. Bell, J. L'Ecuyer, R. D. Gill, B. C. Robertson, I. S. Towner, and H. J. Rose, Nucl. Phys. A **133**, 337 (1969).

[248] D. M. Mahon and E. Browne, *AveTools*, website: `http://people.physics.anu.edu.au/~txk103/`.

[249] M. U. Rajput and T. D. M. Mahon, Nucl. Instr. Meth. Phys. Res. A **312**, 289 (1992).

[250] Private Communication from Dr. Balraj Singh: Department of Physics & Astronomy, McMaster University, Canada.

[251] *SPANC*, website: `http://wnsl.physics.yale.edu/astro/software/index.html`.

[252] J. F. Ziegler and H. H. Andersen, *The Stopping and Ranges of Ions in Matter* (Pergamon, New York, 1977), Vol. 3.

[253] J. F. Ziegler and H. H. Andersen, *The Stopping and Ranges of Ions in Matter* (Pergamon, New York, 1977), Vol. 5.

[254] Private Communication from Prof. Alan L. Nichols: Department of Physics, University of Surrey, UK.

[255] K. Setoodehnia, A. A. Chen, J. Chen, J. A. Clark, C. M. Deibel, S. D. Geraedts, D. Kahl, P. D. Parker, D. Seiler, and C. Wrede, Phys. Rev. C **82**, 022801(R) (2010).

[256] A. H. Bethe, Rev. Mod. Phys. **9**, 69 (1937).

[257] A. H. Bethe and G. Placzek, Phys. Rev. **51**, 462 (1937).

[258] E. W. Lamb, Phys. Rev. **55**, 190 (1939).

[259] E. J. Williams, Phys. Rev. Sol. A **135**, 105 (1932).

[260] T. Walcher, Exp. Meth. Heavy Ion Phys. (Lect. Not. Phys.) **83**, 236 (1978).

[261] T. Joy, Nucl. Instr. Meth. **106**, 237 (1973).

[262] Y. Fujita, S. Morinobu, M. Fujiwara, I. Katayama, T. Yamazaki, and H. Ikegami, Nucl. Instr. Meth. Phys. Res. A **225**, 298 (1984).

[263] D. H. Wilkinson, ed., *Isospin in Nuclear Physics* (Amsterdam: North Holland Publication Company, 1969), p. 302 – 303.

[264] M. S. Antony, J. Britz, J. B. Bueb, and A. Pape, At. Data Nucl. Data Tables **33**, 447 (1985).

[265] J. Jänecke, Phys. Rev. **147**, 735 (1966).

[266] C. Iliadis, P. M. Endt, N. Prantzos, and W. J. Thompson, Astrophys. J. **524**, 434 (1999).

[267] R. J. D. Meijer, H. F. J. V. Royen, and P. J. Brussaard, Nucl. Phys. A **164**, 11 (1971).

[268] Private Communication from Prof. Christian Iliadis: Department of Physics & Astronomy, University of North Carolina at Chapel Hill, USA.

[269] P. R. Bevington and D. K. Robinson, *Data Reduction and Error Analysis for the Physical Sciences* (McGraw-Hill, 2002), 3^{rd} Edn., Chapter 3.

[270] W. Catford (University of Surrey), *CATKIN, Microsoft Excel Spreadsheet*, website: http://personal.ph.surrey.ac.uk/~phs1wc/kinematics/index.html.

[271] Private Communication from Prof. Dr. Antonio M. Moro: Departamento de Física Atómica, Molecular y Nuclear - Universidad de Sevilla, Spain.

[272] P. D. Kunz (University of Colorado), *DWUCK4 Instruction*, website: http://spot.colorado.edu/~kunz/DWBA.html.

[273] I. J. Thompson, Comput. Phys. Rep. **7**, 167 (1988), website: http://www.fresco.org.uk/.

[274] *XFRESCO*, website: http://huespedes.cica.es/aliens/dfamnus/famn/amoro/xfresco/index.html.

[275] Private Communication from Prof. Peter D. Kunz: Emeritus faculty at Department of Physics, University of Colorado, USA.

[276] Private Communication from Dr. Daniel W. Bardayan: Oak Ridge National Laboratory, USA.

[277] B. F. Bayman, Nucl. Phys. A **168**, 1 (1971).

[278] J. R. V. Reid, Ann. Phys. (N. Y.) **50**, 411 (1968).

[279] R. E. Tribble and K.-I. Kubo, Nucl. Phys. A **282**, 269 (1977).

[280] A. Kankainen, T. Eronen, D. Gorelov, J. Hakala, A. Jokinen, V. S. Kolhinen, M. Reponen, J. Rissanen, A. Saastamoinen, V. Sonnenschein, et al., Phys. Rev. C **82**, 052501(R) (2010).

[281] Private Communication from Dr. Felix Liang: Oak Ridge National Laboratory, USA.

[282] B. A. Brown and W. A. Richter, Phys. Rev. C **74**, 034315 (2006).

[283] Private Communication from Prof. B. Alex Brown: Department of Physics and Astronomy, and National Superconducting Cyclotron Laboratory, Michigan State University, USA.

[284] Private Communication from Prof. Werner A. Richter: Department of Physics, University of the Western Cape, South Africa.

[285] K. Setoodehnia, A. A. Chen, T. Komatsubara, S. Kubono, D. N. Binh, J. F. Carpino, J. Chen, T. Hashimoto, T. Hayakawa, Y. Ishibashi, et al., Phys. Rev. C **82**, 018803 (2011).

[286] Private Communication from Prof. Lothar Buchmann: TRIUMF National Laboratory, Canada.

[287] L. Gerward, Phys. Perspect. **1**, 367 (1999).

[288] The University of Tsukuba Tandem Accelerator Complex Annual Report (1976), UTTAC-1.

[289] Y. Tagishi and J. Sanada, Nucl. Instr. Meth. **164**, 411 (1979).

[290] M. V. Ardenne, *Tabellen der Electronenphysik, Ionenphysik und Übermikroskopie* (VEB, Deutscher Verlag der Wissenschaften, Berlin, 1956).

[291] Private Communication from Dr. Komatsubara Tetsuro: Institute of Physics, the University of Tsukuba, Japan.

[292] P. Thieberger, H. E. Wegner, M. Mckeown, R. Lindgren, N. Burn, J. H. Broadhurst, T. S. Lund, T. E. Miller, K. Sato, C. E. L. Gingell, et al., Nucl. Instr. Meth. **184**, 121 (1981).

[293] H. E. Wegner, IEEE Report (1969), website: `http://epaper.kek.jp/p69/PDF/PAC1969_0081.PDF`.

[294] R. J. V. de Graaff, Nucl. Instr. Meth. **8**, 195 (1960).

[295] J. Sanada, S. Seki, T. Ishihara, Y. Nagashima, T. Mikumo, M. Yamanouchi, K. Katori, K. Kuriyama, K. Furuno, and T. Aoki, Rev. Phys. Appl. **12**, 1340 (1977).

[296] S. Seki, K. Furuno, T. Ishihara, Y. Nagashima, M. Yamanouchi, T. Aoki, T. Mikumo, and J. Sanada, Nucl. Instr. Meth. **184**, 113 (1981).

[297] F. Pühlhofer, Nucl. Phys. A **280**, 267 (1977), website: `http://www.phys.konan-u.ac.jp/~akimune/Software/cascade_man.html`.

[298] F. Pühlhofer, *CASCADE*, Gesellschaft für Schwerionenforschung Darmstadt Report (1979), (unpublished).

[299] M. Karlsson, Master's thesis, Lund University, Sweden (1997).

[300] V. V. Verbinski, W. R. Burrus, T. A. Love, W. Zobel, and W. N. Hill, Nucl. Instr. Meth. **65**, 8 (1968).

[301] *Scintillators for the Physical Sciences*, Brochure from Nuclear Enterprises Limited, 10 Bankhead Medway, Edinburgh, Midlothian EH11 4BY, United Kingdom.

[302] L. Büermann, S. Ding, S. Guldbakke, H. Klien, T. Novotny, and M. Tichy, Nucl. Instr. Meth. Phys. Res. A **332**, 483 (1993).

[303] H. Klein, Radiat. Prot. Dosim. **107**, 95 (2003).

[304] N. A. Lurie, L. H. Jr., and J. P. Wondra, Nucl. Instr. Meth. **129**, 619 (1975).

[305] *Advanced Measurement Technology, Inc.*, 801 South Illinois Avenue, Oak Ridge, Tennessee, 37831-0895 USA.

[306] K. Debertin and R. G. Helmer, *Gamma- and X-Ray Spectroscopy with Semiconductor Detectors* (Physical Sciences & Engineering Devision of North Holland Co., 1988).

[307] E. Storm and H. I. Israel, Nucl. Data Tables A **7**, 565 (1970).

[308] *Bass Associates Inc.*, 13533 Larkin Drive, Minnetonka, Minnesota, 55305 USA.

[309] *Hoshin Electronics CO., LTD.*, 3-9-12 Miyamaedaira, Miyamae-ku Kawasaki city, 216-0006 Japan.

[310] J. M. Aadams and G. White, Nucl. Instr. Meth. **156**, 459 (1978).

[311] L. Marton, *Advances in Electronics and Electron Physics* (Academic Press, INC., New York, 1972), Vol. 31, p. 82.

[312] S. M. Robinson, S. D. Kiff, E. D. Ashbaker, E. Flumerfelt, and M. Salvitti, Nucl. Instr. Meth. Phys. Res. A **610**, 509 (2009).

[313] *National Nuclear Data Center*, NuDat 2.5, Nucleus: ^{152}Sm, website: `http://www.nndc.bnl.gov/nudat2/getdataset.jsp?nucleus=152SM&unc=nds`.

[314] *National Nuclear Data Center*, NuDat 2.5, Nucleus: ^{60}Ni, website: `http://www.nndc.bnl.gov/nudat2/getdataset.jsp?nucleus=60NI&unc=nds`.

[315] *National Nuclear Data Center*, NuDat 2.5, Nucleus: ^{56}Fe, website: `http://www.nndc.bnl.gov/nudat2/getdataset.jsp?nucleus=56FE&unc=nds`.

[316] K. O. Groenevbld, B. Hubert, R. Bass, and H. Nann, Nucl. Phys. A **151**, 198 (1970).

[317] R. B. Firestone and V. S. Shirley, *Table of Isotopes* (Wiley-Interscience, 1998), Vol. 2 (A = 151 – 272), 8^{th} Edn., p. C-3.

[318] *OriginLab Data Analysis and Graphying Software*, website: `http://www.originlab.com/index.aspx?go=Products/Origin`.

[319] E. Bitterwolf, P. Betz, A. Burkard, F. Glatz, F. Heidinger, T. Kern, R. Lehmann, S. Norbert, J. Siefert, and H. Röpke, Z. Phys. A – Atoms and Nuclei **298**, 279 (1980).

[320] *The Stopping and Range of Ions in Matter (SRIM) Software*, website: `http://www.srim.org/`.

[321] Private Communication from Dr. Daniel Galaviz Redondo: Department of Physics, Universidade de Lisboa, Portugal.

[322] D. E. Alburger and D. R. Goosman, Phys. Rev. C **9**, 2236 (1974).

[323] P. M. Endt and C. V. der Leun, Nucl. Phys. A **124**, 1 (1973).

[324] J. M. Blatt and V. F. Wiesskopf, *Theoretical Nuclear Physics* (John Wiley & Sons, 1963), 7^{th} Edn.

[325] H. Morinaga and T. Yamazaki, *In-Beam Gamma-Ray Spectroscopy* (North Holland Publishing Co., 1976).

[326] J. O. Rasnmssen and T. T. Sugihara, Phys. Rev. **151**, 992 (1966).

[327] L. P. Ekström, A. M. Al-Naser, P. R. G. Lornie, and P. J. Twin, Nucl. Instr. Meth. **158**, 243 (1979).

[328] G. A. P. Engelbertink, L. P. Ekstrgm, D. E. C. Scherpenzeel, and H. H. Eggenhuisen, Nucl. Instr. Meth. **143**, 161 (1977).

[329] E. der Mateosian and A. W. Sunyar, *Table of Attenuation Coefficients for Angular Distribution of Gamma Rays from Partially Aligned Nuclei*, Brookhaven National Laboratory Annual Report (1972).

[330] T. Yamazaki, Nucl. Data A **3**, 1 (1967).

[331] A. E. Litherland and A. J. Ferguson, Can. J. Phys. **39**, 788 (1961).

[332] R. D. Gill, *Gamma Ray Angular Correlations* (Academic Press INC., (London), LTD., 1975).

[333] E. der Mateosian and A. W. Sunyar, At. Data Nucl. Data Tables **13**, 407 (1974).

[334] K. S. Krane and R. M. Steffen, Phys. Rev. C **2**, 724 (1970).

[335] H. J. Rose and D. M. Brink, Rev. Mod. Phys. **39**, 306 (1967).

[336] J. W. Dunworth, Rev. Sci. Instr. **11**, 167 (1940).

[337] D. R. Hamilton, Phys. Rev. **58**, 122 (1940).

[338] A. J. Ferguson, *Angular Correlation Methods in Gamma-Ray Spectroscopy* (North-Holland Publishing Co., Amsterdam, 1965).

[339] K. S. Krane, R. M. Steffen, and R. M. Wheeler, Nucl. Data Tables **11**, 351 (1973).

[340] R. M. Steffen and K. Alder, *The Electromagnetic Interaction in Nuclear Spectroscopy* (North Holland, Amsterdam, 1975), W. D. Hamilton, ed., p. 505.

[341] L. C. Biedenharn and M. E. Rose, Rev. Mod. Phys. **25**, 729 (1953).

[342] A. Krämer-Flecken, T. Morek, R. M. Lieder, W. Gast, G. Hebbinghaus, H. M. Jäger, and W. Urban, Nucl. Instr. Meth. Phys. Res. A **275**, 333 (1989).

[343] E. S. Macias, W. D. Ruhter, D. C. Camp, and R. G. Lanier, Comput. Phys. Commun. **11**, 75 (1976).

[344] Private Communication from Dr. Krishichayan: Cyclotron Institute, Texas A&M University, USA.

[345] *Summary of Bases for Spin and Parity Assignments*, Nucl. Data Sheets, **111**, iv (2010).

[346] J. José, A. Coc, and M. Hernanz, Astrophys. J. **520**, 347 (1999).

[347] C. Rolfs, Nucl. Phys. A **217**, 29 (1973).

[348] H. Mackh, H. Oeschler, G. J. Wagner, D. Dehnhard, and H. Ohnuma, Nucl. Phys. A **202**, 497 (1973).

[349] P. J. Brussaard and P. W. M. Glaudemans, *Shell-Model Applications in Nuclear Spectroscopy* (North-Holland Publishing Co., Amsterdam, New York, 1977), p. 144 – 149.

[350] Private Communication from Dr. Richard Longland: Departament de Física i Enginyeria Nuclear, Universitat Politècnica de Catalunya (Barcelona), Spain.

[351] F. C. Barker, Nucl. Phys. A **637**, 576 (1998).

[352] Private Communication from Prof. Denis Burke: Emeritus faculty at Department of Physics & Astronomy, McMaster University, Canada.

[353] C. Iliadis, Nucl. Phys. A **618**, 166 (1997).

[354] W. J. Thompson and C. Iliadis, Nucl. Phys. A **647**, 259 (1999).

[355] T. W. Anderson and D. A. Darling, Ann. Math. Statist. **23**, 193 (1952).

[356] J. R. Newton, R. Longland, and C. Iliadis, Phys. Rev. C **78**, 025805 (2008).

[357] *NON-SMOKER*, website: `http://nucastro.org/websmoker.html`.

[358] T. Rauscher and F.-K. Thielemann, At. Data Nucl. Data Tab. **75**, 1 (2000).

[359] Private Communication from Prof. Jordi José: Departament de Física i Enginyeria Nuclear, Universitat Politècnica de Catalunya (Barcelona), Spain.

[360] A. Parikh, K. Wimmer, T. Faestermann, R. Hertenberger, J. José, R. Longland, H.-F. Wirth, V. Bildstein, S. Bishop, A. A. Chen, et al., Phys. Rev. C **83**, 045806 (2011).

[361] C. Wrede, J. A. Clark, C. M. Deibel, T. Faestermann, R. Hertenberger, A. Parikh, H.-F. Wirth, S. Bishop, A. A. Chen, K. Eppinger, et al., Phys. Rev. C **81**, 055503 (2010).

[362] W. N. Lennard, K. Setoodehnia, A. A. Chen, and J. Hendriks, Nucl. Instr. Meth. Phys. Res. B **269**, 2726 (2011).

[363] Private Communication from Dr. John O. Stoner, Jr.: ACF Metals Company, Arizona, USA.

[364] *ACF-Metals, the Arizona Carbon Foil Co., Inc.*, Product List (2011).

[365] Private Communication from Prof. Peter Sigmund: Emeritus faculty at Department of Physics & Chemistry, University of Southern Denmark, Denmark.

[366] Private Communication from Dr. Gilles Abel: Institut national de la recherche scientifique, Université du Québec à Montréal, Canada.

[367] M. S. Smith, P. V. Magnus, K. I. Hahn, A. J. Howard, P. D. Parker, A. E. Champagne, and Z. Q. Mao, Nucl. Phys. A **536**, 333 (1992).

[368] C. Wrede, K. Deryckx, B. M. Freeman, A. García, G. C. Harper, A. S. C. Palmer, D. A. Short, and D. I. Will, Nucl. Instr. Meth. Phys. Res. B **268**, 3482 (2010).

[369] *General Ionex Corporation*, 4 Stanley Tucker Drive Newburyport, Massachusetts, 01950 USA, website: `http://www.ishcc.org/MA/Newburyport/general-ionex-corporation-2`.

[370] *Tandetron Accelerator Systems*, Brochure, website: `http://www.highvolteng.com/media/Brochures/Tandetron_broch.pdf`.

[371] J. D. Cockroft and E. T. Walton, Nature **129**, 242 (1932).

[372] J. D. Cockroft and E. T. Walton, Proc. Phys. Soc. London A **136**, 619 (1932).

[373] O. Almen and G. Bruce, Nucl. Instr. Meth. **11**, 257 (1961).

[374] P. Sigmund, Phys. Rev. **184**, 383 (1969).

[375] Y. Yamamura and H. Tawara, At. Data Nucl. Data Tables **62**, 149 (1996).

[376] P. H. Kutt, S. F. Pate, A. H. Wuosmaa, R. W. Zurmühle, O. Hansen, R. R. Betts, and S. Saini, Phys. Lett. B **155**, 27 (1985).

[377] L. K. Fifield and N. A. Orr, Nucl. Instr. Meth. Phys. Res. A **288**, 360 (1990).

[378] S. Vouzoukas, C. P. Browne, U. Giesen, J. Görres, S. M. Graff, H. Herndl, C. Iliadis, L. O. Lamm, J. Meissner, J. G. Ross, et al., Phys. Rev. C **50**, 1185 (1994).

[379] J. R. Tesmer and M. Nastasi, eds., *Handbook of Modern Ion Beam Materials Analysis* (Materials Research Society, Pittsburgh, Pennsylvania, 1995).

[380] M. Mayer, *Rutherford Backscattering Spectrometry*, Lectures given at the Workshop on Nuclear Data for Science and Technology: Materials Analysis (Trieste, 19-30 May 2003), website: `http://users.ictp.it/~pub_off/lectures/lns022/Mayer_1/Mayer_1.pdf`.

[381] S. Rubin, T. O. Passell, and E. Bailey, Anal. Chem. **29**, 736 (1957).

[382] M. Mayer, in *Proceedings of the 15th International Conference on the Applications of Accelerators in Research and Industry*, J. L. Duggan and I. L. Morgans, eds., AIP Conf. Proc. **475**, 541 (1999), website: `http://home.rzg.mpg.de/~mam/`.

[383] K. Konac, S. Kalbitzer, C. Klatt, D. Niemann, and R. Stoll, Nucl. Instr. Meth. Phys. Res. B **136**, 159 (1998).

[384] C. Kittel, *Introduction to Solid State Physics* (John Wiley & Sons, Inc., 1996), 7th Edn., p. 57.

[385] H. G. Tompkins and E. A. Irene, eds., *Handbook of Ellipsometry* (William Andrew Publishing Inc., 2005).